

Hydrodynamic Modelling of Offshore Renewables

Experimental Benchmark Datasets and Numerical Simulation

Andersen, Jacob

DOI (link to publication from Publisher):
[10.54337/aau620115007](https://doi.org/10.54337/aau620115007)

Publication date:
2023

Document Version
Publisher's PDF, also known as Version of record

[Link to publication from Aalborg University](#)

Citation for published version (APA):
Andersen, J. (2023). *Hydrodynamic Modelling of Offshore Renewables: Experimental Benchmark Datasets and Numerical Simulation*. Aalborg Universitetsforlag. <https://doi.org/10.54337/aau620115007>

General rights

Copyright and moral rights for the publications made accessible in the public portal are retained by the authors and/or other copyright owners and it is a condition of accessing publications that users recognise and abide by the legal requirements associated with these rights.

- Users may download and print one copy of any publication from the public portal for the purpose of private study or research.
- You may not further distribute the material or use it for any profit-making activity or commercial gain
- You may freely distribute the URL identifying the publication in the public portal -

Take down policy

If you believe that this document breaches copyright please contact us at vbn@aub.aau.dk providing details, and we will remove access to the work immediately and investigate your claim.

HYDRODYNAMIC MODELLING OF OFFSHORE RENEWABLES

EXPERIMENTAL BENCHMARK DATASETS AND
NUMERICAL SIMULATION

BY
JACOB ANDERSEN

DISSERTATION SUBMITTED 2023



AALBORG UNIVERSITY
DENMARK

Hydrodynamic Modelling of Offshore Renewables

Experimental Benchmark Datasets and
Numerical Simulation

Ph.D. Dissertation
Jacob Andersen

Dissertation submitted October 2023

Dissertation submitted: October 2023

PhD supervisor: Associate Professor Morten Bech Kramer
Aalborg University

PhD co-supervisor: Associate Professor Claes Eskilsson
Aalborg University

PhD committee: Associate Professor Jannie Sønderkær Nielsen (chair)
Aalborg University, Denmark

Professor Peter Troch
Ghent University, Belgium

Associate Professor Luca Martinelli
University of Padova, Italy

PhD Series: Faculty of Engineering and Science, Aalborg University

Department: Department of the Built Environment

ISSN (online): 2446-1636
ISBN (online): 978-87-7573-610-2

Published by:
Aalborg University Press
Kroghstræde 3
DK – 9220 Aalborg Ø
Phone: +45 99407140
aauf@forlag.aau.dk
forlag.aau.dk

© Copyright: Jacob Andersen

Printed in Denmark by Stibo Complete, 2023

Contents

| | |
|-------------------------------------------------------|-------------|
| Preface | v |
| Curriculum Vitae | vii |
| Dissertation Details | ix |
| Abstract | xiii |
| Resumé | xv |
| Nomenclature | xvii |
| 1 Introduction | 1 |
| 1.1 Dissertation Outline | 3 |
| 2 State-of-the-Art | 5 |
| 2.1 Governing Equations | 5 |
| 2.2 Hydrodynamic Modelling Approaches | 8 |
| 2.2.1 Computational Fluid Dynamics | 8 |
| 2.2.2 Linear Potential Flow | 9 |
| 2.2.3 Intermediate Modelling Approaches | 9 |
| 2.3 Verification and Validation | 11 |
| 3 Research Contribution | 15 |
| 3.1 Experimental Benchmark Datasets | 16 |
| 3.1.1 Validation Experiments | 17 |
| 3.1.2 Uncertainty Quantification | 25 |
| 3.2 Benchmarking of Numerical Models | 31 |
| 3.2.1 Normal Flow past a Flat Plate | 31 |
| 3.2.2 Wave Propagation over a Submerged Bar | 35 |
| 3.2.3 Sphere Decay Tests | 40 |
| 3.2.4 Moored FOWT Platform in Focused Waves | 43 |

| | |
|----------------------------------------------------------------------------------------------------------------------------------------------------------------|---------------|
| 3.3 Early Design Investigations | 46 |
| 3.3.1 Perforation of Large Monopiles | 46 |
| 3.3.2 Wave-Activated Body of an OWSC | 48 |
| 4 Conclusions | 51 |
| References | 55 |
| Paper Collection | 67 |
| A Wave Load Mitigation by Perforation of Monopiles | 69 |
| B Highly Accurate Experimental Heave Decay Tests with a Floating Sphere: A Public Benchmark Dataset for Model Validation of Fluid–Structure Interaction | 87 |
| C Detached-Eddy Simulation of Normal Flow past Flat Plates: The Influence from Corner Curvature | 129 |
| D Hydrodynamic Simulations of a FOWT Platform (1st FOWT Comparative Study) Using OpenFOAM Coupled to Moody-Core | 139 |
| E Wave Excitation Tests on a Fixed Sphere: Comparison of Physical Wave Basin Setups | 149 |
| F Development of the Exowave Oscillating Wave Surge Converter | 161 |
| G Wave Propagation over a Submerged Bar: Benchmarking of VoF, Sigma Transformation, and SPH Numerical Models against Physical Wave Flume Tests | 171 |

Preface

In late elementary school, my math teacher Jan one day challenged us to draw impossible geometries like parallel lines that would intersect or triangles with an angular sum of more than 180 degrees. While the tasks at first glimpse seemed contradicting and unsolvable (strictly speaking, they were), Jan helped us challenge our assumptions and push our imagination; for what if lines could warp and bend and the world of straight lines in two-dimensional space were only subsets of something greater?

After elementary school, I have been so fortunate in getting to spend 12 years educating myself further, and if I at any point doing these years got fed up with uncertainty analyses or, God forbid, 2nd order partial differential equations, I liked to think back on moments where mere curiosity and fascination with the fantastic complex world around us sparked. Thank you Jan and great teachers I have met along the way.

At some point teachers changed into lecturers and supervisors while, arguably more importantly, others changed into fellow students and colleagues. Among this mix I am thankful to have found many good friends. I would like to express my gratitude to my Ph.D. supervisors Morten Bech Kramer and Claes Eskilsson for the guidance and countless valuable inputs I have received in experimental and numerical testing (respectively!). Thank you to Thomas Lykke Andersen who was my Master's thesis supervisor and who recommended me as a Ph.D. student. A special salute to my CFD-partner-in-crime and friend Jakob Hærvig who first introduced me to the fantastic, time-consuming world of CFD modelling and who later regretted it due to all the extra hours it consumed out of him.

Lastly, the deepest gratitude to the ones closest to me; my sister and parents for your unwavering support; my fiancée Marie without whom I would have done a better dissertation, but missed out on so much more; and my favorite person in the whole wide world my daughter Ingrid. Be curious.

Jacob Andersen
Aalborg, October 2023

Curriculum Vitae

Jacob Andersen

DATE OF BIRTH:

31 March 1995

WORK ADDRESS:

Aalborg University (AAU)
Department of the Built Environment
Thomas Manns Vej 23
DK - 9220 Aalborg Ø



ACADEMIC CAREER:

| | |
|-------------|--------------------------------------------------------------------------------------------------------------------------------|
| 2021 - 2023 | Ph.D. Fellow, Division of Civil and Environmental Engineering, AAU |
| 2019 - 2021 | Research Assistant, Division of Civil and Environmental Engineering, AAU |
| 2017 - 2019 | M.Sc. in Structural and Civil Engineering, AAU, with 8th semester at the Norwegian University of Science and Technology (NTNU) |
| Summer 2017 | Internship, COWI India Private Ltd., Chennai |
| 2014 - 2017 | B.Sc. in Structural and Civil Engineering, AAU |

EXPERIENCE:

Jacob Andersen's work revolves around experimental and numerical hydrodynamic testing of predominantly offshore renewables and critical components hereof. Key topics of his work are computational fluid dynamics (CFD), physical wave basin tests, verification and validation, and uncertainty analysis. During his employment at AAU, he has collaborated with companies from the wind and wave energy sectors in multiple research projects. He has experience with high-performance computing (HPC) with open-source CFD codes (primarily OpenFOAM) and simple bash-scripting. Besides research, Jacob has supervised and lectured in the topics of hydrodynamics and structural engineering at Bachelor's and Master's levels.

Dissertation Details

| | |
|-----------------------------|------------------------------------------------------------------------------------------------------------------------------------------------------------------------------------------------------------------------------------------------------------------------------------------------------------------------------------------------------------------------------------------------------------------------------------------------------------------------------------------------------------------------------------------------------------------------------------------------------------------------------------------------|
| Dissertation Title: | Hydrodynamic Modelling of Offshore Renewables: Experimental Benchmark Datasets and Numerical Simulation |
| Ph.D. Student: | Jacob Andersen |
| Ph.D. Supervisor: | Assoc. Prof. Morten Bech Kramer, AAU |
| Ph.D. Co-Supervisor: | Assoc. Prof. Claes Eskilsson, AAU |
| Projects: | <p><i>OES Task 10 WEC Modelling Verification and Validation.</i> Funded by the Danish Energy Agency under the Energy Technology Development and Demonstration Program (EUDP, grant agreement no. 64020-1105).</p> <p><i>VALID - Verification through Accelerated testing Leading to Improved wave energy Designs.</i> Funded by the European Union under the Horizon 2020 research and innovation program (grant agreement no. 101006927).</p> <p><i>Exowave, Water, Electricity and PtX.</i> Funded by the Danish Energy Agency under the Energy Technology Development and Demonstration Program (EUDP, grant agreement no. 64022-1062).</p> |

The present dissertation is formatted as a collection of papers. The following seven papers are presented in an extended summary and appended. Six of the papers are peer-reviewed and one (Paper G) is submitted.

- [A] Andersen, J., Abrahamsen, R., Lykke Andersen, T., Andersen, M. T., Baun, T. L., & Neubauer, J. L. (2020). Wave Load Mitigation by Perforation of Monopiles. *Journal of Marine Science and Engineering*, 8(5). <https://doi.org/10.3390/jmse8050352>
- [B] Kramer, M. B., Andersen, J., Thomas, S., Bendixen, F. B., Bingham, H., Read, R., Holk, N., Ransley, E., Brown, S., Yu, Y. H., Tran, T. T., Davidson, J., Horvath, C., Janson, C. E., Nielsen, K., & Eskilsson, C. (2021). Highly Accurate Experimental Heave Decay Tests with a Floating Sphere: A Public Benchmark Dataset for Model Validation of Fluid–Structure Interaction. *Energies*, 14(2). <https://doi.org/10.3390/en14020269>
- [C] Andersen, J., & Eskilsson, C. (2023). Detached-Eddy Simulation of Normal Flow past Flat Plates: The Influence from Corner Curvature. *Proceedings of the Thirty-Third (2023) International Ocean and Polar Engineering Conference* (pp. 2441–2448). International Society of Offshore and Polar Engineers (ISOPE). ISBN: 978-1-880653-80-7.
- [D] Eskilsson, C., Verao Fernández, G., Andersen, J., & Palm, J. (2023). Hydrodynamic Simulations of a FOWT Platform (1st FOWT Comparative Study) Using OpenFOAM Coupled to MoodyCore. *Proceedings of the Thirty-Third (2023) International Ocean and Polar Engineering Conference* (pp. 461-468). International Society of Offshore and Polar Engineers (ISOPE). ISBN: 978-1-880653-80-7.
- [E] Andersen, J., & Kramer, M. B. (2023). Wave Excitation Tests on a Fixed Sphere: Comparison of Physical Wave Basin Setups. *Proceedings of the 15th European Wave and Tidal Energy Conference (EWTEC 2023)*. <https://doi.org/10.36688/ewtec-2023-170>
- [F] Iversen, S. K., Andersen, J., Wigant, L., & Frigaard, P. (2023). Development of the Exowave Oscillating Wave Surge Converter. *Proceedings of the 15th European Wave and Tidal Energy Conference (EWTEC 2023)*. <https://doi.org/10.36688/ewtec-2023-368>
- [G] Andersen, J., Eldrup, M. R., Verao Fernández, G., & Ferri, F. (2023). Wave Propagation over a Submerged Bar: Benchmarking of VoF, Sigma Transformation, and SPH Numerical Models against Physical Wave Flume Tests. Submitted to *Journal of Hydrodynamics*. ISSN: 1878-0342.

Besides the appended papers, the Ph.D. student has co-authored the following reports and papers which are extensions of the works presented in the dissertation.

- [1] Andersen, J., Kramer, M. B., & Ebsen, N. (2020). *Statistical Analysis of Time Series for the Floating Power Plant P80 Device* (1st ed.). DCE Contract Reports No. 209. Department of the Built Environment, Aalborg University.
- [2] Kramer, M. B., Andersen, J., Ebsen, N., & Thomas, S. (2020). *Plans for Wave Basin Tests of the Floating Power Plant P80 Device under the OESA Project and the EUDP O&G Project* (1st ed.). DCE Technical Reports No. 292. Department of the Built Environment, Aalborg University.
- [3] Anton Aguilar, M., Eskilsson, C., Andersen, J., Kramer, M. B., & Thomas, S. (2020). Floating Power Plant Hybrid Wind-Wave Platform: CFD Simulations of the Influence of Chamber Geometry. In C. Guedes Soares (Ed.), *Developments in Renewable Energies Offshore: Proceedings of the 4th International Conference on Renewable Energies Offshore, RENEW 2020* (pp. 265–273). CRC Press. ISBN: 978-0-367-68131-9.
- [4] Kramer, M. B., Andersen, J., & Nielsen, K. (2023). *Wave Excitation Forces on a Sphere: Description of an Idealized Testcase* (1st ed.). DCE Technical Reports No. 307. Department of the Built Environment, Aalborg University.
- [5] Kramer, M. B., & Andersen, J. (2023). *Wave Excitation Forces on a Sphere: Description of an Physical Testcase* (1st ed.). DCE Technical Reports No. 308. Department of the Built Environment, Aalborg University.

Abstract

The transition from fossil fuels to renewable energy sources is critical to reduce greenhouse gas emissions and increase global energy access and security. To harness the abundant renewable energy resources from and at the ocean, the European Union has set ambitious targets to increase its installed capacity of offshore renewable energy technologies to 300 GW of offshore wind energy and 40 GW of ocean energy (e.g., wave and tidal) by 2050. To reach these targets, the levelized cost of energy of emerging offshore renewables must be reduced in which accurate and efficient hydrodynamic models are paramount to maintain low expenditures and agility throughout the design process. The present dissertation revolves around the hydrodynamic modelling of offshore renewables with emphasis on offshore wind turbines (bottom-fixed and floating) and wave energy converters.

Most hydrodynamic models used in the engineering of offshore renewables are numerical models. To establish credibility of simulation results from numerical models, the activities of verification and validation are employed. Validation involves the comparison of simulation results with reality, expressed through experimental data. Validation experiments compose a relatively new type of experiments that has emerged with the increased processing power of modern computers. They differ from traditional experiments in several aspects, aiming to reduce the validation uncertainty and, thus, advance numerical model credibility. Validation of numerical models used for the hydrodynamic modelling of offshore renewables is only feasible at low tiers where the technology geometry is simplified and the physics are decoupled. Only rarely are validation experiments embarked upon within the field of hydrodynamic modelling of offshore renewables. This dissertation accounts for validation experiments dedicated to the construction of public experimental benchmark datasets for i) the heave decay of a floating sphere, ii) the wave excitation of a fixed sphere, and iii) the wave propagation over a submerged bar. The value of preliminary numerical or experimental tests to enhance experimental designs is underlined, and methods for experimental uncertainty quantification are presented.

The predominant hydrodynamic modelling approaches for offshore renewables are introduced, displaying a broad landscape with significantly different

levels of fidelity, computational costs, ease-of-use, etc. The dissertation includes numerical studies into four different flow problems relevant for the hydrodynamic modelling of offshore renewables, i.e., i) the normal flow past a flat plate, ii) the wave propagation over a submerged bar, iii) the heave decay of a floating sphere, and iv) a moored floating offshore wind turbine platform impacted by focused waves. The studies give insights into the numerical modelling of said flow problems and are reviewed focusing on numerical model benchmarking (against conducted validation experiments on flow problems ii and iii).

Finally, the dissertation accounts for hydrodynamic investigations of the early designs of a large monopile with perforations, to reduce fatigue wave loads, and the wave-activated body of a wave energy converter of the oscillating-wave-surge-converter-type.

Resumé

Overgangen fra fossile brændsler til vedvarende energikilder er afgørende for at reducere udledningen af drivhusgasser og øge den globale adgang til energi samt forsyningssikkerhed. For at udnytte den signifikante vedvarende energiressource fra og på havene har den Europæiske Union sat ambitiøse mål om at udvide dennes installerede kapacitet fra offshore vedvarende energikilder til 300 GW offshore vindenergi og 40 GW havenergi (indbefattende eksempelvis bølge- og tidevandsenergi) senest i 2050. For at imødekomme disse mål skal fremspirende vedvarende offshore-energiteknologier gøres mere rentable, hvilket kræver præcise og effektive hydrodynamiske modeller til at opretholde lave omkostninger og fleksibilitet under designprocessen. Nærværende ph.d.-afhandling omhandler hydrodynamisk modellering af vedvarende offshore-energiteknologier med fokus på havvindmøller (med bundfikserede såvel som flydende fundamenter) samt bølgeenergianlæg.

Størstedelen af hydrodynamiske modeller anvendt til at designe vedvarende offshore-energiteknologier er numeriske modeller. Til at underbygge pålideligheden af simuleringresultater fra numeriske modeller benyttes verifikation og validering. Validering involverer sammenligningen af simuleringresultater med virkeligheden udtrykt via eksperimentel data. Valideringseksperimenter udgør en relativt ny type af eksperimenter, der er opstået med den stadigt stigende processorkraft i moderne computere. Disse afviger fra traditionelle eksperimenter i adskillige henseender og er rettet imod at mindske valideringssikkerheder for at forbedre pålideligheden af numeriske modeller. Valideringen af numeriske modeller anvendt til den hydrodynamiske modellering af vedvarende offshore-energiteknologier er kun praktisk mulig med simplifikationen af teknologiens geometri og separationen af fysiske fænomener. Kun få valideringseksperimenter er blevet udført inden for feltet hydrodynamisk modellering af vedvarende offshore-energiteknologier. Denne afhandling præsenterer valideringseksperimenter, der er blevet udført for at udgive offentlige, eksperimentelle datasæt fra i) sætningen af en flydende kugle efter vertikal forskydning, ii) kraften fra indkommende bølger på en fikseret kugle og iii) bølgeudbredelse over en vanddækket barre. Værdien af indledende tests, numeriske og/eller eksperimentelle, til at forbedre forsøgsopstillingen understreges, og

forskellige metoder til at kvantificere den eksperimentelle usikkerhed præsenteres.

De mest udbredte hydrodynamiske modelleringsmetoder inden for vedvarende offshore-energiteknologier introduceres, hvilket fremhæver et bredt spektrum af modeller med vidt forskellig præcision, beregningsomkostninger, brugervenlighed med videre. Afhandlingen redegør for numeriske studier af fire forskellige strømningsproblemer, som er relevante for den hydrodynamiske modellering af vedvarende offshore-energiteknologier. Disse indbefatter i) normal strømning forbi en flad plade, ii) bølgeudbredelse over en vanddækket barre, iii) sætningen af en flydende kugle efter vertikal forskydning og iv) en forankret platform til flydende offshore vindmøller påvirket af fokuserede bølger. Studierne bidrager til forståelsen af numerisk modellering af nævnte strømningsproblemer og er opsummeret med fokus på at sammenligne flere forskellige numeriske modeller.

Slutteligt inkluderer afhandlingen hydrodynamiske undersøgelser af tidlige design af en perforeret monopæl med stor diameter, skabt med henblik på at mindske udmattelseskrafter fra bølger, samt det bølge-exciterede modul fra et bølgeenergi-anlæg.

Nomenclature

Abbreviations

| | |
|-------------|---------------------------------------------------------|
| BC | Boundary Condition |
| BEM | Boundary Element Method |
| CFD | Computational Fluid Dynamics |
| DES | Detached-Eddy Simulation |
| DNS | Direct Numerical Simulation |
| DoF | Degrees of freedom |
| EUDP | Energy Technology Development and Demonstration Program |
| EU | European Union |
| FEM | Finite Element Method |
| FK | Froude-Krylov |
| FNPF | Fully Nonlinear Potential Flow |
| FOWT | Floating Offshore Wind Turbine |
| FVM | Finite Volume Method |
| GCI | Grid Convergence Index |
| GHG | Greenhouse Gas |

| | |
|-------------|-------------------------------------------------------|
| GPU | Graphical Processing Unit |
| GUM | Guide to the Expression of Uncertainty in Measurement |
| HPC | High-Performance Computing |
| IC | Initial Condition |
| IFFT | Inverse Fast Fourier Transform |
| IPCC | Intergovernmental Panel on Climate Change |
| ISO | International Organization for Standardization |
| LCoE | Levelized Cost of Energy |
| LES | Large-Eddy Simulation |
| LPF | Linear Potential Flow |
| OES | Ocean Energy Systems |
| OWSC | Oscillating Wave Surge Converter |
| PF | Potential Flow |
| PTO | Power Take-Off |
| PV | Photovoltaic |
| SMS | Scale-Modelling Simulation |
| SPH | Smoothed-Particle Hydrodynamics |
| SRS | Scale-Resolving Simulation |
| SST | Shear Stress Transport |
| SWL | Still Water Level |
| TPL | Technology Performance Level |
| TRL | Technology Readiness Level |

| | |
|----------------|------------------------------------------|
| UI | Uncertainty Interval |
| URANS | Unsteady Reynolds-Averaged Navier-Stokes |
| V&V | Verification and Validation |
| VoF | Volume of Fluid |
| WEC | Wave Energy Converter |
| WG | Wave Gauge |
| WNPF | Weakly Nonlinear Potential Flow |

Accents

| | |
|-----------|--------------------------------------|
| \bar{x} | Sample mean (arithmetic mean) of x |
| \hat{x} | Estimate of x |

Greek Symbols

| | |
|------------|--------------------------------------|
| α | Phase fraction field |
| δ | Evaluation metric |
| ϵ | Validation comparison error |
| η^* | Surface elevation (measurand) |
| η | Surface elevation (measurement) |
| γ_0 | Convergence rate |
| μ | Dynamic viscosity |
| ν | Kinematic viscosity |
| ω | Turbulence specific dissipation rate |
| ϕ | Phase |
| ψ | Calibration parameter (slope) |

| | |
|---------------|-------------------------------|
| ρ | Density |
| Θ | Measurand |
| θ | Measurement |
| \mathcal{U} | Expanded uncertainty |
| v | Combined standard uncertainty |
| ε | Turbulence dissipation rate |
| φ | Velocity potential |

Latin Symbols

| | |
|-------|-------------------------------------|
| A | Cross-sectional area |
| a | Amplitude |
| b | Systematic standard uncertainty |
| C_A | Coefficient of added mass |
| C_D | Coefficient of drag |
| c_f | Coverage factor |
| D | Diameter |
| D_c | Largest diameter of conical frustum |
| F | Force |
| g | Acceleration due to gravity vector |
| H | Wave height |
| h_c | Conical frustum height |
| h_p | Plate height |
| I_n | Identity Matrix of Size n |

| | |
|-----------|------------------------------------------|
| k | Turbulence kinetic energy |
| K_C | Keulegan-Carpenter number |
| L | Wavelength |
| l | Characteristic cross-sectional dimension |
| N | Sample size |
| p | Pressure |
| q | Structure velocity response |
| r | Corner radius |
| Re | Reynolds number |
| s | Random standard uncertainty |
| s_{td} | Sample standard deviation |
| T | Wave period |
| t | Time |
| t_p | Plate thickness |
| T_{e0} | Damped natural period |
| V | Voltage |
| X_3 | Heave displacement (measurand) |
| x_3 | Heave displacement (measurement) |
| $x_{3,0}$ | Drop height (initial heave displacement) |
| U | Flow velocity vector |

1 | Introduction

The Sixth Assessment Report (IPCC, 2023) from the Intergovernmental Panel on Climate Change (IPCC), under the United Nations, concludes that rapid changes in climate and weather extremes have occurred in all regions of the world causing damages and irreversible losses to nature and people. The report further states that human activities, led by greenhouse gas (GHG) emissions, are unequivocally behind global warming and are likely at the core of observed changes of weather extremes since the 1950s (IPCC, 2023). The transition from fossil fuels to renewable energy sources is a key element in the reduction of GHG emissions to limit and mitigate the adverse impacts of climate change by keeping the global average temperature increase below 2 °C above pre-industrial levels as per the Paris agreement (Gielen et al., 2019). The transition is additionally motivated from the more equal global energy distribution of renewable energy sources, such as wind, solar, bio-, or hydropower, relative to their fossil counterparts of which the majority of resources are owned by few countries (Ritchie et al., 2022). Global energy access and security are thus more readily improved with the transition to renewable energy sources (Gielen et al., 2019) causing decreased risks of energy conflicts, as, e.g., under the ongoing Russo-Ukrainian War, and enhanced energy supply to isolated communities such as small island states.

Substantial renewable energy resources are available at and from the ocean (Bahaj, 2011; Sun et al., 2012). Ocean energy technologies convert energy *from* the oceans as opposed to, e.g., offshore wind turbines or solar photovoltaic (PV) converting wind and solar energy *at* the ocean. To reach GHG emission mitigation targets and accelerate the transition to renewable energy sources, the European Union (EU) has set ambitious targets to increase the capacity of offshore renewable energy technologies by 2050 to 300 GW and 40 GW for offshore wind and ocean energy technologies, respectively (European Commission, 2020). Ocean energy technologies encompass, most notably, wave energy converters (WECs) and tidal energy converters. The installed capacity and maturity of the predominant offshore renewables in the EU are shown in Fig. 1.1. The expansion of the onshore renewable capacity is often limited by land availability, infrastructure, and visual/audible pollution

as, e.g., in the case of onshore wind farms (Sun et al., 2012). Such problems are significantly reduced with offshore deployments where, on the other hand, harsh environments challenge structural designs and accessibility. Bottom-fixed offshore wind have overcome these obstacles and matured to full commercialization with levelized costs of energy (LCoE) competitive to those of fossil fuels (IRENA, 2022). Floating offshore wind and ocean energy technologies are at earlier maturity stages and require further R&D to drive down their LCoE and reach commercialization (European Commission, 2020; IRENA, 2020). These technologies have not converged in their designs as seen prior to the commercialization of onshore and bottom-fixed offshore wind (IRENA, 2020).

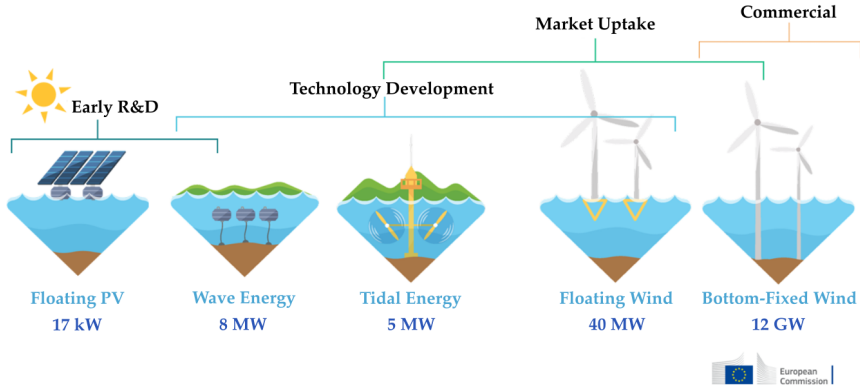


Fig. 1.1: Maturity stages and installed capacities of offshore renewable energy technologies in the EU (2019/2020 levels). Adapted from European Commission (2020).

For a novel offshore renewable energy technology to reach commercialization, the *Performance before Readiness* strategy advocates the optimization of the technology performance level (TPL, associated with LCoE) at low technology readiness levels (TRL, associated with total R&D expenditures) to allow for less expensive technology development and, hence, decrease the risk of bankruptcy before market entry (Weber et al., 2013). Design optimizations to increase the performance and reduce the LCoE of less mature offshore renewables are unfeasible using experimental testing exclusively, and largely depends on accurate and efficient hydrodynamic models (commonly involving numerical simulation).

The present dissertation revolves around the hydrodynamic modelling of offshore renewables with emphasis on offshore wind and wave energy technologies. *Offshore renewables* in the present dissertation, as well as widely acknowledged in the literature and public, denotes renewable energy technologies with a marine deployment and as such covers technologies deployed both off- and nearshore. In contrast, *marine renewables* is often used interchangeably with ocean renewables and thus exclude offshore wind, solar PV, etc.

1.1 Dissertation Outline

The dissertation is based on seven research papers included as appendices (Paper Collection). Chapters 1-4 present an extended summary of the papers. Chapter 1 (Introduction) has motivated the need for offshore renewables and hydrodynamic modelling hereof. Chapter 2 (State-of-the-Art) introduces the predominant methods in the field of hydrodynamic modelling of offshore renewables. Chapter 3 (Research Contribution) reviews the appended papers focusing on three identified research topics of i) experimental benchmark datasets from validation experiments, ii) numerical model benchmarking for selected flow problems, and iii) hydrodynamic investigations of early designs of offshore renewable energy technologies. Chapter 4 (Conclusions) outlines the most important findings and some future perspectives.

2 | State-of-the-Art

The present chapter introduces the governing equations within the hydrodynamic modelling of offshore renewables in Section 2.1 and gives a brief overview of the prevalent methods in the field in Section 2.2. The assessment of model credibility by verification and validation is introduced in Section 2.3.

2.1 Governing Equations

The governing equations of the dynamics of Newtonian fluids, encompassing the field of hydrodynamics, are expressed by the general Navier-Stokes equations (Munson et al., 2013). The general Navier-Stokes equations express the conservation of mass and momentum of a Newtonian fluid accounting for the compressibility of the fluid, i.e., variable density. The general Navier-Stokes equations are given in Eq. (2.1) after imposing the commonly used Stokes hypothesis. To close the system of equations, the general Navier-Stokes equations are complemented with an energy conservation equation and an equation of state. In the context of hydrodynamic modelling of offshore renewables, the inclusion of compressibility is only significant in somewhat limited applications involving primarily high pressure gradients in an air phase, e.g., the modelling of an air chamber in a oscillating-water-column-type WEC as in Bingham et al. (2021) or slamming loads with air entrainment in breaking waves impacting structures as in Bredmose et al. (2009).

Incompressible Flow

Imposing the assumption of constant density yields the incompressible Navier-Stokes equations in Eq. (2.2) which eliminates a dependent variable and, hence, the need for the two additional equations to close the system of equations. The assumption of incompressibility is usually very accurate in the hydrodynamic modelling of offshore renewables (Mach numbers are well below 0.3). Thus, Eq. (2.2) forms the basis of most high-fidelity hydrodynamic models relevant for offshore renewables. While such models remain computationally inefficient,

the review paper of Windt et al. (2018) presented how publications with Navier-Stokes-based hydrodynamic models to simulate WECs have increased over the past decades from virtually zero publications in the early 2000s to about 40 yearly publications by 2017 (with the majority being of the incompressible type). Examples of other applications include the simulation of wave-breaking in, e.g., Fernandez-Mora et al. (2017) and Li et al. (2022) as well as the flow around heave plates of floating offshore wind turbines (FOWT) platforms in, e.g., Jiang et al. (2020), Liu et al. (2017), and Lopez-Pavon and Souto-Iglesias (2015).

Incompressible and Inviscid Flow

With the assumption of inviscid flow, i.e., viscosity is zero, the incompressible Navier-Stokes equations simplify to the Euler equations in Eq. (2.3) where the diffusion (1st RHS) term of the Eq. (2.2) disappears. The Euler equations can be deployed with good accuracy where inertial forces are highly dominant over viscous forces such as in high-Reynolds flows away from boundaries and shear layers. The Euler equations were utilized in the hydrodynamic modelling of the motion response of two moored point absorber WECs in Palm et al. (2018) and the overtopping discharge of an overtopping-type WEC in Eskilsson et al. (2014) showing only slight deviations to viscid models (incompressible Navier-Stokes).

Potential Flow

The assumption of irrotational flow, i.e., vorticity is zero, implies that the velocity vector can be described as the gradient of a scalar potential (velocity potential). Expressing the (incompressible) conservation of mass by the velocity potential yields Laplace's equation of the velocity potential, see Eq. (2.4). This is referred to as ideal or potential flow (PF) theory and is a substantial simplification to the Euler equations as the flow field is now defined from a single equation/variable (instead of four). In PF theory, pressure is decoupled and can be calculated by the Bernoulli equation derived from the conservation of momentum in Eq. (2.3). PF-based models were, for instance, used in the simulation of wave-interactions between several WECs placed in arrays, otherwise infeasible with Navier-Stokes and Euler-based models, in, e.g., Verano Fernández et al. (2018), Borgarino et al. (2012), and Folley and Whittaker (2011).

Overview of Governing Equations

The various governing equations and simplifying assumptions accounted for in the present section are summarized in Fig. 2.1, where $U = [u_x \ u_y \ u_z]^T$ is

the three-dimensional flow velocity vector, ρ is the density, μ is the dynamic viscosity, ν is the kinematic viscosity, g is the acceleration vector due to gravity, I_3 is the three-dimensional identity matrix, and φ is the velocity potential. The relation between the velocity vector and the velocity potential is given by $U = -\nabla\varphi$. Solutions to the equations of Fig. 2.1 is non-trivial for the majority of offshore renewable applications, and often only numerical solutions can be obtained. The computational efficiency of numerical solutions to the governing equations in Fig. 2.1 generally increases with increasing equation numbers (top-down) at the expense of the fidelity (Windt et al., 2018).

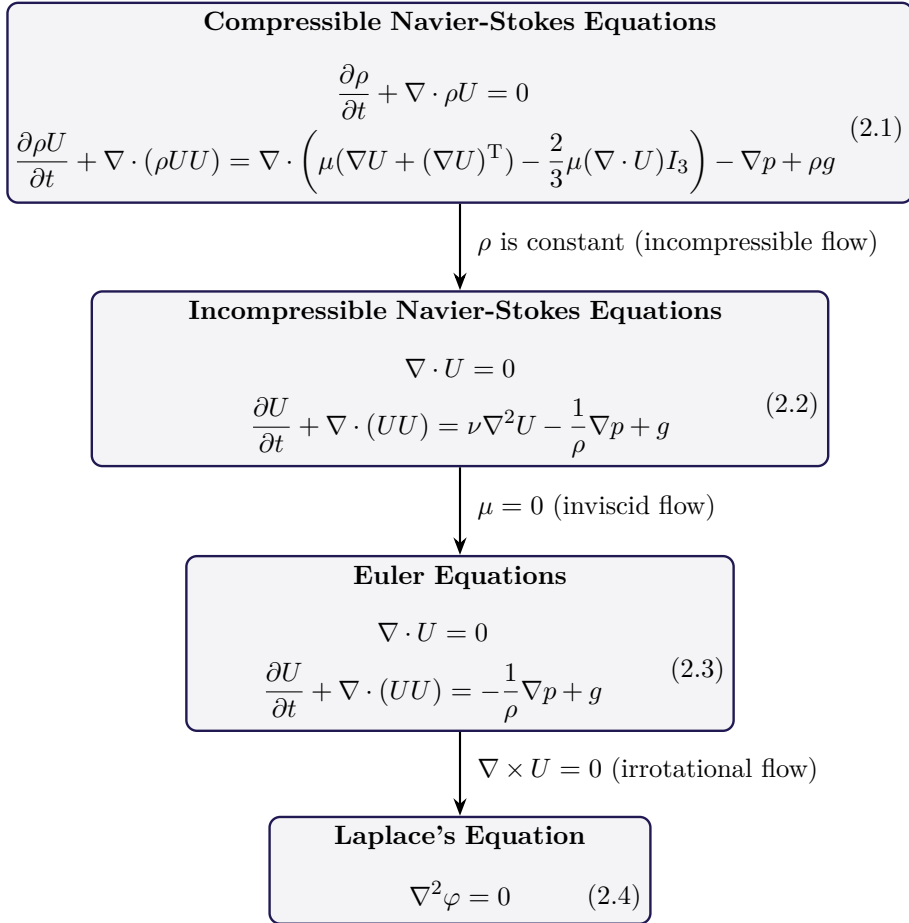


Fig. 2.1: Governing equations of hydrodynamics starting with the compressible Navier-Stokes equations and introducing simplifying assumptions.

2.2 Hydrodynamic Modelling Approaches

Viewing the predominant hydrodynamic modelling approaches in the field of offshore renewables in light of their cost-accuracy trade-off, Navier-Stokes-type computational fluid dynamics (CFD) and linear potential flow (LPF) models make up two opposite extremes. The present section gives a brief introduction to the hydrodynamic models at these two extremes and intermediate to these.

2.2.1 Computational Fluid Dynamics

At the high-fidelity, computationally expensive side of hydrodynamic modelling approaches is CFD which commonly, and in the present dissertation, denotes models numerically solving the Navier-Stokes equations, Eqs. (2.1) or (2.2). Solutions to the Navier-Stokes equations must be approximated from numerical methods as no general analytical solution is available. The discretization of the Navier-Stokes equations are based on i) mesh methods, ii) particle methods, or iii) particle distribution field methods. In the hydrodynamic modelling of offshore renewables, the Eulerian, mesh-based Finite Volume Method (FVM) is among the most common and established methods to represent and numerically solve the Navier-Stokes equations (Davidson & Costello, 2020; Guo & Ringwood, 2021) and is the basis of most industry CFD packages such as **Simcenter Star-CCM+** (Siemens Digital Industries Software, 2023), **Ansys Fluent** (Ansys Inc., 2023b), **Ansys CFX** (Ansys Inc., 2023a), and **OpenFOAM** (Weller et al., 1998). However, Lagrangian, particle-based methods, in specific, Smoothed-Particles Hydrodynamics (SPH), have become increasingly popular in recent years, e.g., from their inherent ability to track the free surface, thus avoiding the need for special free surface treatments as in conventional mesh-based methods (Lind et al., 2020). For example, SPH models were used to simulate interactions of floating bodies and waves in Manenti et al. (2008), Westphalen et al. (2014), and Crespo et al. (2020). Methods based on particle distribution fields such as the Lattice Boltzmann method have had somewhat limited application to hydrodynamic modelling of offshore renewables but have shown potential in accurate and efficient modelling in highly parallelized simulations with graphical processing units (GPUs) and/or large computer clusters (Janßen et al., 2013).

The fidelity of CFD methods is largely dictated from the levels of scale-resolving simulation (SRS) and scale-modelling simulation (SMS) taken on. SRS directly simulates (resolves) all or part of the spatial and temporal scales in a given flow whereas SMS uses models to calculate their effect on averaged quantities, e.g., the ensemble-averaged flow fields in unsteady Reynolds-Averaged Navier-Stokes (URANS) simulations. SRS where all scales are resolved is referred to as direct numerical simulation (DNS) and is computationally too expensive for any practical application for offshore renewables (Davidson &

Costello, 2020). A range of methods to combine SRS and SMS exists, such as large-eddy simulation (LES) and detached-eddy simulation (DES) as discussed in the context of normal flow to a flat plate in Section 3.2.1.

2.2.2 Linear Potential Flow

At the low-fidelity, computationally inexpensive side of hydrodynamic modelling approaches is LPF which encompasses models numerically solving Laplace’s equation, Eq. (2.4), after imposing the further simplifying assumptions of linear wave theory and small body oscillations. These assumptions linearize the Bernoulli equation and boundary conditions (BCs) used to evaluate Laplace’s equation. By the principle of superposition, the velocity potential φ can then be described as

$$\varphi = \varphi_i + \varphi_d + \varphi_r , \quad (2.5)$$

where φ_i is the incident velocity potential, φ_d is the diffracted velocity potential, and φ_r is the radiated velocity potential. φ_i is known analytically (from linear wave theory) whereas φ_d and φ_r are only known analytically for simple geometries such as spheres and cylinders (e.g., Li et al., 2019; Li & Liu, 2019). For arbitrarily shaped bodies, the boundary element method (BEM) is often employed to numerically solve for φ_d and φ_r in the frequency domain (Faltinsen, 1990; Newman, 1977; Wehausen & Laitone, 1960). The significantly higher computational efficiency of LPF models (relative to LES or URANS models) puts these at the core of most industry hydrodynamic models, e.g., the WAMIT (Lee & Newman, 2006), OrcaWave (Orcina Ltd, 2023), and NEMOH (Babarit & Delhommeau, 2015) BEM packages, used in the analysis and performance optimization of WECs and FOWTs as, for example, seen in Andersen (2016) and Thomsen (2017). Transformations into time domain representations can be achieved by application of the Cummins equation (Cummins, 1962) as seen for LPF models in Kramer et al. (2021, Paper B).

2.2.3 Intermediate Modelling Approaches

The above paragraphs have briefly introduced the two major approaches to physics-based hydrodynamic modelling of offshore renewables. Intermediate to CFD and LPF hydrodynamic models are a wide range of hydrodynamic models more computationally efficient than CFD but with less simplifying assumptions than LPF.

Nonlinear Potential Flow

Imposing the instantaneous wetted surface and nonlinear free surface as BCs yields the class of fully-nonlinear potential flow (FNPF) models. The compu-

tational efficiency of FNPF models are substantially less than those of CFD models. For instance, Ransley et al. (2019) benchmarked multiple FNPF and CFD models against experimental data on a floating production and offloading vessel scaled model impacted by focused waves, finding FNPF models to be of similar high accuracy as those of CFD models but with computational costs of about one order of magnitude smaller. Yet, FNPF models are significantly more computationally inefficient relative to LPF models.

Two widespread methods intermediate to FNPF and LPF models in terms of both fidelity and computational cost are the body-exact and weak-scatterer methods. The instantaneous body motion is computed in body-exact methods taking into account nonlinear Froude-Krylov (FK), radiation, diffraction, and hydrostatic forces but linearizing the free surface around $z = 0$. Weak-scatterer methods impose the instantaneous free surface of incident waves allowing the consideration of steep (nonlinear) incident waves. The influence of nonlinear (body-exact) evaluation of hydrostatics and radiation in the heave decay of a sphere were investigated in Kramer et al. (2021, Paper B).

Viscosity and the Morison Equation

As a direct consequence of the assumptions of PF theory (see Section 2.1) viscosity is not inherently accounted for in any PF-based hydrodynamic modelling approach. However, to include the effects of viscosity in the hydrodynamic modelling of offshore renewables, a quadratic drag term is often added to the Cummins' equation (Andersen, 2016; Guo & Ringwood, 2021; Thomsen, 2017). This approach is, e.g., utilized in the LPF-based hydrodynamic modules of the **OpenFAST** (OpenFAST, 2023) and **DeepLines Wind** (Principia, 2023) packages for the simulation of FOWTs. The quadratic drag term originates from the Morison equation (Morison et al., 1950) formulated to express the hydrodynamic force on slender structures (piles). In a relative fluid-structure velocity formulation (e.g., DNV, 2017), the Morison equation expresses the sectional normal force acting on a slender structure f_n as

$$f_n = \underbrace{\rho A \frac{d}{dt} u_n}_{FK} + \underbrace{C_A \rho A \frac{d}{dt} (u_n - q_n)}_{added\ mass} + \underbrace{\frac{1}{2} C_D \rho l |u_n - q_n| (u_n - q_n)}_{drag}, \quad (2.6)$$

where A is the cross-sectional area, l is a characteristic cross-sectional dimension, subscript n denotes the normal axis n component, u_n is the fluid particle velocity, q_n is the structure velocity response, C_A is a coefficient of added mass, and C_D is a coefficient of drag. C_D is calculated from experimental or numerical testing whereas C_A is either calculated analytically for simple geometries imposing PF theory or from experimental or numerical testing. Values of C_D and C_A (collectively referred to as Morison coefficients) can be found

for generic geometries under various flow conditions from look-up tables in, for example, DNV (2017). Eq. (2.6) is applicable for slender structures, i.e., the diffraction parameter $\pi D/L < 0.5$ where D is a characteristic diameter and L is the wavelength (Chakrabati, 2005), and has been widely applied in the assessment of hydrodynamic loads on risers, monopiles, jackets (on a member basis), and mooring lines. For example, the hydrodynamic loads on monopiles and mooring lines were assessed with Morison-type formulations in Andersen et al. (2020, Paper A) and Eskilsson et al. (2023b, Paper D), respectively. Additionally, a hydrodynamic model for a small oscillating wave surge converter (OWSC), relative to wavelengths, was developed based on Eq. (2.6) in Iversen et al. (2023, Paper F). However, for most offshore renewables, intended for large scale energy conversion, the assumption of slenderness is violated and diffraction theory must be integrated into the hydrodynamic model.

Data-Driven Models

A full design loop of offshore renewables typically requires several million hours of operation to be simulated (Davidson & Costello, 2020), making computational efficiency of the essence. Hence, LPF remains the most widely used hydrodynamic modelling approach in spite of the somewhat crude assumptions of potential flow as well as small amplitude waves and body motions. Data-driven models pose as one of the most promising methods to account for nonlinear hydrodynamics while maintaining computational efficiency and have become increasingly popular in the hydrodynamic modelling of offshore renewables with the enhancements of machine learning algorithms and GPU hardware in the recent years (Eskilsson et al., 2023a). Data-driven models to simulate WECs were derived from experimental or numerical data in, e.g., Giorgi et al. (2019), Davidson et al. (2016), Giorgi et al. (2016), and Eskilsson et al. (2023a). However, the application range and quality of such models are strongly dependent on the data on which they are formulated or trained which leads back to the need for accurate and efficient physics-based, numerical models and/or experiments.

2.3 Verification and Validation

Numerical hydrodynamic models are principal in the design of offshore renewables as underpinned in the above sections. The credibility of predictions from numerical models strongly relies on the verification and validation (V&V) activities carried out with the numerical model. While V&V is often considered a subdomain of CFD, it is a broad engineering activity that ought to be applied prior to any practical usage of simulation results from numerical models (Roache, 2016). In simple terms, V&V is the quantification and assessment

of the accuracy and precision of a numerical model in a specific application. It should be noted that a numerical model or code, in itself, cannot be validated but rather the numerical solution (simulation results) of the numerical model can be validated against experimental data. Then, the outcomes of a V&V exercise may be used for inference of the credibility of predictions. The verification activity consists of the two distinct stages of code verification and solution verification (Oberkampf & Roy, 2010). Based on the definitions from ASME (2006), the three stages of V&V are introduced below.

Code verification is the process of assessing code implementation correctness and software bugs.

Solution verification is the process of assessing the accuracy of simulation results (numerical solution) to a numerical model.

Validation is the process of assessing the accuracy of simulation results relative to reality expressed through experimental data.

Per se, the verification stages are an applied mathematics exercise not involving any physical reality whereas the validation stage is an applied physics exercise highly concerned with the relationship to reality. Blottner (1990) famously formulated verification as “solving governing equations right” and validation as “solving right governing equations”.

A flowchart of a full V&V activity is outlined in Fig. 2.2. A reality of interest is identified from the considered engineered concept and intended use of the numerical model. The reality of interest can cover the complete system, subsystem, or component of the engineered concept in which the aim typically changes, in the order given, from safety and performance assessment to capture of physics (ASME, 2006; Yeo, 2020). The reality of interest is idealized into a test case including all relevant physics. Subsequently, the idealized test case is represented using physical and mathematical models, respectively. The mathematical model is implemented into computer code as a numerical model and by simulation of the numerical model a numerical solution or simulation result is obtained. The physical model is implemented into an experimental design with measurement equipment and physical equipment for carrying out the experiments. Validation metrics are identified and uncertainties estimated before the agreement between numerical and physical tests is assessed. If sufficient agreement is assessed relative to the intended numerical model use, the model can be used for predictions with increased credibility, and the V&V activity is either ended, or the next reality of interest is considered. Alternatively, if the acceptable agreement is rejected, the V&V activity must be revised and the idealized test case or any later stages updated. This understanding of V&V, visualized in the flowchart in Fig. 2.2, is widely accepted in modern engineering standards within CFD including CFD in offshore hydrodynamic engineering (ASME, 2009; ITTC, 2021).

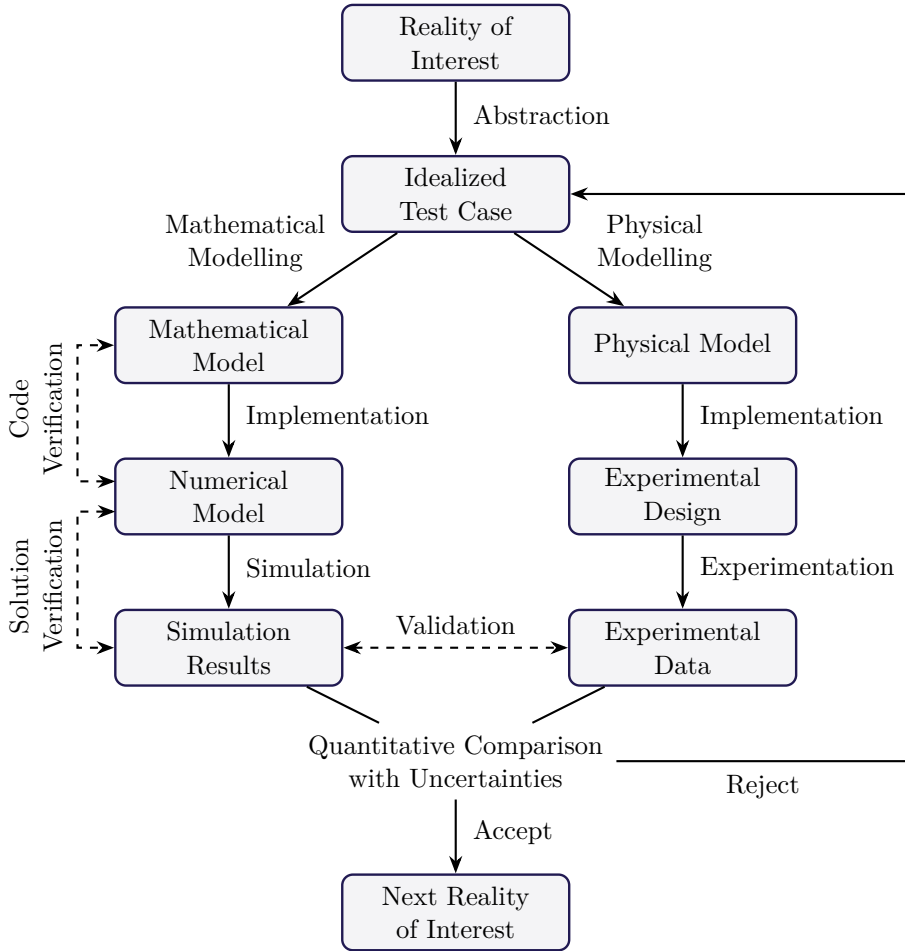


Fig. 2.2: Flow chart of a full V&V activity. Adapted from ASME (2006).

The integral role of physical testing in V&V activities is clearly illustrated in the validation stage in the flowchart of Fig. 2.2. The standards of ASME (2009) and ITTC (2021), among others, require the quantification of both an experimental validation metric and uncertainty in order to properly execute and interpret the validation stage (acceptance or rejection as per Fig. 2.2). However, the disclosure of physical parameters and uncertainty estimates is inadequate for validation purposes in most published papers with experimental data (Oberkampf & Trucano, 2002). Actually, uncertainty quantification in experimental data used for validation exercises in CFD research is often completely neglected in the literature as underpinned by Roache (2016). Experi-

mental setups are often insufficiently described with physical parameters given as nominal values rather than actual measured values (Oberkampf & Trucano, 2002). The lack of physical parameters makes the validation effort virtually impossible without having to include guesses which introduces calibration as opposed to validation of the numerical model. The exclusion of experimental uncertainty quantification will underestimate the validation uncertainty and can potentially lead to false acceptances of the validation activity - hazardous in real-life applications. The option of conducting experiments dedicated to validation remains open but is only rarely embarked on in literature of off-shore renewables. As it will turn out, such experiments make up a distinct type of experiments and often require additional effort and expenditures from the detection and reduction of experimental uncertainties and the associated iterations in the physical models and experimental designs to be expected.

Numerical Model Benchmarking

Engineers may struggle to identify hydrodynamic models of fitting accuracy *and* computational costs for a given application. The model accuracy is largely dictated by the governing physics of the engineering application at hand which may be poorly understood for complex flows - especially for novel concepts involving multiple physical phenomena. Benchmarking of multiple numerical models against an accurate solution can elucidate this. E.g., the variation of numerical model fidelity, say, between Navier-Stokes- and Euler-based models, can shed light on the governing physics (the importance of viscous effects) whereas the variation of numerical framework at the same fidelity level can demonstrate beneficial code implementation or numerics in terms of accuracy and/or computational costs. Thus, numerical model benchmarking denotes the inter-comparison of simulation results for flow problems where an accurate reference solution is known, aiming to assess the relative advantages in terms of accuracy and, potentially, computational costs and ease-of-use of different numerical models. The accurate reference solution is typically derived from experiments. In this sense, the quality of a numerical model benchmarking, similarly to a traditional V&V, depends on the quality of the experimental data.

3 | Research Contribution

Chapter 1 motivated the expansion of the installed capacity of offshore renewable energy technologies to mitigate greenhouse gas emissions while enhancing energy access and security. Central to achieving these goals is the LCoE. Early design investigations (at low TRL) to reduce the LCoE is key to increase the chance of commercialization of novel offshore renewables. Full design processes are unfeasible with purely experimental testing and, hence, rely on accurate and efficient hydrodynamic models. Chapter 2 presented the predominant hydrodynamic modelling approaches in the field of offshore renewables and the intrinsic opposite extremes of computational cost and accuracy. Furthermore, the activity of verification and validation were introduced and the lack of public experimental datasets from experiments dedicated to validation or benchmarking of numerical models for offshore renewables were highlighted. Based on these chapters, three broad research topics with the potential to further advance offshore renewables are identified as:

- Experimental benchmark datasets from validation experiments - to increase numerical model credibility and support developments of numerical models by enhanced validation
- Benchmarking of numerical models - to give insights into the suitability of different numerical models for specific flow problems
- Early design investigations - to assess and improve feasibility of novel offshore renewable energy technologies

The present chapter outlines the approaches taken in addressing these topics and present some of the major results. Section 3.1 introduces the topic of validation experiments and presents the works of Kramer et al. (2021, Paper B), Andersen and Kramer (2023, Paper E), and Andersen et al. (2023, Paper G). Section 3.2 reviews the numerical simulations of four distinct flow problems relevant for offshore renewables as considered in Kramer et al. (2021, Paper B), Andersen and Eskilsson (2023, Paper C), Eskilsson et al. (2023b,

Paper D), and Andersen et al. (2023, Paper G). Lastly, Section 3.3 provides an overview of early design investigations of two distinct offshore renewable energy technologies, i.e., a perforated monopile design for offshore wind turbines suggested by Vestas Wind Systems A/S and the wave-activated body design of an OSWC by Exowave ApS as studied in Andersen et al. (2020, Paper A) and Iversen et al. (2023, Paper F), respectively. The coupling of research topics and appended papers is outlined below.

| Research Topics | <i>Papers</i> |
|-----------------------------------------|-------------------|
| Experimental Benchmark Datasets | <i>B, E, G</i> |
| Benchmarking of Numerical Models | <i>B, C, D, G</i> |
| Early Design Investigations | <i>A, F</i> |

3.1 Experimental Benchmark Datasets

Experiments with complete, complex engineering systems, such as the majority of WEC and FOWT concepts, are typically unfeasible and inappropriate to enter validation activities by themselves (Oberkampff & Roy, 2010). Experimental testing of an actual, complete system in environmental conditions matching the intended use of numerical models is first and foremost associated with vast expenditures and prolonged time frames. Additionally, the complex geometry and physics combined with restrictions in instrumentation (on the operational hardware) will compromise the accuracy of physical parameters for numerical model input and potentially the validation metric(s). In such scenarios, a building-block approach with the V&V activities split into tiers of gradually lower complexity and with decoupled physics can be employed. AIAA (1998) proposed a validation hierarchy of tiers in the form of:

1. Complete system
2. Subsystem
3. Benchmark cases
4. Unit problems

The *complete system* tier includes the actual, full-scale hardware deployed at environments of interest (based on the numerical model use). At the *subsystem* tier, an operational part of the actual complete system is considered with

only limited decoupling of physics. At the *benchmark cases* tier, idealizations, or simplifications, are imposed to the subsystem with emphasis on retaining few principle physical phenomena to allow for rigorous experiments with measurements of most numerical model inputs. The *unit problem* tier is similar to the *benchmark cases* tier but with further simplifying assumptions to the point of full decoupling of physical phenomena. The two top tiers, i.e., *complete systems* and *subsystems*, usually consider system-oriented engineering rather than physics and aim at assessment of functionality, safety, or high-level performance (Oberkampf & Roy, 2010). Accordingly, V&V at the top tiers are typically reserved to specific engineered systems. Nevertheless, the principle physics of many engineered systems build on the same fundamental physics, and V&V efforts at lower tiers, i.e., *benchmark cases* and *unit problems*, can thus have broad application across several engineered concepts. This motivates benchmark datasets of shared low tiers within a particular field of engineered concepts to accelerate the advancement of that field by enhanced numerical model validation and benchmarking.

Section 3.1.1 introduces validation experiments as opposed to traditional experiments and discusses the work of Kramer et al. (2021, Paper B), Andersen and Kramer (2023, Paper E), and Andersen et al. (2023, Paper G) dedicated to the generation of experimental benchmark datasets. Section 3.1.2 encourages experimental uncertainty quantification in the validation activity and reviews the uncertainty analyses of Kramer et al. (2021, Paper B) and Andersen et al. (2023, Paper G).

3.1.1 Validation Experiments

Physical experiments in engineering and science have traditionally adhered to either of the three categories of i) physical discovery tests, ii) model calibration or update tests, and iii) acceptance tests of engineered components (Oberkampf & Roy, 2010). Such traditional experiments aim at gaining knowledge of physical processes, improvement of models to describe physical processes, and improvement of engineered concepts with regard to, e.g., performance or safety. However, with the soaring of computational power following Moore’s law (doubling of transistors every two years) since the early 1970s, a fourth type of experiment has transpired - validation experiments. Validation experiments differ from traditional experiments in the sense that “the code is the customer” as stated in Oberkampf and Trucano (2002) referring to the shift of the main scope from improvement of physical understanding and engineered designs in traditional experiments to the assessment of accuracy of numerical models in validation experiments. Based on guidelines on validation experiments formulated from many years of work on the topic from researchers at Sandia National Laboratories (e.g., Aeschliman & Oberkampf, 1998; Oberkampf et al., 1993; Oberkampf & Trucano, 2002; Walker & Oberkampf, 1992), the characteristics

of validation experiments can be summed up as:

Characteristics of Validation Experiments

- Joint design of experiment by experimentalists and code developers and users
- Disclosure of all physical parameters relevant for the numerical model
- Independence in the analysis of experimental data and simulation results
- Quantification of experimental uncertainty both random and systematic (bias)

Kramer et al. (2021, Paper B), Andersen and Kramer (2023, Paper E), and Andersen et al. (2023, Paper G) account for validation experiments aimed at the accuracy assessment of simulations of hydrodynamic models of WECs (Papers B and E) and wave transformation models (Paper G). The validation experiments were carried out at low level tiers - arguably at the *benchmark cases* tier following the definitions of AIAA (1998) - thus utilizing specially crafted hardware in meticulously designed experiments aimed at capturing physical phenomena common in the field of hydrodynamic modelling of offshore renewables (various levels of physical complexity are present within each idealized test case). Accordingly, the outcomes of the validation experiments can be used in V&V activities for a rather broad range of offshore renewables including multiple concepts within wind and wave energy conversion with off- or nearshore deployment.

The OES Effort on Spheres

The Ocean Energy Systems (OES) program under the International Energy Agency formed a working group on WEC Modelling Verification and Validation, previously named OES Task 10 (IEA, 2016). The group underlined the need for accurate validation experiments in hydrodynamic modelling of WECs and carried out code-to-code comparisons of numerical simulations of generic spherical WECs (Wendt et al., 2019; Wendt et al., 2017). The studies found significant deviations in simulation results between numerical models but lacked accurate benchmarks for numerical benchmarking/validation.

The works of Kramer et al. (2021, Paper B), Andersen and Kramer (2023, Paper E), and Andersen et al. (2023, Paper G) were carried out as part of the OES effort and included validation experiments of the low level tiers of heave

decay of a sphere in initially calm water (Paper B) and wave excitation of a fixed sphere (Paper E). The experiments were carried out in the Ocean and Coastal Engineering Laboratory at Aalborg University. Emphasis on the formulation of idealized test cases was given in both works. The ideal sphere shape was chosen to reduce geometrical complexity allowing for higher precision of the physical model and convenient adaptation in numerical models. To increase usefulness of the validation experiments in the benchmarking of numerical models of various fidelity, the validation experiments were designed to clearly contain varying levels of hydrodynamic nonlinearities, i.e., the drop heights and wave steepness and wave height were varied in the two works, respectively. The investigated drop heights of Kramer et al. (2021, Paper B) are visualized in Fig. 3.1.

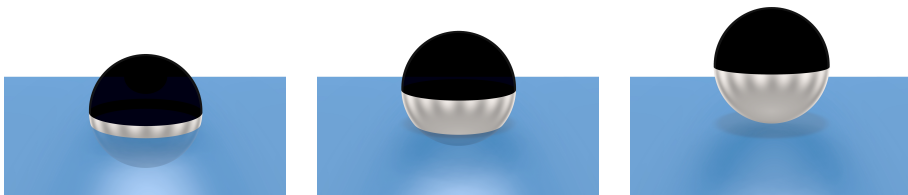


Fig. 3.1: Initial heave displacements (drop heights) in the idealized test case of heave decays of a sphere. From Kramer et al. (2021, Paper B).

Datasets on Wave Propagation over a Submerged Bar

Accurate prediction of wave transformations is fundamental in the design of most marine structures - particularly if deployed in shallow water regions with large gradients of the bathymetry as may be the case for nearshore locations. Beji and Battjes (1993) and Dingemans (1994) conducted seminal works on wave propagation over submerged bars capturing complex wave transformations of shoaling, breaking, nonlinear wave-wave interaction, and decomposition. Though originally being a physical discovery experiment, the work of Beji and Battjes (1993) has been applied for validation and numerical benchmarking purposes in multiple studies, e.g., Beji and Battjes (1994), Kamath et al. (2017), and Gadelho et al. (2014), which are reviewed in Section 3.2. In Dingemans (1994) both (upscaled) experiments based on Beji and Battjes (1993) and numerical model benchmarking of Boussinesq-type models were included. While acknowledging the commendable quality of the experimental tests in Beji and Battjes (1993) and Dingemans (1994), the two experiments fall short in multiple regards to be considered actual validation experiments, e.g., experimental uncertainty estimates are neglected on both measurements and physical parameters. Additionally, for accurate validation activities of high-fidelity numerical models physical parameters such as water density and wave generation theory and ramping are lacking. Validation experiments of

wave propagation over a submerged bar inspired by those of Beji and Battjes (1993) and Dingemans (1994) were executed in Andersen et al. (2023, Paper G) for the purpose of numerical benchmarking of high-fidelity numerical models. The idealized test case described long-crested waves of various levels of linearity, regularity, and breaking propagating over a submerged bar. The bar geometry and location of wave gauges (numbered 1-20) are shown in Fig. 3.2 with x denoting the wave propagation direction.

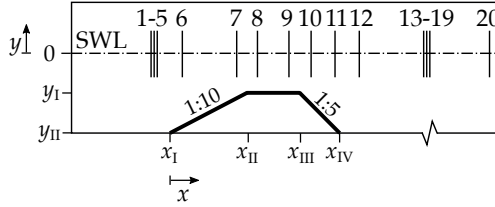


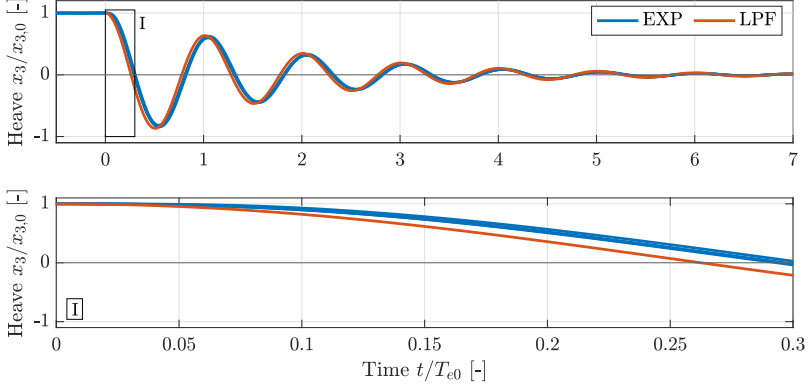
Fig. 3.2: Bar geometry and wave gauges in the idealized test case of wave propagation over a submerged bar. Adapted from Andersen et al. (2023, Paper G).

Analyses of Experimental Designs

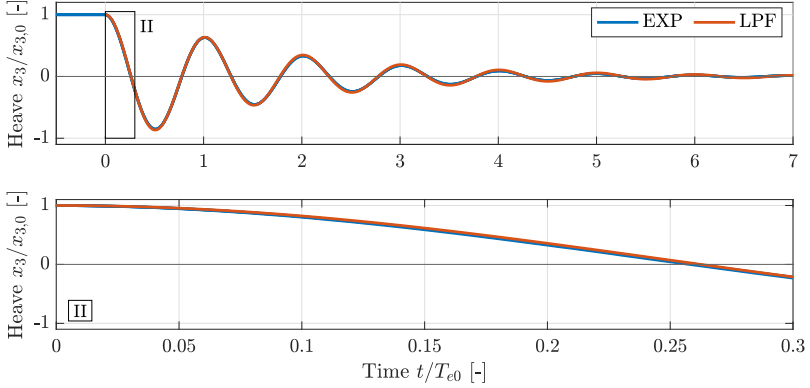
In validation experiments, the experimental embodiment of the idealized test case must be an accurate representation of the idealized geometries and conditions while having rich instrumentation to measure validation metrics and numerical model inputs without altering the physical properties of the test case. As the numerical model must represent the same idealized test case, this step is crucial to ensure an accurate and, indeed, meaningful validation activity. While no true or accurate reference of the idealized test case is available (or else, the validation experiment would lack purpose), the evaluation of the experimental design from preliminary analytical, numerical, and/or experimental analyses can prove exceedingly beneficial.

In Kramer et al. (2021, Paper B), a central assumption of the idealized test case is the instant release of the spheres from the initial displacements in heave. Preliminary numerical models indicated how the duration of the release in the physical experiment was too long to properly represent the idealized test case, i.e., the experimental initial accelerations were too low. Comparison of the heave decay time series from preliminary simulation results by an LPF model to preliminary experimental data show the deviations in the initial acceleration and the derived effect of a phase delay of the experimental heave time series. This can be seen for the lowest investigated drop height in Fig. 3.3a where x_3 is the heave displacement of the sphere from equilibrium (half submergence), $x_{3,0}$ is the drop height (initial heave displacement), and T_{e0} is the damped natural period in heave. The LPF model was expected to be of high accuracy for the low drop height. Optimization of the experimental design from a pulley

system with manual release to a fully mechanical system with a small electrical actuator and pushrod decreased the release duration an order of magnitude (from approximately 1/10 s to <1/960 s) yielding significantly higher compliance of initial conditions (ICs) and heave decay time series, see Fig. 3.3b. The mechanical release system as adopted in the final experiments of Kramer et al. (2021, Paper B) can be seen in Fig. 3.4.



(a) Manual release with pulley.



(b) Mechanical release with electrical actuator and pushrod.

Fig. 3.3: Comparison of numerical and experimental heave decay time series with two different release systems. From preliminary studies.

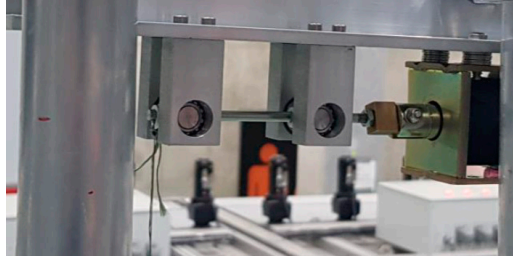


Fig. 3.4: Mechanical release system with electrical actuator and pushrod. From Kramer et al. (2021, Paper B).

The results of a preliminary numerical simulation of wave propagation over a submerged bar from Andersen et al. (2023, Paper G) can be seen in Fig. 3.5 (CFD). Besides from helping to identify potential sources of errors in the experimental design, the preliminary simulation results were useful in the selection of wave conditions, e.g., in estimation of the onset of breaking, and locations of interest of the wave.

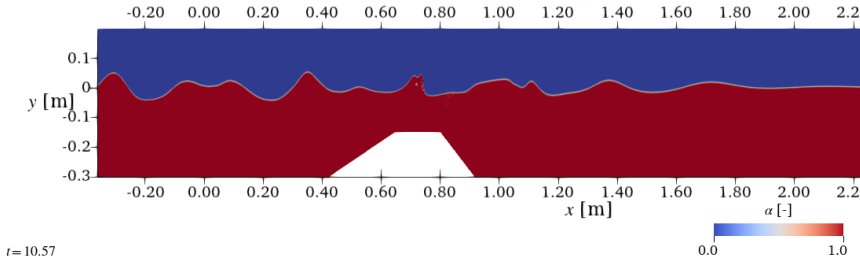
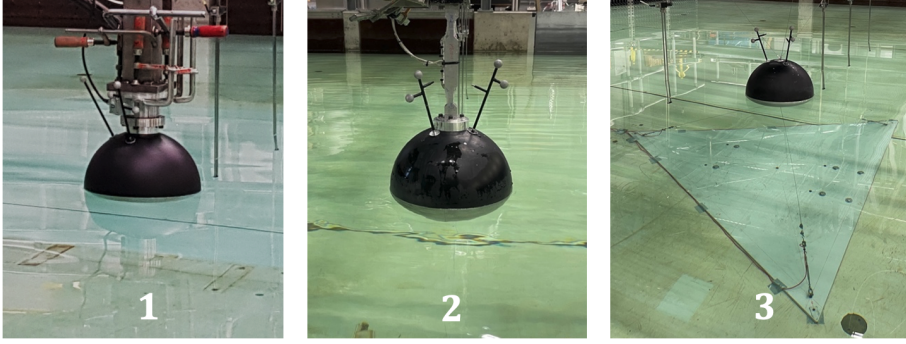


Fig. 3.5: Simulation results of the wave propagation over a submerged bar in Andersen et al. (2023, Paper G). From preliminary studies.

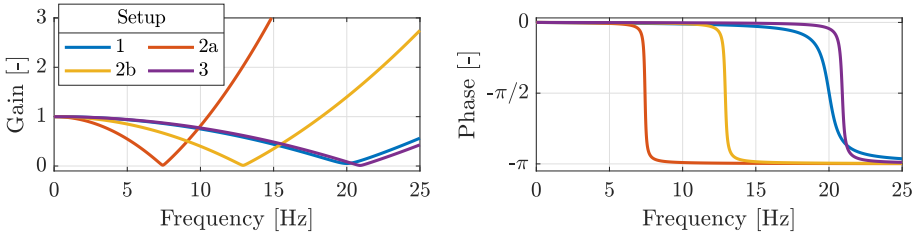
The numerical modelling prior to or during the experimental campaign will necessitate the collaboration between experimentalists and code users (sometimes, it is indeed the same person) at an early stage easing modifications to the experimental design to, for instance, measure physical parameters for numerical model input first overlooked by the experimentalists. On the other hand, significant bugs or inappropriate assumptions (BCs, ICs, turbulence model, etc.) of the preliminary numerical model may also be identified and corrected prior to numerical verification activities, which are commonly aided with high-performance computing (HPC), potentially saving substantial computational resources. The joint design of the validation experiment by both experimentalists and code users is acknowledged as one of the primary forces of validation experiments versus traditional experiments and will often spark synergy between the experimental design and numerical model (Oberkampff & Trucano,

2002). As mentioned in Section 2.3, the application of existing, traditional experiments in the validation stage will reduce confidence of the validation activity typically due to undefined physical parameters for numerical model input and efforts in experimental uncertainty quantification (ASME, 2006). In Kramer et al. (2021, Paper B) and Andersen et al. (2023, Paper G) the respective benchmark datasets were showcased by comparison to multiple numerical models of various fidelity with widespread usage in hydrodynamic modelling of offshore renewables. Multiple numerical simulations with low deviation to experimental data (under fitting physics regimes) together with low experimental confidence bands (Section 3.1.2) underlined the suitability of the datasets as validation benchmarks with sufficient inclusion of physical parameters for (especially, high-fidelity) numerical model input.

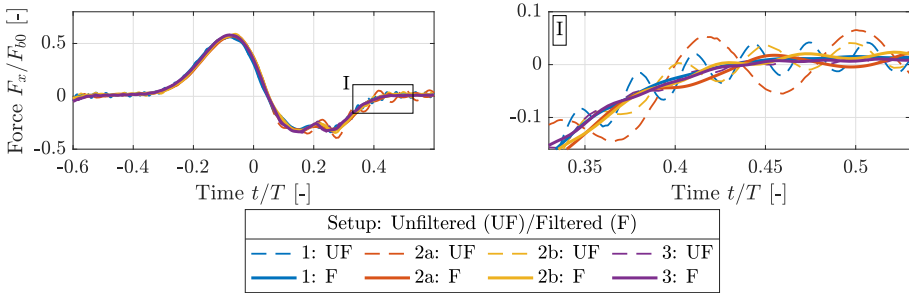
An alternative approach to numerical simulations in assessing how well an experimental design represents a given idealized test case is by comparison of multiple experimental designs. This was the focal point of Andersen and Kramer (2023, Paper E) in which the representation of three governing assumptions of the idealized test case were inter-compared in three physical wave basin setups. The idealized test case encompassed a fixed, rigid sphere subjected to long-crested waves propagating over a horizontal bed. Comparative analyses were conducted on rigidity, sensitivity, and disturbances from the presence of measurement equipment. The investigated experimental setups and part of the comparative analysis can be seen in Fig. 3.6. Fig. 3.6a shows three different experimental designs of the idealized test case of a fixed sphere to be subjected to wave loads (corresponding to ICs). Fig. 3.6b shows the gain and phase of a dynamic amplification filter calculated from the modal parameters of the different setups and Fig. 3.6c shows the compensation due to dynamic amplification for a nonlinear sea state (wave excitation force signal before and after filtering). Setup 3 was identified as the most rigid setup with the least correction due to dynamic amplification. Furthermore, Setup 3 had the least interference with the flow field in the vicinity of the free surface due to the significantly smaller projected area of force measurement equipment (projected to a plane normal to the wave propagation direction). The comparison of data from multiple experiments of the same idealized test case has the important benefit of revealing potential biases in the experiments. Preferably, experiments are executed at different test facilities to cover potential systematic error sources to a greater extent. In Andersen and Kramer (2023, Paper E), a key finding was a low inter-experiment variability on the key metric of wave excitation force which inferred low systematic error in the three experimental designs.



(a) Three experimental designs of a fixed sphere.



(b) Gain and phase of dynamic amplification filter of investigated experimental designs. Setups 2a and 2b included force transducers of different thicknesses.



(c) Influence of dynamic amplification filter on wave excitation force signals.

Fig. 3.6: Comparison of multiple experimental designs of the idealized test case on wave excitation of a fixed sphere. Adapted from Andersen and Kramer (2023, Paper E).

Independence and Joint Design

The emphasis on both independence and joint design in validation experiments may seem contradictory at first glimpse. While the author acknowledges the difficulties that can arise in this regard, the independence requirement aims at avoiding calibration of the numerical models (where validation was intended) whereas the joint design requirement aims at aligning physical properties of the numerical model and experimental setup, via the idealized test case, during the experimental design phase (Oberkampf & Trucano, 2002). The latter ought not include any tuning of (fudge) factors in the numerical model. In Kramer et al. (2021, Paper B), numerical "blind tests", i.e., experimental data were not given to the code developers/users initially, were used to demonstrate the usefulness of the experimental dataset as a benchmark. Such strategies sustain independence and increase the confidence of the validation activity. However, practice shows that the stage of quantitative comparison of experimental and numerical data most often reveal possible shortcomings of the numerical model and/or experimental design and this is where the synergistic effects of the validation activity unfold (Oberkampf & Trucano, 2002). To benefit from these effects, it is much up to the involved partners to sustain independence while improving the experimental design and/or numerical model by adjusting according to physics and not merely results. Preliminary analyses and associated iterations in the experimental design can help identify and mitigate deviations between the idealized test case, numerical model, and experimental design at an early stage, as introduced above with examples of the validation experiments of Kramer et al. (2021, Paper B), Andersen and Kramer (2023, Paper E), and Andersen et al. (2023, Paper G).

3.1.2 Uncertainty Quantification

The validation stage includes the quantitative comparison of validation metrics obtained by numerical simulation and experimentation as introduced in the V&V flowchart in Fig. 2.2. The quantitative comparison is based on the validation comparison error ϵ and the validation uncertainty v_{val} following, e.g., the validation procedures of ASME (2009) and ITTC (2021). The validation comparison error ϵ is the difference between the validation metric as obtained from numerical simulation and experimentation, whereas the validation uncertainty is the combination of experimental uncertainty v_{exp} , numerical uncertainty v_{num} , and (numerical model) input uncertainty v_{input} (ASME, 2009). Assuming independence between the errors corresponding to these uncertainties, the combination hereof is the root-sum-square

$$v_{val} = \sqrt{v_{num}^2 + v_{input}^2 + v_{exp}^2} . \quad (3.1)$$

The comparison of ϵ to v_{val} is used to draw conclusions on the validation activity with or without expansion of v_{val} from assumed error distributions, see, e.g., Eça et al. (2010). The remainder of the present chapter accounts for the quantification of experimental uncertainty in the context of the validation experiments of Kramer et al. (2021, Paper B) and Andersen et al. (2023, Paper G) while a comment on input uncertainty is included in the final paragraph. The subscript of *exp* in denoting experimental uncertainties is omitted for the remainder of the present chapter due to economy of notation.

Uncertainty of the Measurement

In a measurement activity, the measurand Θ denotes the quantity of interest that is being measured or estimated. Observations, or measurements, of Θ is denoted θ . For example, in Kramer et al. (2021, Paper B), the measurand was the (idealized) heave displacement X_3 of the sphere which when realized by measurements was denoted x_3 . As indicated, the measurand is an idealized quantity which cannot be perfectly realized by the measurement activity. However, an estimate $\hat{\Theta}$ of the measurand can be calculated from (multiple) measurements which introduces the unknown difference $\hat{\Theta} - \Theta$ as the measurement error - the potential size of which is expressed as (measurement) uncertainty (Willink, 2013). Uncertainties estimated at the standard deviation level are denoted standard uncertainties.

The main scope of an uncertainty analysis of a measurement activity is usually to determine the uncertainty of $\hat{\Theta}$ in representing Θ . To this end, the elemental sources of measurement error must be identified and characterized before the standard uncertainties hereof can be quantified, combined, and expanded into, practically useful, uncertainty intervals (UI) with a given level of confidence or assurance (Willink, 2013). Sources of uncertainty is categorized into systematic (bias) and random (scatter) in ASME (2019) and Type A and B in BIMP et al. (2008). The latter categorization indicates the method used for the uncertainty quantification where Type A refers to statistical methods and Type B refers to non-statistical methods, e.g., from manufacturer's specifications or engineering judgment. BIMP et al. (2008) is the international standard "Guide to the Expression of Uncertainty in Measurement" (GUM) from the International Organization for Standardization (ISO) and the categorization are henceforth referred to as ISO Types A and B. The categorizations of the GUM are compatible with ASME (2019) and both have been used in the uncertainty analyses of the validation experiments in Kramer et al. (2021, Paper B) and Andersen et al. (2023, Paper G).

With N repetitions of the measurement θ , the measurand is most typically estimated from the sample mean of the measurements (the arithmetic mean), i.e., $\hat{\Theta} = \bar{\theta}$. The random standard uncertainty of $\bar{\theta}$ is then estimated from the

sample standard deviation $s_{td,\theta}$ as

$$s_{\bar{\theta}} = s_{td,\theta} / \sqrt{N} . \quad (3.2)$$

Systematic uncertainties are not quantifiable from repetitions of the experimental tests and are evaluated from the identification and characterization of elemental systematic sources of measurement error. The systematic standard uncertainty $b_{\bar{\theta}}$ is calculated from the estimates of the standard deviation of the distributions of the elemental systematic measurement errors (which is realized and constant in the measurement activity) and is denoted elemental systematic standard uncertainties (ASME, 2019). The elemental systematic standard uncertainty from the k^{th} elemental systematic source of measurement error is denoted $b_{\bar{\theta},k}$. Assuming independent elemental systematic sources of measurement, $b_{\bar{\theta}}$ is calculated as the root-sum-square of $b_{\bar{\theta},k}$ (ASME, 2019). The elemental systematic standard uncertainties estimated in the validation experiment of Kramer et al. (2021, Paper B) are shown in Table 3.1. It should be noted that the calibration uncertainty contains both random and systematic contributions but as the calibration is fixed during the measurement activity it is treated as a systematic uncertainty.

Table 3.1: Systematic uncertainties in the heave decays of a floating sphere. Adapted from Kramer et al. (2021, Paper B).

| Systematic Error Source | k | Elemental Systematic Standard Uncertainty $b_{\bar{x}_{3,k}} \bar{x}_{3,o}$ [mm] | ISO Types |
|------------------------------------------------------------------------------------|-----|-------------------------------------------------------------------------------------|-----------|
| Calibration of optical motion capture system | 1 | 0.01 | A |
| Vibrations of bridge (reference frame) | 2 | 0.01 | B |
| Vibrations of support rods for reflective markers (given for ascending $x_{3,0}$) | 3 | 0.02, 0.06, 0.10 | B |
| Influence from roll and pitch | 4 | Time dependent, <0.02 | A |

The combination of the systematic and random standard uncertainties by the root-sum-square yields the combined standard uncertainty (ASME, 2019)

$$v_{\bar{\theta}} = \sqrt{b_{\bar{\theta}}^2 + s_{\bar{\theta}}^2} . \quad (3.3)$$

The multiplication of the combined standard uncertainty with a coverage factor c_f gives the expanded uncertainty $\mathcal{Y}_{\bar{\theta}}$ used to construct an UI around the

estimate $\bar{\theta}$ with a given level of confidence, see Eq. (3.4). In the validation experiments of Kramer et al. (2021, Paper B) and Andersen et al. (2023, Paper G), a 95% level of confidence was deployed which is typical in most metrology activities (Willink, 2013). In validation experiments the number of repetitions N is usually rather limited (typically, 5-10) and the coverage factor c_f in Eq. (3.4) is commonly chosen as the appropriate Student's t value based on a given number of degrees of freedom (DoF) and level of confidence (ASME, 2019; BIMP et al., 2008). Invoking the central limit theorem, the Student's t distribution in the expansion of $v_{\bar{\theta}}$ is a reasonable approximation even with contributions from non-normal elemental error distributions provided that these are not governing the quantification of $v_{\bar{\theta}}$.

$$\theta \pm c_f v_{\bar{\theta}} = \theta \pm \Upsilon_{\bar{\theta}}. \quad (3.4)$$

In Kramer et al. (2021, Paper B) the sample mean \bar{x}_3 was used as an estimate of the measurand. The random standard uncertainty of the sample mean was estimated from Eq. (3.2) at each logged temporal coordinate and the elemental systematic standard uncertainties of Table 3.1 combined with the root-sum-square. The time-dependent expanded uncertainty on the sample mean $\Upsilon_{\bar{x}_3}$ at the 95% level of confidence can be seen in Fig. 3.7. The larger expanded uncertainty at the initialization of the heave decay from the highest drop height ($x_{3,0} = 0.5D$ where D is the diameter of the sphere) in Fig. 3.7 is ascribed to the increased random error of the motion tracker system in tracking specimens of increased velocities. The increased offsets of $\Upsilon_{\bar{x}_3}$ with increasing drop heights are primarily due to the estimated systematic uncertainty of the deflection/vibration of the support rods of the reflective markers.

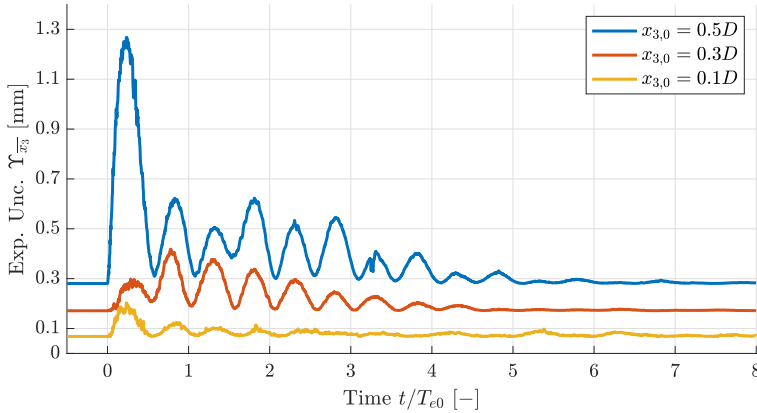


Fig. 3.7: The time-dependent expanded uncertainty on the heave displacement of a sphere at the 95% level of confidence. Adapted from Kramer et al. (2021, Paper B).

Propagation of Uncertainty

In Kramer et al. (2021, Paper B), X_3 was directly estimated from the measurements x_3 . However, often the measurand Θ must be calculated from a functional relationship f of multiple input quantities Θ_j , i.e.,

$$\Theta = f(\Theta_1, \Theta_2, \dots, \Theta_J) , \quad (3.5)$$

where J is the total number of input quantities. Each of the input quantities must be measured/estimated and can, indeed, in themselves be considered (sub-)measurands. The law of propagation of uncertainty (first-order Taylor series approximation) as per BIMP et al. (2008) is commonly used to propagate the uncertainty of the respective input quantities Θ_j to the measurand Θ assuming low nonlinearity of f in $\hat{\Theta}_j \pm \mathcal{Y}_{\hat{\Theta}_j}$ with $j \in \{1, 2, \dots, J\}$. Under the additional assumption of independent input quantities, the law of propagation of uncertainty reads

$$v_{\hat{\Theta}}^2 = \sum_{j=1}^J \left(\frac{\partial f}{\partial \hat{\Theta}_j} \right)^2 v_{\hat{\Theta}_j}^2 . \quad (3.6)$$

In the validation experiment of Andersen et al. (2023, Paper G), the measurand was the surface elevation η^* at multiple wave gauge locations which when realized by measurements is denoted η . Surface elevation was calculated by a calibration function inputted with the instrument voltage from resistance wave gauges as

$$\eta^* = \psi(V - V_0) , \quad (3.7)$$

where V is the instrument voltage, V_0 is the reference instrument voltage evaluated at SWL, and ψ is a calibration parameter (slope). The estimates of V and V_0 were found as the sample means, and the standard uncertainties of the estimates were found from the repeatability (ISO Type A, $N = 5$) and resolution/discretization error (ISO Type B). The estimate and uncertainty estimate of ψ was calculated by the weighted total least square method (errors-in-variables, i.e., accounting for the uncertainties of input variables) by Krystek and Anton (2007) yielding ISO Type A estimates. The uncertainties of the input quantities of the calibration function were propagated to the measurand by Eq. (3.6). Evaluation of the expanded uncertainty at each logged time coordinate yielded the time-dependent UI as shown for the monochromatic, breaking wave condition of Andersen et al. (2023, Paper G) in Fig. 3.8 where H and T_1 are the wave height and wave period, respectively, from the idealized test case. The measurement uncertainty is dominated by the random uncertainty after the onset of wave-breaking which is captured by wave gauge numbers (WGnos.) 10 and 12 in Fig. 3.8. The location of wave gauges can be seen in Fig. 3.2.

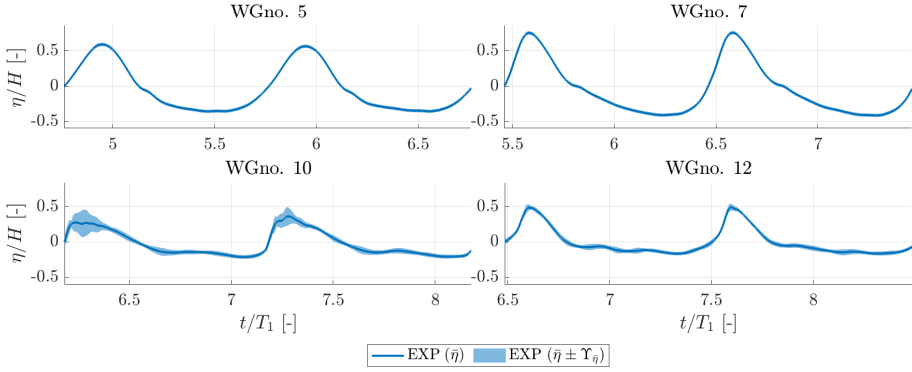


Fig. 3.8: Surface elevation time series with 95% UI at four wave gauge positions from the wave propagation over a submerged bar. Adapted from Andersen et al. (2023, Paper G).

Uncertainty of Physical Parameters

As previously stated in the present chapter, the disclosure of all physical parameters relevant for a given numerical model is a characteristic of validation experiments. In Kramer et al. (2021, Paper B) and Andersen et al. (2023, Paper G), estimates of a wide range of physical parameters and their respective uncertainties are listed. The inclusion of such parametric uncertainty estimates first and foremost serves the purpose of allowing for the immediate interpretation of the accuracy and precision of the validation experiment in representing the idealized test case (and derived from this, the numerical model). An additional benefit is the possibility of propagating the parametric uncertainty into the measurand by application of, e.g., the law of propagation of uncertainty as in Eq. (3.6). That is, the calculation of v_{input} in Eq. (3.1). However, the function f in Eq. (3.5) is typically not known in an analytical form and the partial derivatives (so-called sensitivity factors) of Eq. (3.6) can thus not be calculated exactly. Numerical differentiation of f by simulation results with individually varied physical parameter inputs (e.g., $\pm \gamma_{\hat{\theta}_i}$) may be used to estimate the sensitivity factors. Nevertheless, depending on the fidelity of the numerical models and the number of relevant physical parameters this may be an expensive and time-consuming activity where the inherent numerical model uncertainty along with the magnitude of the physical parameter uncertainties ultimately dictate the added value to the validation activity. Parametric uncertainties were not propagated to the measurands in Kramer et al. (2021, Paper B) and Andersen et al. (2023, Paper G) due to brevity and in order to not introduce numerical uncertainties into the experimental benchmark datasets. Instead, the quantification of physical parameters, with the highest level of detail in Kramer et al. (2021, Paper B), allows the users of the benchmark datasets to propagate uncertainties using a preferred numerical model.

3.2 Benchmarking of Numerical Models

This section reviews and summarizes the numerical work of Andersen and Eskilsson (2023, Paper C), Andersen et al. (2023, Paper G), Kramer et al. (2021, Paper B), and Eskilsson et al. (2023b, Paper D) which focus on the benchmarking of numerical models for four different flow problems relevant for the hydrodynamic modelling of offshore renewables. That is, the normal flow past a flat plate in Section 3.2.1, wave transformation by the wave propagation over a submerged bar in Section 3.2.2, heave decay of a sphere in Section 3.2.3, and a moored FOWT platform in focused waves in Section 3.2.4.

3.2.1 Normal Flow past a Flat Plate

The normal flow past a flat plate at practical Reynolds numbers $Re > 1e5$ is highly dominated by the formation and shedding of turbulent eddies and pose as a canonical flow problem in fluid dynamics due to its complexity and relevance for many engineering problems. In the field of hydrodynamics of offshore renewables, such normal flow problems may be encountered for the wave-activated bodies of OWSCs or heave plates on floating structures, e.g., WECs or FOWTs. Additionally, the aerodynamics of a wind turbine airfoil at stall bears high resemblance to the normal flow past flat plates.

The seminal work of Fage and Johansen (1927) experimentally investigated the normal flow past a nominally two-dimensional flat plate, i.e., a slender plate with the flow around the spanwise ends blocked by walls. In spite of its two-dimensional geometry, this flow problem is highly three-dimensional due to the dominance of the turbulent wake. Scale-modelling CFD such as URANS-based models tend to fail or become unreliable in the simulation of normal flow past flat, slender geometries (Mannini, 2015; Shur et al., 2005; Squires et al., 2002; Wu et al., 2022). As a remedy, SRS such as DNS or LES can be applied. DNS resolves the full range of scales down to the Kolmogorov scale where kinetic energy is transformed to thermal energy, and, consequently, DNS pose as an extreme SRS technique in terms of computational cost infeasible for most engineering flows. LES significantly reduces the computational costs relative to DNS by resolving only the larger eddies and modelling the smaller eddies by a subgrid scale turbulence model. This is often an accurate technique since larger eddies are commonly responsible for the majority of momentum transfer and is sensitive to BCs, whereas smaller eddies are more universally described and only accounts for a fraction of the momentum transfer (Piomelli, 2021). The inaccuracies derived from (turbulence) modelling errors in LES are thus substantially reduced in LES relative to SMS. Nevertheless, SMS is considerably more computationally efficient than SRS and can be employed as a precursor solution in SRS to accelerate flow development and assess resolution requirements. A precursor URANS simulation, with closure from the k - ω -SST

turbulence model (Menter et al., 2003), was used to initiate an LES, with closure from the Smagorinsky subgrid scale turbulence model (Smagorinsky, 1963), in preliminary studies of the flow normal to a flat plate at a high $Re = 1.5e5$. The transition from the URANS simulation to the LES is shown in Fig. 3.9, highlighting the fundamental differences in the capture of flow features between the two modelling approaches.

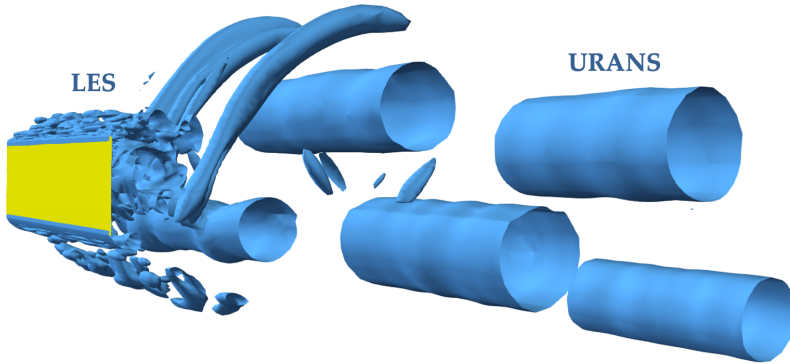


Fig. 3.9: Vortical structures from the transition of a precursor URANS simulation to LES of the normal flow to a flat plate at $Re = 1.5e5$. From preliminary studies.

The resolution requirements for LES is usually based on a given fraction of the local turbulent kinetic energy k to be resolved, e.g., 80% as per Pope (2004). This makes the resolution requirements in attached boundary layers very high. The application of the hybrid-URANS-LES method of DES (Spalart et al., 1997) avoids this issue by utilizing a URANS treatment within attached boundary layers and switching to an LES treatment after separation. Andersen and Eskilsson (2023, Paper C) employed a DES method to investigate the influence from corner curvature of a slender, flat plate in normal flow. The study identified a research gap of how the normal flow past flat plates was influenced by the variation of the corner curvature ranging from hemi-cylindrical to sharp-cornered edges. The focus was on flat plates, i.e., where the curvature of separated shear layers is not affected by the thickness of the plate as, for example, seen for rectangular cylinders (Mannini, 2015). A plate can usually be considered flat with $t_p/h_p < 5\%$ where t_p and h_p denote plate thickness and chordwise height, respectively.

Andersen and Eskilsson (2023, Paper C) deployed the $k-\omega$ -SST formulation of DES (Strelets, 2001) implemented in the open-source CFD framework of OpenFOAM (Weller et al., 1998). To the best of the author's knowledge this is the first application of a DES method to the normal flow past a flat plate. Similar numerical setups to those of LES of normal flow past flat plates in the literature (Díaz-Ojeda et al., 2019; Tian et al., 2014) were utilized to be able

to compare the DES and LES solutions. Cyclic spanwise BCs were used in the numerical setup. A snapshot of the fully developed turbulent flow from DES of the normal flow past a flat plate with the numerical setup of Andersen and Eskilsson (2023, Paper C) is shown in Fig. 3.10.

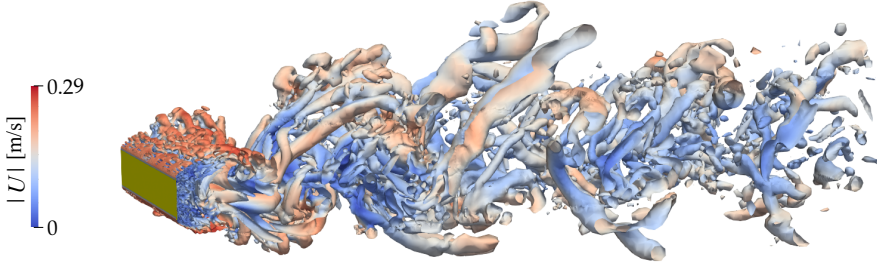


Fig. 3.10: Vortical structures with velocity magnitude (coloring) from DES of the normal past a flat plate at $Re = 1.5e5$. From preliminary studies.

In Andersen and Eskilsson (2023, Paper C), solution verification was carried out by estimating numerical uncertainty, v_{num} as introduced in Eq. (3.1), with the least square grid convergence index (GCI) method of Eça and Hoekstra (2014). The method is based on the estimation of the convergence rate γ_0 from multiple, >3 , grid resolutions, Richardson extrapolation of verification metrics to infinite grid resolution, and the calculation of safety factors based on the convergence (Roache, 1997) to convert error estimates to uncertainty estimates. The time-averaged drag coefficient $\langle C_D \rangle_t$ was chosen as the verification metric in Andersen and Eskilsson (2023, Paper C). The convergence of $\langle C_D \rangle_t$ with grid resolution can be seen in Fig. 3.11 for $r/h_p = 1\%$, where r is the corner radius.

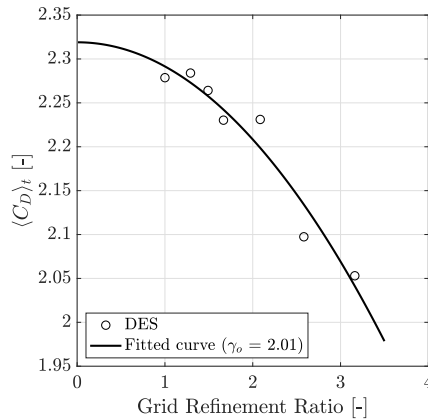


Fig. 3.11: Richardson extrapolation and convergence rate (γ_0) of time-averaged drag coefficient with grid resolution. Adapted from Andersen and Eskilsson (2023, Paper C).

Andersen and Eskilsson (2023, Paper C) collated three global flow quantities with the literature including the time-averaged drag coefficient, the recirculation length, and the Strouhal frequency. The case of normal flow past sharp-cornered flat plates was investigated in Fage and Johansen (1927), Díaz-Ojeda et al. (2019), and Hemmati et al. (2018) utilizing physical tests, LES, and DNS, respectively, with some variation of conditions such as blockage ratio, thickness, and Re (detailed in Andersen and Eskilsson (2023, Paper C)). It should be noted that the Re -dependency on global flow features for the normal flow past flat plates is low at $Re > 1e3$ (Hoerner, 1965). Tian et al. (2014) simulated the normal flow past flat plates with LES, including damping functions for near-wall treatment, for two different corner curvatures, i.e., $r/h_p \in \{0.5, 1\}\%$. Tabulated experimental values of the drag coefficient of rectangular cylinders ($t_p/h_p = 50\%$) with both sharp and rounded corners are given in DNV (2017). The plate edges of Fage and Johansen (1927) and Hemmati et al. (2018) had zero thickness corresponding to $r/h_p = 0$. The studies of Tian et al. (2014), Díaz-Ojeda et al. (2019), and Andersen and Eskilsson (2023, Paper C) used a constant plate thickness of $t_p/h_p = 2\%$ and investigated plate geometries with corner curvatures of $r/h_p \in \{0, 0.5, 1\}\%$ corresponding to those visualized in different shades of grey in Fig. 3.12a. The effect from r/h_p on $\langle C_D \rangle_t$ from the reviewed literature on the normal flow past flat plates is shown in Fig. 3.12b where the legend entries contain the first four letters of the main author surname and the type of test - detailed in Table 1 of Andersen and Eskilsson (2023, Paper C). Numerical uncertainty (95% UI) is indicated by the error bar for $r/h_p = 1\%$ in Fig. 3.12b.

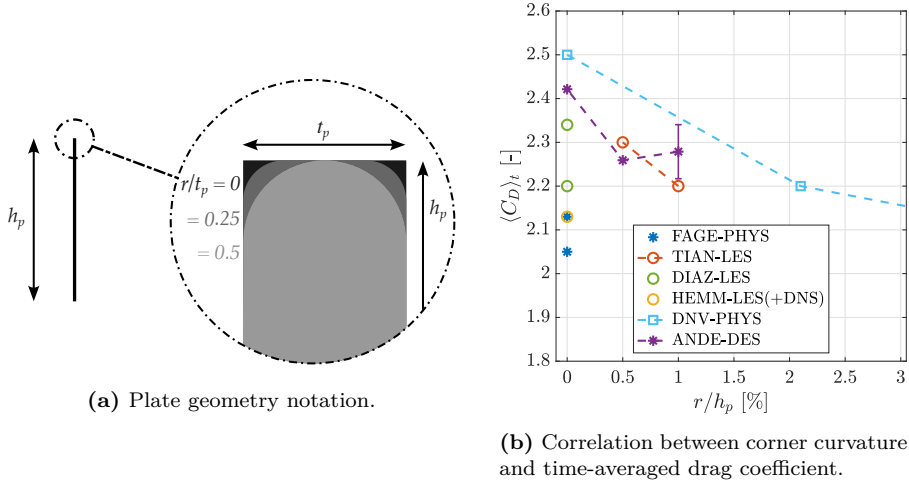


Fig. 3.12: Visualization of corner curvature and its influence on time-averaged drag. Adapted from Andersen and Eskilsson (2023, Paper C).

A monotonic trend of $\langle C_D \rangle_t$ with $r/h_p \in \{0, 0.5, 1\}\%$ was not disclosed in Andersen and Eskilsson (2023, Paper C), but taking into account numerical uncertainty (95% UI) a similar monotonic tendency to those of Tian et al. (2014) and DNV (2017) cannot be rejected. A significant increase of $\langle C_D \rangle_t$ was found when decreasing the corner curvature from $r/h_p = 1\%$ (hemi-cylindrical edges) to $r/h_p = 0\%$ (sharp corners). Good agreement was in general found between the DES simulations of Andersen and Eskilsson (2023, Paper C) and the LES simulations of Tian et al. (2014) and Díaz-Ojeda et al. (2019) with similar subgrid scale turbulence models (in the LES region). This indicates how the global flow is similarly captured with the considered URANS and LES near-wall treatments.

3.2.2 Wave Propagation over a Submerged Bar

Accurate calculation of wave loads, run-up, or scour of offshore renewables depends critically on the accurate assessment of wave transformations which may be significant for especially nearshore deployments or in the vicinity of steep bathymetry gradients.

CFD methods are the most universal hydrodynamic modelling approach to account for complex wave transformation including viscous and rotational effects as, e.g., in plunging breaking waves. As introduced in Section 2.2, several CFD frameworks with fundamentally different discretization, solution, and free surface treatment techniques have been applied in the simulation of ocean waves. FVM-based CFD with the interface capturing methods of either VoF or Level-Set methods to account for the free surface are very widespread but usually have significant computational overhead. The computational overhead associated to interface capturing, or tracking, methods can be avoided with sigma-transformation of the vertical coordinate (as in, e.g., Hicks, 2020; Lin & Li, 2002) which, however, introduce the requirement of a continuous, single-valued free surface - problematic in the simulation of, for example, plunging breaking waves. The particle-based CFD method of SPH inherently describe the free surface and is often beneficial in large surface deformation flows due to its Lagrangian, meshless nature. SPH is readily accelerated by GPU and has been applied in the simulation of wave transformations to an increasing extent with the advancement of GPU hardware in recent years (e.g., Lowe et al., 2019; Zhang et al., 2018; Zhu et al., 2023). The method of SPH is, however, relatively immature and five grand challenges (Vacondio et al., 2021) have been formulated to increase the credibility of SPH in terms of, among others, convergence and consistency.

Benchmarking of existing, widespread CFD methods to capture complex wave transformation is scarce in literature with most studies focusing on qualitative comparisons or excluding experimental benchmarks (e.g. Park et al., 2018; Salis et al., 2023; St-Germain et al., 2014; Wroniszewski et al., 2014).

Exceptions are the recent works of González-Cao et al. (2019) and Gruwez et al. (2020). González-Cao et al. (2019) benchmarked a VoF and an SPH solver for the case of monochromatic waves transforming over a steep foreshore and impacting with a vertical wall with a cantilever structure. Gruwez et al. (2020) benchmarked a VoF, an SPH, and a nonlinear shallow water equation solver for the wave interaction with sea dikes and dike-mounted walls on shallow foreshores. The numerical model benchmarking of these studies focused on the wave impacts on structures and the preceding combined wave transformations over foreshores.

Another strenuous test case in complex wave transformation is that of wave propagation over submerged obstacles where the spectral density of an incident wave field undergoes significant alteration by the combined wave transformations of shoaling, nonlinear wave-wave interactions, breaking, and decomposition. As introduced in Section 3.1, such test cases were investigated experimentally in Beji and Battjes (1993) and Dingemans (1994) with wave propagation over a submerged bar. The experimental results of these works have been used extensively in the benchmarking of lower-fidelity models such as Boussinesq-type or PF-based models (e.g. Dingemans, 1994; Simon et al., 2019; Tissier et al., 2012). Besides, Kamath et al. (2017) compared simulation results from a level-set-based URANS solver under the open-source CFD framework of REEF3D (Bihs et al., 2016) to the data of Beji and Battjes (1993) for both non-breaking and breaking waves. The comparison was mostly qualitative and showed significant over-prediction of crest elevations in the near post-breaking region. In Gadelho et al. (2014) the VoF-based URANS solver **interFoam** under the **OpenFOAM** framework was compared to the data of Beji and Battjes (1993) but only for non-breaking waves. The study showed discrepancies in the free surface elevations down-wave of the horizontal crest of the submerged bar with crest and trough elevations deviating up to 30%. Spectral analyses showed improper energy transfer between frequencies of the simulations relative to the experimental data with close to 100% over-estimation of third order energy. Schmitt et al. (2020) compared the simulation results of the **interFoam** solver to the data of Dingemans (1994), again, only for non-breaking waves, but in contrast to Gadelho et al. (2014) found good agreement at all wave gauge locations.

To the best of the author's knowledge, Andersen et al. (2023, Paper G) was the first study in literature to benchmark multiple CFD models against the test case of wave propagation over a submerged bar including non-breaking and breaking waves. The study benchmarked three fundamentally different CFD models each widespread within their respective category, i.e., an SPH solver and two FVM URANS solvers with VoF-based interface capture and sigma transformation, respectively. The tested CFD models are summarized below and given in detail in Andersen et al. (2023, Paper G).

i-VoF: The VoF-based `interFoam` solver under `OpenFOAM` solving the URANS equations with closure from a nonlinear k - ε -model.

M-sigma: The MIKE 3 Waves FM solver of DHI (2023) with sigma-transformation solving the URANS equations with closure from a k - ε -model.

D-SPH: The weakly compressible delta-SPH solver under `DualSPHysics` (Domínguez et al., 2021).

To increase the accuracy of the benchmark activity, Andersen et al. (2023, Paper G) carried out dedicated validation experiments, inspired by the experiments of Beji and Battjes (1993), in the Ocean and Coastal Engineering Laboratory at Aalborg University as introduced in Section 3.1. The idealized test case of Andersen et al. (2023, Paper G) included long-crested waves propagating over a fully submerged trapezoidal bar. The bar geometry and location of wave gauges are given in Fig. 3.2 which is duplicated below for the convenience of the reader. Four wave conditions of various linearity and regularity were considered which are summarized in Table 3.2.

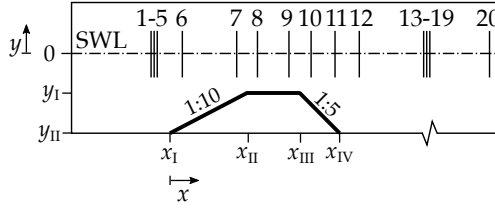


Fig. 3.2: Duplicated from Section 3.1. Bar geometry and wave gauge locations of idealized test case of wave propagation over a submerged bar. Adapted from Andersen et al. (2023, Paper G).

Table 3.2: Wave conditions included in the idealized test case of wave propagation over a submerged bar. Adapted from Andersen et al. (2023, Paper G).

| Wave Condition | Regularity | Linearity |
|----------------|---------------|---------------------|
| 1 | Monochromatic | Close to linear |
| 2 | Monochromatic | Nonlinear |
| 3 | Monochromatic | Nonlinear, breaking |
| 4 | Bichromatic | Nonlinear, breaking |

The study of Andersen et al. (2023, Paper G) benchmarked the different CFD models against the experimental data from i) qualitative comparison of surface elevation time series at selected wave gauge positions, ii) evaluation metrics quantifying normalized, statistical errors on surface elevations, amplitudes, phases, and mean surface elevation at selected wave gauge positions, iii)

spectral analyses to quantify the amplitude and phase content of primary and higher-order harmonics along the length of the wave flume. The comparison of surface elevation time series and evaluation metrics for the breaking wave condition 3 can be seen in Fig. 3.13, where δ denotes evaluation metrics with the error types given as subscripts, refer to Andersen et al. (2023, Paper G) for their definitions. The comparison of the evolution of amplitude, a , and phase, ϕ , along the wave flume for wave condition 3 can be seen in Fig. 3.14, where f_1 is the primary wave frequency and $x > x_{refl}$ is the subdomain where reflections from the (physical) passive absorption do not enter the spectral analyses. Andersen et al. (2023, Paper G) employed a convergence criterion of evaluation metrics (evaluated relative to the finest resolution) less than 5% and only minor deviations (with emphasis on extremes) in the qualitative comparison of surface elevation time series. Convergence analyses of each CFD model, for each wave condition, were undertaken and documented.

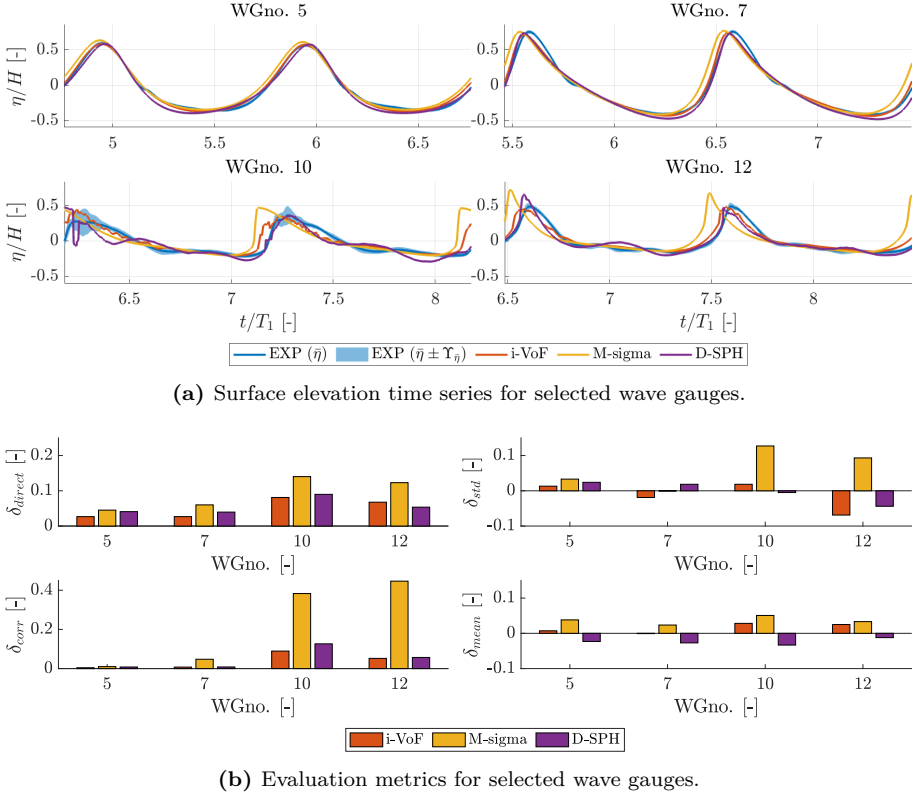
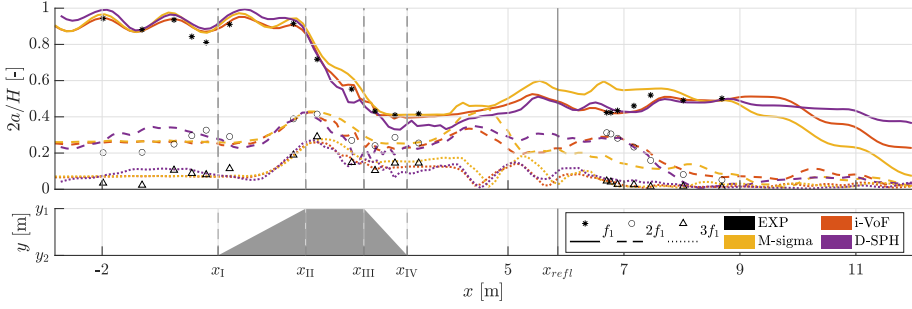
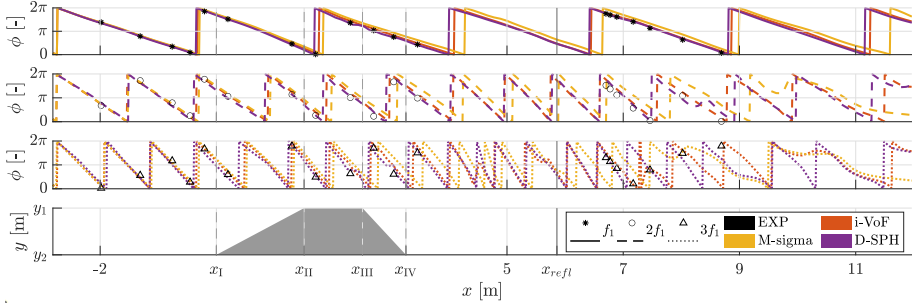


Fig. 3.13: Benchmarking of CFD models against validation experiments of wave propagation over a submerged bar in time domain for wave condition 3. Adapted from Andersen et al. (2023, Paper G).



(a) Amplitude evolution along wave flume length.



(b) Phase evolution along wave flume length.

Fig. 3.14: Benchmarking of CFD models against validation experiments of wave propagation over a submerged bar in frequency domain for wave condition 3. Adapted from Andersen et al. (2023, Paper G).

WGno. 10 in Fig. 3.13a shows the surface elevation time series of a turbulent bore formed from wave-breaking. Notably from Fig. 3.13a is the nearly vertical bore-front of the M-sigma model activating energy dissipation from shock capturing schemes while not overturning as per the sigma transformation. Furthermore, crest elevations are overestimated from the M-sigma and D-SPH models at WGno. 12 in Fig. 3.13a. The overall lowest magnitude of evaluation metrics are found for i-VoF while somewhat large errors on phase (*corr*) and amplitude (*std*) are shown for the M-sigma model in Fig. 3.13b. The breaking-induced energy dissipation at the horizontal crest of the submerged bar is evident from Fig. 3.14a, and while all models capture the major trends in this rapid energy dissipation (between x_{II} and x_{III}), the i-VoF model has the closest agreement with the experimental data. In Fig. 3.14b, the phase evolutions along the wave flume show how the M-sigma model has some overestimation of the wave celerity in the near post-breaking region.

While the **interFoam** solver has previously been compared to the case of wave propagation over a submerged bar, the results on its accuracy differed.

In general, Andersen et al. (2023, Paper G) found high agreement between simulation results of the investigated CFD models and the experimental data. Besides from adding to the credibility of the tested CFD frameworks and solvers to simulate complex wave transformation including wave-breaking, the study led to the main conclusions listed below as well as several subtleties included in Andersen et al. (2023, Paper G).

1. The M-sigma model performed best regarding the cost-accuracy trade-off with computational costs orders of magnitude lower than those of i-VoF and D-SPH and similar overall accuracy.
2. The accuracy of the numerical models were virtually identical for the non-breaking wave conditions.
3. The accuracy of the i-VoF model was higher than those of M-sigma and D-SPH for the breaking wave conditions (in the capture of breaking-induced energy dissipation and crest elevations downwave of the submerged bar).
4. Converged results were considerably more difficult to obtain with the D-SPH model for the breaking wave conditions where divergence and inconsistency occurred for certain configurations.

3.2.3 Sphere Decay Tests

Decay tests pose as a reduced-physics flow problem of offshore renewables often used to characterize system hydrodynamic properties. The heave decay of a semi-submerged sphere, at equilibrium, was selected as a suitable test case to represent a simple point-absorber WEC under the benchmarking of numerical models to simulate WECs under the OES effort as introduced in Section 3.1 and with the research outputs of, e.g, Wendt et al. (2019) and Kramer et al. (2021, Paper B). Inter-model comparisons of a similar idealized test case to that of Kramer et al. (2021, Paper B), that is, $x_{3,0} \in \{0.1D, 0.3D, 0.5D\}$ (visualized in Fig. 3.1), but with $D = 10$ m, were undertaken in Wendt et al. (2019). The study inter-compared LPF, weakly nonlinear PF (by nonlinear hydrostatic contribution), FNPF, and URANS numerical models. Large deviations were found in terms of both amplitude and phases of the heave decay time series between the different groups of models (FNPF and RANS models were grouped together), with the largest internal group scattering in the high-fidelity group of FNPF and URANS models (presumably due to their increased number of inputs). The study lacked an accurate reference solution to benchmark the numerical models. Such a solution was generated with the validation experiments of Kramer et al. (2021, Paper B) conducted with $D = 0.3$ m. Based on the idealized test case of Kramer et al. (2021, Paper B), numerical models of various fidelity were simulated independently between different participants of the OES working group. Numerical models encompassed LPF with various

nonlinear corrections, FNPF, and URANS (in total, 11 numerical models were inter-compared with 6 being FNPF and URANS models). Unsurprisingly, the accuracy of the LPF-based models decreased with increasing drop heights, see Fig. 3.15. However, in contrast to the findings of Wendt et al. (2019), the higher-fidelity models of FNPF and URANS-types were found to be of consistently high accuracy over the tested range of drop heights, see Figs. 3.15 and 3.16.

At the lowest drop height, $x_{3,0} = 0.1D$, the accuracies of the LPF models are similar to those of the FNPF/URANS models which underlines the suitability of LPF to simulate body motions of this magnitude. More nonlinear corrections are imposed to the LPF models with increasing numbering (LPF0, LPF1, LPF2, etc.) outlined in Appendix C of Kramer et al. (2021, Paper B). Interestingly, the introduction of nonlinear hydrostatics (in LPF2) yields a larger deviation at initialization of the decays than seen with the simpler LPF0 and LPF1 models. This is a prime example of error cancellation and how it can lead to false conclusions. The error from the linear hydrostatics of the LPF1 model exactly cancels out the error from having a constant added mass at initialization. However, phase errors are significantly reduced with the nonlinear hydrostatics (making the water-plane area draft dependent) as also found in Wendt et al. (2019).

At the highest drop height, $x_{3,0} = 0.5D$, URANS and FNPF models deviate with less than 3% and 5% of $x_{3,0}$, respectively, whereas the maximum of deviations of the LPF models are an order of magnitude larger. The URANS models perform with similar accuracy but the associated computational cost varies from a few CPU-hours for 2-D domains (URANS5) with an axisymmetric wedge geometry to multiple thousands CPU-hours for 3-D domains with the full sphere geometry (URANS1-4). The high compliance between the heave decay series of all URANS models indicate that the flow problem can effectively be considered axisymmetric. The accuracy of URANS and FNPF models are close to identical at the first crest and trough (where velocity gradients are largest), see Fig. 3.16. Nonetheless, the deviations of, particularly, FNPF increase over time which are attributed to the accumulation of numerical errors or increased rotational and viscous effects from the accumulation of eddies and high-frequency perturbations of the free surface. The computational cost of the FNPF model, simulating the decay in 3-D, was in the same order of magnitude as that of the 2-D axisymmetric URANS model speaking in favor of the FNPF model when non-axisymmetric loading such as incident waves are to be taken into account and the small reduction on accuracy, relative to URANS, can be tolerated. Details on the numerical model implementations tested in Wendt et al. (2019) and Kramer et al. (2021, Paper B) are given in the respective papers.

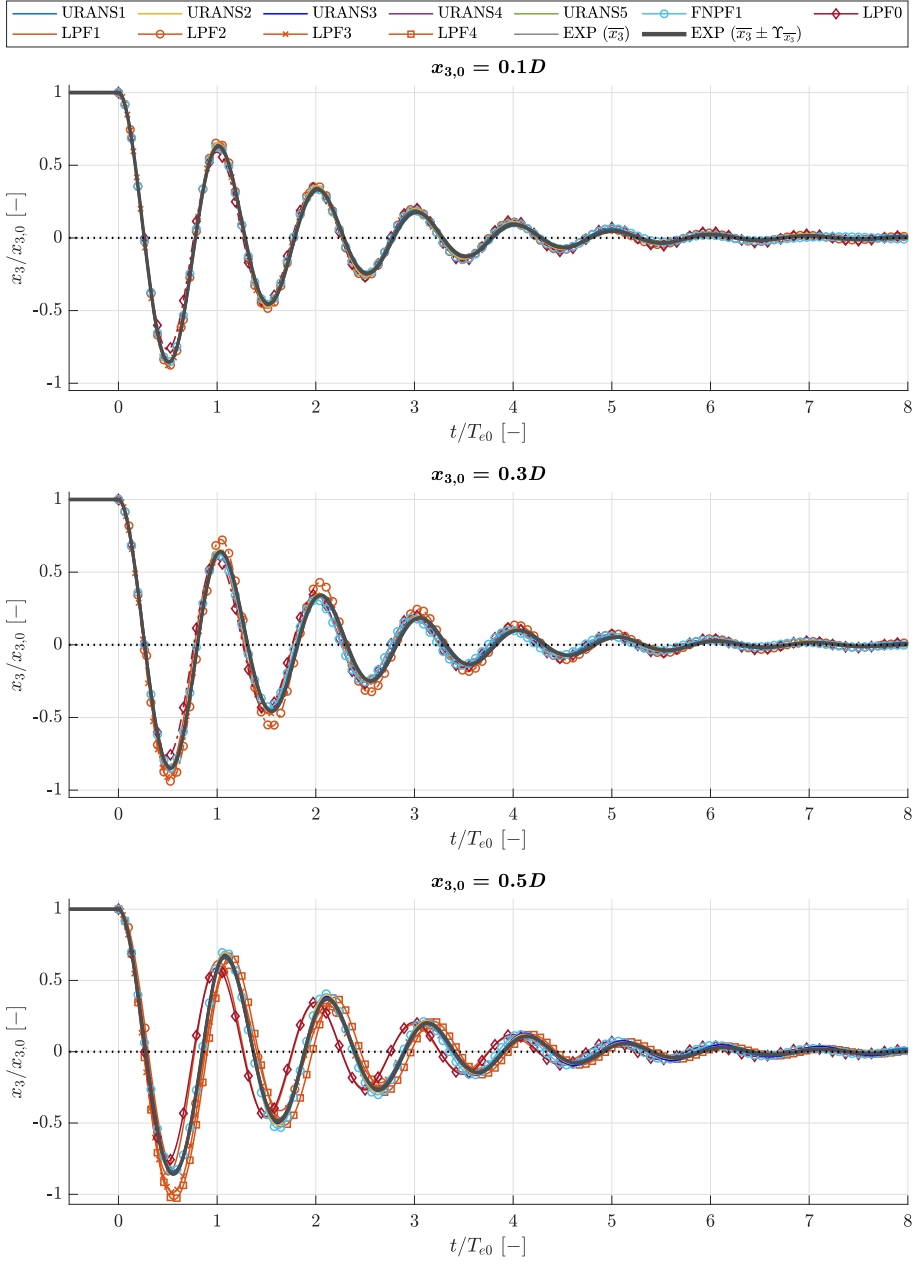


Fig. 3.15: Benchmarking of heave decays of a floating sphere from numerical models of various fidelity for all investigated drop heights. Adapted from Kramer et al. (2021, Paper B).

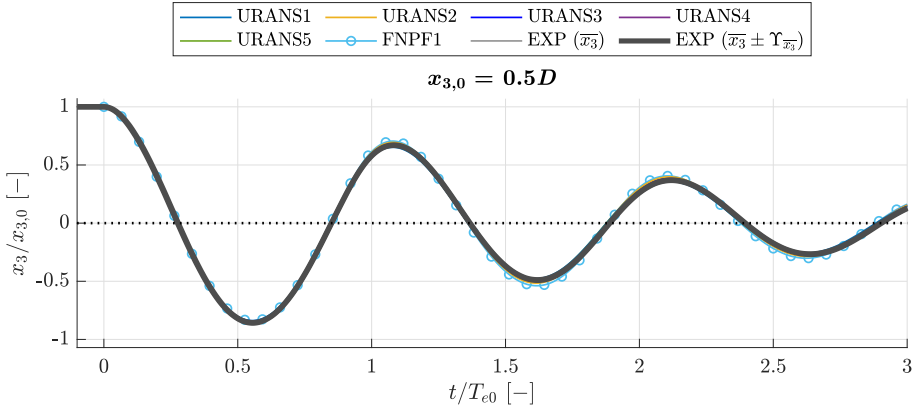


Fig. 3.16: Benchmarking of heave decays of a floating sphere from high-fidelity numerical models for the highest investigated drop height. Adapted from Kramer et al. (2021, Paper B).

3.2.4 Moored FOWT Platform in Focused Waves

The numerical modelling of FOWTs is usually carried out based on aero-elasto-control-hydro-mooring packages such as **OpenFAST** (OpenFAST, 2023) or **DeepLines Wind** (Principia, 2023). The platform hydrodynamic models of these packages are based on LPF which is the standard modelling approach for large-scale simulations due to its computational efficiency as introduced in Section 2.2. The assumptions of small amplitude waves and body motions may be more accurate for an FOWT platform relative to a WEC which is often controlled to approach resonance. However, in extreme load cases with highly nonlinear waves, the LPF theory becomes increasingly inaccurate. As a remedy, higher-fidelity CFD such as URANS solvers can be applied. Mooring models are typically dynamic and discretized by either a lumped mass approach or a finite element method (FEM).

A URANS solver and a dynamic FEM mooring solver were coupled in the work of Eskilsson et al. (2023b, Paper D) to simulate the motion response and mooring forces of an FOWT platform in static equilibrium, decay, and focused wave impact tests, comparing against experimental data. A two-way coupling of the platform six-DoF body solver and the mooring solver was applied.

Burmester et al. (2020) has identified how the drag and inertia of the mooring lines can influence the motion response of FOWT platforms. The standard method for hydro-mooring coupling is by a linear combination of inertia and drag terms as per the Morison equation, Eq. (2.6), assuming either still water or flow kinematics as per linear wave theory with superposition of regular waves. Sampling the actual flow kinematics, from the CFD solver, to the mooring model (one-way coupling) has previously been done in only a few works in different CFD frameworks (de Lataillade, 2019; Eskilsson & Palm, 2022; Mar-

tin & Bihs, 2021). The work of Eskilsson and Palm (2022) investigated only mild wave conditions on the DeepCwind platform (Robertson et al., 2017). Eskilsson et al. (2023b, Paper D) expands this work to extreme wave conditions considering a different FOWT platform, i.e., the slack-moored UMaine VoltturnUS-S semisubmersible FOWT platform (Allen et al., 2020). Eskilsson et al. (2023b, Paper D) deploys the VoF-based URANS solver of **interFoam** solver under the **OpenFOAM** framework with the dynamic mooring model of **moodyCore** (Palm & Eskilsson, 2018; Palm et al., 2017). **moodyCore** utilizes a discontinuous Galerkin method (FEM) to solve the elastic cable equations with bending but without torsion. Numerical simulations with and without the sampling of CFD flow kinematics to the mooring finite element nodes (one-way coupled) were benchmarked against the experimental data from model tests of the UMaine FOWT semi-sub in scale 1:70 carried out at the COAST Laboratory of Plymouth University (Ransley et al., 2022). The layout of the mesh used for **interFoam** as well as the mooring and platform geometry are shown in Fig. 3.17.

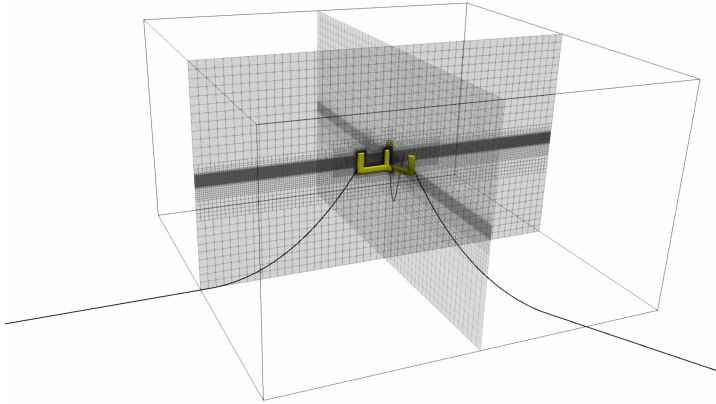
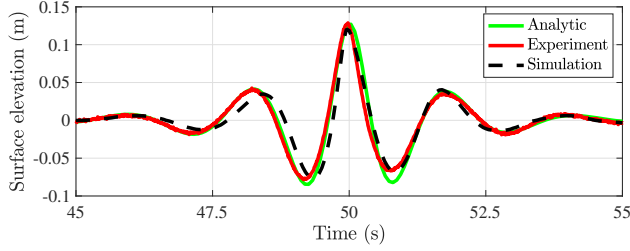


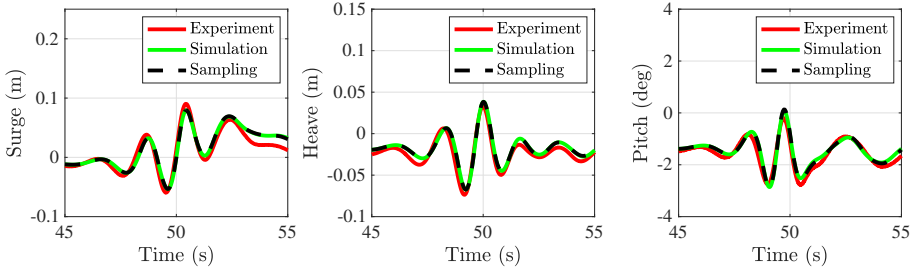
Fig. 3.17: Conceptual layout of mesh for **interFoam** as well as mooring and FOWT platform geometry. Adapted from Eskilsson et al. (2023b, Paper D).

The analytical (NewWave theory), experimental, and numerical surface elevations of the investigated focused wave groups of Eskilsson et al. (2023b, Paper D) can be seen in Fig. 3.18a. The motion responses of the platform and mooring tensions from experiments and the **interFoam**-**moodyCore** coupled numerical model with and without sampling of flow kinematics to the mooring model nodes are compared in Figs. 3.18b and 3.18c. In general, there is fairly high compliance between the simulation results and the experimental data. The simulation results are expected to lie within the experimental uncertainty. It should be noted that the experimental data do not stem from validation experiments. From the higher tiers the experiments represent (complicated ge-

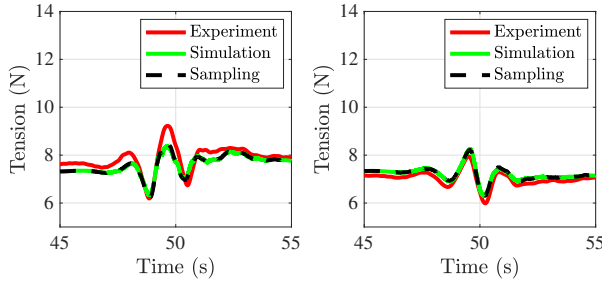
ometry, multi-physics), the experimental data are associated with considerable uncertainties both in terms of measurement uncertainty and input uncertainty (as presented in Section 3.1). However, as the scope of the study was to assess the accuracy of a coupled URANS-mooring model and the influence of flow kinematics sampling a higher tier experiment with inclusion of mooring in the physical tests was key. The sampling of flow kinematics to the mooring nodes yielded some increase in the mooring tensions while only slight effects on the platform motion responses were found. Larger effects from the sampling are expected for prolonged time series embedded with focused waves.



(a) Free surface elevation of focused waves.



(b) Motion response of FOWT platform.



(c) Mooring tensions.

Fig. 3.18: Comparison of experimental and numerical (*interFoam-moodyCore*) results for interactions of focused waves with a moored FOWT platform with and without sampling of flow kinematics to mooring nodes. From Eskilsson et al. (2023b, Paper D).

3.3 Early Design Investigations

The influence on hydrodynamic loading from the variation of the geometrical designs of two distinct offshore renewables was investigated in Andersen et al. (2020, Paper A) and Iversen et al. (2023, Paper F). Andersen et al. (2020, Paper A) investigated a perforated monopile design for offshore turbines and Iversen et al. (2023, Paper F) investigated the wave-activated body of an OWSC. The two works are outlined in Sections 3.3.1 and 3.3.2, respectively.

3.3.1 Perforation of Large Monopiles

Bottom-fixed, offshore wind energy has reached full commercialization as introduced in Chapter 1. Monopiles are the predominant type of foundation and are employed for more than 80% of the installed bottom-fixed offshore wind capacity of Europe in 2020 (WindEurope, 2021). The continuous increase of rated capacity of wind turbines (driven by larger rotor diameters) as well as offshore deployments at increased water depths have led to the emergence of monopiles with diameters exceeding 8 m - often referred to as XL monopiles (Santos et al., 2022). The natural frequency is generally decreased for wind turbines with higher rated capacity supported by larger monopiles, thus nearing typically significant wave frequencies (Velarde et al., 2020). As a combined effect of this and the increased magnitudes of wave loads, the design loads of XL monopiles are significantly altered from those of more common, slender monopiles and are largely governed by wave-induced fatigue (Velarde et al., 2020). Andersen et al. (2020, Paper A) investigated a novel XL monopile design, suggested by Vestas A/S, incorporating perforations of the monopile shell in the proximity of the free surface with the aim of reducing wave loads. A conceptual layout of the perforated monopile design can be seen in Fig. 3.19. In prototype scale, the design is 10 m in diameter and targeted for depths of 35-40 m.

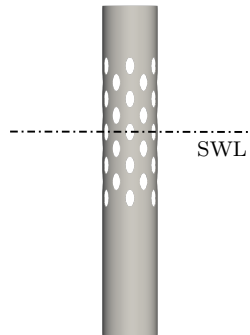


Fig. 3.19: Conceptual layout of the investigated perforated monopile design. Adapted from Andersen et al. (2020, Paper A).

In Andersen et al. (2020, Paper A), wave flume tests were carried out at the Ocean and Coastal Laboratory at Aalborg University for models in scale 1:80 of the perforated monopile as well as a conventional XL monopile (non-perforated, circular cylinder) as reference. Both regular and irregular wave conditions were tested using Froude similarity law. The tested wave conditions covered Keulegan-Carpenter numbers K_C between 0.3 and 9, corresponding to force regimes of *large inertia* and *inertia and drag*, respectively, for the flow past a smooth, circular cylinder as per Chakrabati (2005). Time series of the horizontal force in the wave propagation direction and its point of attack were measured with a bending beam force transducer. A wave gauge was installed behind a guide wall at the same distance from the wave maker as the monopile models. Photos of the wave flume tests are shown in Fig. 3.20.



Fig. 3.20: Photos of the wave flume tests on the perforated monopile model. Adapted from Andersen et al. (2020, Paper A).

Substantial reductions of 10-75% of the peak loads were found for $K_C < 2$ in both regular and irregular wave conditions. The ratios between peak forces of the perforated and conventional monopiles for regular wave conditions are included in Fig. 3.21 where F^* denotes the peak forces normalized with the respective measured wave heights behind the guide wall and error bars of plus/minus one standard deviation are included for repeated wave conditions ($N = 5$). A hyperbolic tangent function was fitted to the experimental data. The load reduction increases with decreasing $K_C < 2$ and stagnates for increasing $K_C > 2$, see Fig. 3.21. The Morison equation, as introduced in Eq. (2.6), was fitted to the measured force time series to estimate drag and inertia coefficients. The inertia loads were decreased in all tested wave conditions for the perforated monopile design and the relative importance of drag increased.

The wave loads from wave conditions of $K_C < 2$ can contribute significantly to the fatigue damage of XL monopiles, depending on the metocean conditions and wind turbine availability, as found in Velarde et al. (2020). Consequently, the reduction of wave loads from the perforation of monopiles as found in the study of Andersen et al. (2020, Paper A) has the potential to mitigate signif-

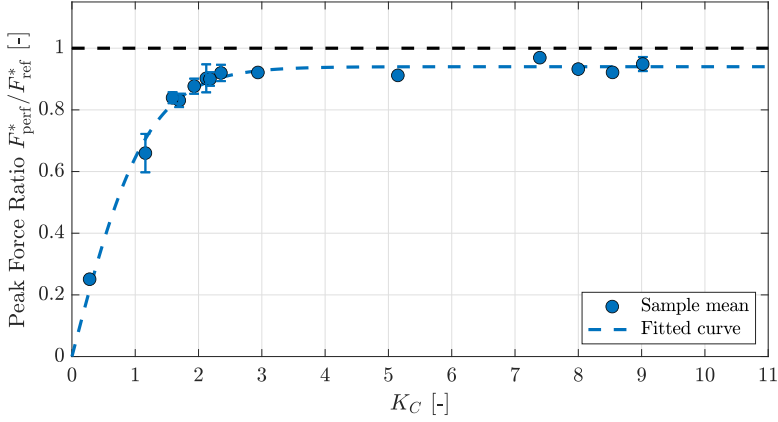


Fig. 3.21: Correlation between K_C and the reduction of peak forces from the perforations (given as the ratio of peak forces, perforated-to-conventional). Adapted from Andersen et al. (2020, Paper A).

icant, wave-induced fatigue loads which may decrease the fatigue damage and ultimately the LCoE. However, the perforations introduce stress concentrations and complicate the manufacturing and installation compared to conventional XL monopiles, requiring detailed cost-benefits analyses to be carried out to assess its commercial potential. Further possible advantages of the perforated monopile design encompass potentially reduced scour and corrosion protection as outlined in Andersen et al. (2020, Paper A).

3.3.2 Wave-Activated Body of an OWSC

The early design of an OWSC concept from Exowave ApS was investigated in Iversen et al. (2023, Paper F). The considered OWSC concept, henceforth referred to as the *Exowave device*, employs a hydraulic power take-off (PTO) and consists of a wave-activated body connected to a gravity-based foundation through a hinge allowing motion in pitch under wave excitation (effectively operating as a one-DoF system). A visualization of three Exowave devices on a shared foundation can be seen in Fig. 3.22.

The aim of Iversen et al. (2023, Paper F) was to develop a simple one-DoF numerical model to get a first assessment of the feasibility of the Exowave device in terms of power output and structural loads and how various geometrical shapes of the wave-activated body influenced these. The characteristic length scale of the Exowave device was assumed small relative to the wavelengths of the planned sites for deployment from which a Morison approach was adopted to the hydrodynamic model.

A numerical model to solve the one-DoF (rotational) equation of motion was formulated with the resultant moment derived from the hydraulic PTO,

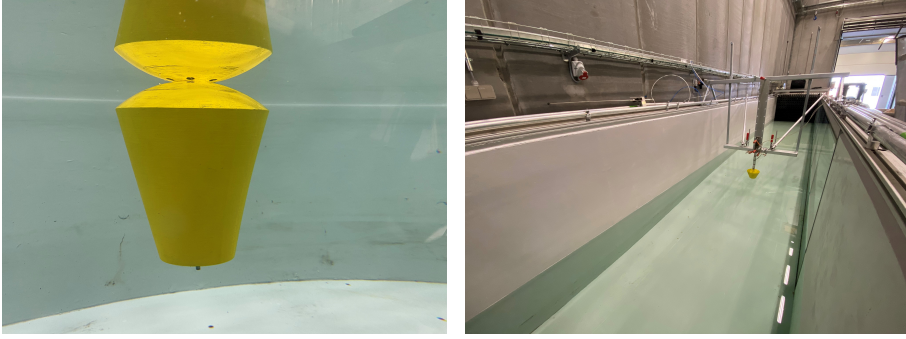
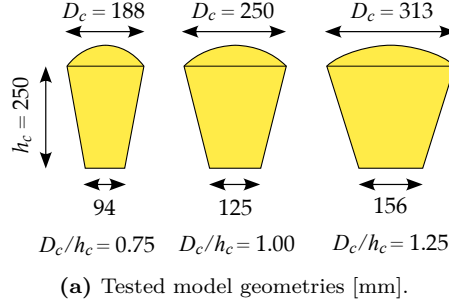


Fig. 3.22: Conceptual layout of three Exowave devices on a shared foundation. From Iversen et al. (2023, Paper F).

hydrostatics, and hydrodynamics via the relative velocity formulation of the Morison equation, see Eq. (2.6). Wave kinematics were calculated from linear wave theory with irregular waves realized from parameterized JONSWAP spectra by the inverse fast Fourier transform (IFFT) random phase method. Only long-crested were considered. For enhanced computational efficiency, time marching was carried out with a variable time step, variable order Runge-Kutta scheme (Cash & Karp, 1990).

Preliminary analyses with various geometrical shapes ranging from flat bodies to wider, axisymmetric bodies, such as circular cylinders and truncated cones (conical frustums), were carried out with Morison coefficients, somewhat crudely, estimated from DNV (2017). Higher power outputs were found for the latter type of bodies due to increased inertia loads. Conical frustums with increased diameters closer to the free surface, where particle velocities and moment arms are higher, were selected for further analysis.

Wave flume tests on conical frustums with three different diameter-to-height ratios D_c/h_c , where D_c and h_c are characteristic diameters and heights of the conical frustums, were carried out at the Ocean and Coastal Engineering Laboratory at Aalborg University in scale 1:40 (Froude similarity law was applied), see Fig. 3.23. The conical frustums were placed close to the free surface and regular wave conditions corresponding to seven values of K_C between 1 and 8 were tested for all shapes. The calculation of drag coefficients from the wave flume tests would be highly uncertain due to inertia-dominated forces. Accordingly, drag coefficients were calculated from CFD simulations of the conical frustums subjected to uniform current ($Re \approx 1e5$) with a free surface using the **interFoam** solver of **OpenFOAM**. Inertia coefficients were found to vary significantly, between 1.5 and 1.9, over the tested K_C whereas only modest variation with the three designs were found. Based on the CFD analyses, a drag coefficient of 0.8 was found for the conical frustum designs close to the free surface.



(b) Photos of the wave flume setup.

Fig. 3.23: Wave flume tests on three geometries representing the wave-activated body of the Exowave device. Adapted from Iversen et al. (2023, Paper F).

The numerical model with the estimated Morison coefficients from wave flume tests and CFD (as well as some inter- and extrapolation) were used extensively in the gross assessment of power output and structural loads for various geometrical designs and configurations of the Exowave device under the Danish Energy Technology Development and Demonstration Program (EUDP) project *Exowave, Water, Electricity and PtX*. The project ended with an open ocean demonstration of the Exowave device with a conical frustum as wave-activated body at Blue Accelerator off the coast of Belgium. Further development of the numerical model as well as validation against experimental data are recommended, and wave basin tests with emulated PTO and short-crested waves have been planned in a new EUDP project.

4 | Conclusions

The dissertation introduced how GHG emissions from human activity are evidently behind global warming and are likely the main driver of the ongoing climate change. The transition from fossil fuels to renewable energy sources is critical to mitigate GHG emissions and its adverse impacts on nature and people. Significant renewable energy resources are available offshore where common restrictions of onshore renewables on infrastructure, land availability, and visual and audible pollution are generally decreased. To harness this resource, the EU has set ambitious targets to increase the EU capacity of offshore renewables including offshore wind and ocean energy technologies by 2050. Bottom-fixed offshore wind turbines have reached full commercialization but is limited to relatively shallow waters. Floating offshore wind turbines and ocean technologies are promising in relation to increasing the offshore renewable energy capacity, e.g., from deployment at deeper waters and increased utilization of marine space and electrical infrastructure by co-location. However, these technologies require further optimization to reduce their LCoE and reach commercialization. To facilitate the *Performance before Readiness* strategy, increasing the chance of successful market entry, accurate and efficient hydrodynamic models are vital.

The predominant, state-of-the-art hydrodynamic modelling approaches of offshore renewables were reviewed. CFD models solving the Navier-Stokes equations numerically as well as LPF models solving Laplace's equation numerically with linearized BCs pose as two opposite extremes in regard to fidelity and computational cost. The number of numerical methods to solve the governing equations of hydrodynamics at either of these fidelity levels and intermediate hereto is vast, and the importance of verification and validation activities to assess their credibility for given engineering problems were underlined. Validation experiments as opposed to traditional experiments and their lack in literature of hydrodynamic modelling of offshore renewables were addressed. It was emphasized how experimental datasets from low tier validation experiments can enhance numerical model validation and benchmarking relevant to a broad range of offshore renewable energy technologies sharing fundamental physics.

Validation experiments at the low tiers of heave decays of a floating sphere, wave excitation of a fixed sphere, and wave propagation over a submerged bar were carried out and presented. Preliminary analyses, numerical and/or experimental, to detect and reduce experimental uncertainties and derived iterations of experimental designs were highlighted as key to generate accurate experimental benchmark datasets. Quantification of experimental uncertainty by measurement uncertainty and propagation of uncertainties were accounted for.

Numerical model benchmarking is highly useful to inter-compare numerical model accuracy, and, potentially, applicability from computational costs, ease-of-use, etc., improving the engineer's choice of numerical models for particular flow problems. Four studies on the numerical simulation of distinct flow problems relevant to the hydrodynamic modelling of offshore renewables were executed and reviewed focusing on numerical model benchmarking.

A hybrid-RANS-LES model was used to simulate the normal flow past a flat plate at a high Re for various corner curvatures and results were collated with results from physical tests, LES, and DNS from literature. By comparison of multiple global flow quantities, similar accuracy to that of LES was found.

Three fundamentally different CFD models were benchmarked against the validation experiments of wave propagation over a submerged bar for four wave conditions of various linearity, regularity, and breaking. The CFD models were based on an SPH solver and two FVM URANS solvers with VoF-based interface capture and sigma transformation, respectively. Similar overall accuracies were found with only a slight increase of the accuracy with the FVM URANS VoF-based model under breaking wave conditions. The best cost-accuracy trade-off was found for the FVM URANS sigma transformation model.

The validation experiments on heave decays of a floating sphere were used to benchmark numerical models of different levels of fidelity encompassing URANS, FNPF, and LPF models (the latter with various nonlinear corrections). As the nonlinearities (drop heights) of the heave decays were increased, a clear separation of the accuracies of models at different fidelity levels was demonstrated. URANS and FNPF models were found to be of similar high accuracy for all drop heights, while LPF models deteriorated for the higher drop heights. A URANS model with a 2-D, wedge domain maintained high accuracy with three orders of magnitude lower computational costs than the 3-D URANS models.

Focused wave interaction with a moored FOWT platform was simulated with a URANS VoF-based model coupled to a dynamic FEM mooring model with and without sampling of the flow kinematics to the mooring nodes. Simulation results on mooring tensions and the motion response of the platform were benchmarked against experimental data. Mooring tensions were altered to some extent from the sampling of flow kinematics while the platform motion response was only affected very slightly. Good agreement with experimental

data was found in general.

Lastly, hydrodynamic investigations of early designs of a perforated monopile for bottom-fixed, offshore wind turbines and the wave-activated body of a OWSC were carried out. Based on physical wave flume tests, the perforation of large monopiles was found to have a significant potential to reduce wave-induced fatigue loads, driving the design of XL monopiles, and future feasibility studies were recommended. A Morison-based numerical model, with Morison coefficients estimated from physical wave flume tests, CFD, and DNV (2017), was formulated to assess the influence from geometrical design variations of a small OWSC (relative to wavelengths). Based on this, the geometrical shape of the wave-activated body was altered from a flat body to a conical frustum - increasing the estimated power output at planned sites. Further development and validation of the numerical model were recommended.

Future work to extent the presented research has been planned, covering the full publication of experimental benchmark datasets from the validation experiments of wave excitation of a fixed sphere as well as the execution of validation experiments of a radiating sphere and a moving sphere with PTO under wave excitation. Additionally, numerical simulation, and specifically numerical model benchmarking, has been planned for the normal oscillatory flow of flat plates with finite aspect ratios, close to the free surface, and with ranging plate flexibility, aiming to advance the understanding of the governing hydrodynamics of these flow problems to improve numerical models of, e.g., plate-type OWSCs.

References

- Aeschliman, D. P., & Oberkampf, W. L. (1998). Experimental Methodology for Computational Fluid Dynamics Code Validation. *AIAA Journal*, 36(5), 733–741. <https://doi.org/10.2514/2.461>
- AIAA (1998). *Guide for the Verification and Validation of Computational Fluid Dynamics Simulations (AIAA G-077-1998)*. American Institute of Aeronautics and Astronautics. Reston, VA. <https://doi.org/10.2514/4.472855.001>
- Allen, C., Viscelli, A., Dagher, H., Goupee, A., Gaertner, E., Abbas, N., Hall, M., & Barter, G. (2020). *Definition of the UMaine VoltturnUS-S Reference Platform Developed for the IEA Wind 15-Megawatt Offshore Reference Wind Turbine*. <https://doi.org/10.2172/1660012>
- Andersen, J., Abrahamsen, R., Lykke Andersen, T., Andersen, M. T., Baun, T. L., & Neubauer, J. L. (2020). Wave Load Mitigation by Perforation of Monopiles. *Journal of Marine Science and Engineering*, 8(5). <https://doi.org/10.3390/jmse8050352>
- Andersen, J., Eldrup, M. R., Verao Fernández, G., & Ferri, F. (2023). Wave Propagation over a Submerged Bar: Benchmarking of VoF, Sigma Transformation, and SPH Numerical Models against Physical Wave Flume Tests. Submitted to *Journal of Hydrodynamics*. ISSN: 1878-0342.
- Andersen, J., & Eskilsson, C. (2023). Detached-Eddy Simulation of Normal Flow past Flat Plates: The Influence from Corner Curvature. *Proceedings of the Thirty-Third (2023) International Ocean and Polar Engineering Conference* (pp. 2441–2448). International Society of Offshore and Polar Engineers (ISOPE). ISBN: 978-1-880653-80-7.
- Andersen, J., & Kramer, M. B. (2023). Wave Excitation Tests on a Fixed Sphere: Comparison of Physical Wave Basin Setups. *Proceedings of the 15th European Wave and Tidal Energy Conference (EWTEC 2023)*. <https://doi.org/10.36688/ewtec-2023-170>
- Andersen, M. T. (2016). *Floating Foundations for Offshore Wind Turbines* (Doctoral dissertation). Faculty of Engineering and Science, Aalborg University. <https://doi.org/10.5278/vbn.phd.engsci.00175>

- Ansys Inc. (2023a). Ansys CFX. <https://www.ansys.com/products/fluids/ansys-cfx>
- Ansys Inc. (2023b). Ansys Fluent. <https://www.ansys.com/products/fluids/ansys-fluent>
- ASME (2006). *ASME V&V 10-2006: Guide for Verification and Validation in Computational Solid Mechanics*. American Society of Mechanical Engineers. New York, NY.
- ASME (2009). *ASME V&V 20-2009: Standard for Verification and Validation in Computational Fluid Dynamics and Heat Transfer*. American Society of Mechanical Engineers. New York, NY.
- ASME (2019). *ASME PTC 19.1-2018: Test Uncertainty (Performance Test Codes)*. American Society of Mechanical Engineers. New York, NY.
- Babarit, A., & Delhommeau, G. (2015). Theoretical and numerical aspects of the open source bem solver {nemoh}. *Proceedings of the 11th European Wave and Tidal Energy Conference (EWTEC 2015)*.
- Bahaj, A. S. (2011). Generating Electricity from the Oceans. *Renewable and Sustainable Energy Reviews*, 15(7), 3399–3416. <https://doi.org/10.1016/j.rser.2011.04.032>
- Beji, S., & Battjes, J. A. (1993). Experimental investigation of wave propagation over a bar. *Coastal Engineering*, 19, 151–162. [https://doi.org/10.1016/0378-3839\(93\)90022-Z](https://doi.org/10.1016/0378-3839(93)90022-Z)
- Beji, S., & Battjes, J. A. (1994). Numerical simulation of nonlinear wave propagation over a bar. *Coastal Engineering*, 23, 1–16. [https://doi.org/10.1016/0378-3839\(94\)90012-4](https://doi.org/10.1016/0378-3839(94)90012-4)
- Bihs, H., Kamath, A., Alagan Chella, M., Aggarwal, A., & Arntsen, Ø. A. (2016). A New Level Set Numerical Wave Tank with Improved Density Interpolation for Complex Wave Hydrodynamics. *Computers & Fluids*, 140, 191–208. <https://doi.org/https://doi.org/10.1016/j.compfluid.2016.09.012>
- BIMP, IEC, IFCC, ILAC, ISO, IUPAC, IUPAP, & OIML (2008). *100:2008 evaluation of measurement data—guide to the expression of uncertainty in measurement*. JCGM. https://www.bipm.org/documents/20126/2071204/JCGM_100_2008_E.pdf/cb0ef43f-baa5-11cf-3f85-4dcd86f77bd6.
- Bingham, H. B., Yu, Y.-H., Nielsen, K., Tran, T. T., Kim, K.-H., Park, S., Hong, K., Said, H. A., Kelly, T., Ringwood, J. V., Read, R. W., Ransley, E., Brown, S., & Greaves, D. (2021). Ocean Energy Systems Wave Energy Modeling Task 10.4: Numerical Modeling of a Fixed Oscillating Water Column. *Energies*, 14(6). <https://doi.org/10.3390/en14061718>
- Blottner, F. G. (1990). Accurate Navier-Stokes Results for the Hypersonic Flow over a Spherical Nosetip. *Journal of Spacecraft and Rockets*, 27(2), 113–122. <https://doi.org/10.2514/3.26115>

- Borgarino, B., Babarit, A., & Ferrant, P. (2012). Impact of wave interaction effects on energy absorbtion in large arrays of wave energy converters. *Ocean Engineering*, 41, 79–88.
- Bredmose, H., Peregrine, D. H., & Bullock, G. N. (2009). Violent breaking wave impacts. Part 2: modelling the effect of air. *Journal of Fluid Mechanics*, 641, 389–430. <https://doi.org/10.1017/S0022112009991571>
- Burmester, S., Vaz, G., el Moctar, O., Gueydon, S., Koop, A., Wang, Y., & Chen, H. (2020). High-Fidelity Modelling of Floating Offshore Wind Turbine Platforms. *Proceedings of the 39th International Conference on Ocean, Offshore & Arctic Engineering*.
- Cash, J. R., & Karp, A. H. (1990). A Variable Order Runge-Kutta Method for Initial Value Problems with Rapidly Varying Right-Hand Sides. *ACM Transactions of Mathematical Software*, 16(3), 201–222. <https://doi.org/10.1145/79505.79507>
- Chakrabati, S. K. (2005). Loads and Responses. In S. K. Chakrabati (Ed.), *Handbook of Offshore Engineering* (pp. 133–196). Elsevier. <https://doi.org/10.1016/B978-008044381-2.50007-2>
- Crespo, A. J., Ropero, P., Domínguez, J. M., Gómez-Gesteira, M., Altomare, C., Tagliaferro, B., & Viccione, G. (2020). SPH Modelling of Extreme Loads Exerted onto a Point Absorber WEC. *Developments in Renewable Energies Offshore: Proceedings of the 4th International Conference on Renewable Energies Offshore, RENEW 2020* (pp. 206–213). <https://doi.org/10.1201/9781003134572-25>
- Cummins, W. (1962). *The Impulse Response Function and Ship Motions*. Department of the Navy, David Taylor Model Basin Bethesda, MD, USA.
- Davidson, J., & Costello, R. (2020). Efficient Nonlinear Hydrodynamic Models for Wave Energy Converter Design - A Scoping Study. *Journal of Marine Science and Engineering*, 8(1). <https://doi.org/10.3390/jmse8010035>
- Davidson, J., Giorgi, S., & Ringwood, J. V. (2016). Identification of Wave Energy Device Models from Numerical Wave Tank Data - Part 1: Numerical Wave Tank Identification Tests. *IEEE Transactions on Sustainable Energy*, 7(3), 1012–1019. <https://doi.org/10.1109/TSTE.2016.2515512>
- de Lataillade, T. (2019). *High-Fidelity Computational Modelling of Fluid-Structure Interaction for Moored Floating Bodies* (Doctoral dissertation). University of Edinburgh.
- DHI (2023). MIKE 3 Wave Model FM. <https://www.mikepoweredbydhi.com/products/mike-3-wave-fm>
- Díaz-Ojeda, H. R., Huera-Huarte, F. J., & González-Gutiérrez, L. M. (2019). Hydrodynamics of a Rigid Stationary Flat Plate in Cross-Flow Near the Free Surface. *Physics of Fluids*, 31(10). <https://doi.org/10.1063/1.5111525>

- Dingemans, M. W. (1994). *Comparison of Computations with Boussinesq-Like Models and Laboratory Measurements (Report No. H1684.12)*. Deltares (WL).
- DNV (2017). *Environmental Conditions and Environmental Loads* (August 2017). DNV.
- Domínguez, J. M., Fourtakas, G., Altomare, C., Canelas, R. B., Tafuni, A., García-Feal, O., Martínez-Estévez, I., Mokos, A., Vacondio, R., Crespo, A. J. C., Rogers, B. D., Stansby, P. K., & Gómez-Gesteira, M. (2021). Dualsphysics: From fluid dynamics to multiphysics problems. *Computational Particle Mechanics*. <https://doi.org/10.1007/s40571-021-00404-2>
- Eça, L., & Hoekstra, M. (2014). A Procedure for the Estimation of the Numerical Uncertainty of CFD Calculations Based on Grid Refinement Studies. *Journal of Computational Physics*, 262, 104–130. <https://doi.org/https://doi.org/10.1016/j.jcp.2014.01.006>
- Eça, L., Vaz, G., & Hoekstra, M. (2010). A Verification and Validation Exercise for the Flow Over a Backward Facing Step Flow. In J. C. F. Pereira & A. Sequeira (Eds.), *ECCOMAS CFD*. <https://www.researchgate.net/publication/262142241>
- Eskilsson, C., & Palm, J. (2022). High-Fidelity Modelling of Moored Marine Structures: Multi-Component Simulations and Fluid-Mooring Coupling. *Journal of Ocean Engineering and Marine Energy*, 8(4), 513–526.
- Eskilsson, C., Palm, J., Kofoed, J., & Friis-Madsen, E. (2014). CFD Study of the Overtopping Discharge of the Wave Dragon Wave Wnergy Converter. *Proceedings of the 1st International Conference on Renewable Energies Offshore (RENEW 2014)*. ISBN: 978-1-138-02871-5 <https://doi.org/10.1201/b18973-42>
- Eskilsson, C., Pashami, S., Holst, A., & Palm, J. (2023a). A Hybrid Linear Potential Flow - Machine Learning Model for Enhanced Prediction of WEC Performance. *Proceedings of the 15th European Wave and Tidal Energy Conference (EWTEC 2023)*. <https://doi.org/10.36688/ewtec-2023-321>
- Eskilsson, C., Verao Fernández, G., Andersen, J., & Palm, J. (2023b). Hydrodynamic Simulations of a FOWT Platform (1st FOWT Comparative Study) Using OpenFOAM Coupled to MoodyCore. *Proceedings of the Thirty-Third (2023) International Ocean and Polar Engineering Conference* (pp. 461–468). International Society of Offshore and Polar Engineers (ISOPE). ISBN: 978-1-880653-80-7.
- European Commission (2020). *An EU Strategy to Harness the Potential of Offshore Renewable Energy for a Climate Neutral Future*. European Commission. <https://eur-lex.europa.eu/legal-content/EN/TXT/?uri=COM:2020:741:FIN>

- Fage, A., & Johansen, F. C. (1927). On the Flow of Air behind an Inclined Flat Plate of Infinite Span. *Proceedings of The Royal Society A: Mathematical, Physical and Engineering Sciences*, 116, 170–197. <https://api.semanticscholar.org/CorpusID:119513692>
- Faltinsen, O. (1990). *Sea Loads on Ships and Offshore Structures*. Cambridge University Press. ISBN: 0521458706.
- Fernandez-Mora, A., Ribberink, J. S., van der Zanden, J., van der Werf, J. J., & Jacobsen, N. G. (2017). Rans-vof modeling of hydrodynamics and sand transport under full-scale non-breaking and breaking waves. *Coastal Engineering Proceedings*, 1, sediment.29. <https://doi.org/10.9753/icce.v35.sediment.29>
- Folley, M., & Whittaker, T. (2011). The Adequacy of Phase-Averaged Models for Modelling Wave Farms. *ASME 2011 30th International Conference on Ocean, Offshore and Arctic Engineering (OMAE2011)*, 663–671. <https://doi.org/10.1115/OMAE2011-49810>
- Gadelho, J., Lavrov, A., & Soares, C. G. (2014). Modelling the Effect of Obstacles on the 2D Wave Propagation with OpenFOAM. In C. G. Soares & E. L. Peña (Eds.). Taylor & Francis Group. ISBN: 978-1-138-00124-4.
- Gielen, D., Boshell, F., Saygin, D., Bazilian, M. D., Wagner, N., & Gorini, R. (2019). The Role of Renewable Energy in the Global Energy Transformation. *Energy Strategy Reviews*, 24, 38–50. <https://doi.org/10.1016/j.esr.2019.01.006>
- Giorgi, S., Davidson, J., Jakobsen, M., Kramer, M., & Ringwood, J. V. (2019). Identification of Dynamic Models for a Wave Energy Converter from Experimental Data. *Ocean Engineering*, 183, 426–436. <https://doi.org/10.1016/j.oceaneng.2019.05.008>
- Giorgi, S., Davidson, J., & Ringwood, J. V. (2016). Identification of Wave Energy Device Models from Numerical Wave Tank Data - Part 2: Data-Based Model Determination. *IEEE Transactions on Sustainable Energy*, 7(3), 1020–1027. <https://doi.org/10.1109/TSTE.2016.2515500>
- González-Cao, J., Altomare, C., Crespo, A. J. C., Domínguez, J. M., Gómez-Gesteira, M., & Kisacik, D. (2019). On the Accuracy of DualSPHysics to Assess Violent Collisions with Coastal Structures. *Computers & Fluids*, 179, 604–612. <https://doi.org/10.1016/j.compfluid.2018.11.021>
- Gruwez, V., Altomare, C., Suzuki, T., Streicher, M., Cappietti, L., Kortenhaus, A., & Troch, P. (2020). An Inter-Model Comparison for Wave Interactions with Sea Dikes on Shallow Foreshores. *Journal of Marine Science and Engineering*, 8. <https://doi.org/10.3390/jmse8120985>
- Guo, B., & Ringwood, J. V. (2021). Geometric Optimisation of Wave Energy Conversion Devices: A Survey. *Applied Energy*, 297, 117100. <https://doi.org/10.1016/j.apenergy.2021.117100>
- Hemmati, A., Wood, D. H., & Martinuzzi, R. J. (2018). On Simulating the Flow Past a Normal Thin Flat Plate. *Journal of Wind Engineering*

- and *Industrial Aerodynamics*, 174, 170–187. <https://doi.org/https://doi.org/10.1016/j.jweia.2017.12.026>
- Hicks, J. B. H. (2020). *Development of a High-order Potential Flow Solver for Nonlinear Wave-Structure Interaction* (Doctoral dissertation). Technical University of Denmark (DTU).
- Hoerner, S. F. (1965). *Fluid-dynamic drag: Theoretical, experimental, and statistical information*. Published by the Author.
- IEA (2016). *IEA OES Wave Energy Converters Modelling Verification and Validation*. <https://www.ocean-energy-systems.org/oes-projects/wave-energy-converters-modelling-verification-and-validation/>
- IPCC (2023). Summary for Policymakers. In Core Writing Team, H. Lee, & J. Romero (Eds.), *Climate Change 2023: Synthesis Report. Contribution of Working Groups I, II and III to the Sixth Assessment Report of the Intergovernmental Panel on Climate Change* (pp. 1–34). IPCC. <https://doi.org/10.59327/IPCC/AR6-9789291691647.001>
- IRENA (2020). *Fostering a Blue Economy: Offshore Renewable Energy*. International Renewable Energy Agency. ISBN: 978-92-9260-288-8.
- IRENA (2022). *Renewable Power Generation Costs in 2022*. International Renewable Energy Agency. ISBN: 978-92-9260-544-5.
- ITTC (2021). *Recommended Procedures and Guidelines: Uncertainty Analysis in CFD Verification and Validation Methodology and Procedures*. International Towing Tank Conference. <https://www.ittc.info/media/9765/75-03-01-01.pdf>
- Iversen, S. K., Andersen, J., Wigant, L., & Frigaard, P. (2023). Development of the Exowave Oscillating Wave Surge Converter. *Proceedings of the 15th European Wave and Tidal Energy Conference (EWTEC 2023)*. <https://doi.org/10.36688/ewtec-2023-368>
- Janßen, C. F., Grilli, S. T., & Krawczyk, M. (2013). On Enhanced Non-Linear Free Surface Flow Simulations with a Hybrid LBM–VOF Model. *Computers & Mathematics with Applications*, 65(2), 211–229. <https://doi.org/10.1016/j.camwa.2012.05.012>
- Jiang, Y., Hu, G., Zong, Z., Zou, L., & Jin, G. (2020). Influence of an Integral Heave Plate on the Dynamic Response of Floating Offshore Wind Turbine Under Operational and Storm Conditions. *Energies*, 13(22). <https://doi.org/10.3390/en13226122>
- Kamath, A., Chella, M. A., Bihs, H., & Arntsen, Ø. A. (2017). Energy Transfer due to Shoaling and Decomposition of Breaking and Non-Breaking Waves over a Submerged Bar. *Engineering Applications of Computational Fluid Mechanics*, 11(1), 450–466. <https://doi.org/10.1080/19942060.2017.1310671>
- Kramer, M. B., Andersen, J., Thomas, S., Bendixen, F. B., Bingham, H., Read, R., Holk, N., Ransley, E., Brown, S., Yu, Y. H., Tran, T. T., Davidson, J., Horvath, C., Janson, C. E., Nielsen, K., & Eskilsson,

- C. (2021). Highly Accurate Experimental Heave Decay Tests with a Floating Sphere: A Public Benchmark Dataset for Model Validation of Fluid–Structure Interaction. *Energies*, 14(2). <https://doi.org/10.3390/en14020269>
- Krystek, M., & Anton, M. (2007). A weighted total least-squares algorithm for fitting a straight line. *Measurement Science and Technology*, 18, 3438. <https://doi.org/10.1088/0957-0233/18/11/025>
- Lee, C. H., & Newman, J. N. (2006). *Wamit user manual*. Version 7.4. WAMIT Inc.
- Li, A.-j., Liu, Y., & Li, H.-j. (2019). New Analytical Solutions to Water Wave Radiation by Vertical Truncated Cylinders through Multi-Term Galerkin Method. *Meccanica*, 54, 429–450. <https://doi.org/10.1007/s11012-019-00964-x>
- Li, A.-j., & Liu, Y. (2019). New Analytical Solutions to Water Wave Diffraction by Vertical Truncated Cylinders. *International Journal of Naval Architecture and Ocean Engineering*, 11(2), 952–969. <https://doi.org/10.1016/j.ijnaoe.2019.04.006>
- Li, Y., Larsen, B. E., & Fuhrman, D. R. (2022). Reynolds stress turbulence modelling of surf zone breaking waves. *Journal of Fluid Mechanics*, 937, A7. <https://doi.org/10.1017/jfm.2022.92>
- Lin, P., & Li, C. W. (2002). A sigma-Coordinate Three-Dimensional Numerical Model for Surface Wave Propagation. *International Journal for Numerical Methods in Fluids*, 38, 1045–1068. <https://doi.org/https://doi.org/10.1002/fld.258>
- Lind, S. J., Rogers, B. D., & Stansby, P. K. (2020). Review of Smoothed Particle Hydrodynamics: Towards Converged Lagrangian Flow Modelling. *Proceedings of the Royal Society A: Mathematical, Physical and Engineering Sciences*, 476(2241), 20190801. <https://doi.org/10.1098/rspa.2019.0801>
- Liu, Y., Xiao, Q., Incecik, A., Peyrard, C., & Wan, D. (2017). Establishing a fully coupled cfd analysis tool for floating offshore wind turbines. *Renewable Energy*, 112, 280–301. <https://doi.org/10.1016/j.renene.2017.04.052>
- Lopez-Pavon, C., & Souto-Iglesias, A. (2015). Hydrodynamic Coefficients and Pressure Loads on Heave Plates for Semi-Submersible Floating Offshore Wind Turbines: A Comparative Analysis using Large Scale Models. *Renewable Energy*, 81, 864–881. <https://doi.org/10.1016/j.renene.2015.04.003>
- Lowe, R. J., Buckley, M. L., Altomare, C., Rijnsdorp, D. P., Yao, Y., Suzuki, T., & Bricker, J. D. (2019). Numerical Simulations of Surf Zone Wave Dynamics using Smoothed Particle Hydrodynamics. *Ocean Modelling*, 144, 101481. <https://doi.org/https://doi.org/10.1016/j.ocemod.2019.101481>

- Manenti, S., Panizzo, A., Ruol, P., & Martinelli, L. (2008). SPH Simulation of a Floating Body Forced by Regular Waves. In P. Maruzewski (Ed.), *Proceedings of 3rd spheric workshop* (pp. 38–41).
- Mannini, C. (2015). Applicability of URANS and DES Simulations of Flow Past Rectangular Cylinders and Bridge Sections. *Computation*, 3(3), 479–508. <https://doi.org/10.3390/computation3030479>
- Martin, T., & Bihs, H. (2021). A Numerical Solution for Modelling Mooring Dynamics, Including Bending and Shearing Effects, Using a Geometrically Exact Beam Model. *J. Mar. Sci. Eng.*, 9, 486.
- Menter, F. R., Kuntz, M., Langtry, R., Hanjalic, K., Nagano, Y., & Tummers, M. J. (2003). Ten Years of Industrial Experience with the SST Turbulence Model. *4th Internal Symposium on Turbulence, Heat, and Mass Transfer*, 4, 625–632. ISBN: 1567001963.
- Morison, J., O'Brien, M., Johnson, J., & Schaaf, S. (1950). The Force Exerted by Surface Waves on Piles. *J Pet Technol*, 189, 149–154. <https://doi.org/10.2118/950149-G>
- Munson, B. R., Okiishi, T. H., Huebsch, W. W., & Rothmayer, A. P. (2013). *Fluid Mechanics SI Version*. WILEY.
- Newman, J. (1977). *Marine Hydrodynamics*. MIT Press. ISBN: 9780262140263.
- Oberkampf, W. L., Aeschliman, D. P., Tate, R. E., & Henfling, J. F. (1993). *Experimental Aerodynamics Research on a Hypersonic Vehicle*. SAND92-1411, Sandia National Laboratories. <https://www.osti.gov/biblio/6532053>
- Oberkampf, W. L., & Roy, C. J. (2010). *Verification and Validation in Scientific Computing*. Cambridge University Press. <https://doi.org/10.1017/CBO9780511760396>
- Oberkampf, W. L., & Trucano, T. G. (2002). *Verification and Validation in Computational Fluid Dynamics*.
- OpenFAST (2023). <https://github.com/OpenFAST/openfast>.
- Orcina Ltd (2023). *OrcaWave User Manual*. Orcina Ltd.
- Palm, J., & Eskilsson, C. (2018). *MOODY: User's Manual Version 2.0*. <https://github.com/johannep/moodyAPI/releases>
- Palm, J., Eskilsson, C., & Bergdahl, L. (2017). An *hp*-adaptive Discontinuous Galerkin Method for Modelling Snap Loads in Mooring Cables. *Ocean Engineering*, 144, 266–276.
- Palm, J., Bergdahl, L., & Eskilsson, C. (2018). Parametric Excitation of Moored Wave Energy Converters using Viscous and Non-Viscous CFD simulations. *Proceedings of the 3rd International Conference on Renewable Energies Offshore (RENEW 2018)*.
- Park, H., Do, T., Tomiczek, T., Cox, D. T., & van de Lindt, J. W. (2018). Numerical Modeling of Non-Breaking, Impulsive Breaking, and Broken Wave Interaction with Elevated Coastal Structures: Laboratory Vali-

- dation and Inter-Model Comparisons. *Ocean Engineering*, 158, 78–98. <https://doi.org/10.1016/j.oceaneng.2018.03.088>
- Piomelli, U. (2021). Large-Eddy Simulations. In P. Durbin (Ed.), *Advanced Approaches in Turbulence* (pp. 83–131). Elsevier. ISBN: 978-0-12-820774-1 <https://doi.org/https://doi.org/10.1016/B978-0-12-820774-1.00009-4>
- Pope, S. B. (2004). Ten Questions Concerning the Large-Eddy Simulation of Turbulent Flows. *New Journal of Physics*, 6(1), 35. <https://doi.org/10.1088/1367-2630/6/1/035>
- Principia (2023). <http://www.principia-group.com/wp-content/uploads/2016/12/2-DeepLines-Wind-Presentation.pdf>.
- Ransley, E., Brown, S., Edwards, E., Tosdevin, T., Monk, K., Reynolds, A., Greaves, D., & Hann, M. (2022). *Hydrodynamic Response of a Floating Offshore Wind Furbine (1st FOWT Comparative Study Dataset)*. PEARL Research Repository. <https://doi.org/10.24382/71J2-3385>
- Ransley, E., Yan, S., Brown, S., Mai, T., Graham, D., Ma, Q., Musiedlak, P., Engsig-Karup, A., Eskilsson, C., Li, Q., Wang, J., Xie, Z., Venkatachalam, S., Stoesser, T., Zhuang, Y., Li, Q., Wan, D., Chen, G., Chen, H., ... Greaves, D. (2019). A Blind Comparative Study of Focused Wave Interactions with a Fixed FPSO-Like Structure (CCP-WSI Blind Test Series 1). *International Journal of Offshore and Polar Engineering*, 29(2), 113–127. <https://doi.org/10.17736/ijope.2019.jc748>
- Ritchie, H., Roser, M., & Rosado, P. (2022). Energy. *Our World in Data*. <https://ourworldindata.org/%20/energy>
- Roache, P. J. (1997). Quantification of Uncertainty in Computational Fluid Dynamics. *Annual Review of Fluid Mechanics*, 29(1), 123–160. <https://doi.org/10.1146/annurev.fluid.29.1.123>
- Roache, P. J. (2016). Verification and Validation in Fluids Engineering: Some Current Issues. *Journal of Fluids Engineering*, 138(10), 101205. <https://doi.org/10.1115/1.4033979>
- Robertson, A., Wendt, F., Jonkman, J., Popko, W., Dagher, H., Gueydon, S., J., Q., Vittori, F., Uzunogulo, E., & Harries, R. (2017). OC5 Project Phase II: Validation of Global Loads of the DeepCwind floating semisubmersible wind turbine. *Energy Procedia*, 137, 38–57.
- Salis, N., Franci, A., Idelsohn, S., Reali, A., & Manenti, S. (2023). Lagrangian Particle-Based Simulation of Waves: A Comparison of SPH and PFEM Approaches. *Engineering with Computers*. <https://doi.org/10.1007/s00366-023-01831-w>
- Santos, F. d. N., Noppe, N., Weijtjens, W., & Devriendt, C. (2022). Results of Fatigue Measurement Campaign on XL Monopiles and Early Predictive Models. *Journal of Physics: Conference Series*, 2265(3), 32092. <https://doi.org/10.1088/1742-6596/2265/3/032092>

- Schmitt, P., Windt, C., Davidson, J., Ringwood, J. V., & Whittaker, T. (2020). Beyond vof: Alternative openfoam solvers for numerical wave tanks. *Journal of Ocean Engineering and Marine Energy*, 6, 277–292. <https://doi.org/10.1007/s40722-020-00173-9>
- Shur, M., Spalart, P., Squires, K., Strelets, M., & Travin, A. (2005). Three-Dimensionality in Reynolds-Averaged Navier-Stokes Solutions Around Two-Dimensional Geometries. *AIAA Journal*, 43, 1230–1242. <https://doi.org/10.2514/1.9694>
- Siemens Digital Industries Software (2023). Simcenter Star-CCM+. <https://www.plm.automation.siemens.com/global/en/products/simcenter/STAR-CCM.html>
- Simon, B., Papoutsellis, C., Benoit, M., & Yates, M. (2019). Comparing Methods of Modeling Depth-Induced Breaking of Irregular Waves with a Fully Nonlinear Potential Flow Approach. *Journal of Ocean Engineering and Marine Energy*, 5, 365–383. <https://doi.org/10.1007/s40722-019-00154-7>
- Smagorinsky, J. (1963). General Circulation Experiments with the Primitive Equations. *Monthly Weather Review*, 91(3), 99–164. [https://doi.org/10.1175/1520-0493\(1963\)091<0099:GCEWTP>2.3.CO;2](https://doi.org/10.1175/1520-0493(1963)091<0099:GCEWTP>2.3.CO;2)
- Spalart, P. R., Jou, W.-H., Strelets, M., Allmaras, S. R., Liu, C., Liu, Z., & Sakell, L. (1997). Comments on the Feasibility of LES for Wings, and on a Hybrid RANS/LES Approach. *Advances in DNS/LES: Direct Numerical Simulation and Large Eddy Simulation*, 137–148. ISBN: 1570743657.
- Squires, K., Forsythe, J., Morton, S., Strang, W., Wurtzler, K., Tomaro, R., Grismer, M., & Spalart, P. (2002). Progress on Detached-Eddy Simulation of Massively Separated Flows. *40th AIAA Aerospace Sciences Meeting & Exhibit*. <https://doi.org/10.2514/6.2002-1021>
- St-Germain, P., Nistor, I., Readshaw, J., & Lamont, G. (2014). Numerical Modelling of Coastal Dike Overtopping using SPH and Non-Hydrostatic NLSW Equations. *Coastal Engineering Proceedings*, 1(34). <https://doi.org/10.9753/icce.v34.structures.10>
- Strelets, M. (2001). Detached eddy simulation of massively separated flows. *39th AIAA Aerospace Sciences Meeting & Exhibit*. <https://doi.org/10.2514/6.2001-879>
- Sun, X., Huang, D., & Wu, G. (2012). The Current State of Offshore Wind Energy Technology Development. *Energy*, 41(1), 298–312. <https://doi.org/10.1016/j.energy.2012.02.054>
- Thomsen, J. B. (2017). *Mooring Solutions for Large Wave Energy Converters* (Doctoral dissertation). Faculty of Engineering and Science, Aalborg University. <https://doi.org/10.5278/vbn.phd.eng.00045>
- Tian, X., Ong, M. C., Yang, J., & Myrhaug, D. (2014). Large-Eddy Simulation of the Flow Normal to a Flat Plate Including Corner Effects at a

- High Reynolds Number. *Journal of Fluids and Structures*, 49, 149–169. <https://doi.org/https://doi.org/10.1016/j.jfluidstructs.2014.04.008>
- Tissier, M., Bonneton, P., Marche, F., Chazel, F., & Lannes, D. (2012). A New Approach to Handle Wave Breaking in Fully Non-Linear Boussinesq Models. *Coastal Engineering*, 67, 54–66. <https://doi.org/https://doi.org/10.1016/j.coastaleng.2012.04.004>
- Vacondio, R., Altomare, C., Leffe, M. D., Hu, X., Touzé, D. L., Lind, S., Marongiu, J.-C., Marrone, S., Rogers, B. D., & Souto-Iglesias, A. (2021). Grand Challenges for Smoothed Particle Hydrodynamics Numerical Schemes. *Computational Particle Mechanics*, 8, 575–588. <https://doi.org/10.1007/s40571-020-00354-1>
- Velarde, J., Kramhøft, C., Sørensen, J. D., & Zorzi, G. (2020). Fatigue Reliability of Large Monopiles for Offshore Wind Turbines. *International Journal of Fatigue*, 134, 105487. <https://doi.org/10.1016/j.ijfatigue.2020.105487>
- Verao Fernández, G., Balitsky, P., Stratigaki, V., & Troch, P. (2018). Coupling Methodology for Studying the Far Field Effects of Wave Energy Converter Arrays over a Varying Bathymetry. *Energies*, 11. <https://doi.org/10.3390/en11112899>
- Walker, M. M., & Oberkampf, W. L. (1992). Joint Computational/Experimental Aerodynamics Research on Hypersonic Vehicle, Part 2: Computational results. *AIAA Journal*, 30(8), 2010–2016. <https://doi.org/10.2514/3.11173>
- Weber, J., Costello, R., & Ringwood, J. (2013). WEC technology performance levels (TPLs)- metric for successful development of economic WEC technology. *Proceedings of the 10th European Wave and Tidal Energy Conference (EWTEC 2013)*. <https://mural.maynoothuniversity.ie/6793/>
- Wehausen, J. V., & Laitone, E. V. (1960). Surface Waves in Fluid Dynamics III. *Handbuch der Physik* 9 (pp. 446–778). Springer.
- Weller, H. G., Tabor, G., Jasak, H., & Fureby, C. (1998). A tensorial approach to computational continuum mechanics using object-oriented techniques. *Computer in Physics*, 12, 620–631. <https://doi.org/10.1063/1.168744>
- Wendt, F., Nielsen, K., Yu, Y.-H., Bingham, H., Eskilsson, C., Kramer, M., Babarit, A., Bunnik, T., Costello, R., Crowley, S., Gendron, B., Giorgi, G., Giorgi, S., Girardin, S., Greaves, D., Heras, P., Hoffman, J., Islam, H., Jakobsen, K.-R., ... Yasutaka, I. (2019). Ocean Energy Systems Wave Energy Modelling Task: Modelling, Verification and Validation of Wave Energy Converters. *Journal of Marine Science and Engineering*, 7(11). <https://doi.org/10.3390/jmse7110379>
- Wendt, F., Yu, Y.-H., Nielsen, K., Ruehl, K., Bunnik, T., Touzon, I., Woo Nam, B., Seok Kim, J., Kim, K.-H., Erik Janson, C., Jakobsen, K.-R., Crow-

- ley, S., Vega, L., Rajagopalan, K., Mathai, T., Greaves, D., Ransley, E., Lamont-Kane, P., Sheng, W., ... Hoffman, J. (2017). International Energy Agency Ocean Energy Systems Task 10 Wave Energy Converter Modeling Verification and Validation. *The 12th European Wave and Tidal Energy Conference (EWTEC 2017)*.
- Westphalen, J., Greaves, D., Raby, A., Hu, Z., Causon, D. M., Mingham, C., Omidvar, P., Stansby, P. K., & Rogers, B. (2014). Investigation of Wave-Structure Interaction Using State of the Art CFD Techniques. *Open Journal of Fluid Dynamics*, 4(1), 18–43. <https://doi.org/10.4236/ojfd.2014.41003>
- Willink, R. (2013). *Measurement Uncertainty and Probability*. Cambridge University Press. ISBN: 978-1-107-02193-8.
- WindEurope (2021). *Offshore Wind in Europe: Key Trends and Statistics 2020*.
- Windt, C., Davidson, J., & Ringwood, J. V. (2018). High-Fidelity Numerical Modelling of Ocean Wave Energy Systems: A Review of Computational Fluid Dynamics-Based Numerical Wave Tanks. *Renewable and Sustainable Energy Reviews*, 93, 610–630. <https://doi.org/10.1016/j.rser.2018.05.020>
- Wroniszewski, P. A., Verschaeve, J. C. G., & Pedersen, G. K. (2014). Benchmarking of navier–stokes codes for free surface simulations by means of a solitary wave. *Coastal Engineering*, 91, 1–17. <https://doi.org/10.1016/j.coastaleng.2014.04.012>
- Wu, H., Fernandes, A. C., & Cao, R. (2022). Three-Dimensional Numerical Simulation of a Flat Plate Perpendicularly Submitted to Current With a Blockage Ratio of 0.214: URANS and Detached Eddy Simulation. *Journal of Offshore Mechanics and Arctic Engineering*, 144(2), 21907. <https://doi.org/10.1115/1.4053316>
- Yeo, D. (2020). A Summary of Industrial Verification, Validation, and Uncertainty Quantification Procedures in Computational Fluid Dynamics. <https://doi.org/10.6028/NIST.IR.8298>
- Zhang, F., Crespo, A., Altomare, C., Domínguez, J., Marzeddu, A., Shang, S.-p., & Gómez-Gesteira, M. (2018). DualSPHysics: A Numerical Tool to Simulate Real Breakwaters. *Journal of Hydrodynamics*, 30, 95–105. <https://doi.org/10.1007/s42241-018-0010-0>
- Zhu, G., Hughes, J., Zheng, S., & Greaves, D. (2023). Development of a Two-Dimensional Coupled Smoothed Particle Hydrodynamics Model and Its Application to Nonlinear Wave Simulations. *Computers & Fluids*, 266, 106044. <https://doi.org/https://doi.org/10.1016/j.compfluid.2023.106044>

Paper Collection

Paper A

Wave Load Mitigation by Perforation of Monopiles

Jacob Andersen
Rune Abrahamsen
Thomas Lykke Andersen
Morten Thøtt Andersen
Torben Ladegaard Baun
Jesper Lykkegaard Neubauer

The paper has been published in
Journal of Marine Science and Engineering 8(5),
DOI: 10.3390/jmse8050352, 2020.



Journal of
*Marine Science
and Engineering*



Article

Wave Load Mitigation by Perforation of Monopiles



Jacob Andersen, Rune Abrahamsen, Thomas Lykke Andersen, Morten Thøtt Andersen,
Torben Ladegaard Baun and Jesper Lykkegaard Neubauer



<https://doi.org/10.3390/jmse8050352>

Article

Wave Load Mitigation by Perforation of Monopiles

Jacob Andersen ^{1,*} , Rune Abrahamsen ¹, Thomas Lykke Andersen ¹ ,
Morten Thøtt Andersen ¹, Torben Ladegaard Baun ² and Jesper Lykkegaard Neubauer ²

¹ Division of Reliability, Dynamics and Marine Engineering, Aalborg University (AAU),
Thomas Manns Vej 23, 9220 Aalborg Øst, Denmark

² Vestas Wind Systems A/S, Hedeager 42, 8200 Aarhus N, Denmark

* Correspondence: jacob@build.aau.dk

Received: 10 April 2020; Accepted: 9 May 2020; Published: 16 May 2020



Abstract: The design of large diameter monopiles (8–10 m) at intermediate to deep waters is largely driven by the fatigue limit state and mainly due to wave loads. The scope of the present paper is to assess the mitigation of wave loads on a monopile by perforation of the shell. The perforation design consists of elliptical holes in the vicinity of the splash zone. Wave loads are estimated for both regular and irregular waves through physical model tests in a wave flume. The test matrix includes waves with Keulegan–Carpenter (KC) numbers in the range 0.25 to 10 and covers both fatigue and ultimate limit states. Load reductions in the order of 6%–20% are found for KC numbers above 1.5. Significantly higher load reductions are found for KC numbers less than 1.5 and thus the potential to reduce fatigue wave loads has been demonstrated.

Keywords: wave loads; monopiles; perforation; hydrodynamics; wave flume tests

1. Introduction

The capacity of offshore wind energy in Europe is increasing relatively more than the onshore [1]. The relative increase in the offshore capacity over recent years may come as a result of the maturing of the offshore wind industry, where continuous optimization and development of know-how cause expenditures to drop. Levelized Cost of Energy (LCoE) for offshore wind energy has dropped more than 50% since 2013 [2].

In the offshore wind energy sector, monopiles are by far the most common foundation type. By 2018, more than 80% of the grid-connected offshore wind turbines in Europe were installed with monopiles [3]. The extensive use of monopiles has been key in driving down offshore wind LCoE. Monopiles have the benefits of simple manufacturing procedures and relatively quick installations, traditionally for water depths less than 30 m [4]. However, to utilize offshore wind power in the proximity of areas with challenging bathymetry or simply to locate wind turbines further offshore due to e.g., less visual impact or larger wind resources, wind turbines often need to be installed at locations with intermediate waters, 30 to 50 m, or even deep waters more than 50 m [3,5].

For bottom-fixed foundations, higher water depths increase the structural demands significantly. In intermediate and deep waters, jacket substructures are traditionally installed to obtain larger lateral stiffness and footprint to withstand mudline moments [6]. Wave load contributions to the fatigue lifetime of a jacket substructure is small, and in general wave and current loads on jacket substructures are less compared to monopiles [7]. Relative to monopiles, jackets further have the advantage of low material usage and low scour [6,8]. Nevertheless, the installation and manufacturing of jackets are costly and laborious relative to conventional monopiles, and especially fatigue design of joints may be costly [6,9].

Monopiles with extra large diameters ranging up to 10 m, can be a less costly substitute to jacket substructures at intermediate or deep waters. Application of large diameter monopiles at these depths

instead of jackets will maintain a relatively easy installation and manufacturing process, whilst some of the excessive know-how on monopiles can continue to be utilized [2].

The design of large diameter monopiles at intermediate to deep waters will ultimately be dominated by fatigue wave loads [8]. Optimizing the design of the substructure is recognized by [2,9] to be one of the highest potential cost reductions on offshore wind energy. According to [10], the share from substructures and foundations on the LCoE for bottom-fixed, offshore energy is approximately 13.5%. This is based on a reference case with 30 m water depth, 30 km to onshore interconnection, and 30 km to port for operation and maintenance.

Problem Statement

Vestas Wind Systems A/S has proposed an alternative design for large diameter monopiles (henceforth monopiles). The design includes perforation of a monopile with a diameter of 10 m aimed at locations with water depths of around 35–40 m. The perforation of the alternative monopile is concentrated in the vicinity of the free surface, cf. Figure 1.

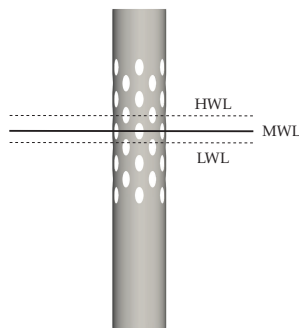


Figure 1. Conceptual illustration of the perforated monopile design with approximate mean water level (MWL) and water level variation (highest water level (HWL) to lowest water level (LWL)).

Perforation changes the flow pattern completely, thus the consequences with respect to loads are difficult to assess. However, as the perforation allows for a discharge through the monopile, it is expected that the perforation will decrease the downflow and associated horseshoe vortices, ultimately reducing the local scour. The run-up might also be decreased, due to the discharge of water through the monopile at wave impact. Cathodic protection of the interior of conventional monopiles has led to extreme water acidification and formation of hydrogen sulfide inside monopiles, which has caused special corrosive environments to develop. Perforation of monopiles to create a flow of ambient seawater through the interior of monopiles has been proved to mitigate the emerging of such corrosive environments [11]. Similar to artificial reefs, perforated monopiles have been found to cause fisheries and marine ecosystems to prosper [11].

Though being categorized as, and having the closest resemblance to a monopile, the perforated monopile has certain resemblances to a jacket substructure. The perforation may potentially enhance the monopile design by exploiting some of the advantages of a jacket substructure. In addition to the aforementioned indicated advantages, this includes mitigation of hydrodynamic loads, in particular fatigue wave loads.

The aim of the present paper is to examine the effect on mitigation of wave loads by perforation of monopiles. This is done by assessing the wave loads on a perforated and a conventional monopile through physical wave flume experiments.

2. Experimental Setup and Test Procedure

Hydraulic model tests were carried out in the wave flume of Department of Civil Engineering at Aalborg University, Denmark. The scale used in the model tests was 1:80. Unless otherwise specified, all values given in this paper are prototype values converted from model scale according to Froude model law.

Model tests were conducted for a monopile with a diameter of 10 m with 54 holes, see Figure 2. The 54 holes are placed in 12 equiangular spaced columns with 30 degrees interval, see Figure 2a,c. Every second column has 5 holes, and every second column has 4 holes. The model was oriented so that in the up-wave and down-wave directions there was always 5 holes. A conventional monopile was also tested as a reference. Henceforth, the models are referred to as ‘the perforated monopile’ and ‘the reference monopile’, respectively. It should be noted that neighboring columns of holes are overlapping with 0.1 m, see Figure 2a,b. The projected area of the perforated monopile oriented as seen in Figure 2a is approximately 89% of the projected area of the reference monopile. The models were tested sequentially and the generation file for each sea state was saved to use identical steering signals for wave generation with the two models.

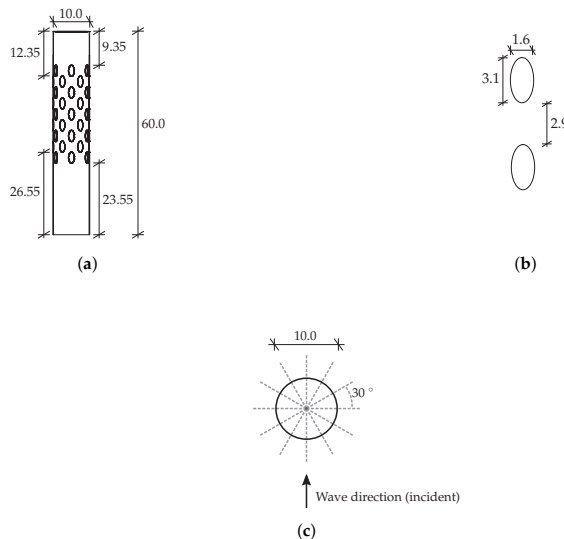


Figure 2. The perforated monopile. All measures are in m. (a) Perforated pile geometry as seen from the wavemaker. (b) Hole geometry. (c) Top view of the perforated pile. The dashed lines indicate the center lines of the elliptical holes.

The experimental setup in the wave flume is seen in Figures 3 and 4. Three perforated steel plates were installed close to the wavemaker, up-wave of the model position, in order to minimize transverse waves (cross-modes). The model was supported at the top by a load cell. The bottom of the flume was horizontal. The vertical distance between the models and the seabed was 3 mm (model scale). The models were placed in the middle between the flume side and an installed guide wall (a smooth steel plate). One wave gauge was installed in-line with the model, but behind the guide wall, see Figure 3a. The guide wall was installed in order to shield this wave gauge from diffracted waves from the model. A secondary wave gauge was installed approximately two meters in front of the model (up-wave). This wave gauge was installed to validate the measurements of the first wave gauge.

The thickness of the guide wall was 3.0 mm (model scale). Furthermore, in order to assess the wave height at the model position relative to the measured wave height behind the guide wall, the model was removed, and a wave gauge was installed at the model position. With this setup, selected sea states were repeated without the model in place.

The wave gauge behind the guide wall is seen to the right in Figure 4a. In the background of the photo the perforated plates for damping cross-modes can be seen in front of the piston wavemaker. It should be noted that the secondary wave gauge has not yet been installed in this photo. In Figure 4b, the perforated plates are visible in the foreground, and the secondary wave gauge up-wave of the perforated model has been installed.

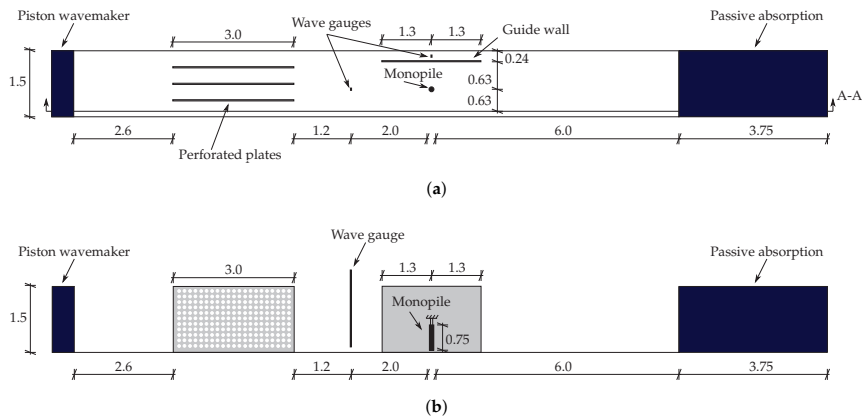


Figure 3. Setup of the wave flume used in the experiments. All measures are in m in model scale. (a) Wave flume seen from above. (b) Section A-A shown in (3a).

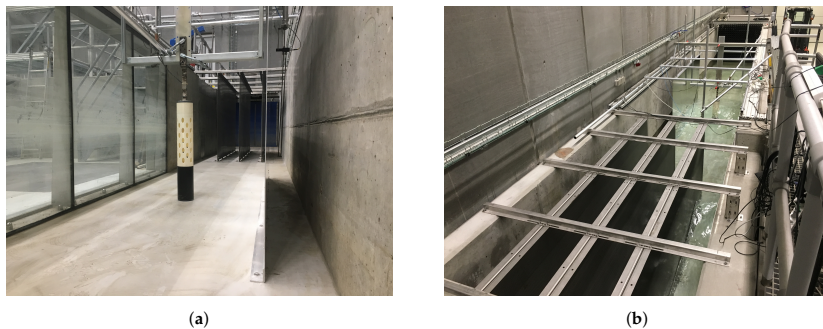


Figure 4. Photos of the experimental setup in the wave flume. (a) Setup seen from the passive absorber. (b) Setup seen from the wavemaker.

The force transducer contained two electrical circuits each with four strain gauges set up in a full Wheatstone bridge to measure only bending in the wave propagation direction. The two circuits were placed with a spatial offset in the longitudinal direction of the transducer of 150 mm (model scale), which made it possible to calculate the horizontal force and its attack point. The output voltage from the strain gauge amplifiers (analogue signal) were measured and logged. The signal was filtered by an

analog low-pass filter with a cut-off frequency of 10 Hz (model scale). The logging of the signals from the force transducer and the wave gauges was done using the software package WaveLab 3.816 [12]. WaveLab was also used to calculate the eigenfrequencies and damping ratios by exciting the models by an impulsive load, see Table 1. Through WaveLab, the eigenfrequencies and damping ratios of the models were calculated whenever the water depth was changed or the model switched.

The output voltage signals from the force transducer were filtered from dynamic amplification by use of WaveLab. In regard to the dynamic amplification filtering, a low-pass cut-off frequency of 0.67 Hz (6 Hz in model scale) was applied for the reference monopile, and a cut-off frequency of 0.56 Hz (5 Hz in model scale) for the perforated monopile. Cut-off frequencies were chosen in order not to upscale noise. The reason for the difference in cut-off frequency is the difference in eigenfrequencies of the two models. The sample frequency was set to 11.2 Hz (100 Hz in model scale). The logging was initiated by a trigger signal from the wavemaker.

Table 1. Eigenfrequencies and damping ratios.

| Water Depth [m] | Undamped Eigenfrequency [Hz] | | Damping Ratio [-] | |
|-----------------|------------------------------|-----------|-------------------|-----------|
| | Perforated | Reference | Perforated | Reference |
| 33 | 0.405 | 0.493 | 0.0224 | 0.0185 |
| 35 | 0.402 | 0.491 | 0.0202 | 0.0186 |
| 38 | 0.399 | 0.480 | 0.0207 | 0.0170 |

Tested Program

The wave parameters of the tests conducted in the physical wave flume are seen in Table 2. Sea states 11–16 were chosen in order to have three pairs of sea states with approximately the same Keulegan–Carpenter (KC) number in order to assess if this governs a potential load reduction. The KC number was calculated from

$$KC = \frac{u_{\max} T}{D},$$

where

- T wave period,
- D monopile diameter,
- u_{\max} maximum particle velocity at MWL.

u_{\max} was calculated through stream function theory, i.e., in specific by application of the Fourier approximation method by [13]. The KC numbers were calculated based on the wave parameters in Table 2. The spectral significant wave height, H_{m0} , and the peak period, T_p , were applied in calculating KC numbers for the irregular sea states. Three different water depths, h , were investigated to see if typical variations of the water level, and thus location of the hole geometry relative to the water level, influenced any potential load reductions. The values in Table 2 are listed with mean values \pm one standard deviation for the repeated sea states without the model in place. No repetitions were made for Sea states 3–5 and 9–10, and the values in Table 2 are from the wave gauge behind the guide wall with the reference monopile in place.

Regular waves were generated by approximate stream function (SF) wavemaker theory by [14] or second order wavemaker theory by [15] with modification by [16]. The minimum number of Fourier coefficients applied for the approximate stream function theory was $N = 10$.

The irregular sea states were generated from the inverse fast Fourier transform random phase method. The target spectrum was a JONSWAP spectrum with a peak enhancement factor of 3.3. Irregular waves were generated by second order wavemaker theory by [15] with modification by [16]. Active absorption was applied in order to minimize re-reflected waves [17]. The peak period, T_p ,

and the significant wave height, H_{m0} , of Sea state 9 were so small in model scale that the high frequencies were truncated significantly.

Table 2. Tested sea states. H is the wave height, and T is the wave period.

| Sea State | Type | Wavemaker Theory | h [m] | H or H_{m0} [m] | T or T_p [s] | KC [-] |
|-----------|-----------|------------------|---------|---------------------|------------------|----------|
| 1 | Regular | Approx. SF. | 38 | 19.2 ± 0.05 | 14.4 | 8.00 |
| 2 | Regular | Approx. SF. | 38 | 18.5 ± 0.20 | 16.4 | 9.02 |
| 3 | Regular | Approx. SF. | 33 | 16.3 | 14.4 | 7.39 |
| 4 | Regular | Approx. SF. | 33 | 16.1 | 16.4 | 8.54 |
| 5 | Regular | 2nd order | 35 | 0.90 | 4.7 | 0.28 |
| 6 | Regular | 2nd order | 35 | 3.8 ± 0.04 | 7.3 | 1.16 |
| 7 | Regular | Approx. SF. | 35 | 7.8 ± 0.03 | 11.8 | 2.94 |
| 8 | Regular | Approx. SF. | 35 | 10.8 ± 0.01 | 15.1 | 5.15 |
| 9 | Irregular | 2nd order | 35 | 1.6 | 5.1 | 0.49 |
| 10 | Irregular | 2nd order | 35 | 8.2 | 12.9 | 3.33 |
| 11 | Regular | Approx. SF. | 35 | 3.7 ± 0.02 | 14.9 | 1.70 |
| 12 | Regular | Approx. SF. | 35 | 4.6 ± 0.02 | 10.3 | 1.59 |
| 13 | Regular | Approx. SF. | 35 | 3.4 ± 0.02 | 20.4 | 2.12 |
| 14 | Regular | Approx. SF. | 35 | 4.1 ± 0.01 | 15.3 | 1.93 |
| 15 | Regular | Approx. SF. | 35 | 3.8 ± 0.01 | 20.1 | 2.35 |
| 16 | Regular | Approx. SF. | 35 | 4.5 ± 0.01 | 15.7 | 2.18 |

The wave force regimes of the sea states in Table 2 on a $D = 10$ m vertical cylinder are illustrated in Figure 5. The chart used in Figure 5 is given in [18], and is made under the assumption of linear theory. The sea state within the diffraction region is Sea state 5. The sea states within the inertia and drag region are Sea states 1–4.

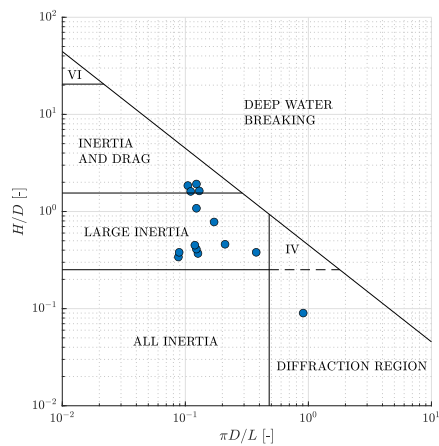


Figure 5. Graphical representation of the wave force regimes of tested sea states from Table 2.

3. Results

In the present section the results obtained from the physical wave flume tests are first presented for regular waves and subsequently for irregular waves. Finally, drag and inertia coefficients are calculated for the measured resulting force time series for regular waves using the Morison equation.

3.1. Regular Waves

The wavemaker was set with a ramp time of 10 s. The first fully developed wave was defined between two following zero-downcrossings, approximately 10 s after the first wave was visible in the wave gauge time series. The force history did not vary significantly after the selected first fully developed wave, and thus results are given for this wave. In Figure 6a, the wave heights measured behind the guide wall for the tests with the perforated monopile are shown relative to the tests with the reference monopile. In Figure 6b, the measured wave heights at model position without the model in place are shown relative to the wave heights measured behind the guide wall with the models in place (average of H_{perf} and H_{ref}) for the repeated sea states. All measured wave heights are given as absolute values in Appendix A.

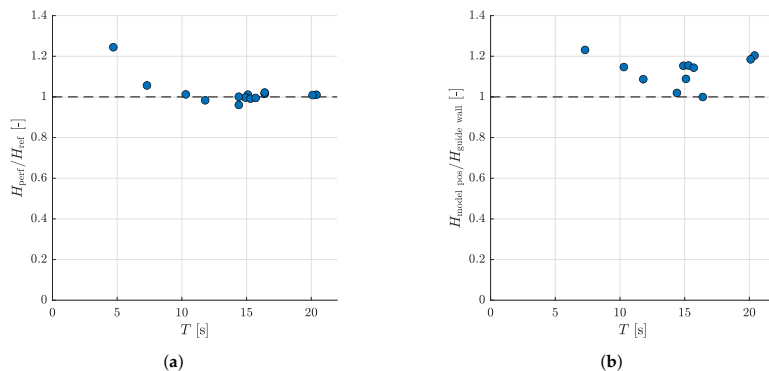


Figure 6. Relative wave heights. (a) Wave heights for tests with the perforated monopile relative to wave heights for tests with the reference monopile. (b) Wave heights at model position without the model in place relative to the average wave heights behind the guide wall with the models in place.

Figure 6a shows that the measured wave heights for the reference monopile correspond well to the measured wave heights for the perforated monopile, allowing direct comparison of forces and moments acting on the two models. Sea state 5 ($T = 4.7$ s) differs as a rather high deviation between the measured wave heights is present (around 25%). In model scale, the wave height for this sea state was 1.4 cm, which makes deviations of the generated waves in the order of millimeters quite significant, relatively. Figure 6b shows that the measured wave heights behind the guide wall with the model in place are in average 10% lower than those in the model position without the model in place. This is ascribed to diffracted waves interfering with the incident waves. The scope of this paper is to assess the relative effect of perforation of monopiles. Hence, the deviation between measured waves heights behind the guide wall and at the model position in Figure 6b does not compromise the scope. However, in calculating the force coefficients the difference is important and thus values without the model in place are used for that purpose.

In Figure 7, the peak resulting force and mudline moment on the perforated monopile can be seen relative to the peak resulting force and mudline moment on the reference monopile, respectively. The asterisk, $*$, denotes that the resulting forces and mudline moments have been normalized with respect to the respective measured wave heights by the wave gauge behind the guide wall, i.e., $F^* = F/H$ and $M^* = M/H$.

Uncertainties were quantified for the repeated sea states by sorting the resulting forces and mudline moments for the perforated monopile in descending order, and in ascending order for the reference monopile. The calculated ratio of each sea state were used to calculate the mean and standard deviation. Error bars indicating one standard deviation are included in Figure 7 for the sea states

where repetitions have been carried out. Five repetitions of Sea states 6 and 11–16 were performed. In order to increase the statistical certainty of the results for the higher waves, i.e., Sea states 1–4, five repetitions were carried out for Sea state 2. The water level for each load reduction is indicated by colors in Figure 7.

The reduction of peak loads, $\Gamma(KC)$, is described by a hyperbolic tangent function, see Equation (1), fitted to the normalized force reductions.

$$\Gamma(KC) = b \tanh(a KC). \quad (1)$$

Minimizing the squared error between Equation (1) and the normalized force reductions yields the coefficients; $a = 0.84$ and $b = 0.94$.

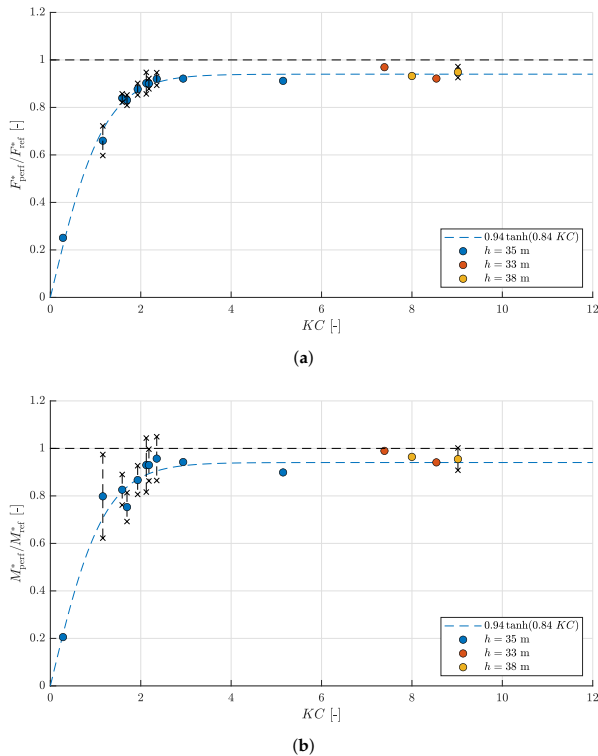


Figure 7. Load reduction for different Keulegan–Carpenter (KC) numbers and water levels. KC is calculated based on the measured wave parameters in Table 2. (a) Normalized resulting force on perforated monopile relative to reference monopile. (b) Normalized mudline moment on perforated monopile relative to reference monopile.

3.2. Irregular Waves

Two irregular sea states were tested; Sea states 9 and 10 in Table 2. In Figure 8, the mean, the mean of the highest third, the 98% fractile, and the maximum resulting force and mudline moment in the irregular model tests are given for the perforated monopile relative to the reference monopile. The characteristic values are found for the maxima of forces and moments, respectively. The KC

numbers are calculated based on the respective characteristic wave heights and periods. It is assumed that $T_{H_{2\%}} = T_{H_{1/3}}$. The values are calculated using WaveLab.

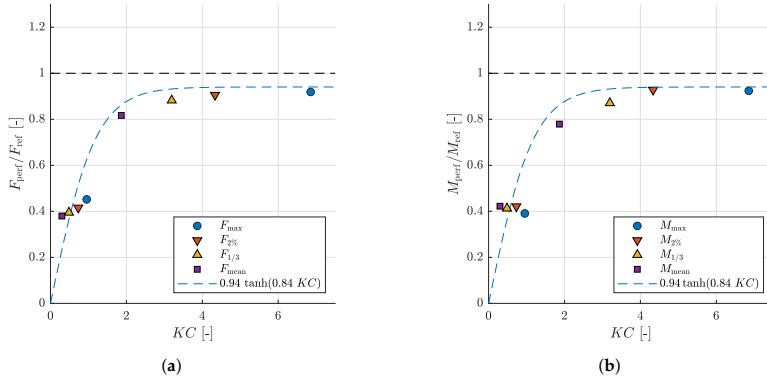


Figure 8. Load reductions for the two irregular sea states. KC is calculated based on time domain analysis of the measured wave elevations. (a) Relative resulting forces. (b) Relative mudline moments.

3.3. Drag and Inertia by the Morison Equation

At the center of many engineering approaches of calculating wave loads is the Morison equation [19]. The Morison equation yields the distributed inline wave force to the flow direction per unit length, modeled as a sum of drag and inertia forces acting normal to the structure. The Morison equation applied to a vertical cylinder is seen in Equation (2) [20].

$$f(z, t) = \underbrace{\frac{\pi}{4} \rho C_M D^2 \frac{d(u(x, z, t))}{dt}}_{\text{inertia}} + \underbrace{\frac{1}{2} \rho C_D D |u(x, z, t)| u(x, z, t)}_{\text{drag}}, \quad (2)$$

where

- f distributed Morison force (force per unit length of structure height),
- ρ density of water,
- C_M inertia coefficient,
- D structural diameter,
- $u(x, z, t)$ horizontal particle velocity at the center line of the structure ($x = 0$),
- C_D drag coefficient.

The resulting Morison force (F) is found by integrating f from the sea bed to the surface. Drag and inertia coefficients strongly depend on the flow conditions and the geometry of the structure. Based on potential flow theory, the value of the inertia coefficients may be estimated. However, in most cases potential flow is not valid, and thus the coefficients are based on experimental work. Drag and inertia coefficients are given in [21] for prototype conditions (supercritical flow). For model scaled tests and more complex structures, such as the perforated monopile treated in the present paper, drag and inertia coefficients are determined experimentally. In the present paper a least square approach inspired by [22] is used, see Appendix B. Sea state 5 is in the diffraction regime (Figure 5) and is not considered. The wave kinematics are calculated from stream function theory based on the measured wave height, wave period, and water depth in each experiment. From Figure 6a, the effect from variations in wave heights within the same sea states are assessed to be negligible. The measured wave heights behind the guide wall with the model in place are underestimated due to diffraction from the model, see Figure 6b. An underestimation of wave height leads to underestimation of wave

kinematics. Thus to avoid an overestimation of the drag and inertia coefficients, the wave heights at model position are used as the basis for any calculation of force coefficients.

The measured surface elevations without the model in place are aligned with the those measured behind the guide wall with the model in place. Theoretical surface elevations are aligned with surface elevation zero-downcrossings at $\theta = 0$ and $\theta = 2\pi$. Figure 9a shows the measured surface elevation at the model location without the model in place and the theoretical surface elevation from stream function theory. The measured crest and trough are slightly underestimated. In Figure 9b,c, the force histories from the fitted drag and inertia coefficients are seen for all repetitions of Sea state 12. In order to capture the peak forces on the perforated monopile, force coefficients are scaled to give identical peak forces, see Figure 9c. Force coefficients are based on the entire structure height, even though the perforation only acts in the upper part of the water column.

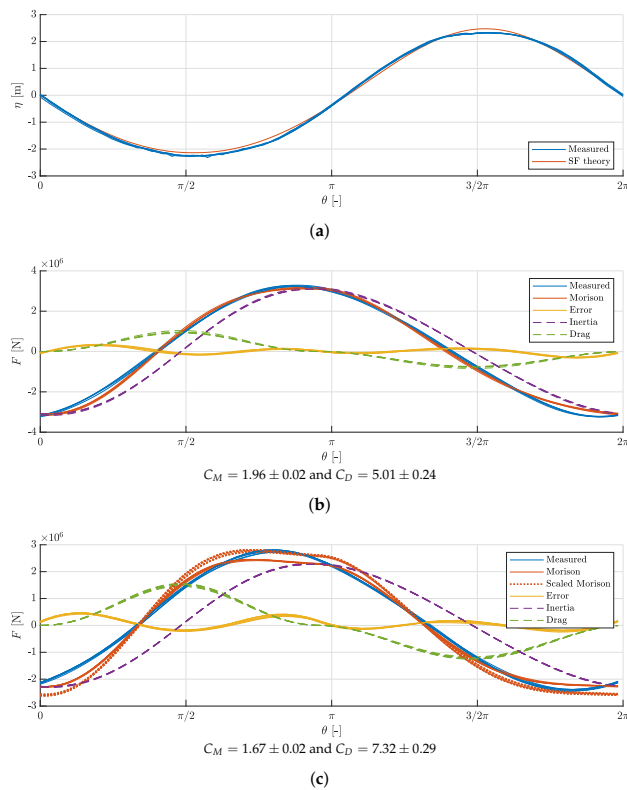


Figure 9. Surface elevations and force histories for Sea state 12; $H = 4.6$ m, $T = 10.3$ s, $h = 35$ m, $KC = 1.59$. Wave heights are measured at the model location without the model in place. Force coefficients are given as the mean values \pm one standard deviation. (a) Surface elevation at model location. (b) Reference monopile. (c) Perforated monopile.

Figure 10a,b show the calculated force coefficients for both the perforated monopile (scaled to fit peak forces) and the reference (not scaled). Curves from experiments in [23] are included for relevant Reynolds numbers (Re). Re of the low KC sea states range from approximately 1.5×10^4 to 2.2×10^4 . Re for the higher KC sea states are given in Figures 10a,b. Full correlation between the force coefficients

calculated for wave motions and the oscillating flow in a U-tube in [23] cannot be expected, due to the difference in velocity profiles, superharmonics, and free surface effects. It should be noted that the majority of the drag coefficients are calculated in the inertia dominated regime, and that these should not be ascribed high accuracy. Sea states 6 and 12 (lowest KC numbers) are excluded in Figure 10b due to brevity. All force coefficients are given in Appendix B.

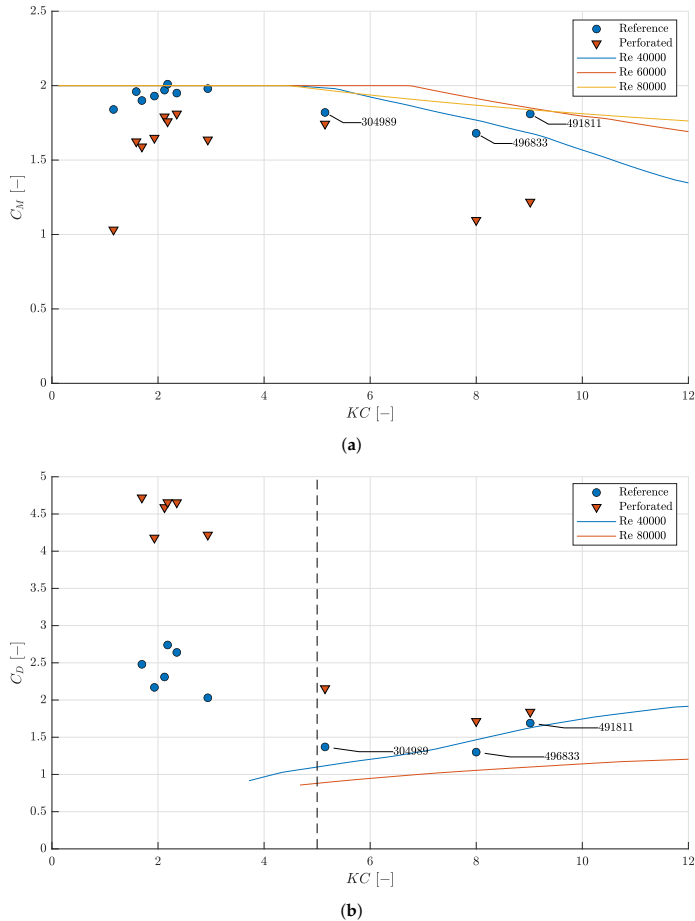


Figure 10. Mean value of force coefficients as function of KC based on mean wave heights measured without models in place. Lines are from [23]. (a) Inertia coefficients. (b) Drag coefficients. The vertical dashed line marks the upper limit of the inertia dominated region for a cylinder.

4. Discussion

The reduction of peak loads from the perforated design was found to be largest for Sea states 5 and 6, see Figure 7. The relative wave heights of Sea state 5 is associated with rather high uncertainties. However, as load reductions are based on normalized load peaks, and the load reduction of Sea state 5 is very substantial (calculated as 75%), this sea state does indicate the continuous increase of load

reductions as KC decreases at $KC < 1.5$. For Sea state 6, the reduction of the resulting force and mudline moment on the perforated monopile was approximately 30% and 20%, respectively. For KC numbers larger than 2, the load reduction stagnates at around 6% (as seen from $1 - b = 0.06$ in Equation (1)). From the tested typical variations of the water level, the load reductions seem invariant of the relative location of the hole geometry to the water level, see Figure 7. However, as the water level variations were only tested for high KC values (ULS cases), this trend still needs validation at low KC numbers. In general, the repeatability of the force reductions are high ($\pm 10\%$), while the moment reductions are associated with lower repeatability. From Figure 7, a rather significant load reduction is present for KC numbers lower than 2. Thus, the greatest load reductions from the perforation are in the inertia dominated regime. Correspondingly, the load reductions for the irregular waves are most significant for the lower KC numbers, see Figure 8. In Sea state 10 (the four highest KC numbers in Figure 8), the mean load reductions are largest. This observation is in accordance with the findings from the regular wave tests, as the mean load reduction is the load reduction in Figure 8 containing results from most low KC waves. The mean value does not differ to the same extent in Sea state 9, where all waves in the wave train are low KC waves.

The perforated monopile has a broader force peak due to an increase of the relative importance of drag, see Figure 9c. The maximal resulting force on the reference monopile is almost coinciding with the maximal inertia force as expected due to inertia domination at low KC numbers in accordance to [18], see Figure 9b. From Figure 9c, it follows that the Morison equation with the least square fitted force coefficients does not capture the force peaks on the perforated monopile correctly. Force coefficients for the perforated monopile are thus scaled up to fit the maximum absolute force peaks. The inertia contributions in all tested sea states are reduced for the perforated monopile compared to the reference. The extreme forces are decreased at zero-crossings where the magnitudes of the accelerations are largest. A broader force peak occurs, as the extreme forces shift towards the crest and troughs, i.e., an increased importance of drag.

Recommendations for Further Work

From the found wave load mitigation by the perforation of monopiles, it is recommended to further map the potential of perforated monopiles. For both regular and irregular sea states, the load reductions for $KC < 1.5$ were found to increase significantly, compared to $KC > 1.5$. The contribution from $KC < 1.5$ wave loads to the total fatigue lifetime should be estimated. This requires the stress concentration factors of the perforated monopile to be calculated, and furthermore the wave conditions of a given site to be known.

If $KC < 1.5$ wave loads are found to be significant for the total fatigue lifetime, it is recommended to conduct further model tests at $KC < 1.5$. In order to estimate the wave loads reductions at $KC < 1.5$ from wave flume experiments, the model to prototype scale must increase in order to mitigate uncertainties related to small wave heights and high wave frequencies. Thus, the tested irregular sea states at low KC numbers will not be as severely truncated as was seen for Sea state 9. Alternatively, numerical tests can be conducted.

Sea states with $KC > 10$ have not been investigated. Higher KC sea states increase the influence of drag. As the relative influence from drag is larger on the perforated monopile relative to a conventional monopile (see Table A2), the effect of the perforation for high KC sea states should be investigated as well.

In the present paper, the wave load reduction from the perforation of monopiles have only been estimated from model scale experiments. It is recommended to perform numerical experiments in prototype scale in order to estimate scale effects.

In order to map the commercial potential, a weight and cost comparison between a perforated and a conventional monopile should be carried out, and different production methods for the perforated monopile should be investigated, e.g., casting (in segments), segmented, and assembly. Furthermore, a stiffness analysis of the perforated monopile should be made, and influences on the performance

of the wind turbine generator assessed. It is also recommended to perform investigations on the mitigation of local scour and run-up by the perforation of monopiles in order to further map the potential. Larger holes in the perforated monopile design are expected to increase load reductions for higher KC numbers. An optimization study of the geometry, number, and spacing of holes is recommended with respect to both stress concentrations and load reductions.

5. Conclusions

In the present paper, the perforation of monopiles is found to mitigate wave loads. The load reductions are largest for sea states with low KC numbers, i.e., under fatigue wave conditions. Load reductions of approximately 10%–20% are found for both regular and irregular sea states with KC numbers between approximately 1.5 and 3. Significantly higher load reductions are found for $KC < 1.5$. For $KC > 5$, the load reductions are found to stagnate at around 6%. The reduction of forces and mudline moments are of the same order of magnitude. The repeatability is highest for the force reductions. Varying the water level relative to the hole geometry is not found to alter the load reductions.

The fit of drag and inertia coefficients based on the measured force histories yields a good prediction of the force histories on the reference monopile. The inertia coefficients are generally estimated with less uncertainty than the drag coefficients as most tested sea states are within the inertia dominated regime.

It should be stressed that the present paper only takes into account the mitigation of wave loads on a force and moment level and not on a stress level. The wave load mitigation is largest for fatigue sea states. The perforation introduces stress concentrations on the monopiles. Hence, the fatigue lifetime might not increase even though forces and moments on the perforated monopile decrease for fatigue sea states. The importance of the recommended further work is stressed by the authors.

Author Contributions: Formal analysis, J.A. and R.A.; investigation, All; conceptualization, T.L.B. and J.L.N.; resources, T.L.A. and M.T.A.; data curation, J.A., R.A., T.L.A., and M.T.A.; writing—original draft preparation, J.A., R.A., and T.L.A.; writing—review and editing, J.A., R.A., T.L.A., and M.T.A.; supervision, T.L.A. and M.T.A.; project administration, T.L.A., J.A., and R.A.; funding acquisition, T.L.A. All authors have read and agreed to the published version of the manuscript.

Funding: This research is supported by Vestas Wind Systems A/S.

Conflicts of Interest: The authors declare no conflict of interest.

Appendix A. Wave Heights

In Table A1, the wave heights measured from the wave gauge behind the guide wall are shown for all regular sea states in the test program. The wave heights measured from the repeated tests without the model in place are shown at model location and behind the guide wall.

Table A1. Measured wave heights for the regular sea state tests with and without the model in place.

| Sea State | With Model | | Without Model | |
|-----------|-----------------------|----------------------|-----------------------------|----------------------------|
| | H_{perf} [m] | H_{ref} [m] | $H_{\text{guide wall}}$ [m] | $H_{\text{model pos}}$ [m] |
| 1 | 18.88 | 18.86 | 19.47 ± 0.03 | 19.24 ± 0.05 |
| 2 | 18.62 ± 0.19 | 18.34 ± 0.10 | 19.34 ± 0.42 | 18.47 ± 0.20 |
| 3 | 15.61 | 16.25 | | |
| 4 | 16.49 | 16.14 | | |
| 5 | 1.12 | 0.90 | | |
| 6 | 3.18 ± 0.04 | 3.01 ± 0.10 | 3.55 ± 0.03 | 3.81 ± 0.04 |
| 7 | 7.10 | 7.22 | 7.76 ± 0.05 | 7.78 ± 0.03 |
| 8 | 9.99 | 9.88 | 10.66 ± 0.02 | 10.82 ± 0.01 |
| 11 | 3.18 ± 0.02 | 3.19 ± 0.02 | 3.46 ± 0.02 | 3.67 ± 0.02 |
| 12 | 4.04 ± 0.03 | 3.99 ± 0.02 | 4.37 ± 0.02 | 4.61 ± 0.02 |
| 13 | 2.85 ± 0.01 | 2.82 ± 0.01 | 3.15 ± 0.01 | 3.41 ± 0.02 |
| 14 | 3.53 ± 0.01 | 3.56 ± 0.02 | 3.91 ± 0.01 | 4.09 ± 0.01 |
| 15 | 3.26 ± 0.01 | 3.23 ± 0.01 | 3.61 ± 0.02 | 3.84 ± 0.01 |
| 16 | 3.93 ± 0.01 | 3.95 ± 0.02 | 4.33 ± 0.02 | 4.51 ± 0.01 |

Appendix B. Force Coefficients

The drag and inertia coefficients are calculated by a least square approach inspired by [22]. The squared error, ε , is integrated and minimized over one wave period, $\theta = \frac{2\pi}{T}t \in [0; 2\pi]$, see Equation (A1). Consequently, the calculated drag and inertia coefficients are time invariants.

$$\varepsilon = \int_0^{2\pi} (F_{\text{meas}} - F(C_D, C_M))^2 d\theta, \quad (\text{A1})$$

where

F_{meas} measured resulting force time series,
 $F(C_D, C_M)$ resulting Morison force time series calculated based on Equation (2).

The drag and inertia coefficients are calculated by minimizing ε in Equation (A1). Table A2 includes calculated drag and inertia coefficients based on the mean wave heights at model position, see Table A1. Only sea states tested without models in the wave flume are included.

Table A2. Fitted drag and inertia coefficients for regular sea states. Mean values with +/− one standard deviation are listed for the repeated sea states.

| Sea State | Reference Monopile | | | Perforated Monopile | | Perforated Monopile Scaled Coefficients | |
|-----------|--------------------|-------------|--------------|---------------------|--------------|-----------------------------------------|--------------|
| | KC [−] | C_M [−] | C_D [−] | C_M [−] | C_D [−] | C_M [−] | C_D [−] |
| 1 | 8.00 | 1.68 | 1.30 | 1.24 | 1.69 | 1.10 | 1.72 |
| 2 | 9.02 | 1.81 ± 0.02 | 1.69 ± 0.06 | 1.43 ± 0.04 | 2.16 ± 0.11 | 1.22 ± 0.04 | 1.84 ± 0.09 |
| 6 | 1.16 | 1.84 ± 0.02 | 15.75 ± 1.95 | 0.98 ± 0.01 | 14.18 ± 0.50 | 1.03 ± 0.02 | 14.96 ± 0.41 |
| 7 | 2.94 | 1.98 | 2.03 | 1.54 | 3.97 | 1.64 | 4.22 |
| 8 | 5.15 | 1.82 | 1.37 | 1.52 | 1.88 | 1.74 | 2.16 |
| 11 | 1.70 | 1.90 ± 0.03 | 2.48 ± 0.23 | 1.49 ± 0.02 | 4.42 ± 0.14 | 1.59 ± 0.03 | 4.72 ± 0.14 |
| 12 | 1.59 | 1.96 ± 0.02 | 5.01 ± 0.24 | 1.44 ± 0.01 | 7.85 ± 0.23 | 1.62 ± 0.01 | 8.88 ± 0.29 |
| 13 | 2.12 | 1.97 ± 0.02 | 2.31 ± 0.13 | 1.59 ± 0.01 | 4.08 ± 0.17 | 1.79 ± 0.02 | 4.59 ± 0.25 |
| 14 | 1.93 | 1.93 ± 0.01 | 2.17 ± 0.15 | 1.52 ± 0.01 | 3.90 ± 0.16 | 1.65 ± 0.03 | 4.18 ± 0.18 |
| 15 | 2.35 | 1.95 ± 0.02 | 2.64 ± 0.12 | 1.56 ± 0.02 | 4.01 ± 0.06 | 1.81 ± 0.03 | 4.65 ± 0.10 |
| 16 | 2.18 | 2.01 ± 0.02 | 2.74 ± 0.23 | 1.61 ± 0.02 | 4.27 ± 0.26 | 1.76 ± 0.01 | 4.66 ± 0.33 |

References

1. WindEurope. *Wind Energy in Europe in 2018, Trends and Statistics*; Walsh, C., Pineda, I., Eds.; WindEurope: Brussels, Belgium, 2019.
2. LEANWIND Consortium. *Driving Cost Reductions in Offshore Wind*; McAuliffe, F.D., Murphy, J., Lynch, K., Desmond, C., Norbeck, J.A., Nonås, L.M., Attari, Y., Doherty, P., Sørensen, J.D., Giebhardt, J., et al., Eds.; LEANWIND: Cork, Ireland, 2017.
3. WindEurope. *Offshore Wind in Europe, Key Trends and Statistics 2018*; Walsh, C., Ed.; WindEurope: Brussels, Belgium, 2019.
4. Bahaj, A.S.; Barnhart, C.J.; Bhattacharya, S.; Carbajales-Dale, M.; Cui, L.; Dai, K.; Dower, B.; Erdem, E.; Fried, L.; Gao, K.; et al. Civil Engineering Aspects of a Wind Farm. In *Wind Energy Engineering*, 1st ed.; Letcher, T.M., Ed.; Academic Press: Cambridge, MA, USA, 2017; ISBN: 978-0-12-809451-8.
5. IRENA (International Renewable Energy Agency). Floating Foundations: A Game Changer for Offshore Wind Power. *J. Phys. Conf. Ser.* **2016**, *753*. [[CrossRef](#)]
6. Schaumann, P.; Böker, C. Can Jackets and Tripods compete with Monopiles? In Proceedings of the Copenhagen Offshore Wind Conference, Copenhagen, Denmark, 26–28 October 2005.
7. Gong, W. Lattice Tower Design of Offshore Wind Turbine Support Structures. Master's Thesis, Norwegian University of Science and Technology (NTNU), Trondheim, Norway, June 2011.
8. Seidel, M. Substructures for offshore wind turbines—Current trends and developments. *Festschrift Peter Schaumann* **2014**. [[CrossRef](#)]

9. Damiani, R.; Dykes, K.; Scott, G. A comparison study of offshore wind support structures with monopiles and jackets for U.S. waters. *J. Phys. Conf. Ser.* **2016**, *753*. [\[CrossRef\]](#)
10. Stehly, T.; Beiter, P.; Heimiller, D.; Scott, G. *2017 Cost of Wind Energy Review*; National Renewable Energy Laboratory: Golden, CO, USA, 2018. [\[CrossRef\]](#)
11. Maher, M.M.; Swain, G. The Corrosion and Biofouling Characteristics of Sealed vs. Perforated Offshore Monopile Interiors, Experiment Design Comparing Corrosion and Environment Inside Steel Pipe. In Proceedings of the OCEANS 2018 MTS/IEEE Charleston, Charleston, SC, USA, 22–25 October 2018.
12. Frigaard, P.; Andersen, T.L. *Analysis of Waves: Technical Documentation for WaveLab 3*; Department of Civil Engineering, Aalborg University: Aalborg, Denmark, 2014; ISSN: 1901-7286.
13. Rienecker, M.M.; Fenton, J.D. A Fourier approximation for steady water waves. *J. Fluid Mech.* **1981**, *104*. [\[CrossRef\]](#)
14. Zhang, H.; Schäffer, H.A. Approximate Stream Function wavemaker theory for highly non-linear waves in wave flumes. *Ocean Eng.* **2007**, *34*. [\[CrossRef\]](#)
15. Schäffer, H.A. Second-order wavemaker theory for irregular waves. *Ocean Eng.* **1996**, *23*. [\[CrossRef\]](#)
16. Eldrup, M.R.; Andersen, T.L. Applicability of Nonlinear Wavemaker Theory. *J. Mar. Sci. Eng.* **2019**, *7*. [\[CrossRef\]](#)
17. Andersen, T.L.; Clavero, M.; Frigaard, P.; Losada, M.; Puyol, J.I. A new active absorption system and its performance to linear and non-linear waves. *Coast. Eng.* **2016**, *114*. [\[CrossRef\]](#)
18. Chakrabarti, S.K. *Hydrodynamics on Offshore Structures*, 1st ed.; Springer: Berlin/Heidelberg, Germany, 1987; ISBN: 0-387-17319-6.
19. Morison, J. R.; O'Brien, M.; Johnson, J.; Schaaf, S. The Forces Exerted by Surface Waves on Piles. In *Petroleum Transactions*; AIME: New York, NY, USA, 1950; Volume 189.
20. Journée, J.M.J.; Massie, W.W. *Offshore Hydromechanics*, 1st ed.; Delft University of Technology: Delft, The Netherlands, 2001.
21. DNV GL AS. *DNVGL-ST-0437: Loads and Site Conditions for Wind Turbines*; DNV GL: Oslo, Norway, 2016.
22. Burcharth, H.F. *Strøm- og Bølgekræfter på Stive Legemer* (Danish), 2nd ed.; Aalborg Universitet: Aalborg, Denmark, 2002.
23. Sarpkaya, T. *Wave Forces on Offshore Structures*; Cambridge University Press: Cambridge, UK, 2014.



© 2020 by the authors. Licensee MDPI, Basel, Switzerland. This article is an open access article distributed under the terms and conditions of the Creative Commons Attribution (CC BY) license (<http://creativecommons.org/licenses/by/4.0/>).

Paper B

Highly Accurate Experimental Heave Decay Tests with a Floating Sphere: A Public Benchmark Dataset for Model Validation of Fluid–Structure Interaction

Morten Bech Kramer
Jacob Andersen
Sarah Thomas
Flemming Buus Bendixen
Harry Bingham
Robert Read
Nikolaj Holk
Edward Ransley
Scott Brown
Yi-Hsiang Yu
Thanh Toan Tran
Josh Davidson
Csaba Horvath
Carl-Erik Janson
Kim Nielsen
Claes Eskilsson

The paper has been published in
Energies 14(2), DOI: 10.3390/en14020269, 2021.



energies

Article

Highly Accurate Experimental Heave Decay Tests with a Floating Sphere

A Public Benchmark Dataset for Model Validation of Fluid–Structure Interaction

Morten Bech Kramer, Jacob Andersen, Sarah Thomas, Flemming Buus Bendixen,
Harry Bingham, Robert Read, Nikolaj Holk, Edward Ransley, Scott Brown,
Yi-Hsiang Yu, Thanh Toan Tran, Josh Davidson, Csaba Horvath, Carl-Erik Janson,
Kim Nielsen and Claes Eskilsson

Energies **2021**, *14*(2), 269; doi:10.3390/en14020269

Article

Highly Accurate Experimental Heave Decay Tests with a Floating Sphere: A Public Benchmark Dataset for Model Validation of Fluid–Structure Interaction

Morten Bech Kramer ^{1,2,*}, Jacob Andersen ¹, Sarah Thomas ², Flemming Buus Bendixen ³, Harry Bingham ⁴, Robert Read ⁴, Nikolaj Holk ¹, Edward Ransley ⁵, Scott Brown ⁵, Yi-Hsiang Yu ⁶, Thanh Toan Tran ⁶, Josh Davidson ⁷, Csaba Horvath ⁷, Carl-Erik Janson ⁸, Kim Nielsen ^{1,9} and Claes Eskilsson ^{1,10}

- ¹ Department of the Built Environment, Aalborg University (AAU), Thomas Mann Vej 23, 9220 Aalborg, Denmark; mmk@build.aau.dk (M.B.K.); jacob@build.aau.dk (J.A.); nh@build.aau.dk (N.H.); KIN@ramboll.com (K.N.); claes@build.aau.dk (C.E.)
- ² Floating Power Plant (FPP), Park Allé 382, 2625 Vallensbæk, Denmark; mk@floatingpowerplant.com (M.B.K.); st@floatingpowerplant.com (S.T.)
- ³ Sintex, Jyllandsvej 14, 9500 Hobro, Denmark; fbb-sintex@grundfos.com (F.B.B.)
- ⁴ Department of Mechanical Engineering, Technical University of Denmark (DTU), Nils Koppels Allé, Building 403, 2800 Kgs Lyngby, Denmark; hbb@mek.dtu.dk (H.B.); rrea@mek.dtu.dk (R.R.)
- ⁵ School of Engineering, Computing and Mathematics, University of Plymouth (UoP), Plymouth, Devon PL4 8AA, UK; edward.ransley@plymouth.ac.uk (E.R.); scott.brown@plymouth.ac.uk (S.B.)
- ⁶ National Renewable Energy Laboratory (NREL), 15013 Denver West Parkway, Golden, CO 80401, USA; yi-hsiang.yu@nrel.gov (Y.-H.Y.); thanhtoan.tran@nrel.gov (T.T.T.)
- ⁷ Department of Fluid Mechanics, Budapest University of Technology and Economics, Műegyetem rkp. 3, 1111 Budapest, Hungary; joshuadavidson.jd@gmail.com (J.D.); horvath@ara.bme.hu (C.H.)
- ⁸ Department of Mechanics and Maritime Sciences, Chalmers University of Technology (CTH), 40482 Gothenburg, Sweden; carl-erik.janson@chalmers.se (C.-E.J.)
- ⁹ Ramboll Group A/S, Hannemanns Allé 53, DK-2300 Copenhagen S, Denmark; kin@ramboll.com (K.N.)
- ¹⁰ Research Institutes of Sweden (RISE), P.O. Box 857, SE-50115 Borås, Sweden; claes.eskilsson@ri.se (C.E.)
- * Correspondence: mmk@build.aau.dk; Tel.: +45-61697711

Citation: Kramer, M.B.; Andersen, J.; Thomas, S.; Bendixen, F.B.; Bingham, H.; Read, R.; Holk, N.; Ransley, E.; Brown, S.; Yu, Y.-H.; et al. Highly Accurate Experimental Heave Decay Tests with a Floating Sphere: A Public Benchmark Dataset for Model Validation of Fluid–Structure Interaction. *Energies* **2021**, *14*, 269. <https://doi.org/10.3390/en14020269>

Received: 27 November 2020

Accepted: 21 December 2020

Published: 6 January 2021

Publisher's Note: MDPI stays neutral with regard to jurisdictional claims in published maps and institutional affiliations.



Copyright: © 2021 by the authors. Licensee MDPI, Basel, Switzerland. This article is an open access article distributed under the terms and conditions of the Creative Commons Attribution (CC BY) license (<https://creativecommons.org/licenses/by/4.0/>).

Abstract: Highly accurate and precise heave decay tests on a sphere with a diameter of 300 mm were completed in a meticulously designed test setup in the wave basin in the Ocean and Coastal Engineering Laboratory at Aalborg University, Denmark. The tests were dedicated to providing a rigorous benchmark dataset for numerical model validation. The sphere was ballasted to half submergence, thereby floating with the waterline at the equator when at rest in calm water. Heave decay tests were conducted, wherein the sphere was held stationary and dropped from three drop heights: a small drop height, which can be considered a linear case, a moderately nonlinear case, and a highly nonlinear case with a drop height from a position where the whole sphere was initially above the water. The precision of the heave decay time series was calculated from random and systematic standard uncertainties. At a 95% confidence level, uncertainties were found to be very low—on average only about 0.3% of the respective drop heights. Physical parameters of the test setup and associated uncertainties were quantified. A test case was formulated that closely represents the physical tests, enabling the reader to do his/her own numerical tests. The paper includes a comparison of the physical test results to the results from several independent numerical models based on linear potential flow, fully nonlinear potential flow, and the Reynolds-averaged Navier–Stokes (RANS) equations. A high correlation between physical and numerical test results is shown. The physical test results are very suitable for numerical model validation and are public as a benchmark dataset.

Keywords: physical tests; sphere; benchmark dataset; heave decay; wave energy converters; linear potential flow; fully nonlinear potential flow; CFD; RANS; fluid–structure interaction

1. Introduction

Numerical models with complex fluid–structure interactions are often developed to simulate motions of floating bodies in the ocean, which can be applied to assess the performances of wave energy devices; see, e.g., [1,2]. Despite the complexity of such models, the discretization and assumptions needed to formulate the numerical model mathematically inevitably introduce errors, for many of which the influences are unknown. Engineers may struggle to identify whether linear wave theory can be applied with sufficient accuracy or more advanced computational fluid dynamics (CFD) methods should be used. Physical tests of high accuracy and reproducibility are paramount for validation and calibration purposes when using such advanced methods; see, e.g., [3,4].

The International Energy Agency Technology Collaboration Programme for Ocean Energy Systems (OES) has initiated the OES Wave Energy Converters Modelling Verification and Validation working group (formerly OES Task 10). Here, multiple research institutions and R&D companies from 12 countries collaborate with the focus on the development of numerical models for simulating wave energy converters (WECs) [5]. A floating sphere was chosen as a practical representation of a simple wave energy converter buoy, and numerical modelling of the decay of a sphere was completed as an initial test case [6–8]. The resulting simulations from the different members showed widespread simulation results, which highlighted the need for knowing the true, real-world results for the considered test case together with the associated measurement uncertainties. In order to validate and calibrate numerical models, a high-quality benchmark dataset was needed. Such datasets were lacking, so during a Danish-granted EUDP project [9] a sphere model was built, and tests were performed in the wave basin in the Ocean and Coastal Engineering Laboratory at Aalborg University in Denmark. The test design, namely, the release mechanism and the construction of the sphere, was optimized through several stages to mitigate sources of uncertainties. A 300 mm diameter aluminum sphere model with changeable ballasts—see Figure 1—was chosen as the most practical and accurate representation of a sphere for physical heave decay tests dedicated to producing a highly accurate benchmark dataset. The benchmark dataset is publicly available in the Supplementary Materials of the present paper; see Appendix A. The iterations in the design and construction process of the physical test setup are described in [10], which is also included as Supplementary Materials in the *Descriptions* folder. In [10], the tests are referred to as the *Kramer Sphere Cases*.

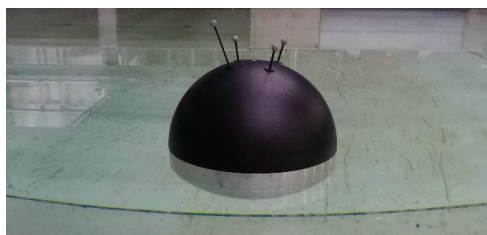


Figure 1. The sphere model used in the heave decay tests.

A new test case was formulated to accurately represent the performed tests and allow for numerical replications for model validation against the benchmark. Three different drop heights were investigated. The aim of the present study was to estimate the precision and accuracy of the physical decay tests using uncertainty analysis and comparisons to state-of-the-art hydrodynamic numerical models for all three drop heights. Using this approach, the applicability of the benchmark dataset to validation of numerical modelling of the presented test case is accounted for. The presented uncertainty analysis is based on the ASME Performance Test Code *Test Uncertainty* [11], which is in accordance with

the methodologies and nomenclature of the ISO/IEC Guide 98-3 *Guide to Expression of Uncertainty in Measurement* (GUM) [12], but contains a more technical treatment.

In Section 1.1, the test case is presented. All physical parameters are given to mimic the setup of the conducted heave decay tests. The reader can set up his/her own numerical model based on the information given herein, and thereafter apply the generated benchmark dataset for comparison/validation. Dedicated measurements of certain physical parameters, such as air pressure and viscosity, are not included in the test case. These are instead considered in the uncertainty analysis in Section 3.

The test case was given to participants of the OES working group, who independently formulated numerical models to simulate the decay tests utilizing miscellaneous modelling approaches. In the order of descending fidelity, these models included finite volume method (FVM) 3D unsteady Reynolds-averaged Navier–Stokes (URANS) models, boundary element method (BEM) fully nonlinear potential flow (FNPF) models, and BEM linear potential flow (LPF) models. The utilized numerical modelling approaches are presented in Section 1.2.

1.1. The Test Case

Consider an ideal sphere with a diameter D and a mass m . In a local Cartesian coordinate system, the origin coincides with the geometrical center of the sphere and with the z -axis vertical oriented upwards. The center of gravity is CoG. The local acceleration due to gravity is g .

The sphere floats between an air and a water phase, when at rest (equilibrium). The water phase has the density ρ_w , while the density of air is disregarded. A fixed global Cartesian coordinate system is defined from the still water level; the xy -plane coincides with the plane of the free water surface, and the z -axis is vertical oriented upwards towards the air phase; see Figure 2. The sphere is half-submerged when at rest, and with the CoG on the z -axis (underneath the center of buoyancy), the local and global coordinate system axes will coincide when the sphere is at rest; see Figure 2. The seabed is horizontal with a depth of $d = 3D$.

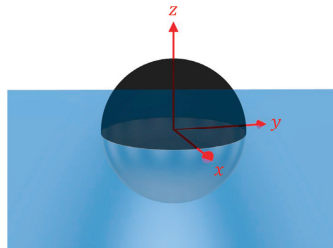


Figure 2. Fixed global coordinate system and the sphere at rest.

Initial conditions of zero velocity and zero acceleration are applied in all test setups. Under the assumption of a rigid body, the sphere has six degrees of freedom (DoF). Translations relative to the rest condition in the directions of the local x , y , and z -axes are defined as surge x_1 , sway x_2 , and heave x_3 , respectively. Rotations relative to the rest condition around the local x , y , and z -axes are defined as roll x_4 , pitch x_5 , and yaw x_6 , respectively. Three initial test setups are investigated with displacements of the sphere in positive heave given by the drop height $H_0 = \{0.1D, 0.3D, 0.5D\}$; see Figure 3.

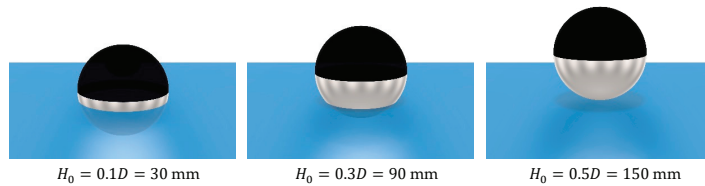


Figure 3. Tested initial submergences and drop heights.

The sphere is released, and around eight natural periods in heave should be captured for comparison to the benchmark dataset. The physical parameters of the test case are presented in Table 1. The utilized initial conditions match those of previous tests carried out under the OES working group.

Table 1. Values of the test case physical parameters.

| Parameter | D | m | CoG | g | H_0 | ρ_w | d |
|-----------|-----|-------|---------------|------------------|-------------|-------------------|-----|
| Unit | mm | kg | mm | m/s ² | mm | kg/m ³ | mm |
| Value | 300 | 7.056 | (0, 0, −34.8) | 9.82 | {30 90 150} | 998.2 | 900 |

1.2. Numerical Modelling Blind Tests of the Test Case

Participants of the OES working group independently developed numerical models to simulate the test case presented in Section 1.1 and to compare results against the benchmark. Only the governing physical parameters of the test case, given in Table 1, were shared with the participants, and the numerical modelling of the test case was thus carried out in blind without any shared information on domain geometry, resolution, turbulence modelling, etc. Various types of numerical models were developed by the participants. The specifications of the numerical model developed by each participant are presented in Appendix B. In general, three categories of numerical models were used: (i) FVM-based Reynolds-averaged Navier–Stokes (RANS) models, (ii) BEM-based fully nonlinear potential flow (FNPF) models, and (iii) BEM-based LPF models. These are introduced in the following subsections.

An analytical solution of the Navier–Stokes (N–S) equations would yield an exact model of the fluid flow of any Newtonian fluid, such as water. In their most general form, the N–S equations are the formulation of conservation of mass, momentum, and energy into a set of nonlinear partial differential equations. Currently, no analytical solutions to the N–S equations exist, but several numerical solutions have been established, introducing various simplifying assumptions and levels of inaccuracies. In general, decreasing the complexity of the mathematical problem by simplifying assumptions will yield less accurate numerical models, but increase the computational efficiency creating more feasible models. The influences of the errors introduced by the numerical model are strongly case-specific, and no generic model with a perfect balance of accuracy and efficiency is currently available.

1.3. RANS Models

Within high-fidelity CFD modelling of WECs, RANS models have become the model of choice [13]. The RANS equations are based on Reynolds decomposition and ensemble-averaging of the N–S equations. This reformulation of the N–S equations introduces a term referred to as the Reynolds stress, which accounts for the contribution of turbulent fluctuations to the fluid momentum. Turbulence structures are not resolved in RANS models, and thus computational effort is significantly decreased relative to, e.g., direct numerical simulations (DNS). Larger unsteady mean flow structures are captured from the unsteady RANS (URANS) formulation (see, e.g., [14]), to the extent allowed by the

temporal resolution. In the present paper, URANS models are developed from the open-source framework of OpenFOAM (versions 5.0, 7, and v1912) [15] and the commercial code StarCCM+ 13.06 [16]. The numerical models utilize the FVM to discretize the RANS equations. The interface between the two fluid phases is tracked by a volume of fluid (VOF) advection scheme; see, e.g., [17]. The models further assume incompressible, isothermal, immiscible flows.

1.4. FNPF Models

In the FNPF category of CFD models, further assumptions for the second-order non-linear N-S equations are made; i.e., the fluid domain is assumed inviscid and irrotational, thereby introducing potential flow theory, which reduces the governing equations of the fluid domain to Laplace's equation [18]. The boundaries of the fluid domain evolve in time, to be able to capture finite-amplitude waves and have a time-varying wetted body surface. The boundary conditions of the fluid domain are fully nonlinear in the sense that the velocity potential satisfies the nonlinear kinematic and dynamic boundary conditions at the free surface. No-flow boundary conditions are satisfied at solid boundaries [19]. In this study, the FNPF commercial code SHIPFLOW-Motions 6 [20] was applied. Here, a mixed Eulerian and Lagrangian (MEL) scheme [21] is utilized to capture the nonlinear free surface. The positions of free surface particles are then tracked in time in a Lagrangian representation of the flow problem, allowing for the advection of mesh nodes [22]. A rigid six-DoF model is included to update the position of the wetted surface at each time step.

1.5. LPF Models

At the low-fidelity end of CFD models to simulate WECs are the LPF models, which despite rather gross assumptions of linearity in both the governing equation (Laplace) and the boundary conditions, produce useful simulations for engineering purposes and indeed are very time-efficient; see, e.g., [23]. The dynamic response of marine structures is commonly analyzed in the frequency domain using LPF theory [23–26]. Time-domain models are based on hydrodynamic coefficients solved in the frequency domain and inserted into the Cummins equation [27,28]; see Appendix C for further information. In the present paper, hydrodynamic coefficients are calculated in the frequency domain from the BEM-based LPF software WAMIT [29]. Five models of various levels of accuracy are considered. The *LPF0* model is based on the solution to a traditional one-DoF mass-spring-damper system with constant hydrodynamic coefficients; i.e., the added mass, the hydrodynamic damping, and the hydrostatic stiffness are merely evaluated at a single frequency (damped natural frequency). Furthermore, the draft-dependency is disregarded in the calculation of the hydrodynamic coefficients, in which the sphere is considered static at the neutrally buoyant position (submergence to the equator). The *LPF1–4* models are based on the Cummins equation, allowing the description of arbitrary motions (multiple frequencies) rather than a regular motion (single frequency). For *LPF1*, the hydrodynamic coefficients in the frequency domain are calculated for the neutrally buoyant position and are assumed as linear. Various levels of nonlinearities (draft-dependencies) are added as extension of each other to *LPF2*, 3, and 4: Respectively, the hydrostatic stiffness, the added mass at infinite frequency, and the convolution part of the radiation force are nonlinearized. The utilized LPF models are thoroughly presented in Appendix C.

2. Materials and Experimental Setup

In the present section, the materials and setup of the physical heave decay tests conducted at Aalborg University are presented. Four repetitions were carried out for each drop height.

2.1. The Sphere Model

The sphere model was constructed using computer numerical control (CNC) machining of two aluminum blocks into two hemisphere shells of equal outer radii. A thread

was cut internally at the equator of the sphere to be able to assemble and disassemble the two hemisphere shells; see Figures 4 and 5a. A thin rubber gasket was installed to seal the model when assembled; see Figure 5b. The sphere was designed with an adjustable internal ballast system. A thread was tapped internally at the bottom of the model to fix ballast weights; see section view A-A in Figure 4.

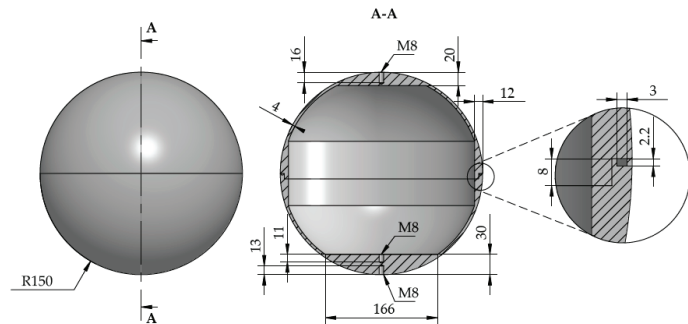


Figure 4. Technical drawing of the two hemisphere shells. Measurements are in mm.



Figure 5. Unballasted hemisphere shell with a diameter of 300 mm (a). Ballasted hemisphere shell with rubber gasket (b).

Additional threads were tapped externally at the top and bottom of the sphere to allow attachment of lines for decay tests and future tests, including mooring and power take-off (PTO). For line attachment to the sphere model, custom-made M8 nuts were used; see Figure 6a. In the presented tests, a line was merely mounted to the top of the sphere to displace it in the positive z -direction as the initial condition. A nut was installed at the bottom external thread with a cover of polyvinyl chloride (PVC) tape; see Figure 6b,c. The sphere model was marked with thin lines to have a reference system of x and y , as also seen in Figure 6b,c.

An optical 3D motion capture system was utilized to track four reflective markers installed on top of the model. In order to minimize the reflections from the model itself, the upper hemisphere shell was painted matte black. Ballast weights were CNC machined from stainless steel and mounted internally at the bottom of the lower hemisphere; see Figure 7.

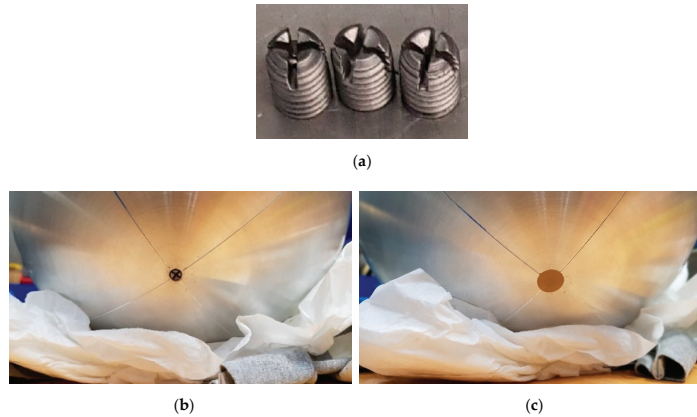


Figure 6. Custom-made nuts (a) mounted at the bottom hemisphere (b) with a cover of PVC tape (c).

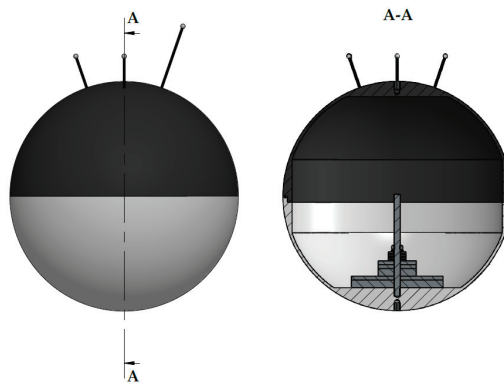


Figure 7. The sphere model after installation of reflective markers, ballasts, and rubber gaskets.

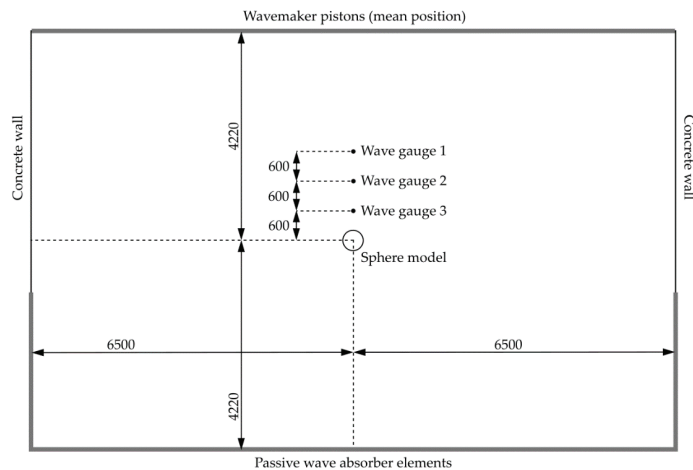
The machined components (i.e., the hemisphere shells and the ballast weights), were constructed with a precision of 0.1 mm. The dimensions of the additional components (i.e., nuts and reflective markers), were known with the same precision. The weight of each of the individual components of the sphere model was measured on precision scales with a precision of 0.1 g. A 3D computer-aided design (CAD) drawing of the sphere model was created in which densities were ascribed to the individual components from the measured weights. The total mass, total center of gravity (in the local coordinate system defined in Section 1.1), and total moments of inertia of the sphere model installed with ballast to generate half-submergence are given in Table 2. In the Supplementary Materials under the *Descriptions* folder, the dimensions, weights, and centers of gravity are given for all individual components.

Table 2. Inertial specifications of the sphere model (in the local coordinate system).

| Parameter | M | CoG | I_{xx} | I_{yy} | I_{zz} | I_{xz} | I_{xy}, I_{yz} |
|-----------|------|---------------|--------------------|--------------------|--------------------|------------------|------------------|
| Unit | g | mm | gmm ² | gmm ² | gmm ² | gmm ² | gmm ² |
| Value | 7056 | (0, 0, −34.8) | $98251 \cdot 10^3$ | $98254 \cdot 10^3$ | $73052 \cdot 10^3$ | $0 \cdot 10^3$ | $10 \cdot 10^3$ |

2.2. Experimental Setup and Equipment

The decay tests were carried out in the wave basin in the Ocean and Coastal Engineering Laboratory at Aalborg University in Denmark. The wave basin measured 13.00×8.44 m, and a water depth of 900 mm was used for all tests. The wave basin had vertical wavemaker pistons and vertical passive wave absorber elements installed. The wavemaker pistons were inactive during the tests. The sphere model was released in the middle of the basin; see Figure 8. A camera was mounted for documentation purposes, and three wave gauges were installed to measure the radiated waves from the decays and reflected waves; see Figures 8 and 9. Wave gauge data were collected, partly to assess reflections, and partly to analyze radiated waves in further work. The position of the sphere model was tracked by a Qualisys Motion Capture System; four Oqus7+ cameras at 300 fps with invisible, infrared strobes were mounted in the air phase, pointing towards the model; see Figures 9 and 10.

**Figure 8.** Test setup and measurements of the wave basin. Measurements are given in mm.

The release of the sphere model was initiated by a mechanical system consisting of a pushrod and a small electrical actuator; see Figure 11. A line was mounted to the top of the sphere model at the one end and to a small nut at the other end. The nut was supported by the pushrod preceding the initialization of the tests. A trigger signal was sent to the actuator which displaced the pushrod backwards (towards the actuator), thereby removing the support of the sphere model. The release time was measured by highspeed cameras (960 fps) to less than $1/960$ s [10]. The line connecting the sphere model to the pushrod was a Suffix[®] 832 line with 8 braided fibers and 32 weaves per inch (thickness 0.30 mm, weight 0.18 g/m).

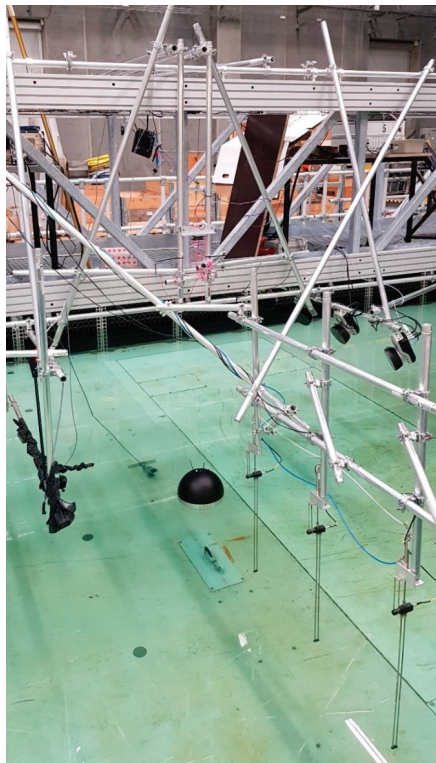


Figure 9. Test setup in the wave basin: center—half-submerged sphere model; left—camera; front—wave gauges; right—motion capture cameras; above—release system fixed to the bridge.

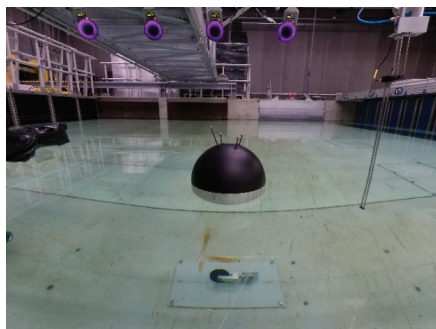
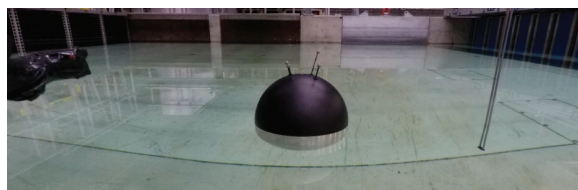


Figure 10. Test setup in the wave basin: center—half-submerged sphere model; background—motion capture cameras (stroboscopes in purple); right—wave gauge (number 3).

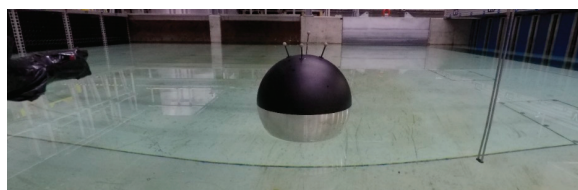


Figure 11. Release system consisting of a pushrod and an electrical actuator.

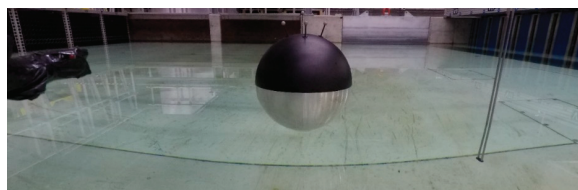
The sphere model was displaced in positive heave to approximately match the test case drop heights H_0 , as given in Table 1. The sphere model was kept at a given drop height, until the model and the free water surface were at rest; see Figure 12. The initial calmness of the sphere model (measured drop heights, velocities, and accelerations) and the free water surface are quantified in Section 3.



(a)



(b)



(c)

Figure 12. Photos of investigated drop heights: $H_0 = 0.1D$ (a), $H_0 = 0.3D$ (b), and $H_0 = 0.5D$ (c).

3. Results

The measured heave decay time series and the associated systematic and random uncertainties are accounted for in the present section. Furthermore, deviations between the ideal test case and the physical tests are quantified and considered. Heave x_3 of the sphere

was measured as the displacement of the sphere in the global z-axis. The influences of rotations in roll and pitch on the heave measurements of the sphere model were included in the uncertainty analysis.

3.1. Decay Measurements and Expanded Uncertainty

The measured heave decay time series are presented for the three investigated drop heights in Figure 13. To mitigate the effect of small variations in the drop height between the repetitions, the heave decay time series were normalized with the respective measured drop heights $H_{0,m}$. Time was normalized with the damped natural period in heave $T_{e0} = 0.76$ s; see Appendix C.

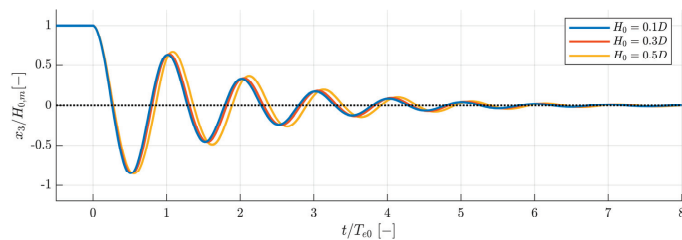


Figure 13. Normalized decay time series for the three investigated drop heights.

The measured heave decay time series included with 95% confidence intervals (CIs) around the sample mean are presented for each of the investigated drop heights in Figure 14. To be able to distinguish the 95% CIs from the sample mean, a zoom of the first trough is included in Figure 14. Both the normalized and raw heave decay time series can be found in larger formats in Appendix D, where the 95% CIs are upscaled to be able to visualize the time-dependency of the CIs. The 95% CIs were calculated from the Taylor series method (TSM) in accordance with the recommendations in [11]. The calculation of both the random and systematic uncertainties in the physical heave decay tests are described in the present section.

The time-dependent, two-sided 95% CI on the sample mean $\bar{X}(t)$ was established from expanding the combined standard uncertainty $u_{\bar{X}}(t)$ by the value t_{Cv} following the Student's t distribution [30]. C refers to the confidence level and v is the number of degrees of freedom (not to be confused with the previously introduced rigid body motions, but rather the independent variables in the calculation of $u_{\bar{X}}$) given by $v = N - 1$ with N being the number of repetitions.

$$\bar{X}(t) \pm t_{0.95,3} u_{\bar{X}}(t) = \bar{X}(t) \pm U_{\bar{X}}(t), \quad (1)$$

where $U_{\bar{X}}(t)$ is referred to as the expanded uncertainty, and $t_{0.95,3} = 3.182$ [30].

The combined standard uncertainty $u_{\bar{X}}(t)$ was calculated as the root-sum-square of the random standard uncertainty $s_{\bar{X}}$ and the systematic standard uncertainty $b_{\bar{X}}$ as per TSM [11]:

$$u_{\bar{X}}(t) = \sqrt{b_{\bar{X}}(t)^2 + s_{\bar{X}}(t)^2}. \quad (2)$$

The random standard uncertainty of the sample mean was directly calculated from the sample standard deviations at each instant of time (ISO Type A) as

$$s_{\bar{X}}(t) = \frac{s_X(t)}{\sqrt{N}}. \quad (3)$$

The systematic standard uncertainty was calculated as the root-sum-square of the elemental systematic standard deviations; see Table 3. The quantification of the elemental systematic standard deviations is accounted for later in the present section.

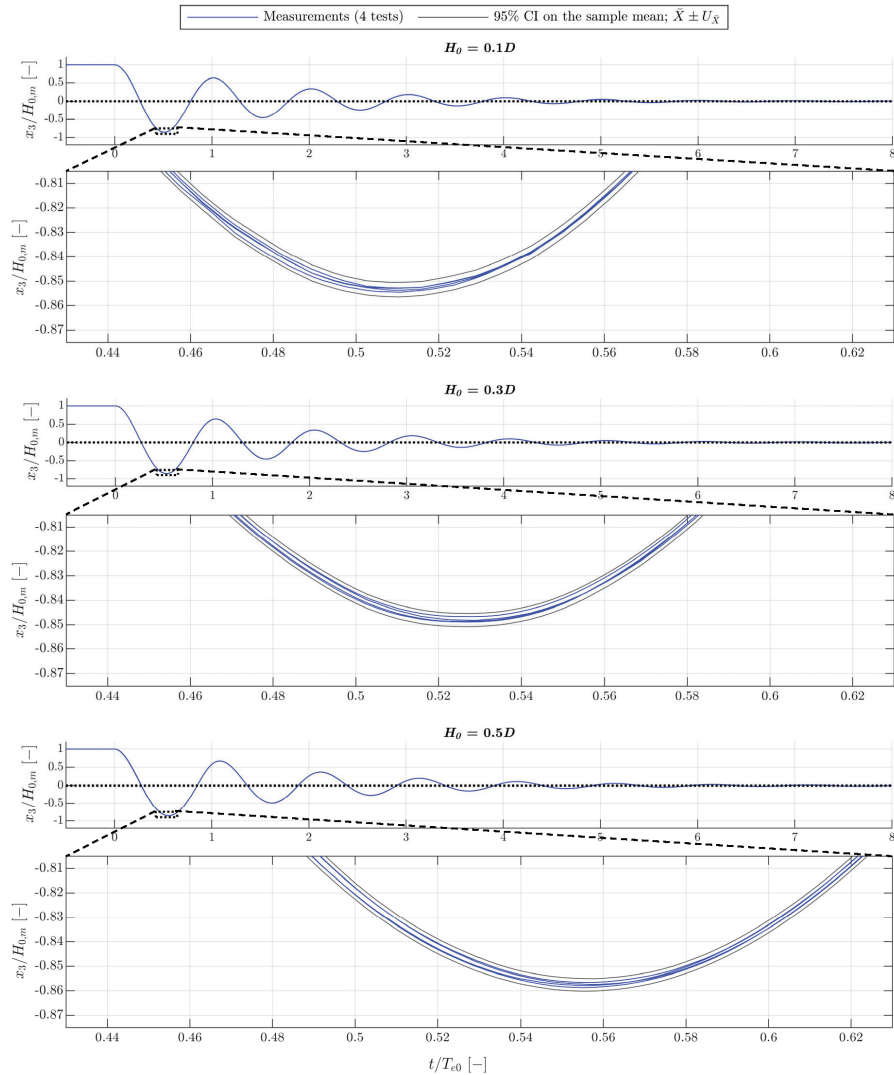
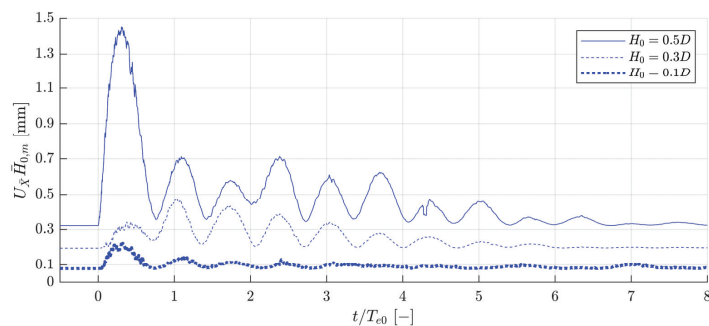


Figure 14. Normalized heave decay time series and 95% CIs with a zoom of the first trough.

Table 3. Classification and quantification of systematic errors.

| Systematic Error Source k | Elemental Systematic Standard Uncertainty $b_{X,k}\bar{H}_{0,m}$ [mm] | ISO Types |
|-------------------------------------------------------------------------|-----------------------------------------------------------------------|-----------|
| Calibration of motion capture system (Oqus7+) | 0.01 | A |
| Vibrations of bridge (reference frame) | 0.01 | B |
| Vibration of support rods for reflective markers (for ascending H_0) | 0.02, 0.06, 0.10 | B |
| Influence on heave measurements from roll and pitch | Time-dependent, <0.02 | A |

By multiplying the expanded uncertainty time series $U_{\bar{X}}(t)$ for each drop height with the respective averaged measured drop heights $\bar{H}_{0,m}$, each expanded uncertainty (with a confidence level of 95%) was given a physical dimension (length in mm); see Figure 15.

**Figure 15.** Expanded uncertainty time series for the three investigated drop heights.

The precision of the motion capture system (incl. calibration) was assessed from displacements of the sphere model in heave with high-precision blocks 50.0 mm in height. By comparing position time series, the systematic standard uncertainty of the motion capture system setup was found to be 0.01 mm (ISO Type A); refer to [10] for further information. The systematic standard uncertainty introduced by vibrations of the bridge (reference frame for the motion capture system) after release of the sphere model was conservatively assessed through a simple supported beam analogy to be less than 0.1 mm (ISO Type B). The systematic standard uncertainties from the deflections of the support rods of the reflective markers were estimated from the magnitude of the change in acceleration of the decaying sphere from time zero to the first trough in the heave time series ($\sim 16.5 \text{ m/s}^2$ for $H_0 = 0.5D$), which is in the same order of magnitude as g , allowing the deflection to be assessed by including the weight of an additional reflective marker. Conservatively, the systematic standard uncertainties introduced from deflections in the global z -direction of the support rods of the reflective markers were included as 0.1 mm (ISO Type B) for $H_0 = 0.5D$. The systematic standard uncertainties for the lower drop heights were linearly scaled down.

Rotations in roll and pitch resulted in small deviations between the measured heave of the sphere model (global coordinate system) and the actual heave, as the reflective markers were placed at a certain distance from the center of rotation (305 mm on average). The motions in heave resulting from the time-dependent roll and pitch were calculated, and the systematic standard uncertainty on the measured heave was found by the root-sum-square (ISO Type A). The maximum measured rotation in pitch or roll is 0.5° —see Figure 16—corresponding to an approximately 0.01 mm decrease of the global z -coordinate of the reflective markers.

The mean values of the expanded uncertainty time series for $0 < t/T_{e0} < 8$ multiplied with $\bar{H}_{0,m}$ are 0.44, 0.24, and 0.09 mm for the target drop heights of $0.5D$, $0.3D$, and $0.1D$, respectively, which correspond to about 0.3% of the drop height for all cases.

3.2. Six DoF Motions

In Figure 16, time series of the six-DoF rigid body motions of the sphere model measured from the optical motion capture system are presented for $H_0 = 0.5D$. The measured six-DoF motions for $H_0 = \{0.1D, 0.3D\}$ are presented in Appendix D. The influences on the heave measurements from roll and pitch of the sphere model were included in the uncertainty analysis; see Table 3.

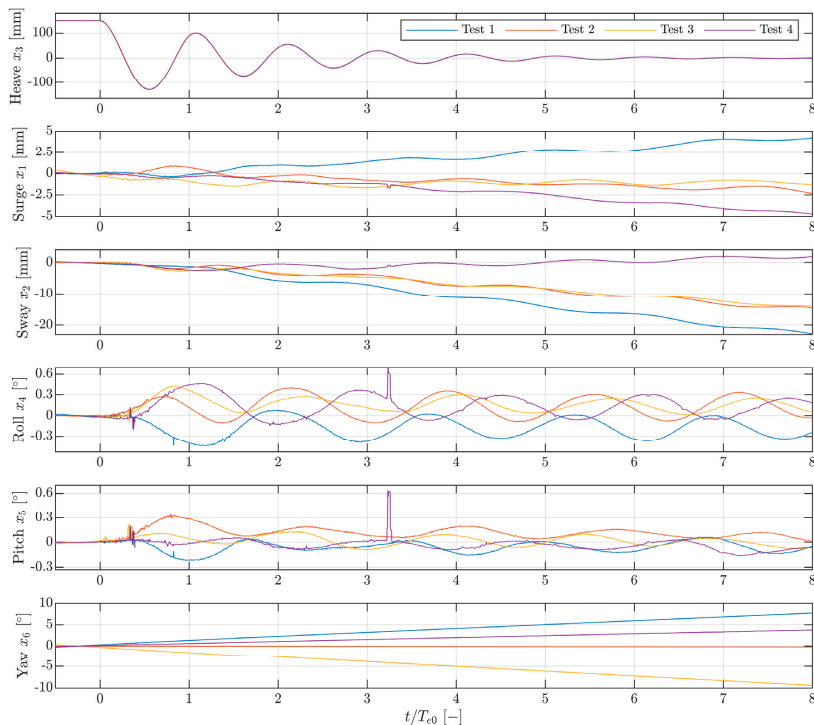


Figure 16. Measured six-DoF motion time series for $H_0 = 0.5D$.

3.3. Initial Calmness of the Sphere Model

The test case imposes zero velocity and zero acceleration as initial conditions on the sphere. To investigate the initial calmness of the sphere model, the heave (position) time series and time derivatives preceding the drop (i.e., for $-0.3 < t/T_{e0} < 0$), were assessed; see Figure 17. The position time series were subtracted with the respective measured drop heights to get zero as reference value. A moving average filter with a size of 21 samples was utilized to filter the acceleration time series.

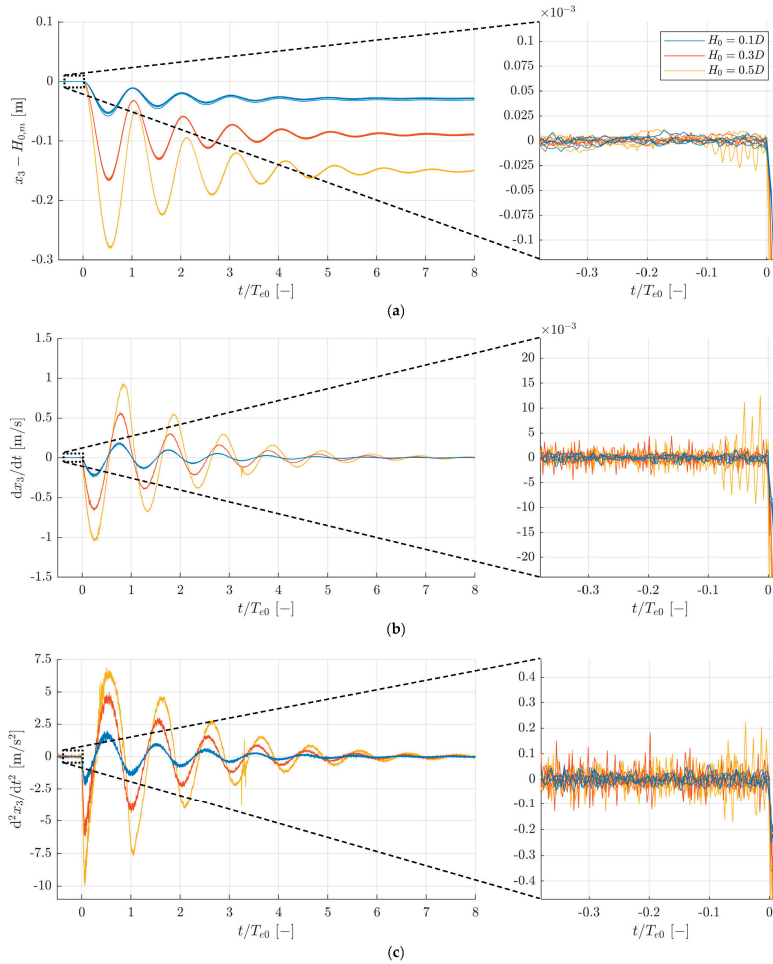


Figure 17. Position (a), velocity (b), and acceleration (c) time series with zooms of the limits $-0.3 < t/T_{e0} < 0$.

The mean and standard uncertainty of the position, velocity, and acceleration time series for all repetitions and drop heights averaged over $-0.3 < t/T_{e0} < 0$ were calculated. The mean and standard uncertainty of the position time series are both 0.0000 m (0.0 mm). The mean and standard uncertainty of the velocity time series are 0.0000 m/s and 0.0004 m/s, respectively. The mean and standard uncertainty of the acceleration time series are -0.0002 m/s^2 and 0.0097 m/s^2 , respectively.

3.4. Frequency Content

The three normalized heave decay time series (Figure 13) with $0 < t/T_{e0} < 8$ were converted to a periodic signal by mirroring about $t/T_{e0} = 0$; see Figure 18a. The one-sided spectral densities were calculated through FFT analysis; see Figure 18b.

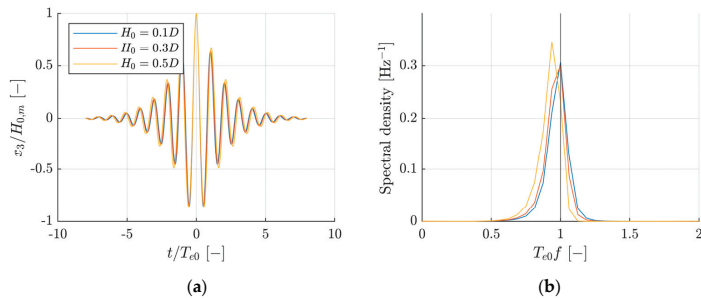


Figure 18. Conversion to periodic signal (a) and spectral density for all drop heights (b).

3.5. Reflections and Initial Calmness of the Water Phase

The measured surface elevation time series at the three wave gauges can be seen for the highest drop height (four repetitions) in Figure 19. Reflective walls (wave maker) were at 4.22 m from the sphere model location; see Figure 8. A radiated wave needed to travel to the reflective wall and back (i.e., $2 \cdot 4.22 = 8.44$ m), before reaching the sphere model. The time $t_{r0} = 8.44/c$, where c is the celerity of a linear wave with period T_{e0} , is included in Figure 19. Reflected waves propagated past the locations of wave gauges 1, 2, and 3 for around 2.0, 1.3, and 0.7 periods before t_{r0} , respectively. Decay time series presented up to $t/T_{e0} = 8$ are not under the influence of reflections from waves with the period T_{e0} ; see Figure 19. This can be considered a conservative estimate, as the main wave front of radiated waves would have propagated with the group velocity rather than the phase velocity. The measured surface elevations from the other drop heights are included in Appendix D.

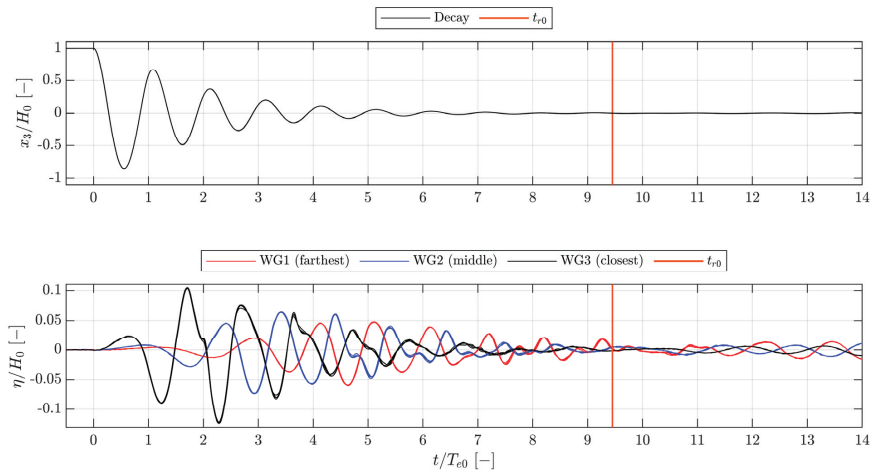


Figure 19. Decay and surface elevation time series for $H_0 = 0.5D$.

The initial calmness of the free water surface was assessed by the surface elevation time series prior to the release of the sphere model; see Figure 20.

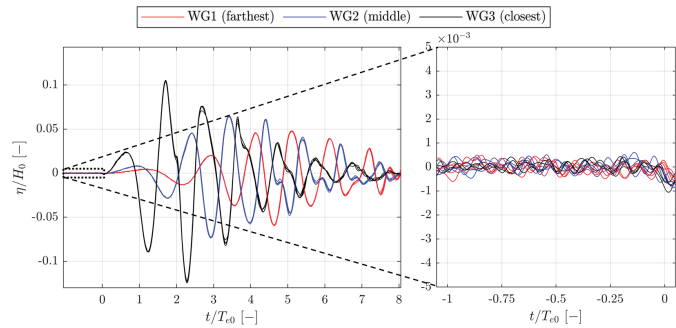


Figure 20. Surface elevation time series with a zoom of the limits $-1 < t/T_{e0} < 0$ for $H_0 = 0.5D$.

The mean and standard uncertainty of the surface elevation time series for all repetitions and wave gauges over $-1 < t/T_{e0} < 0$ are both 0.0000 m.

3.6. Uncertainties of Physical Parameters

The values and standard uncertainties of the physical parameters from the test case in Section 1.1 are presented for the physical tests in Table 4. Standard uncertainties were calculated from the sample standard deviations; see Equation (3). Physical parameters not included in the test case—the influences of which were found to vary insignificantly between indoor laboratories of about 20 °C—are also included in Table 4 to easily be available to the reader (for inclusion in high-fidelity numerical models).

Table 4. Values and standard uncertainties for physical parameters in the test setup.

| | Parameter | Value | Standard Uncertainty | Unit | ISO Type |
|----------------------------------------------------------------|---------------------------------------------------------------------------------------------------|------------------------------------------------------|-------------------------------------------|-------------------|----------|
| Test case values | Diameter of sphere | 300 | 0.1 | mm | B |
| | Mass of sphere | 7056 | 1 | g | B |
| | Centre of gravity | (0.0, 0.0, −34.8) | (0.1, 0.1, 0.1) | mm | B |
| | Acceleration due to gravity | 9.82 | 0.003 | m/s ² | B |
| | Drop heights (mean); $H_0 = \{0.1D, 0.3D, 0.5D\}$ | [29.16, 89.18, 150.06] | [0.8, 0.5, 0.3] | mm | A |
| | Density of water [31] | 998.2 | 0.4 | kg/m ³ | B |
| | Water depth | 900 | 1 | mm | B |
| | Initial velocity in heave | 0.0000 | 0.0004 | m/s | A |
| | Initial acceleration in heave | −0.0002 | 0.0097 | m/s ² | A |
| Additional values (Recommended for high-fidelity models) | Temperature of air and water | 20 | 2 | °C | B |
| | Kinematic viscosity of water [31] | $1.0 \cdot 10^{-6}$ | $0.1 \cdot 10^{-6}$ | m ² /s | B |
| | Density of air [31] | 1.20 | 0.012 | kg/m ³ | B |
| | Kinematic viscosity of air [31] | $15.1 \cdot 10^{-6}$ | $0.2 \cdot 10^{-6}$ | m ² /s | B |
| | Surface tension water-air [31] | 0.07 | 0.004 | N/m | B |
| | Moments of inertia of the sphere model; $I = [I_{xx}, I_{yy}, I_{zz}, I_{xy}, I_{yz}, I_{zx}]$ | {98251, 98254, 73052, 0, 10, 0} · 10 ³ | {37, 37, 1, 0, −77, 96} · 10 ³ | gmm ² | B |
| | Initial surface elevation | 0.0 | 0.01 | mm | A |

3.7. Comparison of Decay Measurements to Numerical Modelling Blind Tests

In the present section, the numerical heave decay time series are presented that were obtained from the numerical models of the test case by modelling approaches of various fidelity, as introduced in Section 1.2, and with the properties outlined in Appendices A and B.

Comparisons of the full time series for all drop heights are shown in Figure 21. In Figure 22 the initiation of the decay for $H_0 = 0.5D$ is shown. The first trough and crest of the decay time series are shown in Figures 23 and 24, respectively. In Figure 25, the comparison of decay time series is shown merely for the numerical models of higher fidelity, i.e., FNPF and RANS models.

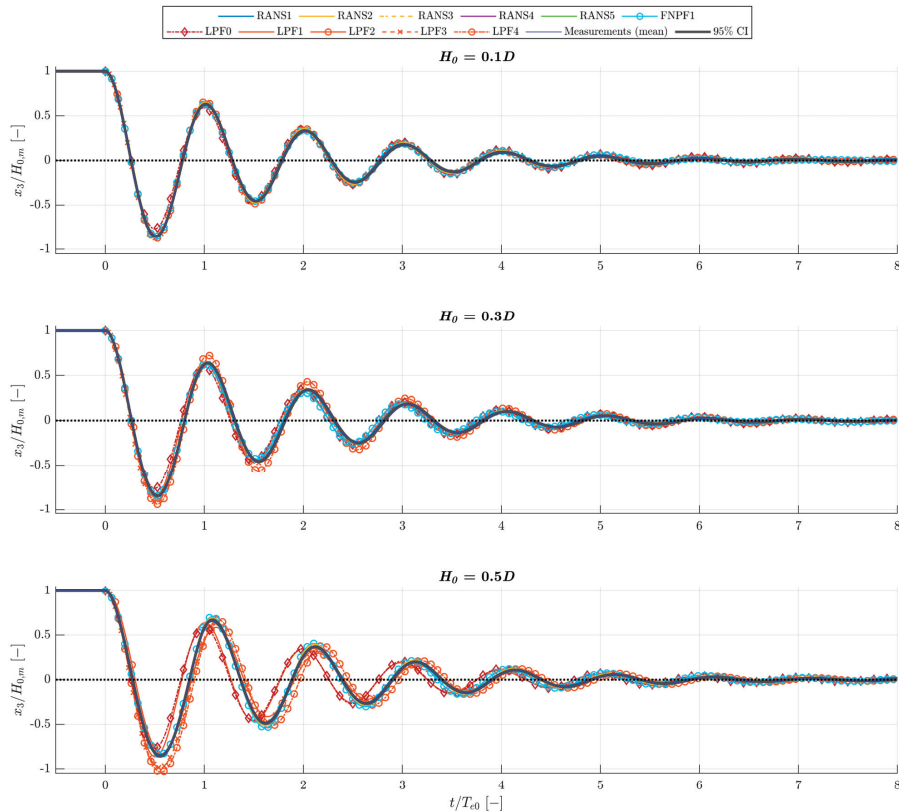


Figure 21. Comparison of physical and numerical test results.

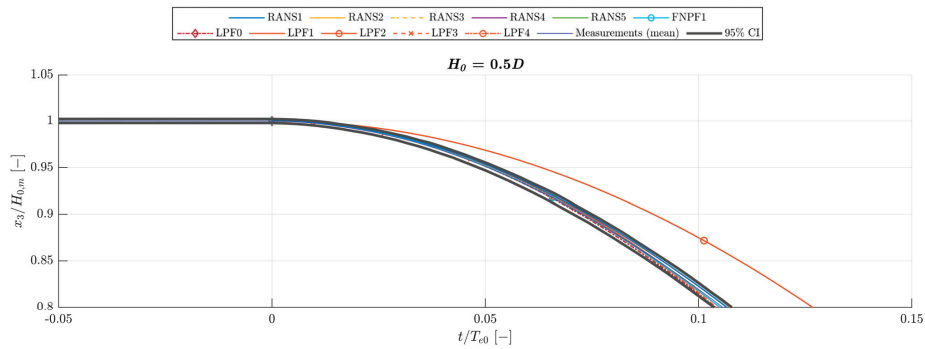


Figure 22. Comparison of physical and numerical test results at the initiation.

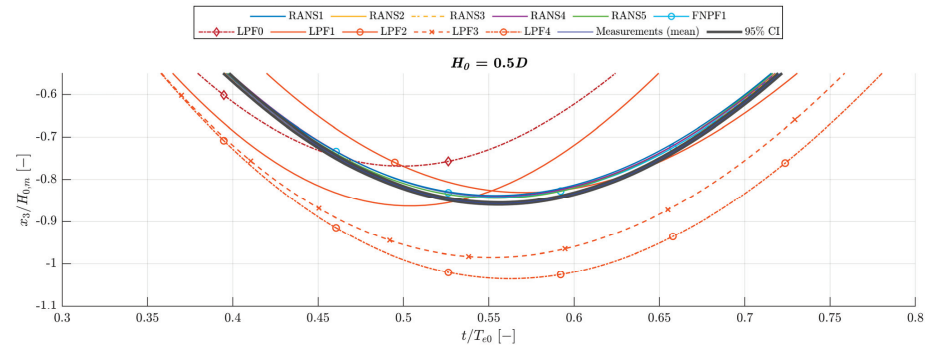


Figure 23. Comparison of physical and numerical test results at the first trough.

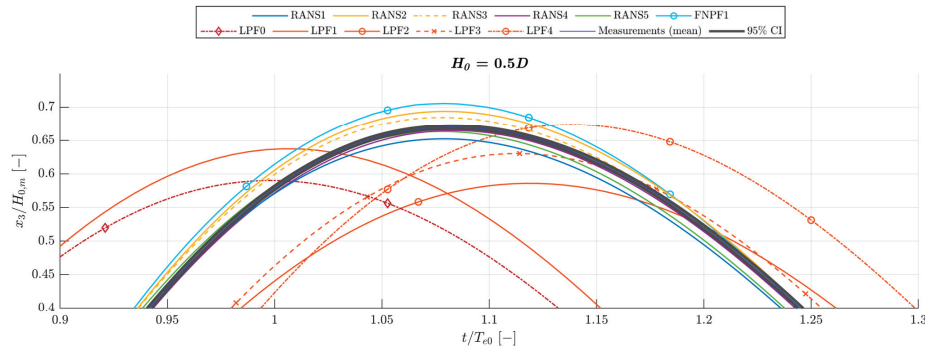


Figure 24. Comparison of physical and numerical test results at the first crest.

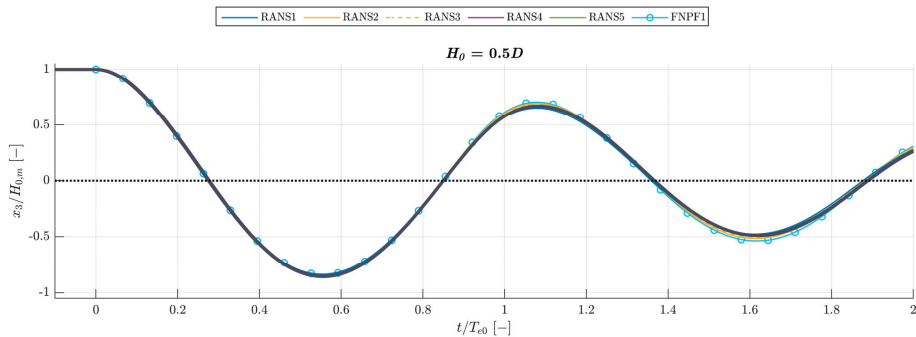


Figure 25. Comparison of physical and high-fidelity numerical test results with a zoom of $0 < t/T_{c0} < 2$.

4. Discussion

The measured heave decay time series are seen in Figure 14. The repeatability between the test repetitions is very high for each of the three drop heights, as seen both from Figure 14 and from the random standard uncertainties of the heave decay time series. On average, these are around 0.07, 0.03, and 0.01 mm, respectively, for the three drop heights in descending order, corresponding to less than 0.1% of the initial respective drop heights. However, the random standard uncertainty is largely time-dependent, and the maxima are factors of 4–7 times larger than the average. In general, the random uncertainty decreases when the sphere model decreases in speed and vice versa. This is both visible over time and over the three investigated drop heights. Over time, two maxima (in magnitude) are expected in the speed time series per natural period, and these maxima damp out over time (to less than 10% of the first maxima after $\sim 5T_{c0}$; see Figure 17b). This broadly correlates with the time-variation of the expanded uncertainty in Figure 15, for which the time-variation is governed by the random uncertainty (over the systematic). Over the three drop heights, the random uncertainty decreases with the drop height, where obviously the sphere model will oscillate with lower speeds for lower drop heights; see Figures 15 and 16b. The observations of dependence between the random uncertainties and the speed of the sphere model are ascribed to marker-image-shape-distortions increased by higher relative speeds between the optical motion capture system and the test specimen, as reported in [32].

Apart from the systematic uncertainty modelled from the influences of roll and pitch on the heave measurements, the systematic uncertainty is modelled as a time-invariant. The systematic standard uncertainty stemming from the roll and pitch time series does not exceed 0.02 mm, and as the total systematic standard uncertainty is taken as the root-sum-square of elemental systematic standard uncertainties of significantly higher values, the total systematic uncertainty is practically modelled as a time-invariant. As the random uncertainty largely is dictated by the sphere model speed (equal to zero twice per natural period), the dominating nature of the time-varying uncertainty is alternately systematic and random. As the sphere model damps out, it will eventually be dominated by the systematic uncertainties, seen as the offsets in Figure 15. The reader should note that systematic uncertainties are not directly modelled from the test measurements as with random uncertainties, but rather on estimates and engineering judgment. This is indicated by the ISO Type categorization in Section 3; see [11] for further information.

In Figure 13, the normalized heave decay time series for the three drop heights can be seen relative to one another. Most notably, for increasing drop heights, the initial damped natural period in heave increases. This is in accordance with the spectra shown in

Figure 18, where the peak in the spectrum for the highest drop height is shifted to a slightly lower frequency.

The ideal heave decay tests described as the test case in Section 1.1 only allow oscillations in heave (one-DoF system). Naturally, imperfections will activate additional DoFs, which under the assumption of rigid body motions are quantified in Figure 16 for $H_0 = 0.5D$. As reflective markers are mounted on the upper hemisphere of the sphere model, rotations in pitch and/or roll influence the measurement of the position of the sphere model in the global coordinate system. These influences were accounted for in the uncertainty analysis; see Table 3. Slight drifts occur in surge, sway, and yaw during the decay. The drifts have a negligible influence on the heave decays.

The physical parameters from the test case are listed in Table 4; associated standard uncertainties and values of additional physical parameters are not given for the test case. The values given in Table 4 quantify the certainty with which the governing physical parameters of the test setup are known. All physical parameters from the test case comply very well with the values given in Table 4. The relative deviations between the measured drop heights are the largest, but are basically without influence on the presented results, since normalizing with respect to the measured drop height in each repetition practically eliminates deviations between repetitions. The initial calmness of the sphere model and water phase are analyzed from time series preceding the drop; see Figures 16 and 20. Both the sphere model and the water phase are considered completely calm for practical applications.

Comparison to Numerical Modelling Blind Tests

Numerical models have successfully been formulated to represent the test case presented in Section 1.1. The majority of the numerical models depict the heave decay time series from the physical tests very well; see Figure 21. The largest deviations between physical and numerical tests occur for the LPF models, where the deviations are more pronounced for higher drop heights. This was expected, as nonlinearities increasingly govern the heave decay as the drop height is increased. The *LPF0* and *LPF1* models, introduced in Appendix C, have a significant negative phase shift within the first natural period relative to the physical tests and the models of higher fidelity; see Figures 21–24. As a result of the phase shift, large deviations from the 95% CI from the physical tests of around 50 mm (i.e., 33% of H_0), occur for the *LPF0* and *LPF1* models at $H_0 = 0.5D$. Not considering the phase shifts, but merely the magnitudes of troughs and crests, the *LPF0* and *LPF1* models, respectively, deviate with around 12–13 and 1–5 mm (i.e., 9% and 1–3% of H_0) at the first trough and crest; see Figures 23 and 24. The *LPF0* model oscillates with the damped natural frequency of a one-DoF spring-mass-damper system with constant hydrodynamic coefficients, and thus is not capable of including broader frequency contents, which may explain the larger phase shifts for larger drop heights; see Figure 21. The linearization of the hydrostatic force in the *LPF1* model spuriously increases the acceleration, as discussed in Appendix C. As the drop height is decreased, the heave decay will oscillate with T_{e0} and the assumption of linear hydrostatics will become more accurate. Consequently, the *LPF0* and *LPF1* models become increasingly accurate in both amplitude and phase for lower drop heights; see Figure 21. The inclusion of nonlinear hydrostatics in the *LPF2* and 3 models significantly reduces the phase shifts; see, e.g., Figure 23. The constant a_{33}^{∞} term in the *LPF2* model, however, spuriously delays the decay at initiation—see Figure 22—and in general increases the deviation from the physical tests when the sphere is displaced from its rest condition at which the constant a_{33}^{∞} term is evaluated; see Figures 21 and 24. Only including the draft-dependency of the a_{33}^{∞} term in the radiation force as in the *LPF3* model (see Appendix C) introduces large deviations at the first trough at $H_0 = 0.5D$; see Figure 23. The inclusion of draft-dependency of the convolution part of the radiation force, as done in the *LPF4* model (refer to Appendix C for further information), does not yield more accurate results. Despite the large deviations at the first trough, the *LPF3* model captures all subsequent crests and troughs in the $H_0 = 0.5D$ case with an accuracy close to those

of the RANS models, and is thus significantly more accurate than the *LPF2* model with constant a_{33}^{∞} . At $H_0 = 0.1D$, the *LPF2* and 3 models perform with maximum deviations of around 1 mm, which are comparable to the deviations of the models of higher fidelity.

The FNPf and RANS models deviate with less than 1 mm for $H_0 = 0.1D$, corresponding to 3% of H_0 . At the first trough, the models *FNPf1*, *RANS1* and *RANS5* lie within the 95% CI of the physical measurements, while the *RANS2* and *RANS4* models deviate with less than 0.3 mm (i.e., less than 1% of H_0). Deviations at the first trough have the same order of magnitude for $H_0 = 0.3D$, whereas at $H_0 = 0.5D$, the deviations increase to around 1–3 mm (i.e., 1–2% of H_0), with the exception of the *RANS2* and *RANS3* models, which are actually within the (narrow) 95% CI. The kinematics, and thus velocity gradients, are largest within the first natural period, leading to high demands on the near-wall meshing and treatment (mesh morphing, wall functions, etc.) in the RANS models. However, from Figure 25, there is a general tendency of the largest deviations to occur at $1 < t/T_{e0} < 4$ (even when taking into account the decrease of the CI width; see Figure 15). Assuming the time-error of the motion capture system to be negligible, the reasoning behind the tendency of largest deviations to not occur during the first natural period is two-fold: (i) in a RANS model, errors from the numerical discretization and iterations accumulate, and (ii) turbulence increases over the first periods and when the sphere changes direction. The former includes numerical errors of turbulence parameters if calculated in a turbulence model, while the latter refers to the increase of the complexity of the water phase over time (emergence of high-frequency perturbations of the free surface and sub-grid vortices) and how model errors of either not including a turbulence model (laminar simulations) or the inaccuracies associated with a given model thus become more pronounced with time. The deviations tend to reduce for $4 < t/T_{e0}$ which is ascribed to the low amplitudes themselves rather than an increase in the accuracy, as the continued increase in the phase shifts (up to around 0.04 s, i.e., $0.05T_{e0}$) also suggests. An increased accuracy from inclusion of a turbulence model (*k*-omega-SST) can be seen by comparing the *RANS2* and *RANS3* models in Figure 25.

Troughs and crests for the RANS models are calculated with deviations of maximally 1 mm, 2 mm, and 4 mm, respectively, for the three drop heights in ascending order. This corresponds to deviations up to 3% of H_0 . The FNPf model has similar deviations for the two lowest drop heights, while the deviations at $H_0 = 0.5D$ are up to 8 mm or 5% of H_0 . For $H_0 = 0.5D$, the maximum of deviations at troughs and crests are an order of magnitude higher for the LPF models than the RANS models, which indicates the potential pitfalls of LPF models for large-amplitude motions.

5. Conclusions

A sphere model was constructed to accurately represent the formulated test case. Physical parameters of the test setup were quantified, and associated uncertainties were generally found to be low. The precision of the physical test results is very high and was quantified by time-varying systematic and random uncertainties of the heave time series. At a 95% confidence level, the uncertainties were on average 0.09, 0.24, and 0.44 mm for the target drop heights in ascending order, corresponding to about 0.3% of the respective drop heights. The uncertainty of the optical motion capture system increased with larger velocities of the test specimen, and for the largest drop height the uncertainty was less than 1.5 mm, corresponding to less than 1% of the drop height.

Strong correlations were found between the physical test results and the results from independent numerical modelling blind tests for LPF, FNPf, and RANS models, ranged with increasing fidelities. At the lowest drop height, the deviations are less than 1 mm for all models, which corresponds to less than 3% of the drop height (disregarding the regular motion model *LPF0*). Deviations of the LPF models increase for higher drop heights. The performance of the FNPf model is in general better than the LPF models, but deviations are larger than those of the RANS models for the highest drop height. RANS models produce heave decay time series with deviations of 0–4 mm at troughs and crests for the highest

drop height, which correspond to 0–3% of the drop height. Deviations are smaller for the lower drop heights. It should be mentioned that the results from the RANS models have a larger spread than the physical results, and various models are outside of the 95% CIs at various periods during the decay. The comparison of the numerical and physical test results suggests that the LPF and partly the FNPF models should be used with care in applications with motions of very large amplitudes, whereas the RANS models, if proper convergence is reached, are capable of producing accurate results for all drop heights.

The high correlations of multiple independent numerical modelling blind tests with the physical tests demonstrate the use of the test case and the physical test results in validating numerical models. Taking this into account, together with the high repeatability and quantified uncertainties of the physical tests, the measured heave decay time series of the sphere model provide a highly accurate solution to the test case, and are thus highly appropriate for numerical model validation. The heave decay time series are made public as a benchmark dataset in the Supplementary Materials of the present paper.

It is the intention of the authors to perform further tests in the future, including motion of the sphere model in waves with PTO and motions in multiple DoF. If the reader is interested in following the future work, he/she is encouraged to become a member of the international working group by contacting the coordinator of the OES modelling task, Kim Nielsen (please request his contact details from the authors of this paper).

Supplementary Materials: The benchmark dataset of the physical heave decay tests is publicly available from the supplementary material of the present paper online at <https://www.mdpi.com/1996-1073/14/2/269/s1> and at the OES webpage [5]. In addition, all numerical modelling blind tests of the test case are available. Refer to Appendix A for detailed information about the contents of the supplementary material.

Author Contributions: Conceptualization, M.B.K.; methodology, M.B.K. and J.A.; software, M.B.K., C.E., J.A., E.R., S.B., Y.-H.Y., T.T.T., J.D., C.H., and C.-E.J.; validation, M.B.K., J.A., and H.B.; investigation, M.B.K.; formal analysis, J.A. and M.B.K.; resources, M.B.K., N.H., and F.B.B.; data curation, M.B.K. and J.A.; writing—original draft, J.A.; writing—review and editing, M.B.K.; visualization, J.A. and M.B.K.; supervision, M.B.K., H.B., K.N., R.R., and S.T.; project administration, M.B.K.; funding acquisition, M.B.K. and K.N. All authors have read and agreed to the published version of the manuscript.

Funding: The work related to planning and analyzing the physical test results was funded by the Energy Technology Development and Demonstration Program (EUDP) under the Danish Energy Agency. NREL was funded by the U.S. Department of Energy under Contract DE-AC36-08GO28308.

Acknowledgments: The authors would like to thank the laboratory technicians at the Ocean and Coastal Engineering Laboratory at Aalborg University for assistance with the sphere model design and construction. A special thanks to Flemming Buus Bendixen and Sintex for the design, construction, and tests of a magnetic release mechanism, which eventually was not included in the final test design.

Conflicts of Interest: The authors declare no conflict of interest.

Appendix A

The Supplementary Materials to the present paper is structured under the folder *Datafile* with subfolders *Descriptions*, *Experimental results*, and *Numerical results*; see Figure A1. The folder *Descriptions* includes technical descriptions of the sphere model and the test setup (referred to in Sections 1 and 2). The folders *Experimental results* and *Numerical results* contain the results from the heave decay tests performed physically and numerically, respectively. Eleven numerical modelling approaches were performed on the test case, and thus eleven subdirectories are located under *Numerical results*; see Figure A1. For further information on the specifications of the numerical models, refer to Appendix B.

The results are given as text-files with columns containing time t [s] and heave x_3 [m]; see Figure A2. The three columns WG1, WG2, and WG3 [m] contain the surface elevation time series at three wave gauges locations, introduced in Section 2.2, and are included

for the experimental results and for certain numerical results. Four repetitions were performed of the physical heave decay tests, all of which are included in the result files under *Experimental results*. The heave decay time series are presented in a raw and in a normalized format, as explained in Section 3. The normalized results are also represented in a file containing the sample mean and the upper and lower bounds of the 95% CI around the sample mean; see Section 3.

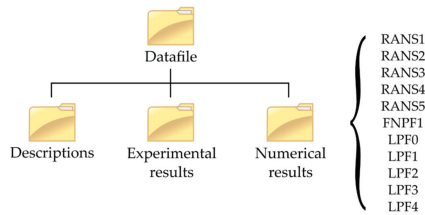


Figure A1. Directory structure of the Supplementary Materials.

05D_Measured4_Raw - Notepad

| File | Edit | Format | View | Help |
|------------|-----------|------------|------------|------------|
| t [s] | x3 [m] | WG1 [m] | WG2 [m] | WG3 [m] |
| -0.3780000 | 0.1507666 | 0.0000236 | -0.0000400 | -0.0000284 |
| -0.3760000 | 0.1507664 | 0.0000180 | -0.0000415 | -0.0000337 |
| -0.3740000 | 0.1507648 | 0.0000114 | -0.0000413 | -0.0000376 |
| -0.3720000 | 0.1507653 | 0.0000041 | -0.0000398 | -0.0000400 |
| -0.3700000 | 0.1507702 | -0.0000038 | -0.0000369 | -0.0000409 |

(a)

| 05D_CI95_Normalized - Notepad | | | | |
|-------------------------------|------------|------------|------------------------|------------------------|
| File | Edit | Format | View | Help |
| t/Te0 [-] | x3/H_{0,m} | (mean) [-] | Lower 95% CI bound [-] | Upper 95% CI bound [-] |
| -0.4999339 | 1.0000092 | 0.9978673 | 1.0021512 | |
| -0.4972887 | 0.9999992 | 0.9978571 | 1.0021412 | |
| -0.4946436 | 0.9999894 | 0.9978475 | 1.0021313 | |
| -0.4919984 | 0.9999937 | 0.9978517 | 1.0021356 | |
| -0.4893533 | 1.0000064 | 0.9978642 | 1.0021486 | |

(b)

Figure A2. Structure of result files. Example with first part of raw measurements (a) and mean of normalized data with 95% CI (b).

Appendix B

As explained in Section 1.2, three categories of numerical models have been applied to the test case: (i) Reynolds-averaged Navier–Stokes (RANS) models, (ii) fully nonlinear potential flow (FNPF) models based on the boundary element method (BEM), and (iii) linear potential flow (LPF) models based on BEM.

Table A1. Numerical models from the participants in the OES working group.

| Name | Institution and Authors | Framework | Description | Comp. Effort [CH] * |
|-------|-------------------------------------------------------------|---------------------------|------------------------------------------------------------------------------------------------------------------------------------------------------------------------------------------------------------------------------------------------------------------------------|---------------------|
| RANS1 | Aalborg University; C.E., J.A. | OpenFOAM-v1912 | 3D URANS model. Incompressible, isothermal. Volume of fluid method. Two vertical symmetry planes. Reflective side walls. Mesh morphing using SLERP method. Cell count of 6–9 M cells. No turbulence model. Second-order accurate in time and space. CFL criterion of 0.5 | ~3000–6500 |
| RANS2 | University of Plymouth; E.R., S.B. | OpenFOAM 5.0 | 3D URANS model. Incompressible, isothermal. Volume of fluid. Two vertical symmetry planes. Reflective side walls. Mesh morphing using SLERP method. Cell count of ~12 M cells. No turbulence model. CFL criterion of 0.5. | ~1000–4200 |
| RANS3 | University of Plymouth; E.R., S.B. | OpenFOAM 5.0 | Same as RANS2 except k-Omega SST turbulence model. Only conducted for $H_0 = 0.5D$. | ~1800 |
| RANS4 | National Renewable Energy Lab.; Y.-H.Y., T.T.T. | STAR-CCM+ 13.06 | 3D URANS model. Incompressible, isothermal. Volume of fluid. Two vertical symmetry planes. Cell count of 6 M cells. Mesh morphing with one DOF. k-Omega SST turbulence model. second-order accurate in time and space. CFL criterion of 0.5. Max. time step of 0.1 ms. | ~1000–2600 |
| RANS5 | Budapest University of Technology and Economics; J.D., C.H. | OpenFOAM 7 | 2D URANS model. Incompressible, isothermal. Volume of fluid method. Axisymmetric wedge geometry. Cell count of approx. 20 K cells. No turbulence model. second-order accurate in time and space. CFL criterion of 0.25. Water depth changed to 1.8 m to allow mesh morphing. | ~0.5–2.5 |
| FNPF1 | Chalmers University of Technology; C.-E.J. | SHIPFLOW-Motions 6 | Fully nonlinear potential flow BEM. 1600 panels were used on the sphere and 4600 panels were used on the free surface. The time step was 0.005 s. | ~6 |
| LPF0 | Aalborg University; M.B.K., J.A. | WAMIT and MatLab | Analytical solution to one-DoF mass-spring-damper system with hydrodynamic coefficients from BEM (for $\omega = \omega_{c0}$) | - ** |
| LPF1 | Floating Power Plant; M.B.K. | WAMIT and MatLab/Simulink | Model with linear hydrostatics and linear coefficients from BEM. Time-step: 1 ms, solver: ode4 (Runge-Kutta). | - ** |
| LPF2 | Floating Power Plant; M.B.K. | WAMIT and MatLab/Simulink | Model with nonlinear hydrostatics and linear coefficients from BEM. Time-step: 1 ms, solver: ode4 (Runge-Kutta). | - ** |
| LPF3 | Floating Power Plant; M.B.K. | WAMIT and MatLab/Simulink | Model with nonlinear hydrostatics, linear radiation function from linear BEM but position dependent infinity added mass. Time-step: 1 ms, solver: ode4 (Runge-Kutta). | - ** |
| LPF4 | Floating Power Plant; M.B.K. | WAMIT and MatLab/Simulink | Model with nonlinear hydrostatics and position dependent radiation functions (based on linear coefficients from BEM). Time-step: 1 ms, solver: ode4 (Runge-Kutta). | - ** |

* Core-hours for one decay; ** order of seconds for MATLAB/Simulink simulations using precomputed WAMIT coefficients.

Appendix C

In the present Appendix, the utilized LPF models are presented. The principles of the linearization of hydrostatics are presented first. Then, the formulation of the grossly linearized, regular *LPF0* model is presented. Subsequently, the time domain *LPF1–4* models

with various levels of nonlinearities are introduced. Physical test measurements of the draft-dependency of the hydrostatics of the sphere model are presented and compared to the linear and nonlinear analytical expressions of the hydrostatic force. Numerical results of the draft-dependency of the added mass at infinite frequency and the convolution part of the radiation force are presented. Lastly, a comparison of simulation results from the LPF1–4 models is included.

Appendix C.1. Linearization of Hydrostatics

The exact nonlinear hydrostatic force is calculated using the analytical equation of the submerged volume—i.e.,

$$f_h = f_b - f_g = V_s \rho g - mg, \quad (\text{A1})$$

where V_s is the exact submerged volume of the sphere, calculated by

$$V_s = \left(\left(\pi h^2 \right) / 3 \right) (3D/2 - h), \quad (\text{A2})$$

where $h = D/2 - x_3$ is the draft with limits 0 and D . In the linear case the hydrostatic force is linearized to

$$f_h \cong -\rho g A_{WP} x_3, \quad (\text{A3})$$

where $A_{WP} = \pi(D/2)^2$ is the water plane area (i.e., the area of a circle with diameter D). With $C_{33} = \rho g A_{WP}$ being the hydrostatic stiffness in heave, the linearized hydrostatic force can be written as

$$f_h \cong -C_{33} x_3. \quad (\text{A4})$$

Appendix C.2. The LPF0 Model

The dynamic one-DoF system can be considered as a traditional mechanical oscillator composed of a mass-spring-damper system with constant mass, damping, and spring stiffness; i.e., merely a regular motion (single frequency) is modelled. When restricted to a regular motion, the linear equation of motion for a free oscillation in heave is written as

$$(m + A_{33}(\omega))\ddot{x}_3(t) + B_{33}(\omega)\dot{x}_3(t) + C_{33}x_3(t) = 0, \quad (\text{A5})$$

where m is the mass of the sphere; A_{33} , B_{33} , and C_{33} are the added mass, hydrodynamic damping, and hydrostatic stiffness in heave, respectively. Note that the right-hand side of the equation is zero as there is no external forcing on the system; i.e., no incident waves and no PTO forces. Drag forcing due to viscous effects are not included in any of the models based on linear theory. The frequency dependent added mass and hydrodynamic damping coefficients for the given water depth are calculated using traditional BEM theory utilizing the commercial LPF code WAMIT.

The natural frequency, the damped natural frequency, and the logarithmic decrement of the one-DoF system are calculated using the hydrodynamic coefficients for the statically neutrally buoyant position [7]. From [28], the solution to the free oscillation is

$$x_3(t) = (C_1 \cos \omega_{e0}t + C_2 \sin \omega_{e0}t)e^{-\delta t} \quad (\text{A6})$$

As an initial check the reader is encouraged to compare the results of this equation to his/her own simulation results. The hydrodynamic coefficients, the damped natural frequency (and period), the logarithmic decrement, and the added mass and damping coefficients at the damped natural frequency are given in Table A2.

Table A2. Hydrodynamic coefficients and modal parameters utilized in the *LPF0* model.

| T_{e0} | ω_{e0} | δ | $A_{33}(\omega_{e0})$ | $B_{33}(\omega_{e0})$ | C_{33} | C_1 | C_2 |
|----------|---------------|----------|-----------------------|-----------------------|----------|-------|-------------|
| [s] | [rad/s] | [rad/s] | [kg] | [Ns/m] | [N/m] | [m] | [m] |
| 0.76 | 8.30 | 0.695 | 2.97 | 13.95 | 692.89 | H_0 | $0.0839H_0$ |

Appendix C.3. The LPF1–4 Models

Through the Cummins equation [27], the linear equation of motion is expressed in the time domain as

$$(m + a_{33}^{\infty})\ddot{x}_3(t) + f_{r,conv}(t) + C_{33}x_3(t) = 0, \quad (A7)$$

where $f_{r,conv}$ is the convolution part of the radiation force—i.e.,

$$f_{r,conv} = \int_0^t K_{33}(t - \tau)\dot{x}_3(\tau)d\tau. \quad (A8)$$

WAMIT directly outputs the infinite frequency added mass coefficient a_{33}^{∞} , and the radiation impulse response functions (IRF) is calculated based on the damping coefficients:

$$K_{33}(t) = \frac{2}{\pi} \int_0^{\infty} B_{33}(\omega) \cos(\omega t) d\omega. \quad (A9)$$

For a strictly linear model the coefficients are found for the structure located at rest at its statically neutrally buoyant position in the water. The results of such a model are given in the *LPF1* model. However, one may try to extend the linear case by introducing nonlinear coefficients. When doing this the effects of the motion of the structure (i.e., the draft of the sphere) are included, but the water surface is considered calm. The easiest and most common first step is to include nonlinear buoyancy, which is done in *LPF2*. Further, the draft dependency of a_{33}^{∞} is included in *LPF3*, and finally, in addition, the radiation convolution function is included in *LPF4*. The models are outlined in Table A3.

Table A3. Overview of the *LPF1–4* models.

| Model | Hydrostatics C_3 | Added Mass a_{33}^{∞} | Radiation Convolution Function K_{33} |
|-------|--------------------|------------------------------|-----------------------------------------|
| LPF1 | Constant | Constant | Constant function |
| LPF2 | Draft-dependent | Constant | Constant function |
| LPF3 | Draft-dependent | Draft-dependent | Constant function |
| LPF4 | Draft-dependent | Draft-dependent | Draft-dependent functions |

Appendix C.4. Measured Hydrostatics

Measurements were performed using a force sensor which was connected to the mooring line. Two tests were performed, one test where the sphere was slowly lifted out of the water and the sensor was mounted at the mooring line going upward, and another test where the sphere was slowly submerged into the water and in this case the sensor was mounted under the water at a mooring line going downward. Simultaneous position and force measurements were recorded; see Figure A3. It is seen that the nonlinear Equation (A1) represents the measurements accurately, whereas the linear Equation (A3) is about 50% off when the sphere is fully submerged ($x_3/D = -0.5$) or just lifted out of the water ($x_3/D = 0.5$). Equation (A1) is utilized in the models with a nonlinear implementation of the hydrostatic force; i.e., *LPF2*, 3, and 4.

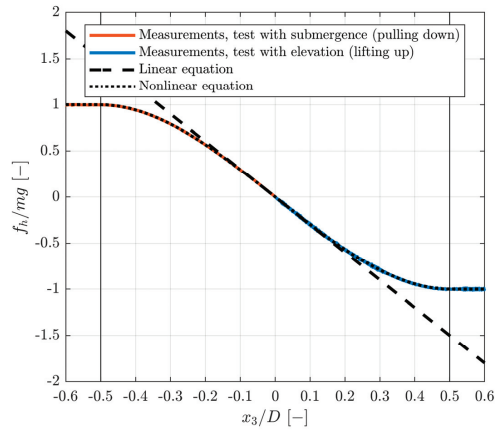


Figure A3. Measured hydrostatic forces as function of the draft. Nonlinear (Equation (A1)) and linear (Equation (A3)) analytical expressions of the hydrostatic force are included.

Appendix C.5. Added Mass at Infinite Frequency

The added mass at infinite frequency coefficient a_{33}^{∞} was calculated in WAMIT using different values of the draft of the sphere. The data were fitted to a fifth order polynomial; see Figure A4. This fit was subsequently used in the models with nonlinear implementation of a_{33}^{∞} ; i.e., LPF3 and 4.

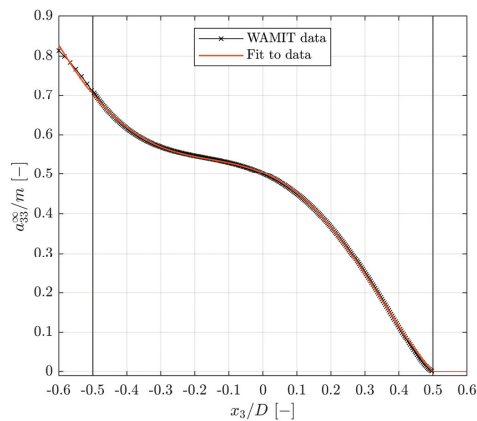


Figure A4. Draft-dependent normalized added mass at infinite frequency with a fifth order polynomial fit.

Appendix C.6. Radiation IRF

The radiation IRF K_{33} , see Equation (A9), was calculated using WAMIT hydrodynamic damping coefficients for different drafts of the sphere. The curves in Figure A5 show the spread in the functions when going from zero draft (flat curve) to full submergence with draft equal to the diameter D (largest curve). A resolution in draft of 1 mm was used

(a total of 300 functions). The radiation impulse function to be used at a particular time step during the simulation was thus pieced together of the radiation impulse functions corresponding to the drafts of previous time history. Linear interpolation in the functions was used to get the values corresponding to the actual drafts.

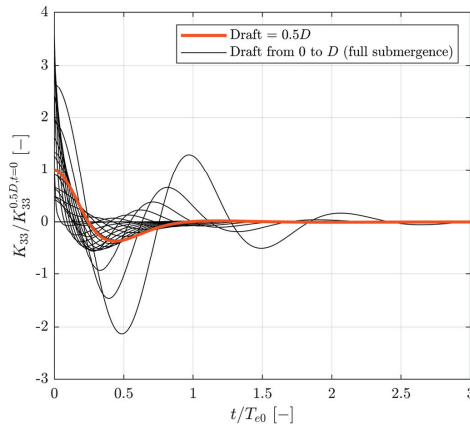


Figure A5. Normalized radiation impulse response functions for different drafts. Steps of 15 mm draft are shown for better visualization.

Appendix C.7. Comparison of the LPF1–4 Models

A comparison of the simulation results from the LPF1–4 models with various levels of nonlinearities is particularly interesting for the tests conducted with the highest drop height—i.e., $H_0 = 0.5D$. These are shown in Figure A6 for the first two natural periods in heave. For these tests, the initial buoyancy force on the sphere is zero, as the draft is zero. The LPF1 model, however, under-predicts the initial downward hydrostatic force, see Figure A6, since in the linearized hydrostatics assumption, Equation (A1), the buoyancy of a cylinder with a radius and a height equal to the spherical radius is subtracted from the rest condition at $x_3 = 0$ (zero hydrostatic force). In the LPF2 model, the initial downward acceleration of the sphere is over-predicted due to the inclusion of a constant added mass term (the added mass should ideally be zero at initiation). The LPF1 model weighs out this error by the former mentioned error induced by the subtraction of the buoyancy of the cylinder, where it ideally should be the buoyancy of half a sphere. The volume of a cylinder is 1.5 times the volume of a sphere, causing the under-predicted hydrostatic force to exactly balance out the extra added mass ($a_{33,LPF1}^\infty = 0.5m$) at initiation. Hence, the LPF1 model accelerates by g at initiation, as is the case with the models LPF3 and 4, where the added mass at infinite frequency is calculated as a function of the draft. Regarding the convolution part of the radiation force, the LPF4 model is predicting a different force time series with higher frequency content. Consequently, the LPF4 model has a different response in the heave decay when compared to the LPF3 model.

Not including any nonlinearities as in LPF1 model or only including nonlinear hydrostatics, as in the LPF2 model, produces large deviations from the more accurately formulated models with draft-dependent radiation forces implemented; see Figure A6. It is stressed that the comparison to physical tests or numerical models of higher fidelity is needed to evaluate the accuracy of any of the LPF models; see Sections 3 and 4.

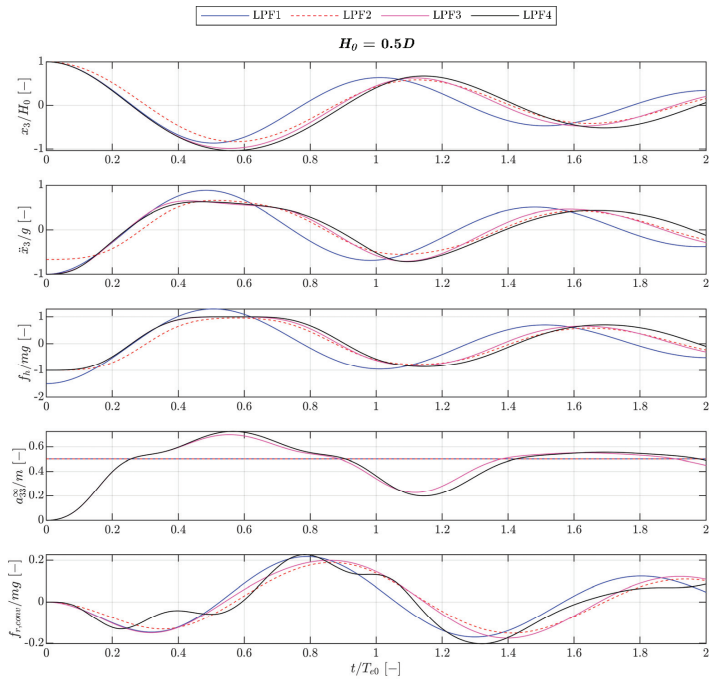


Figure A6. Results from the different LPF models for the first two natural periods.

Appendix D

Raw and normalized heave decay time series are presented in Figures A7 and A8, respectively. The measured surface elevation time series for the drop heights $H_0 = 0.1D$ and $H_0 = 0.3D$ are presented in Figure A9. The locations of wave gauges can be seen in Figure 8. The measured motions in all six DoF for the drop heights $H_0 = 0.1D$ and $H_0 = 0.3D$ are presented in Figures A10 and A11, respectively.

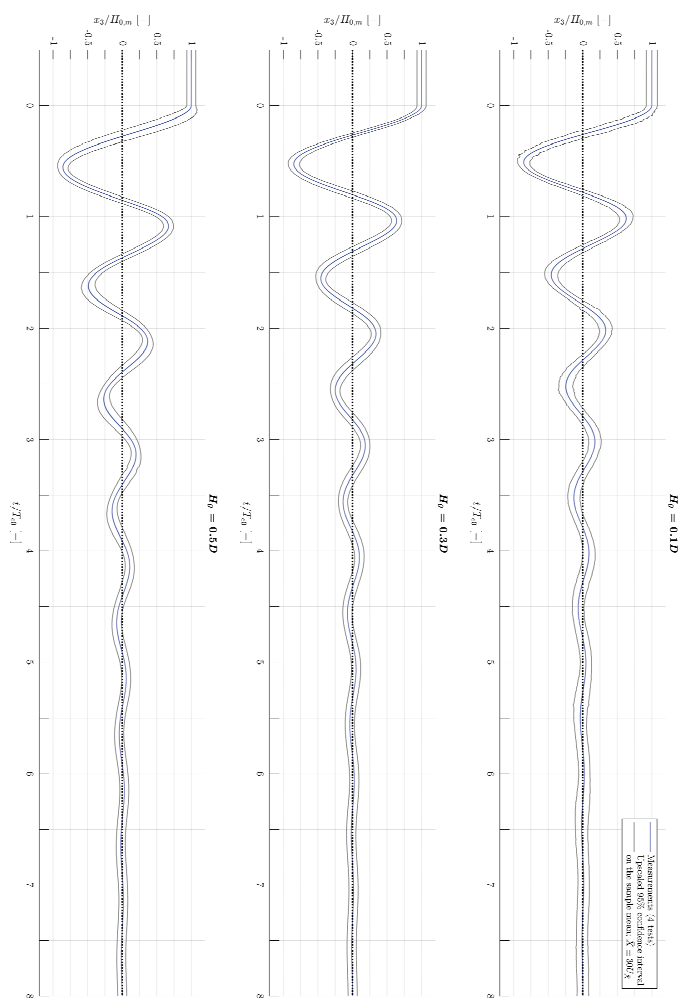


Figure A7. Normalized decay time series for the three investigated drop heights (enlarged version). The 95% CI was scaled up by a factor of 30 to be able to visualize the time-dependency.

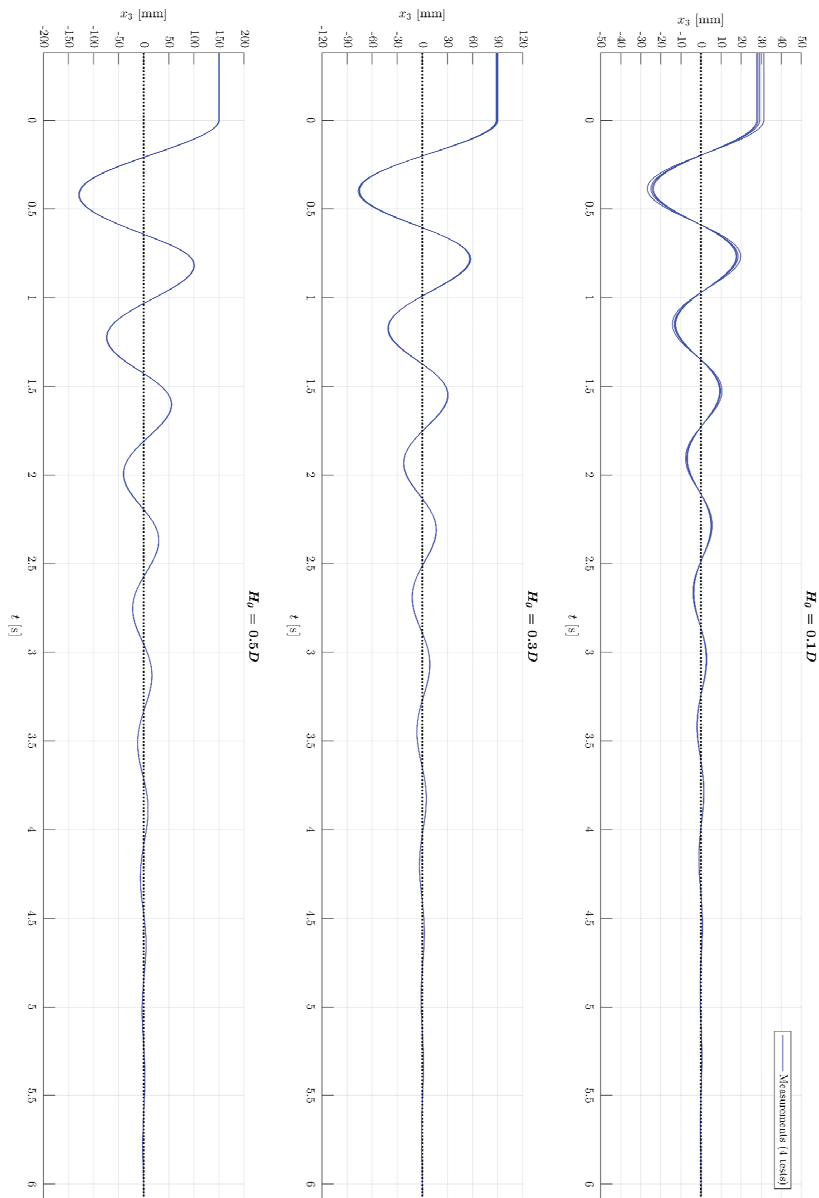


Figure A8. Raw decay time series for the three investigated drop heights.

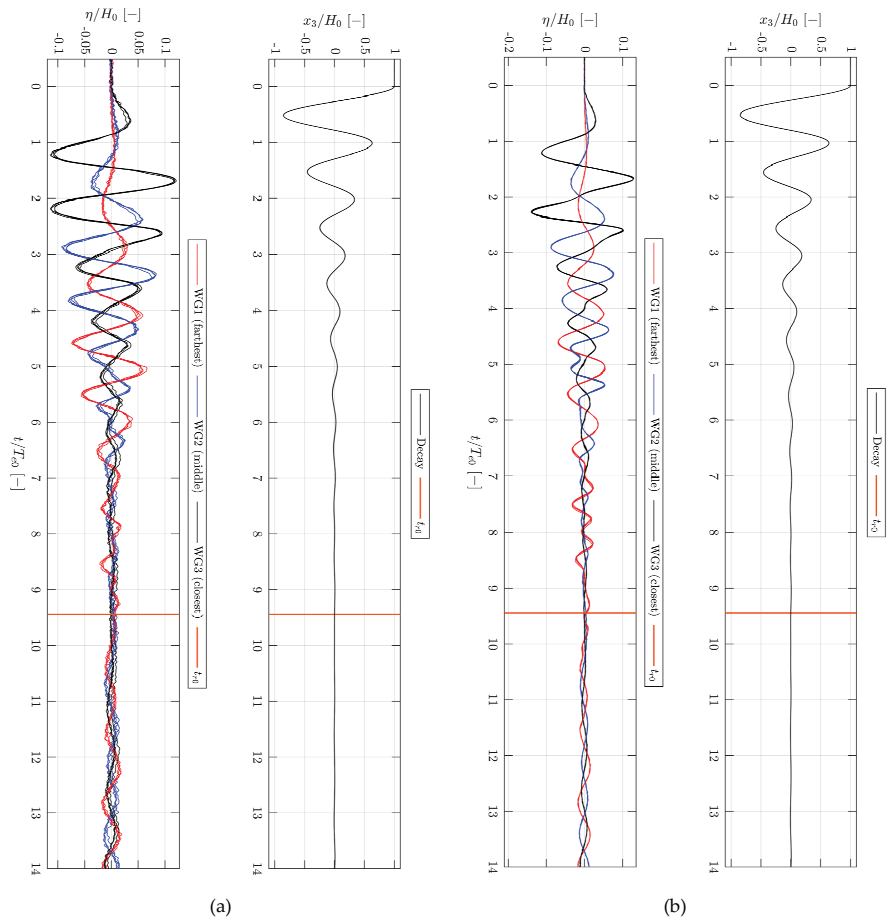


Figure A9. Surface elevation time series for tests with $H_0 = 0.1D$ (a) and $H_0 = 0.3D$ (b).

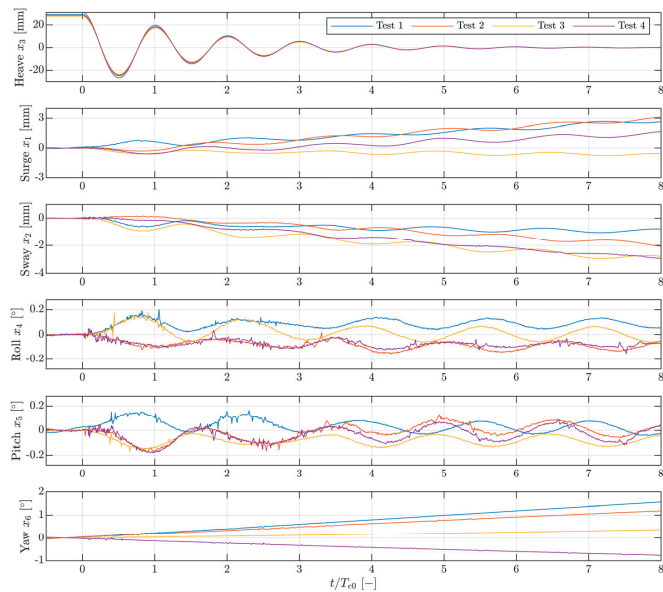


Figure A10. Time series of the measured motions in six DoF for $H_0 = 0.1D$.

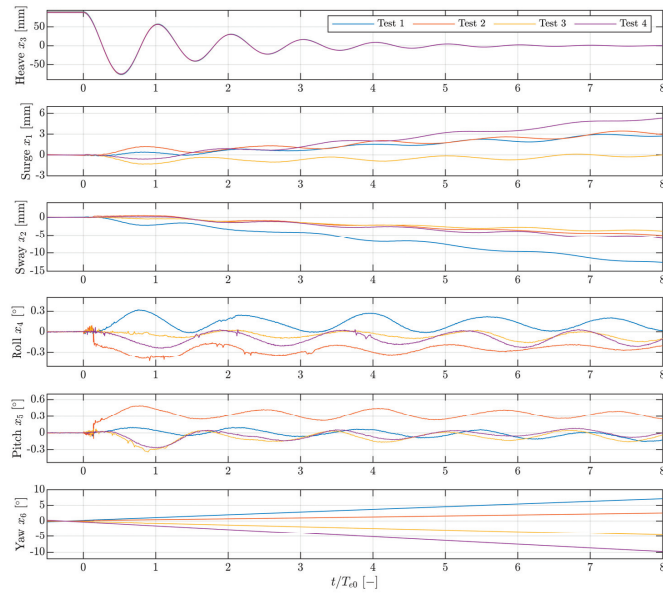


Figure A11. Time series of the measured motions in six DoF for $H_0 = 0.3D$.

References

- Devolder, B.; Stratigaki, V.; Troch, P.; Rauwoens, P. CFD Simulations of Floating Point Absorber Wave Energy Converter Arrays Subjected to Regular Waves. *Energies* **2018**, *11*, 641. [CrossRef]
- Windt, C.; Davidson, J.; Ransley, E.J.; Greaves, D.; Jakobsen, M.; Kramer, M.; Ringwood, J.V. Validation of a CFD-based numerical wave tank model for the power production assessment of the Wavestar ocean energy converter. *Renew. Energy* **2019**, *146*, 2499–2516, ISSN 0960-1481. [CrossRef]
- Pecheur, A.F.S.; Kofoed, J.P. (Eds.) *Handbook of Ocean Wave Energy*; Ocean Engineering & Oceanography; Springer: Berlin/Heidelberg, Germany, 2017; Volume 7. [CrossRef]
- Ransley, E.; Yan, S.; Brown, S.; Hann, M.; Graham, D.; Windt, C.; Schmitt, P.; Davidson, J.; Ringwood, J.; Wang, M.; et al. A blind comparative study of focused wave interactions with floating structures (CCP-WSI Blind Test Series 3). *Int. J. Offshore Polar Eng.* **2020**, *30*, 1–10. [CrossRef]
- IEA OES Wave Energy Converters Modelling Verification and Validation. Available online: <https://www.ocean-energy-systems.org/oes-projects/wave-energy-converters-modelling-verification-and-validation/> (accessed on 22 July 2020).
- Wendt, F.; Nielsen, K.; Yu, Y.-H.; Bingham, H.; Eskilsson, C.; Kramer, M.; Babarit, A.; Bunnik, T.; Costello, R.; Crowley, S.; et al. Ocean Energy Systems Wave Energy Modelling Task: Modelling, Verification and Validation of Wave Energy Converters. *J. Mar. Sci. Eng.* **2019**, *7*, 379. [CrossRef]
- Nielsen, K.; Wendt, F.; Yu, Y.-H.; Ruehl, K.; Touzon, I.; Nam, B.W.; Kim, J.S.; Kim, K.-H.; Crowley, S.; Wanan, S.; et al. OES Task 10 WEC heaving sphere performance modelling verification. In *Advances in Renewable Energies Offshore, Proceedings of the 3rd International Conference on Renewable Energies Offshore (RENEW 2018), Lisbon, Portugal, 8–10 October 2018*, 1st ed.; Guedes Soares, C., Ed.; CRC Press: London, UK, 2018; pp. 265–273.
- Wendt, F.; Yu, Y.-H.; Nielsen, K.; Ruehl, K.; Bunnik, T.; Touzon, I.; Nam, B.W.; Kim, J.S.; Kim, K.-H.; Janson, C.E.; et al. International Energy Agency Ocean Energy Systems Task 10 Wave Energy Converter Modelling Verification and Validation. In *Proceedings of the 12th EWTEC—European Wave and Tidal Energy Conference, Cork, Ireland, 27 August–1 September 2017*; Volume 12.
- OES Task10 WEC Modelling, Verification & Validation. Available online: <https://energiforskning.dk/node/9035> (accessed on 22 July 2020).
- Kramer, M. Highly Accurate Experimental Tests with a Floating Sphere—Kramer Sphere Cases. OES TASK 10 WEC Modelling Workshop 3 on 14 and 15 of November 2019, Amsterdam. Available online: <https://www.wecanet.eu/oes-task-10-workshop> (accessed on 4 January 2021).
- ASME. ASME PTC 19.1-2018: Test Uncertainty (Performance Test Code); ASME: New York, NY, USA, 2019.
- ISO/IEC. Guide 98-3 Uncertainty of Measurement—Part 3: Guide to the Expression of Uncertainty in Measurement (GUM:1995), 1st ed.; ISO/IEC: Geneva, Switzerland, 2008.
- Windt, D.; Davidson, J.; Ringwood, J. High-fidelity numerical modelling of ocean wave energy systems: A review of computational fluid dynamics-based numerical wave tanks. *Renew. Sustain. Energy Rev.* **2018**, *93*, 610–630. [CrossRef]
- Yang, Z. Assessment of unsteady-RANS approach against steady-RANS approach for predicting twin impinging jets in a cross-flow. *Cogent Eng.* **2014**, *1*, 1. [CrossRef]
- Weller, H.; Taber, G.; Jasak, H.; Fureby, C. A tensorial approach to computational continuum mechanics using object-oriented techniques. *Comput. Phys.* **1998**, *12*, 620–631. [CrossRef]
- STAR-CCM+, Siemens Digital Industries Software. Available online: <https://www.plm.automation.siemens.com/global/en/products/simcenter/STAR-CCM.html> (accessed on 31 August 2020).
- Deshpande, S.; Anumolu, L.; Trujillo, M.F. Evaluating the performance of the two-phase flow solver interFoam. *Comput. Sci. Discov.* **2012**, *5*, 014016. [CrossRef]
- Davidson, J.; Costello, R. Efficient Nonlinear Hydrodynamic Models for Wave Energy Converter Design—A Scoping Study. *J. Mar. Sci. Eng.* **2020**, *8*, 35. [CrossRef]
- Grilli, S. Fully Nonlinear Potential Flow Models Used for Long Wave Runup Prediction. 1996. Available online: <https://personal.egr.uri.edu/grilli/long-97.pdf> (accessed on 27 August 2020).
- SHIPFLOW Motions, FLOWTECH International AB. Available online: <https://www.flowtech.se/products/shipflow-motions> (accessed on 31 August 2020).
- Longuet-Higgins, M.S.; Cokelet, E.D. The deformation of steep surface waves—I. A numerical method of computation. *Proc. R. Soc. Lond.* **1976**, *350*, 1–26. [CrossRef]
- Janson, C.-E.; Shiri, A.; Jansson, J.; Moragues, M.; Castanon, D.; Saavedra, L.; Degirmenci, C.; Leoni, M. Nonlinear computations of heave motions for a generic Wave Energy Converter. In *Proceedings of the NAV 2018, 19th International Conference on Ships and Maritime Research, Trieste, Italy, 20–22 June 2018*; Marinò, A., Bucci, V., Eds.; IOS Press BV: Amsterdam, The Netherlands, 2018.
- Ferrandis, J.D.Á.; Bonfiglio, L.; Rodríguez, R.Z.; Chrysostomidis, C.; Faltinsen, O.M.; Triantafyllou, M. Influence of Viscosity and Nonlinearities in Predicting Motions of a Wind Energy Offshore Platform in Regular Waves. *J. Offshore Mech. Arct. Eng.* **2020**, *142*, 062003. [CrossRef]
- Wehausen, J.V.; Laitone, E.V. Surface Waves in Fluid Dynamics III. In *Handbuch der Physik* 9; Flugge, S., Truesdell, C., Eds.; Springer: Berlin, Germany, 1960; pp. 446–778.
- Newman, J. *Marine Hydrodynamics*; MIT Press: Cambridge, MA, USA, 1977; ISBN 9780262140263.
- Faltinsen, O. *Sea Loads on Ships and Offshore Structures*; Cambridge University Press: Cambridge, UK, 1990; ISBN 0521458706.
- Cummins, W.E. The Impulse Response Function and Ship Motions. *Schiffstechnik* **1962**, *9*, 101–109.

-
28. Falnes, J. *Ocean. Waves and Oscillating Systems—Linear Interactions Including Wave-Energy Extraction*; Cambridge University Press: Cambridge, UK, 2002; ISBN 9780511754630.
 29. Lee, C.H.; Newman, J.N. *WAMIT User Manual Version 7.3*; WAMIT, Inc.: Chestnut Hill, MA, USA, 2019.
 30. Ayyub, B.M.; McCuen, R.H. *Probability, Statistics, and Reliability for Engineers and Scientists*, 2nd ed.; Chapman & Hall/CRC: Boca Raton, FL, USA, 2003; ISBN 1-58488-286-7.
 31. Brorsen, M.; Larsen, T. *Lærebog i Hydraulik (Danish)*, 2nd ed.; Aalborg Universitetsforlag: Aalborg, Denmark, 2009; ISBN 978-87-7307-978-2.
 32. Carter, S.; Gutierrez, G.; Batavia, M. The Reliability of Qualisys' Oqus System. In Proceedings of the APTA NEXT 2015 Conference and Exposition, National Harbor, MD, USA, 3–6 June 2015.



Paper C

Detached-Eddy Simulation of Normal Flow past Flat Plates: The Influence from Corner Curvature

Jacob Andersen
Claes Eskilsson

The paper has been published in:
*Proceedings of the Thirty-Third (2023) International Ocean and Polar
Engineering Conference* (pp. 2441–2448), ISOPE,
ISBN: 978-1-880653-80-7, 2023.

Detached-Eddy Simulation of Normal Flow past Flat Plates: The Influence from Corner Curvature

Jacob Andersen¹ and Claes Eskilsson¹

¹ Department of the Built Environment, Aalborg University
 Aalborg, Denmark

ABSTRACT

Normal flow past flat plates at high Reynolds numbers appears in various engineering contexts. To accurately model such flows for slender plates in Computational Fluid Dynamics requires scale-resolving rather than scale-modelling methods. The present paper uses Detached-Eddy Simulation to investigate the influence of plate corner curvature on global flow quantities such as the time-averaged drag coefficient. The effect of corner curvature is mapped and collated with the literature. Solution verification is carried out to quantify the numerical uncertainty. The time-averaged drag coefficient increases significantly between semi-cylindrically rounded ($(C_D)_t=2.28$) and sharp-cornered ($(C_D)_t=2.42$) plates.

KEY WORDS: drag coefficient, flat plate, CFD, scale-resolving simulations; DES.

INTRODUCTION

Normal flow past flat plates is a canonical research topic within fluid dynamics with seminal works of, e.g., Fage and Johansen (1927) and Fail et al. (1959). The topic remains relevant to modern engineering due to its complexity and vast application range. Flat plates in normal flows are thus seen in engineering applications such as interceptors on high-speed crafts, energy collectors of oscillating surging type wave energy converters, and heave plates on offshore floating substructures for, e.g., wind turbine generators or solar PV. At practical Reynolds numbers Re (say, $>1e5$), see Eq. 1, the drag is governed by the turbulent wake generated from the flow separation and shedding of large eddies at the plate edges. The normal flow past flat plates is dominated by pressure (form) drag, and for plate thicknesses approaching zero the contribution from skin friction will equal zero. For sharp-cornered plates, the separation points are fixed and the Re -dependency on the drag coefficient C_D , see Eq. 2, is very weak for $Re > 1e3$ (Hoerner, 1965). The influence of the aspect ratio (width to height) was studied in Fail et al. (1957) for flow past flat plates with aspect ratios ranging from one (square) to 20. The classic work of Fage and Johansen (1927) considered the normal flow at $Re = 1.5e5$ past a flat plate of so-called infinite span or aspect ratio – referring to a physical test setup where flow over the spanwise edges was restricted by wind tunnel walls. The tested plate was therefore nominally two-dimensional, which is an assumption often adopted in both physical and numerical tests of flow past high aspect

ratio, i.e., slender, plates. Despite a nominally two-dimensional geometry, the problem remains three-dimensional due to the inherent three-dimensionality of turbulence.

Computational Fluid Dynamics (CFD) is widely used in the field of fluid mechanics where it allows for the extraction of virtually any flow variable of interest without affecting the flow; has a highly controllable test setup/environment; and generally, poses a cost-effective alternative to physical tests. CFD from Scale-Modelling Simulation (SMS) techniques in the form of Unsteady Reynolds-Averaged Navier-Stokes (URANS) models coupled with Boussinesq-viscosity (industry standard) turbulence models have proven unreliable in large curvature flows past nominally two-dimensional (slender) geometries (Squires et al., 2001, Vatsa et al., 2003, Wu et al., 2022, Shur et al., 2005, Mannini, 2015). Thus, for example Shur et al. (2005) reported how URANS simulations of the high- Re flow past a NACA 0012 airfoil at 90° angle of attack depended considerably on the turbulence model, spanwise dimension, and initial conditions. Only SMS started from the solution from a Scale-Resolving Simulation (SRS) was able to consistently sustain three-dimensionality, and these simulations still significantly overpredicted the time-averaged drag coefficient relative to physical tests and SRS – indicating the increased accuracy of SRS relative to SMS in such flow types. SRS with Large-Eddy Simulation (LES) resolves large energetic scales, which tends to be dependent on geometry, boundary conditions, etc., and models small scales, which tends to be more universal and homogeneous. LES resolves scales accounting for about 80% or more of the local turbulence kinetic energy, k , as suggested by Pope (2004). Thus, LES requires high resolutions in time and space – especially within boundary layers where small scales govern – making LES computational costly. This is partially circumvented by the Detached-Eddy Simulation (DES) approach due to Spalart et al. (1997). DES is a hybrid-URANS-LES method which switches from scale-modelling (URANS) to scale-resolving (LES) between attached and detached flow regions. The idea from LES of resolving only the large energetic scales and modelling the small scales is thus further exploited in DES in the sense scale-modelling is used to account for k in attached boundary layers where the accuracy of turbulence models is often high (Durbin, 2021). The present paper focuses on the application of DES to simulate the case of normal flow past a nominally two-dimensional flat plate. The adopted global flow values of interest are the time-averaged drag coefficient $\langle C_D \rangle_t$, the relative recirculation length L_C , and the Strouhal number S_t ; refer to the succeeding section for the definitions applied in the present paper.

Table 1: Summary of the present literature on normal flow past flat plates. *Smag* refers to the Smagorinsky subgrid model.

| Reference | Legend ref. | Type | r/h [%] | t/h [%] | h/h_c [-] | $\langle C_D \rangle_t$ [-] | Re [-] | $\langle L_c \rangle_{t,s}$ [-] | S_t [-] |
|--------------------------|-------------|----------|--------------|--------------|----------------|--------------------------------|-------------|------------------------------------|--------------|
| Tian et al. (2014) | TIAN | LES Smag | 1 | 2 | 0.0625 | 2.20 | 1.5e5 | 2.28 | 0.155 |
| Tian et al. (2014) | TIAN | LES Smag | 0.5 | 2 | 0.0625 | 2.30 | 1.5e5 | 2.13 | 0.155 |
| Diaz-Ojeda et al. (2019) | DIAZ | LES Smag | 0 | 2 | 0.0625 | 2.34 | 1.5e5 | 2.4 | 0.166 |
| Diaz-Ojeda et al. (2019) | DIAZ | LES WALE | 0 | 2 | 0.0625 | 2.20 | 1.5e5 | - | - |
| Fage and Johansen (1927) | FAGE | Physical | 0 | 0-3 | 0.0714 | 2.13 | 1.5e5 | - | 0.146 |
| Fage and Johansen (1927) | FAGE | Physical | 0 | 0-3 | 0.0476 | 2.05 | 1.5e5 | - | - |
| Hemmati et al. (2018) | HEMM | LES Smag | 0 | 0 | 0.0625 | 2.13 | 1.2e3 | 2.51 | 0.158 |
| Hemmati et al. (2018) | HEMM | DNS | 0 | 0 | 0.0625 | 2.13 | 1.2e3 | 2.65 | 0.158 |
| DNV (2017) | DNV | Physical | 0 | 50 | - | 2.5 | 1e5 | - | - |
| DNV (2017) | DNV | Physical | 2.1 | 50 | - | 2.2 | 1e5 | - | - |
| DNV (2017) | DNV | Physical | 8.3 | 50 | - | 1.9 | 1e5 | - | - |

LES of the normal flow past flat plates at $Re = 1.5e5$ (as that of Fage and Johansen, 1927) was carried out in the works of Tian et al. (2014) and Diaz-Ojeda et al. (2019). Both works utilized cyclic spanwise boundaries to represent nominally two-dimensional plate geometries and had identical domain sizes as well as plate thicknesses (normalized with the plate height h). In Tian et al. (2014) the relative corner curvature r/h was varied between 0.5% and 1.0% (corresponding to r/t ratios of 25% and 50%, respectively), whereas sharp corners ($r = 0$) were applied in Diaz-Ojeda et al. (2019), see Fig. 1.

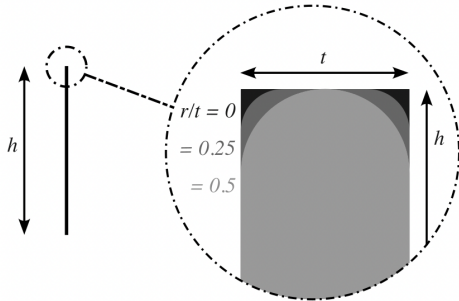


Fig. 1: Notion for plate geometry as seen from the spanwise plane.

The physical tests in Fage and Johansen (1927) were carried out on a steel plate with a flat front and a rear weakly tapering from the center ($t/h = 0.03$) towards the sharp edges ($t/h \approx 0$). The blockage ratio h/h_c , where h_c is the height of the wind tunnel, was varied between 0.024-0.095. In Hemmati et al. (2018), DNS and LES were carried out for the normal flow past zero-thickness plates (so-called baffles) at moderate $Re = 1.2e3$, thus just inside the range of Re where the global flow values are practically Re -independent according to Hoerner (1987) and Hemmati et al. (2018). All considered numerical test setups have applied either slip, symmetry, or freestream boundary conditions at the chordwise boundaries, which are assessed to have similar blockage effects assuming constant blockage ratio. The environmental load standard DNVGL-RP-C205 (DNV, 2017) presents the time-averaged drag coefficients of rectangular cylinders (rather than flat plates) of $t/h \geq 0.5$ as function of r/h . Information on h/h_c , L_c , and S_t are not given in the DNV standard.

The reviewed literature is summarized in Table 1, where abbreviated

reference names are introduced for brevity in figure legends. The influence of corner curvature, by r/h , on the time-averaged drag coefficient is mapped in Fig. 2.

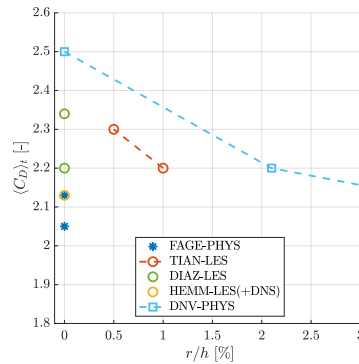


Fig. 2: Corner curvature versus time-averaged drag coefficient from selected literature, see Table 1. $r/h = 1\%$ corresponds to semi-cylindrical edges for plates of $t/h = 2\%$.

For $Re > 1e3$, flow separation occurs at the upstream corners irrespective of t/h . In the case of flat plates (say, $t/h \lesssim 5\%$), the separated shear layers do not interact with the downstream part of the plate, whereas for higher t/h ratios they do (Mannini, 2015). The curvature of the separated shear layers at the near-wake region increases with t/h until $t/h \approx 0.6$ (Nakaguchi et al., 1968) which poses a global maximum of $\langle C_D \rangle_t$ in the range 0.1-4 (Nakaguchi et al., 1968; Norberg, 1993; Sohankar, 2008). Accordingly, the tests reported in DNV (2017; $t/h = 0.5$) had increased shear layer curvature relative to those of flat plates causing a lower base pressure and consequently larger drag coefficients. That being said, the trend of $\langle C_D \rangle_t$ with r/h in DNV (2017) remains of interest in understanding the same trend in flow past flat plates since the upstream face is identical for constant r/h regardless of t/h , and it is the upstream face which governs the immediate curvature of the separated shear layers (Nakaguchi et al., 1968). The question then remains if the wake-structure interactions at $t/h = 0.5$ drive the correlation of $\langle C_D \rangle_t$ and r/h or if a similar correlation exists for $t/h \ll 1$.

The small geometrical variation of $r/h = 1.0\%$ to 0.5% (from a global

geometry point of view) in Tian et al. (2014) influenced the flow noteworthy and resulted in alterations of the global flow values of $\langle C_D \rangle_t$ and L_c , see Table 1 and Fig. 1, whereas S_t remained constant. Multiple studies investigating the case of normal flow past flat plates with sharp corners has been reviewed. By the collation of these studies, the tendency on $\langle C_D \rangle_t$ and L_c with r/h is inconclusive due to the large spread on $\langle C_D \rangle_t$ and L_c at $r/h = 0$. The collated results include not just the parameter variation of r/h , but also multiple others as h/h_c , Re , turbulence inflow intensity, test methodology errors, etc., which compromises an accurate disclosure of the influence of corner curvature.

The aim of the present paper is to map the influence of corner curvature on global flow quantities $\langle C_D \rangle_t$, S_t , and L_c of the flow past nominally two-dimensional flat plates with $r/h \in \{0.0, 0.5, 1.0\}\%$, where the limits correspond to sharp corners and semicylindrical edges for $t/h = 2\%$. In this, DES is carried out, and solution verification based on the Grid-Convergence Index (GCI) as per Roache (1998) as well as comparison to comparable test setups from LES, DNS and physical experiments are made.

GLOBAL FLOW VALUES

The Reynolds number is calculated from

$$Re = \frac{u_0 h}{\nu}, \quad (1)$$

where h is a characteristic length which for nominal two-dimensional plates simplifies to the plate height, u_0 is the normal freestream velocity, and ν is the kinematic viscosity.

The considered global flow values in the present paper include the time-averaged drag coefficient $\langle C_D \rangle_t$, the relative recirculation length L_c , and the Strouhal number S_t . Throughout the paper the operators $\langle \phi \rangle_t$ and $\langle \phi \rangle_z$ denotes time- and spanwise averaging, respectively, upon the field ϕ . The definitions of the drag coefficient C_D , the relative recirculation length L_c , and the Strouhal number S_t are given in Eqs. 2-4.

$$C_D = \frac{F_{drag}}{2\rho A u_0^2}, \quad (2)$$

where F_{drag} is the total drag force, ρ is the fluid density, and A is the frontal area of the plate.

$$L_c = \frac{L}{h}, \quad (3)$$

in which L is the length of the recirculation bubble as found from the time- and spanwise averaged streamwise velocity field.

$$S_t = \frac{f_p h}{u_0}, \quad (4)$$

where f_p is the peak frequency of the lift spectrum (representing the dominating vortex shedding frequency).

NUMERICAL METHOD

As outlined in the introduction, DES is a hybrid-URANS-LES method. The basis of both URANS and LES is the Navier-Stokes equations which express the conservation of mass and momentum for Newtonian fluids. Under the assumptions of incompressibility (constant density) and

constant viscosity, the Navier-Stokes equations read

$$\begin{aligned} \nabla \cdot U &= 0 \\ \frac{\partial}{\partial t} U + \nabla \cdot (UU) &= \nu \nabla^2 U - \frac{\nabla p}{\rho} + g, \end{aligned} \quad (5)$$

where U is the fluid velocity vector, p is pressure, g is the gravitational acceleration vector, and ∇ is the nabla operator.

Reynolds-Averaged Navier-Stokes Equations

The URANS equations exploit the concept of Reynolds-decomposition where flow variables are decomposed into a mean part (e.g., the ensemble average) and a fluctuation part. For a flow variable ϕ this can be expressed as

$$\phi(P, t) = \bar{\phi}(P, t) + \phi'(P, t), \quad (6)$$

where P is a position vector to any point within a domain, $\bar{\phi}$ denotes the ensemble average of ϕ , and ϕ' denotes the fluctuation of ϕ . The ensemble average of fluctuations then satisfies $\overline{\phi'} = 0$. Reynolds-decomposition and ensemble averaging of Eq. 5 then yields the URANS equations:

$$\begin{aligned} \nabla \cdot \bar{U} &= 0 \\ \frac{\partial}{\partial t} \bar{U} + \nabla \cdot (\bar{U}\bar{U}) &= \nu \nabla^2 \bar{U} - \frac{1}{\rho} \nabla \bar{p} + g - \nabla \cdot (\overline{U'U'}), \end{aligned} \quad (7)$$

which introduces the Reynolds-stress tensor

$$\bar{\sigma}_t = \overline{U'U'}.$$

Commonly, the Reynolds-stress tensor is reformulated from the Boussinesq hypothesis, and a turbulence model brings closure to the system of equations.

Large-Eddy Simulation

The basis of LES is a high-pass scale (low-pass frequency) filter operator of the form

$$\tilde{\phi}(P, t) = \int_D \phi(P', t) G(P - P', \tilde{\Delta}) dP', \quad (8)$$

where $\tilde{\phi}$ denotes the filtering of the flow variable ϕ , G is a convolution filter, $\tilde{\Delta}$ is the filter width, and D is the entire domain (Piomelli, 2021). Imposing Eq. 8 on the flow variables of Eq. 5 yields the filtered Navier-Stokes equations

$$\begin{aligned} \nabla \cdot \bar{U} &= 0 \\ \frac{\partial}{\partial t} \bar{U} + \nabla \cdot (\bar{U}\bar{U}) &= \nu \nabla^2 \bar{U} - \nabla \cdot \frac{\tilde{p}}{\rho} + g - \nabla \cdot (\bar{U}\bar{U} - \bar{U}\bar{U}). \end{aligned} \quad (9)$$

Analogously to the Reynolds-stress tensor in the URANS equations in Eq. 7, a residual stress term arises after filtering, i.e.,

$$\overline{\sigma_{SGS}} = \bar{U}\bar{U} - \bar{U}\bar{U},$$

which is commonly referred to as the subgrid-scale (SGS) stress tensor. As with $\bar{\sigma}_t$, $\overline{\sigma_{SGS}}$ is usually reformulated by the Boussinesq hypothesis and a SGS turbulence model is adopted to bring closure to the system.

Detached-Eddy Simulation

The original DES method of Spalart et al. (1997) substitutes the wall distance d_w as the length scale of the Spalart-Allmaras (S-A) turbulence model with the DES length scale

$$l_{\text{DES-S-A}} = \min(d_w, C_{\text{DES}}\Delta), \quad (10)$$

where Δ is the local cell size and C_{DES} a calibration constant. This reformulation effectively turns the S-A model into a SGS turbulence model of Smagorinsky-like type for $d_w \gg \Delta$, meaning that the turbulent viscosity scales with the magnitude of the local strain rate and the cell size squared (Strelets, 2001). Strelets (2001) formulated and calibrated a DES version of the popular k - ω -SST turbulence model (Menter and Esch, 2001) from its length scale

$$l_{\text{M-SST}} = \sqrt{k}/(\beta^* \omega)$$

with k being the turbulence kinetic energy, β^* a model constant, and ω the turbulence specific dissipation rate. In Strelets (2001), this length scale was substituted with $l_{\text{DES-M-SST}} = \min(l_{\text{M-SST}}, C_{\text{DES}}\Delta)$ in the dissipative term of the k -transport equation, securing Smagorinsky-like behavior at turbulence equilibrium. Furthermore, C_{DES} in the SGS formulation of the k - ω -SST model was calibrated from decaying homogeneous isotropic turbulence tests – similar assumptions used for derivation of the corresponding coefficient in the Smagorinsky model, see Lilly (1966).

TEST SET-UP

All simulations employed the k - ω -SST DES formulation (as per Strelets, 2001) in the open-source framework OpenFOAM-v2106 (OpenCFD, 2023; Weller et al., 1998). OpenFOAM is based on a cell-centred 2nd order finite volume method that supports unstructured polyhedral cells. In the present work the incompressible solver pisoFOAM, based on the PISO algorithm for pressure-velocity coupling, was used. In this work pisoFOAM utilizes implicitly filtered LES, referring to an actual convolution filter kernel never being imposed, but rather the filtering being implicitly defined from the available resolution, numerical truncation errors, and SGS model (Lampitella, 2014).

All spatial discretization schemes are second order accurate. Second-order central differences were chosen for diffusion and for the convection of momentum in LES-mode, as well as for gradient and Laplacian terms. Upwind second-order differences were chosen for the convection of momentum in RANS-mode and for the convection of k and ω . The time-stepping was carried out by a stabilized second-order Crank-Nicolson scheme.

A nominally two-dimensional plate of height h , span $4h$, and thickness $0.02h$ was oriented normally to a constant streamwise velocity u_0 . The corresponding Re was $1.5e5$. The relative curvature radius of the corners was varied as $r/h \in \{0.0, 0.5, 1.0\}\%$, see Fig. 1. The domain dimensions and boundary conditions (BCs) are outlined in Fig. 3. Velocity U is given as Dirichlet and Neumann type BCs at the inlet and outlet, respectively, and vice versa with the pressure p , see Fig. 3. The domain sizes and BCs were chosen to match Tian et al. (2014), where the spanwise dimension of $4h$ was chosen to accommodate multiple spanwise vortical rib structures.

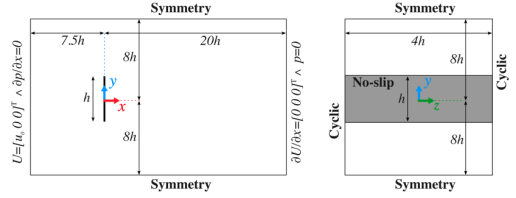


Fig. 3: Conceptual setup of numerical tests. Please note that origin of the global coordinate system is located at the center of the plate.

The OpenFOAM mesh tools blockMesh and refineMesh were used to generate the meshes. The meshes were predominantly hexahedral (98%) while the remainder was of polyhedral type used in intersections between refinement regions. 25 inflation layers were included around the plate with a first cell layer thickness corresponding to $y^+ < 1$ throughout all simulations. The mesh was asymmetrical about the y -axis as higher resolutions and more delicate refinement strategies were applied in the focus region, where the (near) wake transpires, relative to the Euler region in accordance with the DES mesh guidelines in Spalart and Streett (2001). See Fig. 4. A uniform cell spacing was used in z as also employed in Tian et al. (2014) and Díaz-Ojeda et al. (2019). A constant time step was invoked in all simulations.

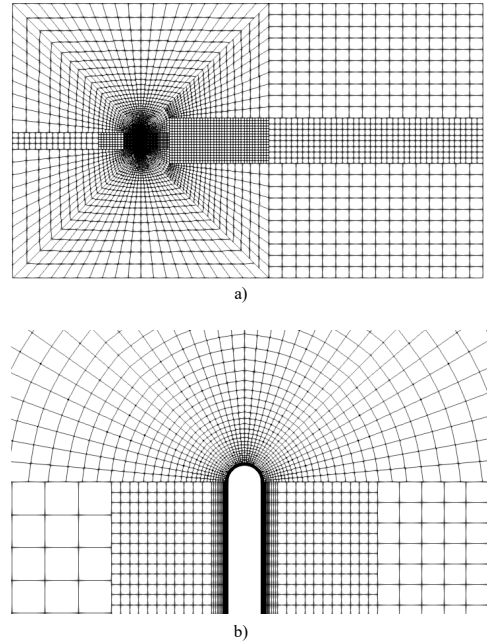


Fig. 4: View of the far- (a) and near-field mesh (b) in the xy -plane for Case 7 in Table 2.

SOLUTION VERIFICATION

Solution verification is carried out by Richardson Extrapolation (RE) and the Grid Convergence Index (GCI) to estimate numerical uncertainties. The procedure follows that of Eça et al. (2011). The verification variable is chosen as the time-averaged drag coefficient, $\langle C_D \rangle_t$. For the present paper, the grid refinement ratio h_i/h_1 is based on the number of cells in the xy -plane, corresponding to

$$h_i/h_1 = (N_{cells,1}/N_{cells,i})^{1/2},$$

where N_{cells} is the total number of cells and subscript i is the grid index which equals 1 for the highest resolution. Numerical uncertainty is widely accepted to be composed of discretization errors, iterative errors, and round-off errors (Eça et al., 2011). Round-off errors are negligible with the use of double precision and iterative errors are closely linked to the time step for unsteady simulations. Sensitivity to the temporal and spanwise resolutions are assessed more loosely than of the xy spatial resolution, and only few coarser temporal and spanwise resolutions have been considered, see Table 2. The tolerances used for residual control were $1e-7$ for velocity and turbulence fields and $1e-6$ for pressure.

Table 2: Investigated spatial and temporal resolutions. N_z denotes the number of cells in the spanwise direction.

| Case | h_i/h_1 [-] | N_{cells} [1e6 cells] | N_z [cells] | $\Delta t u_0/h$ [-] | $\langle C_D \rangle_t$ [-] | Δ_{rel} [%] | $U_{(C_D)_t}$ [%] |
|------|------------------|----------------------------|------------------|-------------------------|--------------------------------|-----------------------|----------------------|
| 1 | 1.00 | 10.3 | 48 | 6e-4 | 2.28 | 0.0 | 2.7 |
| 2 | 1.29 | 6.0 | 48 | 6e-4 | 2.28 | 0.2 | 3.7 |
| 3 | 1.49 | 4.5 | 48 | 6e-4 | 2.26 | 0.6 | 4.6 |
| 4 | 1.66 | 3.6 | 48 | 6e-4 | 2.23 | 2.1 | 5.4 |
| 5 | 2.08 | 2.3 | 48 | 6e-4 | 2.23 | 2.1 | 7.8 |
| 6 | 2.58 | 1.5 | 48 | 6e-4 | 2.10 | 8.0 | 11.3 |
| 7 | 3.16 | 1.0 | 48 | 6e-4 | 2.05 | 9.9 | 16.4 |
| 8 | - | 4.5 | 48 | 1.2e-3 | 2.22 | 1.8 | - |
| 9 | - | 4.5 | 48 | 2.4e-3 | 2.26 | 0.0 | - |
| 10 | - | 4.5 | 48 | 4.8e-3 | 2.25 | 0.4 | - |
| 11 | - | 2.3 | 24 | 6e-4 | 2.19 | 3.1 | - |
| 12 | - | 1.1 | 12 | 6e-4 | 4.06 | 82.1 | - |

Initial conditions were mapped from a preliminary DES solution executed with a high temporal resolution ($\Delta t u_0/h < 6e-5$), a moderate spatial resolution ($N_{cells} = 4.5e6$ cells), and a duration of $30h/u_0$. After mapping, the flow re-developed for $70h/u_0$ (following Tian et al., 2014) before statistical averaging was carried out for a duration of $245h/u_0$.

The variation of temporal and spanwise resolutions suggests that the results are rather insensitive to the choice of resolution for $\Delta t u_0/h \leq 1.2e-3$ and $N_z \geq 24$, which yielded relative deviations, Δ_{rel} , of 1.8% and 3.1% to the reference Case 3. Numerical uncertainty is thus estimated from the discretization errors from the spatial resolution in the xy -plane. Solution verification is only carried out for the plate geometry with $r/h = 1.0\%$. The estimated convergence of $\langle C_D \rangle_t$ with the spatial resolution in the xy -plane can be seen in Fig. 5, where least square fits to power functions of the form $\alpha(h_i/h_1)^{\gamma_0} + \beta$ are imposed to estimate the rate of convergence (γ_0). RE is applied to the least square fits to calculate the numerical uncertainty $U_{(C_D)_t}$ which is the expanded uncertainty at a 95% confidence level (Roache, 2009), see Table 2. The Case 1-3 meshes all have less than 5% numerical uncertainty and can be judged as acceptable resolutions.

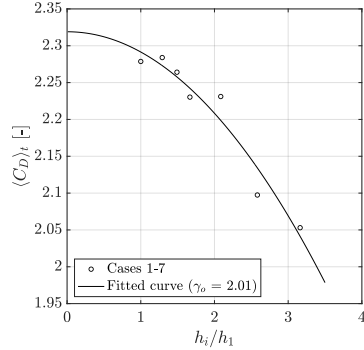


Fig. 5: Estimated convergence of $\langle C_D \rangle_t$ from spatial resolution in the xy -plane. γ_0 denotes the convergence rate.

A special trait of using SRS rather than SMS is that the modelling error (from turbulence) diminishes with the discretization error. This is an effect of the governing equations of DES (in LES mode) being tied directly to the local cell sizes. More accurate turbulence descriptions in the form of extended ranges of resolved scales are thus obtained for higher resolutions using DES. This effect is visualized from isosurfaces by the Q -criterion for $Q = 0.01$ with Cases 6, 4, 2, and 1 in Fig. 6, where finer length scales are resolved for decreasing case numbers (increasing resolutions). Additionally, the departure region is extended further downstream for increasing resolutions improving the accuracy of the “boundary condition” to the focus region (near-wake).

RESULTS

Global flow values are calculated for the three investigated corner curvatures, see Table 3. The Case 1 grid is adopted for the simulations on smaller corner curvatures. The far-field mesh is maintained while the near-field mesh is changed to accommodate the changes in plate geometry. Simulations are initiated in the same way as in the solution verification, meaning that a DES solution with $r/h = 1.0\%$ is mapped after which the flow is allowed to redevelop for $70h/u_0$ before statistical averaging is carried out for a duration of $245h/u_0$. The drag coefficient time series are shown in Fig. 7. The pressure coefficient on the plate is calculated by $C_p = 2(p - p_0)/(\rho u_0^2)$ where p_0 is the reference pressure taken as the inlet pressure at $y = 0$. The time- and spanwise averaged pressure coefficient distribution is shown in Fig. 8. The time- and spanwise averaged x -component of the velocity vector at $y = 0$ is shown in Fig. 9 (used for calculation of the recirculation length). The Strouhal numbers are in Table 3 given from the peak frequency in the lift power spectrum presented in Fig. 10.

Table 3: Global flow values for the investigated corner curvatures.

| r/h [%] | $\langle C_D \rangle_t$ [-] | L_C [-] | S_t [-] |
|--------------|--------------------------------|--------------|--------------|
| 1.0 | 2.28 | 2.10 | 0.157 |
| 0.5 | 2.26 | 2.18 | 0.155 |
| 0.0 | 2.42 | 1.98 | 0.155 |

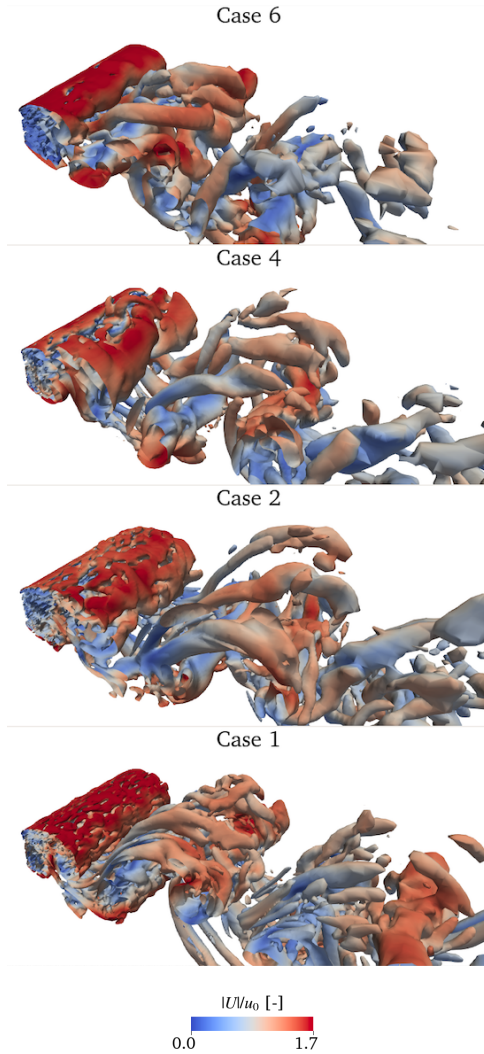


Fig. 6: Effect of mesh resolution on the wake illustrated by Q -isosurface ($Q = 0.01$) for Cases 6, 4, 2, and 1 (see Table 2). Coloring by the normalized magnitude of the velocity vector, $|U|/u_0$.

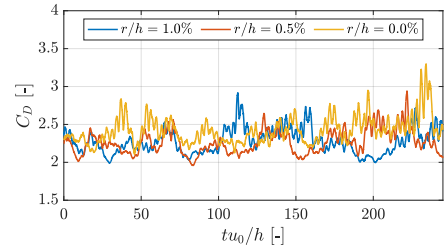


Fig. 7: Time series of the drag coefficient.

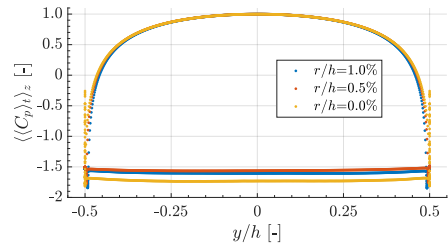


Fig. 8: Time- and spanwise averaged pressure coefficient distribution.

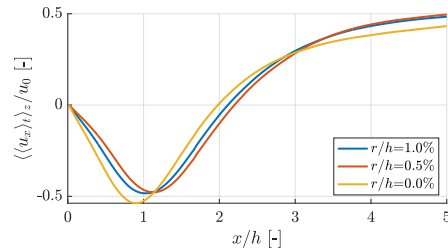


Fig. 9: Time- and spanwise averaged x -component of velocity at $y = 0$.

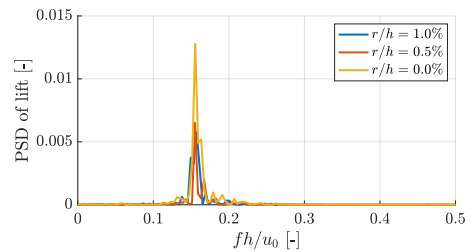


Fig. 10: Power spectral density (PSD) of the lift force.

To further estimate the effect of the corner curvatures on the shape of the wake regions the isosurface of the time-averaged velocity magnitude for $|U|_t/u_0 = 2/3$ is calculated, see Fig. 11.

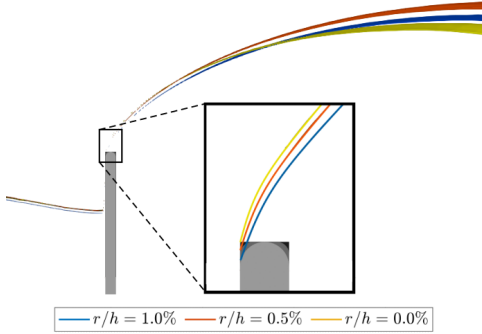


Fig. 11: Isosurface of time-averaged velocity magnitude, $|U|_t/u_0 = 2/3$, for different corner curvatures.

In Fig. 12, $\langle C_D \rangle_t$ from the present work are presented with that of literature (as previously presented in Fig. 5). The result for $r/h = 1.0\%$ is included with an error bar indicating a double-sided 95% confidence interval (CI) from the numerical uncertainty.

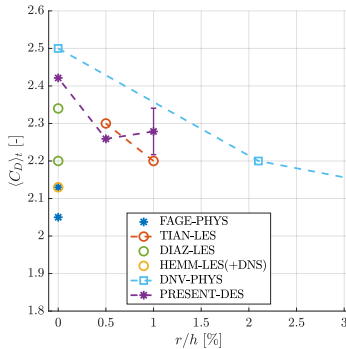


Fig. 12: Present results with 95% CI together with results from literature.

DISCUSSION

From Table 3 and Fig. 12, a monotonic trend of $\langle C_D \rangle_t$ with r/h was not disclosed over the investigated range. The difference between $\langle C_D \rangle_t$ at $r/h = 1.0\%$ and 0.5% is less than the numerical uncertainty at $r/h = 1.0\%$ with a 95% confidence level. However, a significant increase of $\langle C_D \rangle_t$ was found between $r/h = 1.0\%$ (semicylindrical edges) and $r/h = 0.0\%$ (sharp corners). The latter follows the tendency of DNV (2017) and Tian et al. (2014). For $r/h = 1.0\%$ and 0.0% , $\langle C_D \rangle_t$ and L_c are over- and underestimated, respectively, relative to the literature for $t/h \ll 1$ (flat plates). For $r/h = 0.5\%$, $\langle C_D \rangle_t$ and L_c are slightly under- and overestimated, respectively, but in close agreement

with those of Tian et al. (2014), i.e., less than 2.5% deviation. $\langle C_D \rangle_t$ and L_c are thus not consistently either over- or underestimated relative to the literature for the tested range of r/h .

Assuming equal error bars on $\langle C_D \rangle_t$ for $r/h = 0.5\%$ and 0.0% as for 1.0% , the correlation of $\langle C_D \rangle_t$ and r/h in the investigated range cannot be rejected to be equal that of Tian et al. (2014) and DNV (2017). Assuming (somewhat crudely) equal error bars on $\langle C_D \rangle_t$ for all numerical results in Fig. 12, the present DES results is only validated against LES with the Smagorinsky SGS model from Tian et al. (2014) and Diaz-Ojeda et al. (2018) given the same corner curvatures. The relative deviations are 1.8-3.5%, which is commonly accepted as minor deviations in a CFD context. The present DES $k-\omega$ -SST SGS model will in turbulence equilibrium behave Smagorinsky-like and hence similar to the LES in Tian et al. (2014) and Diaz-Ojeda et al. (2018) given comparable resolutions (and numerics). Similar domains and resolutions have been applied in the convergence analysis of Tian et al. (2014), and DES does not seem to improve the accuracy-cost trade-off in the considered application significantly over LES. A point for future investigation is to run LES on the exact same grids as applied in the present work.

As expected, the frequency of vortex shedding (governing the frequency of lift forces) is dominant around a single frequency, see Fig. 10. The Strouhal number is basically invariant with r/h from the present results (Table 3 and Fig. 10) with less than 1% deviation for the tested r/h ratios, and less than 2% deviation relative to Tian et al. (2014) and Hemmati et al. (2018).

C_D varies drastically over time, up to 60% between global minima and maxima, and the temporal evolution suggest distinct modes of the shedding process, see Fig. 7. High and low intensity shedding regimes behind nominally 2-D flat plates are reported in the literature by, e.g., Najjar and Balachandar (1998) and Hemmati et al. (2016), which concluded that global flow values vary notably between the different shedding regimes. Hence, statistical averaging ought only to be carried out for time series containing several high and low regime cycles.

Knowing $\langle C_D \rangle_t$ for the different plate geometries the tendencies are as expected with the pressure coefficient distributions and the recirculation length behind the plate. Base pressure distributions are close to constant over the plate width, y , see Fig. 8. The base pressures vary with r/h and scale with the relative differences of $\langle C_D \rangle_t$, while the pressure distributions on the upstream face only vary close to the edges. Higher base pressures and $\langle C_D \rangle_t$ are associated with lower recirculation lengths, see Fig. 9. The isosurfaces of $|U|_t/u_0 = 2/3$ can be used for visualization of the shape of the time-averaged wake, see Fig. 11. From this, the immediate curvatures of the respective wakes are as expected; steeper slopes and slight, positive offsets in y for lower r/h directly due to the different geometrical features. Further downstream, the isosurfaces with the steeper immediate slopes are expected to curve relatively more as seen for $r/h = 1.0\%$ and 0.0% causing lower recirculation lengths for higher r/h and ultimately higher $\langle C_D \rangle_t$. However, the isosurface for $r/h = 0.5\%$ curves the least and in turn has the highest recirculation length. The relative positioning of the isosurfaces follows the attained global flow values but opposes the expected physics which may be ascribed to too small variations of $\langle C_D \rangle_t$ in (part) of the tested r/h range relative to the numerical uncertainties.

CONCLUSIONS

Global flow quantities in the normal flow past flat plates have been calculated with DES coupled with the $k-\omega$ -SST turbulence model. The corner curvature of the plate has been varied in $r/h = \{0.0, 0.5, 1.0\}\%$.

For $r/h = 1.0\%$, solution verification was carried out and numerical uncertainty was quantified. The expanded uncertainty was estimated as 2.7% of the time-averaged drag coefficient at the 95% confidence level. An insignificant increase in $\langle C_D \rangle_t$ was found by varying $r/h = 1.0\%$ to 0.5%, while a significant increase was found for $r/h = 1.0\%$ (semicylindrical edges) to 0.0% (sharp corners) at the 95% confidence level. The latter had an increase of both $\langle C_D \rangle_t$ and L_C of about 6%. S_L remained close to invariant with r/h . For identical corner curvatures $\langle C_D \rangle_t$ deviated maximally 3.5% between the present DES and LES with the Smagorinsky SGS model from papers with comparable model setups – suggesting little influence of the turbulence description between the two models on integral values for the considered application.

ACKNOWLEDGEMENTS

This work is part of the “Verification through Accelerated testing Leading to Improved wave energy Designs” (VALID) project, funded by the European Union’s Horizon 2020 research and innovation program under grant agreement 101006927. Additional computational resources for the present work were granted by DeIC National HPC under grant agreement DeIC-AAU-N5-202200002. The authors gratefully acknowledge the support.

REFERENCES

- DNV, (2017). *DNVGL-RP-C205: Environmental Conditions and Environmental Loads* (Ed. August).
- Eça, L, Vaz, G, and Hoekstra, M (2010). “A Verification and Validation Exercise for the Flow over a Backward Facing Step”, *ECCOMAS CFD 2010*, Lisbon, Portugal.
- Fage, A and Johansen, FC (1927), “On the Flow of Air behind an Inclined Flat Plate of Infinite Span,” *Proc Math Phys Eng Sci P ROY SOC A-MATH PHY*, 116, 170-197.
- Fail, R, Lawford, JA, and Eyre, RCW (1959). *Low-Speed Experiments on the Wake Characteristics of Flat Plates normal to an Air Stream*, HMSO, London.
- Hemmati, A, Wood, DH, and Martinuzzi, RJ (2018). “On Simulating the Flow past a Normal Thin Flat Plate,” *J Wind Eng Ind*, 174, 170-187.
- Hemmati, A, Wood, DH, and Martinuzzi, RJ (2016). “Characteristics of Distinct Flow Regimes in the Wake of an Infinite Span Normal Thin Flat Plate,” *Int J Heat Fluid Flow*, 62 (B), 423-436.
- Hoerner, SF (1965). *Fluid-Dynamic Drag*, Published by the Author, 3.
- Lampitella, P (2014). *Large-Eddy Simulation for Complex Industrial Flows*, Doctoral dissertation, Politecnico di Milano, Italy.
- Lilly, DK (1967). “The Representation of Small-Scale Turbulence in Numerical Simulation Experiments,” *Proc of IBM Sci Comp Symposium on Env Sci*, Yorktown Heights, New York, USA, 195-210.
- Mannini, C (2015). “Applicability of URANS and DES Simulations of Flow Past Rectangular Cylinders and Bridge Sections,” *Comput*, 3(3), 479-508.
- Menter, FR, Kuntz, M, and Langtry, R (2003). “Ten Years of Industrial Experience with the SST Turbulence Model,” *Proc Int Symp Turbul Heat Mass Transf*, 4, 625-633.
- Najjar, FM and Balachandar, S (1996). “Low-Frequency Unsteadiness in the Wake of a Normal Flat Plate,” *J Fluid Mech*, 370, 101-147.
- Nakaguchi, H, Hashimoto, K, and Muto, S (1968). “An Experimental Study on Aerodynamic Drag of Rectangular Cylinders,” *J Jpn Soc Aeronaut Space Sci*, 16(168), 1-5 (in Japanese).
- Norberg, C (1993). “Flow around Rectangular Cylinders: Pressure Forces and Wake Frequencies,” *J Wind Eng Ind Aerodyn*, 49, 187-196.
- OpenCFD (2023). <https://www.openfoam.com/documentation/>
- Piomelli, U (2021). *Advanced Approaches in Turbulence: Ch. 3, Large Eddy-Simulations*, Elsevier, Durbin, P (Ed.).
- Pope, S (2004). “Ten Questions Concerning the Large-Eddy Simulation of Turbulent Flows,” *New J Phys*, 6(1).
- Roache, PJ (1998). *Verification and Validation in Computational Science and Engineering*, Hermosa Publishers.
- Roache, PJ (2009). *Fundamentals of Verification and Validation*, Hermosa Publishers.
- Spalart, PR, Jou, W-H, Strelets, M and Allmaras, SR (1997). “Comments on the Feasibility of LES for Wings, and on a Hybrid RANS/LES,” *Advances in DNS/LES*, Columbus, Ohio, USA, 137-147.
- Spalart, PR and Streett, C (2001). “Young-Person’s Guide to Detached-Eddy Simulation Grids,” NASA.
- Smagorinsky, J (1963). “General Circulation Experiments with the Primitive Equations: I. The Basic Experiment,” *Mon Weather Rev*, 91(3), 99-164.
- Strelets, M (2001). “Detached Eddy Simulation of Massively Separated Flows,” *AIAA 2001-0879: 39th Aerospace Sciences Meeting and Exhibit*, Reno, Nevada, USA.
- Tian, X, Ong, MC, Yang, J, and Myrhaug, D (2014). “Large-eddy Simulation of the Flow Normal to a Flat Plate including Corner Effects at a High Reynolds Number,” *J Fluids Struct*, 49, 149-169.
- Weller, H, Tabor, G, Jasak, H, and Fureby, C (1998). “A Tensorial Approach to CFD using Object Oriented Techniques,” *Comp in Physics*, 12, 620-631.

Paper D

Hydrodynamic Simulations of a FOWT Platform (1st FOWT Comparative Study) Using OpenFOAM Coupled to MoodyCore

Claes Eskilsson
Gael Verao Fernández
Jacob Andersen
Johannes Palm

The paper has been published in:
*Proceedings of the Thirty-Third (2023) International Ocean and Polar
Engineering Conference* (pp. 461-468), ISOPE, ISBN: 978-1-880653-80-7, 2023.

Hydrodynamic Simulations of a FOWT Platform (1st FOWT Comparative Study) Using OpenFOAM Coupled to MoodyCore

Claes Eskilsson^{1,2}, Gael Veroa Fernandez², Jacob Andersen², Johannes Palm³

¹RISE - Research Institutes of Sweden, Borås, Sweden

²Department of the Built Environment, Aalborg University, Aalborg, Denmark

³Sigma Energy & Marine AB, Gothenburg, Sweden

ABSTRACT

We numerically simulate the hydrodynamic response of a floating offshore wind turbine (FOWT) using CFD. The FOWT under consideration is a slack-moored 1:70 scale model of the UMaine VoltturnUS-S semi-submersible platform. This set-up has been experimentally tested in the COAST Laboratory Ocean Basin at the University of Plymouth, UK. The test cases under consideration are (i) static equilibrium load cases, (ii) free decay tests and (iii) two focused wave cases with different wave steepness. The FOWT is modelled using a two-phase Navier-Stokes solver inside the OpenFOAM-v2006 framework. The catenary mooring is computed by dynamically solving the equations of motion for an elastic cable using the MoodyCore solver. The results of the static and decay tests are compared to the experimental values with only minor differences in motions and mooring forces. The focused wave cases are also shown to be in good agreement with measurements. The use of a one-way fluid-mooring coupling results in slightly higher mooring forces, but does not influence the motion response of the FOWT significantly.

KEY WORDS: Floating offshore wind turbine; mooring; computational fluid dynamics.

INTRODUCTION

Offshore wind is a rapidly expanding industry. In 2019, 146 offshore wind farms with a total of 27.2 GW installed power were in operation globally (WFO 2020). Specifically, floating offshore wind turbines (FOWTs) have entered the commercialization phase. Outside Scotland the 30 MW Hywind farm has been in operation since 2017 using a spar-type design. The 27 MW Windfloat Atlantic was commissioned in 2020 18 km of the Portuguese coast, and the 50MW Kincardine floating offshore wind farm became operational in 2021 in Scottish waters. Both of the latter projects use Principle Power's Windfloat semi-submersible. Still, many new concepts of FOWT are under development, and, in addition, the ever growing turbine size is putting new demands on the floaters.

Numerical modelling of FOWT are typically done with aero-elasto-control-hydro-mooring software, e.g., OpenFAST (OpenFast 2023) and DeepLines Wind (Principia 2023). Focusing on the hydrodynamic modelling these models are based on standard linear potential flow (LPF) assumptions and approximations. The mooring modelling is usually of dynamic type using lumped masses or finite element methods. Models based on LPF are computationally efficient but loose accuracy for survival cases with highly nonlinear waves. Additionally, within the OC5 projects problems relating to low-frequency response were identified when using LPF models, see Wang et al. (2021). High-fidelity models overcome the above problems, but the computational cost is quite high.

Blade resolved high-fidelity modelling of FOWTs have been presented by, e.g., Liu et al. (2017) and Zhou et al. (2022). These are very complete simulations but with a very high computational cost. Often the aerodynamic part is simplified using actuator disc or lines approaches, e.g., Cheng et al. (2019) and Yu et al. (2023).

Focusing specifically on the hydrodynamic part of the floater, Burmester et al. (2020) performed extensive verification and validation (V&V). Also Wang et al. (2021) looked into V&V of the hydrodynamic performance of FOWT. As expected, they found that mesh resolution is the limiting factor for the numerical uncertainty. Looking at the hydro-mooring coupling, Burmester et al. (2020) showed that the inertia and drag of the mooring lines could have an influence on the uncertainty of the overall motion response. Typically, the inertia and drag are found from either quiescent fluid or from a linear super-positioning of regular waves. With regard to the mooring a one-way coupling – to use the fluid velocities sampled in the CFD domain at the mooring nodes and used to compute added mass and drag forces acting on the cables – have been developed in a few studies (de Lataillade 2019, Martin & Bihs 2021, Eskilsson & Palm 2022).

In this paper we model the motion response, due to hydrodynamic loading only, of a slack-moored FOWT using CFD and dynamic mooring. In Eskilsson and Palm (2022) the DeepCwind semi-submersible

(Robertson et al. 2017) was modelled using a one-way fluid-mooring coupling. Virtually no influence of using the real fluid velocity compared to a quiescent fluid was seen in the mooring loads. However, the case investigated in Eskilsson and Palm (2022) was a mild regular wave. In the present work we investigate the effect of including fluid-mooring coupling for a harsh survival condition simulation, realised by focused waves.

NUMERICAL MODELS

Reynolds-Averaged Navier-Stokes equations

We solve the wave-structure interaction problem using the Reynolds Averaged Navier-Stokes equations with air-water interface capturing using the volume of fluid method (VOF-RANS). The numerical model used is the *interFoam* model, which is part of the widely used open-source framework *OpenFOAM* (OpenFOAM 2020, Weller et al. 1998). The 2006 version is employed in this study. *OpenFOAM* is based on a cell-centred 2nd order finite volume method on unstructured polyhedral cells. The standard *k- ω* -SST model (Menter et al. 2003) is used throughout this paper as turbulence model, together with a continuous wall function approach.

Wave generation/absorption is in the present work carried out by means of relaxation zones (Jacobsen et al. 2012).

Mooring

The VOF-RANS model is coupled to a dynamic mooring solver – *moodyCore* (Palm et al. 2017, Palm and Eskilsson 2018). *moodyCore* solves the elastic cable equation – including bending but disregarding torsion – using a high-order discontinuous Galerkin method. *moodyCore* can be coupled to *interFoam* using a quadratic interpolation to account for the difference in time steps size between the CFD and mooring solver (Palm et al. 2016). The cable fairleads are attached to the FOWT using the *externalPoint* boundary condition – meaning that the 3DoF positions of the attachment points are directly transferred from the CFD model to the mooring solver and that *moodyCore* returns the forces in global coordinate system at the attachment points. The *moodyCore* library and the mooring restraint as implemented in *OpenFOAM* can be downloaded from github.com/johannep/moodyAPI.

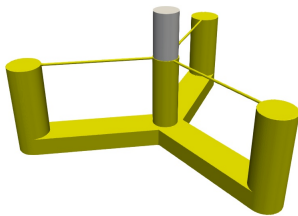


Fig. 1 3D view of the FOWT.

FOWT CASE

The FOWT under consideration is a slack-moored 1:70 scale model of the UMaine VoltturnUS-S semi-submersible platform (Allen et al. 2020). The FOWT is made up of three outer cylinders (diameter 0.1778 m and height 0.5 m) and a central cylinder (diameter 0.143 m and height 0.5 m). The outer cylinders are equiangularly spaced in a distance of 0.7393 m to the center of the central cylinder. The outer and central cylinders are connected by pontoons (width 0.1778 m and height 0.100 m) at the bottom of the cylinders, as well as with braces (diameter 0.013 m) at the top of the cylinders. A tower (diameter 0.13592 m and height 1.851 m) is mounted atop the central column. Attached to the tower is a simplified nacelle-rotor with a hub height of 2.476 m from the bottom of the cylinders. See Fig. 1.

The FOWT has been experimentally tested in the COAST Laboratory Ocean Basin at the University of Plymouth, UK (Ransley et al. 2022). All experimental data used in this work are found in Ransley et al. (2022). We define the origin of the global coordinate system to be located at the still water level free surface at the middle of the central

Table 1 Environmental parameters. * denotes that the coefficient is given as ratio of critical damping.

| | |
|-----------------------------|-------------------------|
| Water density | 998.2 kg/m ³ |
| Ground stiffness | 3.0E05 Pa/m |
| Ground damping coefficient* | 1.0 |
| Ground friction coefficient | 0.3 |

Table 2 Properties of the FOWT (in body coordinate system with origin at the bottom of and in the middle of the centre column).

| | |
|-------------------------------------|-----------------------------------------|
| Mass | 56.3 kg |
| Moments of inertia (Mol) | (26.68, 26.68, 14.18) kg m ² |
| Center of mass (CoM) | (-0.00477, 0.0, 0.26369) m |
| Fairlead position - fore | (-0.8392, 0.0, 0.08571) m |
| Fairlead position - aft-port | (0.4196, -0.7268, 0.08571) m |
| Fairlead position - aft-starboard | (0.4196, 0.7268, 0.08571) m |
| Offset to unmoored equilibrium pos. | (0, 0, -0.26495) m |
| Rotation around unmoored CoM | (0.0, -1.728 0.0)° |
| Offset to moored equilibrium pos. | (-0.01561, 0, -0.28755) m |
| Rotation around moored CoM | (0.0, -1.502 0.0)° |

Table 3 Properties of the mooring system (assuming a global coordinate system with origin at the free surface in the centre column). * denotes values based on the nominal diameter.

| | |
|--------------------------------------|--------------------------|
| Dry mass per meter | 0.144 kg/m |
| Axial stiffness | 1.0E04 kgNs |
| Density | 7850 kg/m ³ |
| Drag coefficient* | 1.5 |
| Added mass coefficient* | 1.0 |
| Anchor position - fore line | (-9.525, 0, -2.86) m |
| Cable length - fore line | 9.685 m |
| Anchor position - aft-port line | (4.412, -7.655, -2.86) m |
| Cable length - aft-port | 9.017 m |
| Anchor position - aft-starboard line | (4.412, 7.655, -2.86) m |
| Cable length - aft-starboard line | 9.017 m |

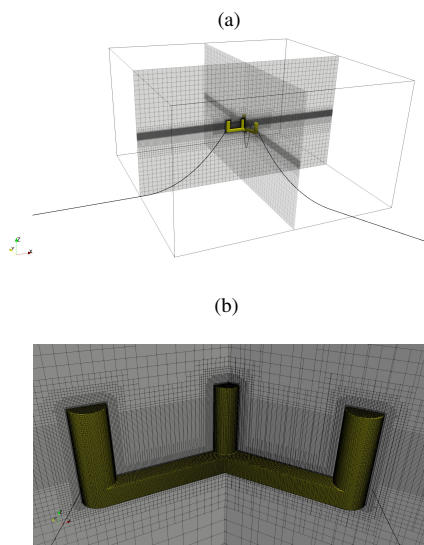


Fig. 2 CFD mesh for the decay cases. (a) global mesh layout, and (b) zoom in on the FOWT structure.

column of the FOWT. The physical wave basin has the dimensions $x \in [-17.3, 17.7]$ m and $y \in [-7.75, 7.75]$ m with a still water depth of 2.86 m. The wave paddles are located at $x = -17.3$ m and there is an absorbing beach starting downstream of the FOWT at $x = 4.5$ m.

The specific parameters for the case are presented in Tables 1–3. Please note that (i) the stiffness and hydrodynamic coefficients for the mooring chain have not been experimentally determined but are taken as standard values (DNV 2010), and (ii) the fore and aft mooring lines were not of equal length in the experiments due to the constraints of the wave basin side walls.

NUMERICAL SET-UP

The computational mesh is created using the `snappyHexMesh` utility in `OpenFOAM`, which creates oct-tree hexahedral dominated meshes from STL surfaces of the body. For the decay tests the computational domain is $x \in [-5, 5]$, $y \in [-5, 5]$, $z \in [-2.86, 2.86]$ m, with 1 m wide sponge zones applied along the outer boundaries. The computational mesh is a full 3D domain made up from 4.2M cells, see Fig. 2. There are refinement zones at the free surface as well as around the FOWT. We disregard the bracing and the tower in the simulations, but keep their inertial contributions. The maximum y^+ values for the FOWT are less than 300 throughout all simulations. For the focused wave cases the computational domain is $x \in [-15, 15]$, $y \in [-5, 5]$, $z \in [-2.86, 2.86]$ m, with 10 m wide sponge zones applied at the upstream and downstream boundaries, yielding a cell count of 27.4M. The mesh resolution is based on 20 cells per wave height and 200 cells per wavelength (based on an equivalent regular wave for the focused wave cases).

All outer side boundaries are treated as walls with slip condition applied. Also the bottom boundary is treated as a slip wall. The upper atmospheric boundary is set to a zero total pressure condition. The numerical schemes used in `interFoam` are second-order van Leer scheme for convection terms, second-order central differences for diffusion terms, while the turbulence equations are solved using the first-order upwind method. The time-stepping is carried out using the first-order backward Euler scheme with a CFL number of 0.5.

The mesh morphing algorithm used for the moving mesh employs a spherical linear interpolation (SLERP) approach (Shoemake 1985). In the present work we use the modified mesh morphing algorithm presented in Palm and Eskilsson (2022). The modified approach decouples the rotational and translation degrees of freedom of the mesh morphing, yielding a more stable mesh morphing for large motions.

The mooring cables are discretized into 20 finite elements of 5:th order and `moodyCore` uses an explicit 3:rd order Runge-Kutta scheme with a CFL number of 0.5 to integrate in time. We did an initial test also with 10 elements for the decay tests presented below, with no visible difference between the simulations. Indeed, with 20 elements we expect a somewhat over-resolved mooring solution, since as a rule of thumb 10 5:th order elements give good results for catenary mooring when no snap loads occur. As seen in Fig. 2, the mooring lines extends outside the CFD domain. Please note that the hydrodynamic loads applied to the mooring lines outside the CFD domain assume quiescent flow.

RESULTS AND DISCUSSION

Mooring forces using measured positions

We start by examining the tensions in the cables of the mooring system defined above by running `moodyCore` as a stand-alone mooring solver. The time-series of the fairlead positions are obtained from the measured CoM and rotations using the `externalRigidBody` boundary condition in `moodyCore` (Palm & Eskilsson 2018). This exercise gives baseline results, helping out to judge the mooring results obtained later, as the mooring system definition is somewhat uncertain. However, please note that we have not used this exercise to alter the mooring system to provide a better fit to the experimental data.

Static case. Running the mooring solver with fixed fairlead positions, using a CoM of $(-0.0204, 0, -0.0239)$ m and a pitch angle of -1.502° , the simulated tensions are 7.22 and 7.39 N in the fore cable and aft cables, respectively. This differs from the recorded tensions of 7.6 and 7.2 N. It is a bit concerning that we get lower tension in the fore line compared to the aft lines, while the measurements show the reverse. Nevertheless, the tensions are in the same order of magnitude. Considering the difficulty in getting accuracy tension readings for scaled devices, and the incomplete data for the mooring system, we are content with this result.

Decay cases. The simulated and experimental mooring tensions for the surge, heave and pitch decay tests are presented in Fig. 3. Generally, the comparisons are favorable. The tension in the fore cable is under-estimated throughout the simulations, the offset originates from the initial tension. There is a good fit for the aft lines.

Focused wave cases. Figure 4 shows the comparison between numerical experimental tensions for the two focused wave cases. As for the decay cases we see that the fore cable tensions capture the dynamics but have an offset throughout the simulations. The aft lines have a smaller tension

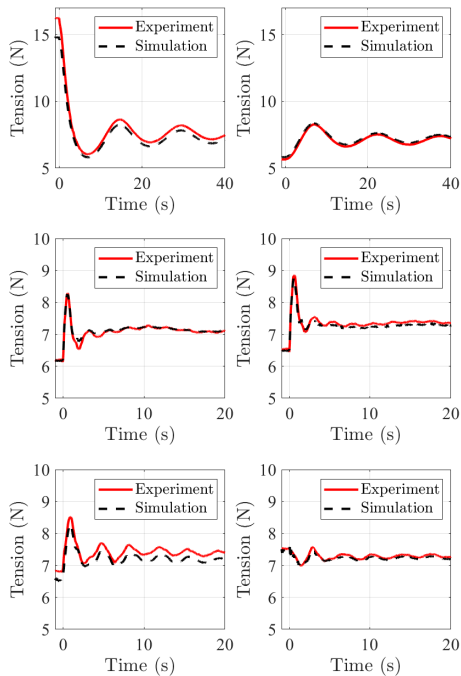


Fig. 3 Tension history for the decay tests using measured CoM. Left column: fore line, and right column: aft lines. Top row: surge decay test, middle row: heave decay test, and bottom row: pitch decay test.

amplitudes and a good fit.

Static equilibrium tests

In order to more rapidly achieve the static equilibrium positions we added damping terms in both the translation and rotational DoF (using damping coefficients of 10 Nm/s and 10 Nms/rad, respectively).

Unmoored case. We start the simulation from the given CoM of (0.0048, 0, -0.0013) m and a pitch angle of -1.728° . After 60 s of simulation time the FOWT is settled on an equilibrium position given by a CoM of (0.0051, 0.0000, 0.0019) m and a pitch angle of -1.464° . The surge position is of course arbitrary and due to initial transients of the surge-pitch coupling. The differences in heave (+0.0031 m) and pitch (0.264°) are deemed small and acceptable.

Moored case. Running moodyCore as a stand-alone mooring solver with the provided static fairlead positions in the previous section, we saw that we got a resulting mooring force of 1.2 N in the surge direction. We thus expect the FOWT to surge a bit until it finds equilibrium, but we nevertheless start from the provided data: CoM at (-0.0204, 0, -0.0239) m and a pitch angle of -1.502° . After 60 s of simulation time the FOWT is settled on an equilibrium position given by

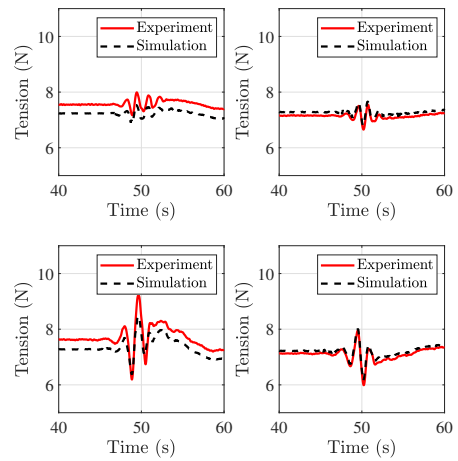


Fig. 4 Tension history for the focused wave tests using measured CoM. Left column: fore line, and right column: aft lines. Top row: benign wave case, and bottom row: harsh wave case.

a CoM of (-0.0128, 0.0000, -0.0188) m and a pitch angle of -1.341° . The differences to the experimental values are: +0.0076 m in surge, +0.0051 m in heave, and $+0.161^\circ$ in pitch.

The resulting tension forces are found to be 7.30 N for the fore cable and 7.34 N for the aft cables. This, again, differs from the measured data, but is smaller than the difference from the fixed fairleads case. The smaller difference is in line with a smaller pitch angle. In all we judge the results to be within the experimental uncertainty.

Moored decay tests

For the decay tests we use the equilibrium position from the previous section as starting position and then apply the offsets for surge, heave and pitch as given in Table 4. Please note that the figures presented below show results from the offsets applied to the equilibrium position recorded in the moored static equilibrium case. Minor discrepancies to the experimental values are thus to be expected.

Surge decay. Figure 5 show the computed surge, heave and pitch motions as well as the tensions in the mooring cables compared to measurements for the surge decay test. Generally, the fit is good. The most notable difference is that the surge amplitude is slightly over-predicted in the simulation compared to the experiment. The offset in heave is as expected from the static condition test. The initial tension

Table 4 Decay tests offset.

| Case | Offset in surge | Offset in heave | Offset in pitch |
|-------------|-----------------|-----------------|-----------------|
| Surge decay | 0.3517m | -0.0012m | -0.7662° |
| Heave decay | -0.0149m | -0.1473m | 0.471° |
| Pitch decay | -0.0031m | -0.0269m | -9.7508° |

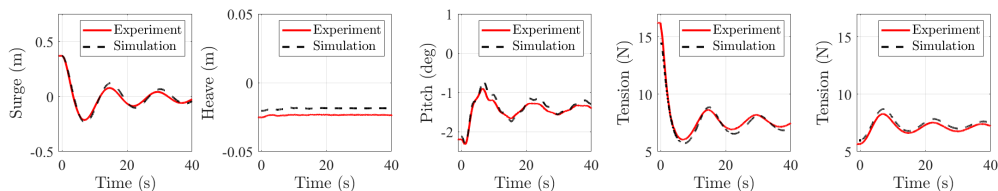


Fig. 5 Surge decay test. From left to right the sub-figures show: surge, heave, pitch, tension fore cable and tension aft cables.

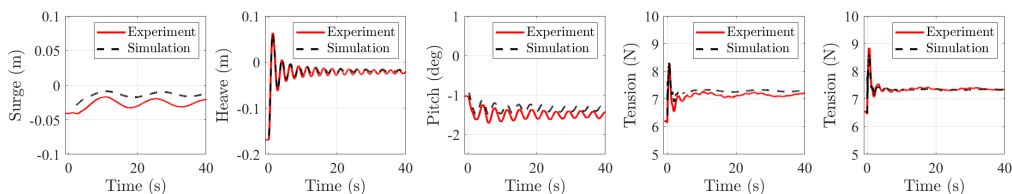


Fig. 6 Heave decay test. From left to right the sub-figures show: surge, heave, pitch, tension fore cable and tension aft cables.

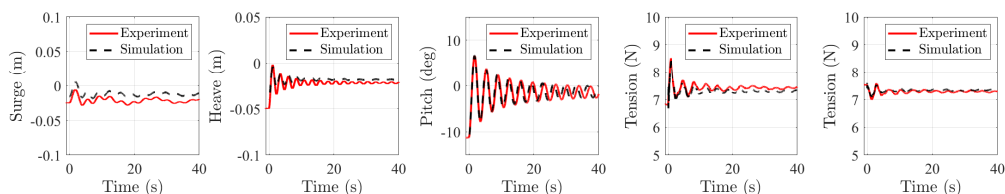


Fig. 7 Pitch decay test. From left to right the sub-figures show: surge, heave, pitch, tension fore cable and tension aft cables.

in the fore cable is slightly under-predicted by the simulation, and subsequently slightly over-predicted for the aft lines.

Heave decay. The simulated surge, heave and pitch motions as well as the tensions in the mooring cables compared to measurements for the surge decay test are presented in Fig. 6. The heave response is very well captured in both amplitude and phase. There is a positive offset in the surge response, causing a slightly larger tension in the fore line.

Pitch decay. Computed and measured surge, heave and pitch motions and mooring line tensions for the pitch decay test are illustrated in Fig. 7. While the simulated pitch amplitude is excellent the pitch period is slightly too small. There are minor positive offsets for the surge and heave response, as expected from the static equilibrium test.

The numerical and experimental data of the decay tests are summarized in Table 5 in terms of decay periods and exponential decay constants. We present only the main mode of motion for each case, e.g. for the surge decay test we present the surge decay period and surge decay constant. The values are computed using the first five oscillations. The decay periods are quite accurately computed, the error ranges between 0.8 to 2.5%. The decay constants show slightly larger errors, in the range of 0.7 to 7.2% error, where it is heave that exhibits the largest error. Please note that all restoring stiffness in surge is due to the mooring system. The ex-

cellent match in surge natural frequency therefore demonstrates that the mooring-coupling does provide accurate low-frequency mooring forces to the FOWT.

Focused wave tests

Two focused wave cases are simulated, one benign state and one harsh state. The focused waves are generated using linear dispersive focusing described by the NewWave theory (Tromans et al. 1991) based on a Pierson-Moskowitz spectrum. The crest amplitude is estimated as $A_{cr} = \sqrt{2H_{m0} \ln(1000)}$, where H_{m0} is the significant wave height. The focus location is $x = 0$ m (in global coordinates) and the focus time is

Table 5 Decay periods and exponential decay constants for the different decay tests.

| Case | Mode | Period (s) | Constant (-) |
|------------|-------|------------|--------------|
| Exp. surge | surge | 14.92 | 7.91E-02 |
| Num. surge | surge | 15.28 | 7.85E-02 |
| Exp. heave | heave | 2.50 | 0.56 |
| Num. heave | heave | 2.52 | 0.52 |
| Exp. pitch | pitch | 3.59 | 2.13E-01 |
| Num. pitch | pitch | 3.50 | 2.14E-01 |

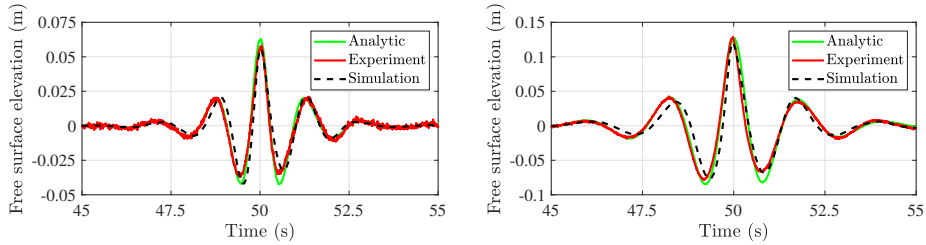


Fig. 8 Free surface elevation at WG6 ($x = 0$ m). Left: benign case, and right: harsh case.

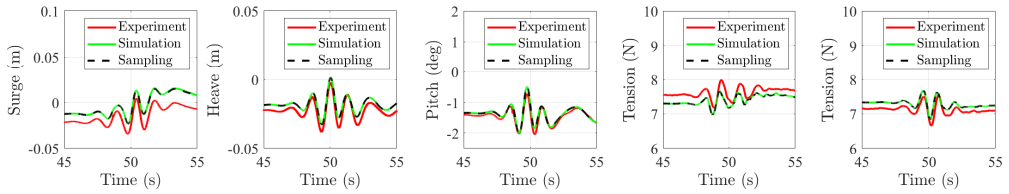


Fig. 9 Benign focused wave test. From left to right the sub-figures show: surge, heave, pitch, tension fore cable and tension aft cables. 'Sampling' denotes simulation using the one-way fluid-mooring coupling.

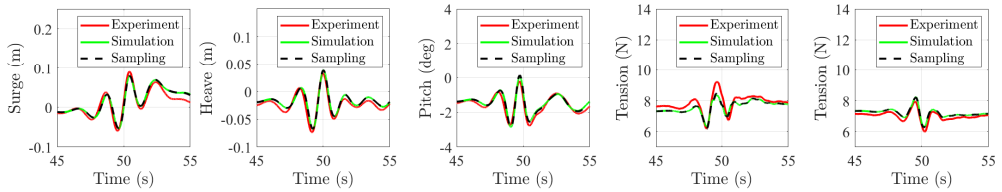


Fig. 10 Harsh focused wave test. From left to right the sub-figures show: surge, heave, pitch, tension fore cable and tension aft cables. 'Sampling' denotes simulation using the one-way fluid-mooring coupling.

$t = 50$ s. The wave parameters for the two cases are presented in Table 6. As the experimental tests employed 112 equidistant wave components in the frequency range $f \in [0.15, 2]$ Hz, we used the *waves2Foam* utility (Jacobsen et al. 2012) to generate 112 equidistant wave components in the same range for the numerical simulations.

The focused wave cases were each simulated using 8 compute nodes at the Tetralith HPC cluster at the National Supercomputer Centre, Linköping University, Sweden. Each compute node consists of two Intel Xeon Gold 6130 CPUs with 16 CPU cores each, giving that the focused wave simulations were run using 256 cores.

Wave propagation. We first compare the simulated free surface elevation for empty tank tests. In the simulations we use a shorter wave basin and we thus only look at the surface elevation recorded at the centred wave gauge (WG6) located at $x = 0$ m. Figure 8 shows the recorded experimental and numerical free surface elevation, as well as the analytical elevation obtained by linear superposition. We see that for both cases the peaks are fairly well predicted both in amplitude and phase. The simulated troughs preceding the peak are lagging in time,

while the following troughs have a better fit with the experimental data. Comparing to the experiments the linear expression predicts a symmetric distribution around the peaks, while both the experimental and numerical records show a deeper preceding trough and a shallower following trough. The difference between the measured and simulated wave elevation is due to a slightly too low resolution in the x -direction, but in order to keep down the cell count we do not further refine the mesh.

Benign case. Figure 9 shows the results for the benign wave case. We see that there is virtually no difference in the simulated results when

Table 6 NewWave parameters using the Pierson- Moskowitz wave spectrum.

| Parameter | Benign case | Harsh case |
|--------------------------------------|-------------|------------|
| Peak period (T_p) | 1.3831 s | 1.9380 s |
| Significant wave height (H_{m0}) | 0.069 m | 0.139 m |
| Crest elevation (A_{cr}) | 0.064 m | 0.127 m |

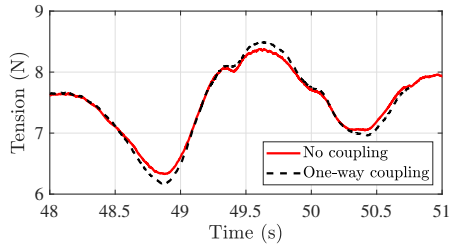


Fig. 11 Tension at the fairlead in the fore cable for the harsh focused wave case.

using the one-way coupling. This is in line with previous experience for cases of rather linear nature. From Fig. 9 we see that the dynamics of the response of the FOWT is in general well captured. The major differences are again the offsets in surge and heave, as well as in the tension.

Harsh case. Like in the benign case the harsh wave case does not show a clear influence of using the one-way coupling, see Fig. 10. However, looking closer on the mooring cables, see Fig. 11, we see that the tension in the fore cable is clearly larger when the coupling is used. However, this difference is not carried over to the motion response. The most obvious difference is that the maximum recorded pitch angle increases with 0.1° , from 0.05° to 0.15° . It is believed that the influence on the response of using the one-way coupling would be more pronounced for an embedded focused wave.

The simulated responses shown in Fig. 10 have good fit to the measured data. Please note that the offsets in surge and heave are similar to the benign case, but are cloaked by the larger responses. The simulated tensions look a lot like the results using the measured fairlead positions (see Fig. 4).

Table 7 shows a comparison of the motion responses between the experiments and simulations in terms of maximum and minimum motions during the impact of the focused waves, i.e. $t \in [48, 52]$ s. We focus on the motion range, simply defined as (max – min), as we then remove the influence of any initial offsets. The largest errors are found

Table 7 Recorded extreme motions for the focused wave cases when $t \in [48, 52]$ s.

| Case | Mode | Max | Min | Max-Min |
|-------------|--------------------|-----------|------------|------------|
| Exp. benign | surge (m) | 4.37E-03 | -34.45E-03 | 38.83E-03 |
| Num. benign | surge (m) | 15.40E-03 | -22.98E-03 | 38.38E-03 |
| Exp. benign | heave (m) | -2.10E-03 | -38.40E-03 | 36.30E-03 |
| Num. benign | heave (m) | 1.35E-03 | -32.77E-03 | 34.13E-03 |
| Exp. benign | pitch ($^\circ$) | -0.72 | -2.05 | 1.33 |
| Num. benign | pitch ($^\circ$) | -0.49 | -2.03 | 1.54 |
| Exp. harsh | surge (m) | 90.31E-03 | -59.43E-03 | 149.74E-03 |
| Num. harsh | surge (m) | 79.11E-03 | -53.56E-03 | 132.67E-03 |
| Exp. harsh | heave (m) | 32.70E-03 | -73E-03 | 106.42E-03 |
| Num. harsh | heave (m) | 38.45E-03 | -67.47E-03 | 105.92E-03 |
| Exp. harsh | pitch ($^\circ$) | -0.21 | -2.78 | 2.56 |
| Num. harsh | pitch ($^\circ$) | 0.64 | -2.86 | 2.92 |

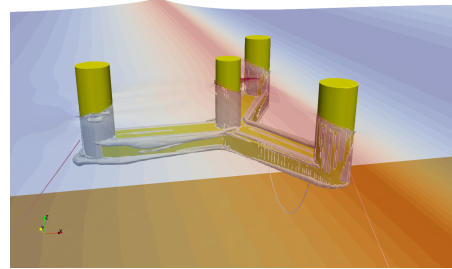


Fig. 12 Snapshot of the FOWT at $t = 50$ s for the harsh focused wave case. The contour show the $Q = 10$ iso-surface.

in the pitch response with 15.5 and 14.1 % error for the benign and harsh cases, respectively. The surge response in the harsh wave show a 11.4 % error, to be compared to only 1.1 % for the benign case, even though the benign case has a larger offset error. The heave response show the smallest error: 5.8 % error for the benign case and 0.5 % for the harsh focused wave.

Figure 12 presents a snapshot of the FOWT at the focus time ($t = 50$ s). We see that the FOWT is rather stable, the pitch angle is small and there is not much vorticity generated. The wave run-up on the central column has not reached the position of the braces, so the omission of the braces and tower in the simulation will not induce any significant errors.

Setting $t \in [30, 100]$ s, we find the computational times for the harsh focused wave case to be 21.1 and 25.3 k CPU hours for using no fluid-mooring coupling and the one-way fluid mooring coupling, respectively. We thus see a 20 % computational overhead from the one-way coupling. This is arguably a high value, however, the implementation uses a simplistic cell-stepping algorithm to locate cells with individual mooring points. A significant speedup is expected when a more efficient cell-search algorithm is implemented.

CONCLUSIONS

A 1:70 scale model of the slack-moored UMaine VoltumUS-S semi-submersible platform was modelled using the incompressible two-phase Navier-Stokes code in the OpenFoam framework coupled to the dynamic mooring solver moodyCore. As the mooring system was a bit undetermined in the experimental campaign, initially the mooring set-up was tested using measured locations of the fairleads. We saw that the numerical simulation using static fairleads did not give as large difference between fore and aft lines as the experiments. Both the decay as focused wave cases showed a good capture of the dynamics but with constant offsets – overall the tension in the fore line is under-predicted by the numerics.

The difference in mooring forces subsequently led to slightly different equilibrium position compared to the experiment. However, the differences are relatively minor, less than a centimeter in translation and 2/10:th of a degree in rotation.

The numerical decay tests showed a good overall agreement to the experiments. The surge amplitude was slightly over-predicted and the pitch period slightly too small, but generally a very satisfactory

comparison to the experiments was found.

Also the focused wave cases showed good overall agreement. The main reason for the discrepancy is likely due to difference in equilibrium position. Also the reduced length of the wave basin introduces a phase error for the preceding trough, as apparent from the empty wave tank tests.

Finally, while we saw that the mooring forces became larger using the fluid-mooring coupling, there was only very minor effect on the motion response of the FOWT. This is likely due to the rather short duration of the focused wave. For an embedded focused wave we expect the one-way coupling to give more accurate results. Unfortunately, the one-way coupling carries a significant computational overhead in its present form. The algorithm of finding the cell to sample for each mooring node is a computational bottleneck, and a significant speedup is expected when an improved method is implemented. This is ongoing work.

ACKNOWLEDGEMENTS

Support for this work was given by the Swedish Energy Agency through Grant No. 44423-2 and EU Horizon through the MSCA-PF Grant No. 101068736. Computations were performed on resources at (i) the National Supercomputer Centre provided by SNIC, partially funded by the Swedish Research Council through Grant Agreement No. 2018-05973; and (ii) LUMI through DeiC National HPC Grant Agreement No. DeiC-AAU-N3-2023017.

REFERENCES

- Allen, C., A. Viscelli, H. Dagher, A. Goupee, E. Gaertner, N. Abbas, M. Hall, & G. Barter (2020). Definition of the UMaine VoltturnUS-S reference platform developed for the IEA wind 15-megawatt offshore reference wind turbine. <https://www.osti.gov/biblio/1660012>.
- Burmester, S., G. Vaz, & O. el Moutar (2020). Towards credible CFD simulations for floating offshore wind turbines. *Ocean Engineering* 209, 107237.
- Burmester, S., G. Vaz, O. el Moutar, S. Gueydon, A. Koop, Y. Wang, & H. Chen (2020). High-fidelity modelling of floating offshore wind turbine platforms. In *Proceedings of the 39th International Conference on Ocean, Offshore & Arctic Engineering*.
- Cheng, P., Y. Huang, & D. Wan (2019). A numerical model for fully coupled aero-hydrodynamic analysis of floating offshore wind turbine. *Ocean Engineering* 173, 183–196.
- de Lataillade, T. (2019). *High-Fidelity Computational Modelling of Fluid–Structure Interaction for Moored Floating Bodies*. Ph. D. thesis, University of Edinburgh.
- DNV (2010). *Position Mooring*. Det Norske Veritas. Offshore standard DNV-OS-301.
- Eskilsson, C. & J. Palm (2022). High-fidelity modelling of moored marine structures: multi-component simulations and fluid-mooring coupling. *Journal of Ocean Engineering and Marine Energy* 8(4), 513–526.
- Jacobsen, N., D. Fuhrman, & J. Fredsoe (2012). A wave generation toolbox for the open-source CFD-library OpenFOAM. *Int. J. Num. Meth. Fluids* 70, 1073–1088.
- Liu, Y., Q. Xiao, A. Incecik, C. Peyrard, & D. Wan (2017). Establishing a fully coupled CFD analysis tool for floating offshore wind turbines. *Renewable Energy* 112, 280–301.
- Martin, T. & H. Bihs (2021). A numerical solution for modelling mooring dynamics, including bending and shearing effects, using a geometrically exact beam model. *J. Mar. Sci. Eng.* 9, 486.
- Menter, F., M. Kuntz, & R. Langtry (2003). Ten years of industrial experience with the SST turbulence model. In *Proceedings of the fourth International Symposium on Turbulence, Heat and Mass Transfer*, Antalya, Turkey, pp. 625–632. Begell House.
- OpenFast (2023). <https://github.com/openfast/openfast>.
- OpenFOAM (2020). <http://www.openfoam.com>.
- Palm, J. & C. Eskilsson (2018). *MOODY: User's manual version 2.0*. Available www.github.com/johannep/moodyAPI/releases.
- Palm, J. & C. Eskilsson (2022). Facilitating large-amplitude motions of wave energy converters in OpenFOAM by a modified mesh morphing approach. *International Marine Energy Journal* 5(3), 257–264.
- Palm, J., C. Eskilsson, & L. Bergdahl (2017). An hp-adaptive discontinuous Galerkin method for modelling snap loads in mooring cables. *Ocean Engineering* 144, 266–276.
- Palm, J., C. Eskilsson, G. M. Paredes, & L. Bergdahl (2016). Coupled mooring analysis for floating wave energy converters using CFD: Formulation and validation. *Int. J. Mar. Energy* 16, 83–99.
- Principia (2023). <http://www.principia-group.com/wp-content/uploads/2016/12/2-deeplines-wind-presentation.pdf>.
- Ransley, E., S. Brown, E. Edwards, T. Tosdevin, K. Monk, A. Reynolds, D. Greaves, & M. Hann (2022). Hydrodynamic response of a floating offshore wind turbine (1st fowt comparative study dataset). Pearl research repository <https://doi.org/10.24382/71j2-3385>.
- Robertson, A., F. Wendt, J. Jonkman, W. Popko, H. Dagher, S. Gueydon, Q. J., F. Vittori, E. Uzunogulo, & R. Harries (2017). OC5 project phase II: Validation of global loads of the DeepCwind floating semisubmersible wind turbine. *Energy Procedia* 137, 38–57.
- Shoemake, K. (1985). Animating rotation with quaternion curves. In *Special Interest Group on Computer Graphics and Interactive Techniques*, Volume 19. San Francisco, USA.
- Tromans, P., A. Anaturk, & A. Hagemeijer (1991). A new model for the kinematics of large ocean waves-application as a design wave. In *Proceedings from the 1st International Offshore and Polar Engineering Conference (ISOPE)*, Edinburgh, UK, pp. 64–71.
- Wang, L., A. Robertson, J. Jonkman, & Y. Yu (2021). Uncertainty assessment of CFD investigation of the nonlinear difference-frequency wave loads on a semisubmersible FOWT platform. *Sustainability* 13(64).
- Weller, H., G. Tabor, H. Jasak, & C. Fureby (1998). A tensorial approach to computational continuum mechanics using object-oriented techniques. *Computers in Physics* 12(6), 620–631.
- WFO (2020). Global offshore wind report 2019. Technical report, World Forum Offshore Wind.
- Yu, Z., Q. Ma, X. Zheng, K. Liao, H. Sun, & A. Khayyer (2023). A hybrid numerical model for simulating aero-elastic-hydro-mooring-wake dynamic responses of floating offshore wind turbine. *Ocean Engineering* 268, 113050.
- Zhou, Y., Q. Xiao, Y. Liu, A. Incecik, C. Peyrard, D. Wan, G. Pan, & S. Li (2022). Exploring inflow wind condition on floating offshore wind turbine aerodynamic characterisation and platform motion prediction using blade resolved CFD simulation. *Renewable Energy* 182, 1060–1079.

Paper E

Wave Excitation Tests on a Fixed Sphere: Comparison of Physical Wave Basin Setups

Jacob Andersen
Morten Bech Kramer

Accepted preprint submitted to the 15th European Wave and Tidal Energy
Conference (EWTEC), 2023, appended.

The paper has been published in:
Proceedings of the 15th European Wave and Tidal Energy Conference,
EWTEC, DOI: 10.36688/ewtec-2023-170, 2023.

Wave Excitation Tests on a Fixed Sphere: Comparison of Physical Wave Basin Setups

Jacob Andersen and Morten Bech Kramer

Abstract— Wave excitation tests on a fixed sphere with the center at the still water level were carried out with three different physical wave basin setups. The tests were completed as a continued effort of the working group OES Wave Energy Converters Modelling Verification and Validation to increase confidence in numerical models of wave energy converters by generation of accurate benchmarks datasets for numerical model validation. An idealized testcase with wave excitation of a fixed sphere to be used with the benchmarks was formulated. The three investigated physical wave basin setups included: 1) a six degree-of-freedom load cell mounted to the top of the sphere, 2) a bending beam force transducer mounted to the top of the sphere, and 3) a system of six pretensioned wires mounted to the top and bottom of the sphere with force transducers attached to each wire. The aim of the present paper is to identify the best representation of the idealized testcase. To this end, the three experimental setups are inter-compared in terms of dynamic properties, sensitivity, and disturbances of the water phase from the presence of measurement equipment. Low inter-experiment variability was disclosed, i.e., 5-8% depending on wave-nonlinearity, indicating accurate representations of the idealized testcase across all setups. Setup 3 was found to be the more accurate representation and further work with this setup to release a public benchmark dataset was planned.

Keywords— physical tests, benchmark dataset, sphere, wave excitation force, WEC, fluid–structure interaction.

I. INTRODUCTION

DESIGN of wave energy converters (WECs) relies on accurate numerical modelling of fluid-structure interaction problems. Prior to the practical usage of numerical models, validation exercises are critical to ensure proper accuracy of the numerical model in conditions representative of the intended model use. The uncertainty of the validation benchmark dictates the lower bound of uncertainty ascribed to the numerical model from validation and in the case of benchmarking of

numerical models from accuracy whether distinctions can be made with a given confidence level. Accordingly, low-uncertainty benchmarks are key in developing accurate numerical models which ultimately can drive lower design costs of WECs as less conservative design values can be attained.

Experiments dedicated to generating highly accurate benchmark datasets for numerical modelling of WECs were developed under the OES Wave Energy Converters Modelling Verification and Validation (formerly, OES

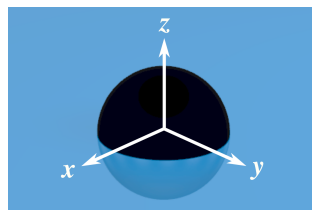


Fig. 1. Sphere under still water conditions with global Cartesian coordinate system (origin at sphere geometrical center).

Task 10) working group and published in [1] with heave decay tests on a floating sphere submerged to the equator. The dataset was showcased by benchmarking numerical models of various fidelity against it and the value of having low uncertainty bounds on the benchmarks was demonstrated. Resultantly, the OES working group decided to extent the work to comprise accurate benchmark datasets on wave excitation tests. To this end, physical wave basin tests were designed and carried out at the Ocean and Coastal Engineering Laboratory of Aalborg University, Denmark, and based on these an idealized testcase on wave excitation of a fixed sphere was formulated, see Section I-A. The idealized testcase is introduced to allow for simple, yet accurate, representation of the physical tests underlying the benchmark dataset in numerical models (as in [1]). Consequently, the physical parameters of the idealized testcase are derived from the physical tests. Idealized

Accepted preprint submitted to the 15th European Wave and Tidal Energy Conference (EWTEC), 3-7 September 2023, Bilbao.

This work was supported under the Danish Energy Technology Development and Demonstration Program (EUDP).

J. Andersen is with the Department of the Built Environment at Aalborg University, Thomas Manns Vej 23, 9220 Aalborg Ø, Denmark (e-mail: jacobaa@build.aau.dk).

M. B. Kramer is with the Department of the Built Environment at Aalborg University, Thomas Manns Vej 23, 9220 Aalborg Ø, Denmark (e-mail: mmk@build.aau.dk), and with Floating Power Plant at Park Allé 382, 2625 Vallengbæk, Denmark (e-mail: mk@floatingpowerplant.com).

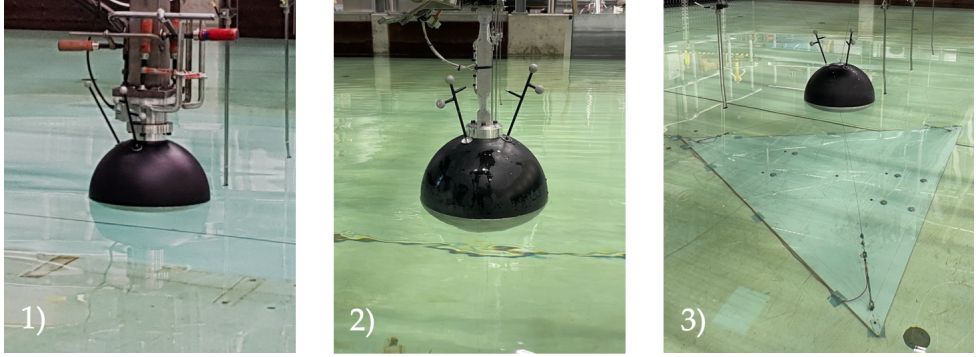


Fig. 2. Investigated experimental setups: 1) six-DoF load cell, 2) bending beam force transducer (2-DoF), and 3) system of six pretensioned wires with one-DoF force transducers.

assumptions are introduced to obtain a simple testcase intuitively adopted for validation exercises by others. The sphere tests are altogether completed as Phase V of the work by the OES working group and are referred to as the *Kramer Sphere Cases*.

A. The Idealized Testcase

Consider a rigid sphere of radius $r = 150$ mm fixed at the interface between an air and a water phase. A global Cartesian coordinate system is defined with the origin at the geometrical center of the sphere, the xy -plane at the still water level (SWL), and z positively oriented upwards, see Fig. 1. The air phase is unbounded whereas the water phase is bounded by a solid, horizontal bed at $z = -h$.

TABLE I
WAVE CONDITIONS

| Case | H (m) | T (s) | $H/(2r)$ (-) | η_{crest}/r (-) | η_{trough}/r (-) | H/L (%) |
|------|------------|------------|-----------------|-------------------------|--------------------------|--------------|
| R01 | 0.0181 | 1.14 | 0.06 | 0.06 | -0.06 | 0.9 |
| R02 | 0.0193 | 0.72 | 0.06 | 0.07 | -0.06 | 2.4 |
| R03 | 0.0182 | 0.51 | 0.06 | 0.06 | -0.06 | 4.4 |
| R04 | 0.0560 | 1.25 | 0.19 | 0.19 | -0.18 | 2.3 |
| R05 | 0.0561 | 0.88 | 0.19 | 0.20 | -0.17 | 4.5 |
| R06 | 0.0512 | 0.62 | 0.17 | 0.19 | -0.15 | 8.0 |
| R07 | 0.1496 | 2.65 | 0.50 | 0.57 | -0.43 | 2.1 |
| R08 | 0.1463 | 1.58 | 0.49 | 0.53 | -0.44 | 4.0 |
| R09 | 0.1534 | 1.08 | 0.51 | 0.58 | -0.44 | 7.9 |
| R10 | 0.2776 | 4.18 | 0.93 | 1.35 | -0.51 | 2.2 |
| R11 | 0.2459 | 2.28 | 0.82 | 0.98 | -0.66 | 4.0 |
| R12 | 0.2611 | 1.42 | 0.87 | 1.02 | -0.72 | 8.1 |

The sphere is subjected to long-crested, incident, regular waves propagating in positive x . 12 regular wave conditions (prefix R) of low to high nonlinearity are given in Table I where H and T denotes wave height and wave period, respectively. The wave steepness H/L and ratio of crest elevation to sphere radius η_{crest}/r as well as trough elevation to sphere radius η_{trough}/r are calculated by stream function theory as per [2]. Please note that the crest

elevations of the R10 and R12 waves are larger than r signifying large wave-overtopping effects in these conditions. $\rho_{water} = 998.2 \text{ kg/m}^3$ is the density of the water phase and $g = 9.82 \text{ m/s}^2$ is the acceleration due to gravity.

B. Scope of the Paper

Three physical wave basin setups were tested to investigate the most accurate representation of a sphere fixed with the center at SWL, i.e., without any support structure, as per the idealized testcase. The experimental setups were all aimed at high rigidity to mimic the fixation from the idealized testcase while maintaining good sensitivity and low disturbances of the force measurement equipment. The three experimental setups included 1) A traditional six degrees of freedom (six-DoF) load cell mounted to the top of the sphere, 2) A bending beam force transducer with two full Wheatstone bridges (two-DoF), 3) A system of six pretensioned wires with a one-DoF force transducer attached to each, see Fig. 2. All setups utilized the CNC machined physical sphere model from the decay tests in [1]. The focus points in the development of the setups were:

- *Rigidity*. Focus was to ensure a highly rigid support of the sphere in order to reduce the influence of dynamic amplification on the measured wave forces.
- *Sensitivity*. The force measurement equipment should have good sensitivity over the tested range of wave conditions.
- *Disturbances*. The influence of the presence of the measurement equipment on the measured wave forces on the sphere should be marginal.

The aim of the present paper is to assess the accuracy of the three experimental setups to represent the idealized testcase. Since no highly accurate benchmark of the testcase is available (the ultimate objective is exactly that) the assessment will be based on inter-experiment

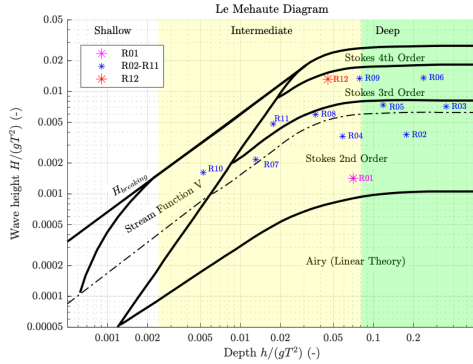


Fig. 3. Wave conditions (Table I) with boundaries from [3].

comparisons with emphasis on modal parameters (rigidity), deformation of the free surface around the sphere from video recordings (disturbances), and time series of the wave excitation force (disturbances, sensitivity). In the present paper the horizontal and vertical wave excitation forces F_x and F_z are considered, although F_x is the sole force measurement extracted in Setup 2. However, if Setup 2 turns out to be the more appropriate, the bending beam force transducer can be oriented to measure F_z in additional tests.

The regular wave conditions included in the idealized testcase Table I are visualized in Le Mehaute's diagram [3] in Fig. 3 where the wave conditions with the highest and lowest steepness are highlighted, i.e., R12 and R01, respectively. These two wave conditions are used as the basis for the assessment of the suitability of the experimental setups to represent the testcase due to brevity and as these constitute the upper and lower bounds of wave height and nonlinearity.

II. EXPERIMENTAL SETUPS

All experimental setups used the sphere model from the heave decay tests of [1], see Fig. 4. Two hemispheres were CNC machined out of aluminum blocks with an accuracy of 0.1 mm. As seen in Fig. 2 the model has two M8 threaded holes, one in the top and one in the bottom. The

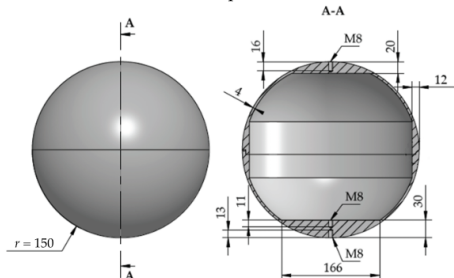


Fig. 4. Technical drawing of the sphere. Measurements in mm. Refer to [1] for further details.

two holes allows for attachment of force measurement equipment. The sphere model is described in detail in [1]. The tests were carried out at the wave basin in the Ocean and Coastal Engineering Laboratory of Aalborg University, Denmark. The wave basin was equipped with piston-type wavemakers and vertical passive absorption. The active area of the wave basin measured 8.44 m (mean piston position to passive absorption) times 13.00 m (between side walls) with the sphere installed at the center. Separate tests without the sphere model were carried out with a wave gauge installed at the position of the sphere model in order to align force time series to incident waves. Waves were generated by second order or approximate stream function wavemaker theory as per [4] and [5], respectively, in accordance with Fig. 3. Identical steering signals were used between tests of same wave condition. Reflective markers were mounted to the top of the sphere model to measure vibrations by an optical motion tracker system. Furthermore, three arrays of wave gauges were installed around the sphere. The motion tracker system and the wave gauge arrays were included for further analyses to be published with the benchmark datasets and are beyond the scope of the present paper.

C. Setup 1 (six-DoF load cell)

A six-DoF load cell, capable of measuring force/moment in three dimensions, was connected to the top of the sphere model via transition pieces in Setup 1, see Fig. 5. The lower transition piece was a solid steel cylinder of 900 mm in diameter with a convex spherical curvature at the bottom

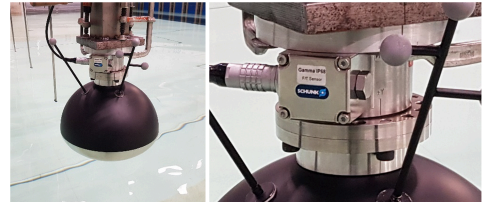


Fig. 5. Close-up of six-DoF load cell in Setup 1.

face of radius 150 mm (fitting the sphere surface) installed for proper load transfer from the sphere model. The upper transition pieces were two steel cylinders of 115 mm in diameter needed for assembly of the load cell. A steel beam mounted to the wave basin bridge was the support of the setup. The load cell was an ATI Industrial Automation Gamma IP68 SI-65-5 with a force measurement range on F_x of 65 N and a resolution of 1/80 N. A calibration certification was provided by the producer ATI declaring the uncertainty of the measured F_x with a semi-interval of 0.75% of the full-scale load, i.e., 0.49 N, at the 95% confidence level. However, tests with precision weights in a truss system to generate accurate F_x excitation indicated that the uncertainty was significantly (about an order of magnitude) lower for F_z at the (relatively low) load levels imposed with the testcase.

D. Setup 2 (bending beam force transducer)

A force transducer with two full Wheatstone bridges to measure bending about the y -axis was mounted through a transition piece to the top of the sphere, see Fig. 6. The internal moments about y at the two bridges were used to

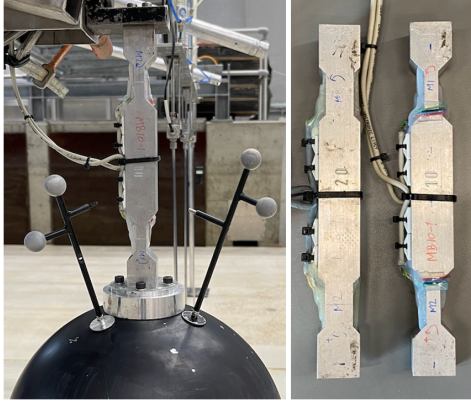


Fig. 6. Close-up of force transducer in Setup 2a (left) and force transducers from Setups 2a and 2b (right).

calculate the resulting force F_x (and its point of attack). Two force transducers were employed with thicknesses at the bridge positions of 10 mm and 20 mm (henceforth referred to as Setup 2a and 2b, respectively) to vary the stiffness of the transducers, see Fig. 6. The transition piece is identical to the lower transition piece of Setup 1, i.e., 900 mm in diameter. The force transducers were made of aluminum and had an inter-bridge distance of 150 mm. With a linear calibration function, the force transducers were calibrated against nine known moments from precision weights supported with different arms.

E. Setup 3 (system of pretensioned wires)

Six wires were pretensioned between the sphere model and two solid triangular steel plates of 10 mm thickness, see Fig. 7. The wires were attached to a M8 steel eyelet lowered into the sphere model at the top and bottom reducing the impact with overtopping waves. The plates

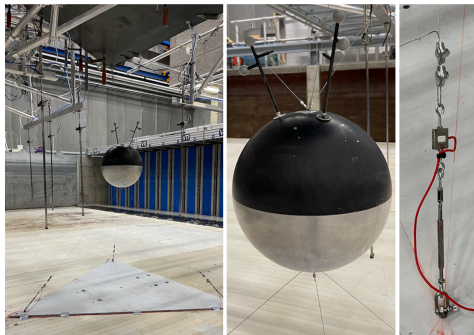


Fig. 7. Setup 3 with close-up of attachment of pretensioned wires (center) and one-DoF force transducer (right).

were clamped to the wave basin bridge or bolted to the bed, respectively. A one-DoF force transducer was assembled to each wire allowing the calculation of forces in three dimensions and moments about x and y given the direction vector of each wire. The direction vectors were derived from meticulous measurement of the coordinates of the fixation points on the sphere model and the triangular support plates. FUTEK LSB210 one-DoF force transducers were utilized which had a range of 450 N. The wires had a diameter of 1 mm and were pretensioned to about 300 N estimated to allow for the maximum tensions from the wave loads while not exceeding the range of the one-DoF force transducers. The one-DoF transducers were calibrated against known forces from precision weights with 10-point linear calibration over a range of 0 to 450 N.

III. DYNAMIC AMPLIFICATION

The modal parameters of the three setups were calculated from force decay time series after excitation of the sphere model with an impulse-like load, see example in Fig. 8. Calculation of modal parameters were limited to the damped eigenfrequency f_{ed} and damping ratio ζ in x in the present paper (stiffness in z of Setups 1 and 2 were very high). The modal parameters of the three setups were calculated with the software package WaveLab 3.877 [6] and are given in Table II.

Based on the modal parameters, corrections to the dynamic amplification were calculated under the assumption of a linear, one-DoF mass-spring-damper-system as per [7], yielding a dynamic amplification filter with gain (inverse dynamic amplification factor) and

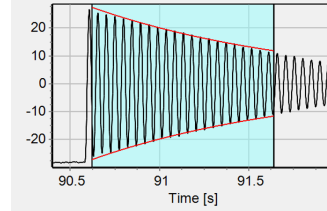


Fig. 8. Force decay time series from Setup 3 used for modal analysis with WaveLab [6]. The y-axis indicate force [N].

TABLE II
MODAL PARAMETERS AND COMPENSATION METRICS

| Setup | f_{ed} (Hz) | ζ (-) | $\beta_{C,R01}$ (%) | $\beta_{C,R12}$ (%) | $\beta_{FC,R01}$ (%) | $\beta_{FC,R12}$ (%) |
|-------|------------------|----------------|------------------------|------------------------|-------------------------|-------------------------|
| 1 | 20.0 | 0.026 | 10.9 | 5.7 | 688 | 142 |
| 2a | 7.4 | 0.009 | 2.8 | 12.7 | 181 | 322 |
| 2b | 12.9 | 0.007 | 1.5 | 5.4 | 100 | 136 |
| 3 | 20.9 | 0.006 | 2.2 | 3.9 | 152 | 100 |

phase (inverse phase) for the three setups as shown in Fig. 9. The gain should ideally be unity indicating no compensation is required. The frequencies of the wave conditions in the idealized testcase are in the range 0.24 to 1.96 Hz which yields gains of minimally 93% in Setup 2a and above 99% for the Setups 1, 2b, and 3 indicating only

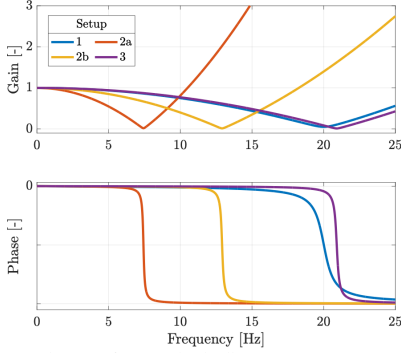


Fig. 9. Close-up of six-DoF load cell in Setup 1.

very little dynamic amplification from the main wave frequency for all setups but Setup 2a which may be questionable to use over the full range of wave conditions especially without compensation measures. The gain is close to zero around the respective eigenfrequencies which together with the damping ratios of Table II signify how the setups are lightly damped. This underlines the importance of having high eigenfrequencies relative to the wave frequencies to reduce inaccuracies from the compensation as much as possible.

The influence of the dynamic amplification filter on the force time series was quantified by a compensation metric β_c which is the standard deviation of the difference between the filtered and unfiltered force time series, i.e.,

$$\beta_c = \frac{\text{std}(F_{x,UF}(t) - F_{x,F}(t))}{\text{std}(F_{x,F}(t))} \quad (1)$$

where std is the standard deviation, t is time, and subscripts UF and F refer to the unfiltered and filtered signals, respectively. β_c was calculated for the three setups employing the dynamic amplification filter with a low-pass cut-off frequency of 25 Hz to the force time series of a

single wave (as extracted in Section V) in wave conditions $R01$ and $R12$, see Table II. β_c is introduced in Table II as the relative compensation metric with the lowest β_c value as reference. Examples of the influence of the dynamic amplification filtering on the measured force time series of the extracted single waves (as explained in Section V) with close-ups are shown for $R01$ and $R12$ in Fig. 10. Forces are normalized with the buoyancy of the sphere at initialization F_{B0} (stagnant water).

The dynamic amplification compensation by β_c , see (1), is in general lower in wave condition $R01$ relative to $R12$ where the larger wave heights and nonlinearity cause larger, more rapid impacts with the setups. The force time series of Setup 1 are compensated the most in $R01$, as also shown in Fig. 10. Despite the eigenfrequencies of Setups 1 and 3 being of approximately equal size, the compensation from dynamic amplification is increased 42% for Setup 1. This may be an effect of the slamming-like loads on the load cell and transition pieces in Setup 1 (as in Setups 2a and 2b) during overtopping of the $R12$ wave which are not present for Setup 3. The highest compensation in $R12$ is seen for Setup 2a which has the same projected area to the yz -plane as Setup 2b but has significantly reduced stiffness.

IV. DISTURBANCES FROM MEASUREMENT EQUIPMENT

Snapshots are extracted from video recordings (framerate of 30 Hz) for all setups at the time coordinate corresponding to the second wave crest after ramp-up have propagated to the center of the sphere, see Fig. 11. Clearly, the wave overtopping is accelerated differently between the three setups due to the presence of the measurement equipment. Setup 1 seems to better guide the overtopped water around the load cell relative to Setup 2 which yields the highest (visible) run-up – presumably due to the cylindrical and rectangular cross-sections of the measurement equipment in Setups 1 and 2, respectively. The wave smoothly overtopped the sphere model in Setup 3 where no acceleration of the water phase

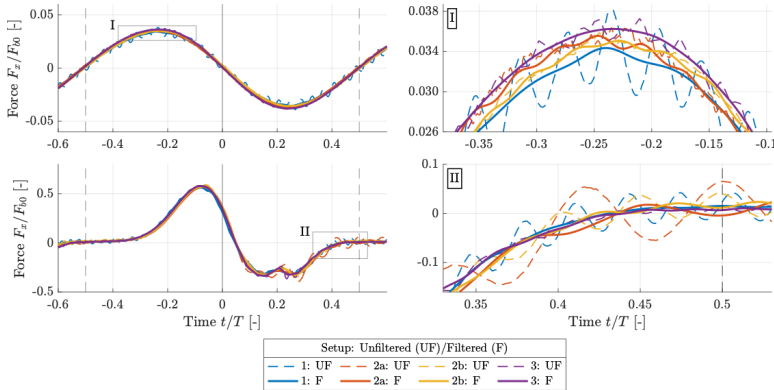


Fig. 10. Influence of dynamic amplification filter on force time series in $R01$ (upper) and $R12$ (lower).

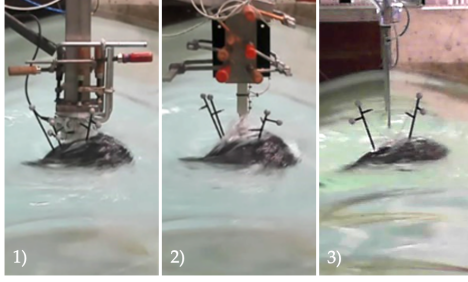


Fig. 11. Wave-overtopping in R12 for Setups 1-3.



Fig. 12. Incident waves and ring wave at the sphere model in R12 for Setup 3 without reflective markers.

from the wires were detected. The snapshots reveal how most of the downwave side of the top hemisphere is exposed due to the formation of an outward propagating ring wave. The ring wave is shown with a smooth incident wave field in Fig. 12 for the same time coordinate as Fig. 11. The minimal interaction between overtopping and measurement equipment in Setup 3 suggests an undisturbed overtopping of the sphere (as idealized in the testcase) of about 50 mm (estimated from video recordings). Despite the small visual intrusion on wave overtopping from the wires in Setup 3, the projected area of the wires and sphere model to the yz -plane (as seen from the wavemaker) is similar to that of Setup 2. Introducing A_{ref} as the projected area to the yz -plane of the idealized testcase, i.e., a circle of radius $r = 150$ mm, the relative increase in the projected area for each setup is calculated in (2).

$$\gamma_A = (A_i - A_{ref})/A_{ref} \quad (2)$$

where A_i is the projected area to the yz -plane of the setups (sphere model, measurement equipment, transition pieces, etc.) between $z = -h$ and $z = z_{ot}$ where z_{ot} is the maximum elevation of overtopping detected in Setup 3, i.e., with the least interference from measurement equipment, which was estimated as $z_{ot} = 200$ mm. The relative increases of the projected areas γ_A are then 7.2%, 4.0%, and 3.7% for Setups 1-3, respectively. Accordingly, the increase of the projected area relative to the idealized testcase is about double in Setup 1 relative to Setup 3 (and 1.8 relative to Setup 2) whereas Setups 2 and 3 varies with less than 10%. It should however be noted that most waves included in the idealized testcase (and indeed wave conditions R01 and R12) are in the deep-water wave regime, as shown in Fig. 3, and particle velocities consequently increases exponentially from the bed to the

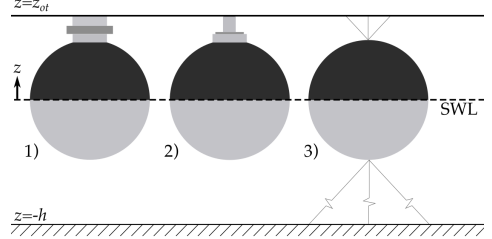


Fig. 13. Projected areas to the yz -plane for Setups 1-3. Identical scaling between setups.

free surface yielding only minor wave forces on the parts of the wires close to the bed. The major differences in the projected area in the vicinity of the free surface and the sphere model from the three setups can be appreciated in Fig. 13 where projected yz -plane views of the setups are identically scaled.

V. WAVE EXCITATION FORCES

Surface elevation time series from the tests with a wave gauge installed at the position of the center of the sphere model (without the sphere model) were used to extract a window of the F_x and F_z force time series corresponding to the first full wave after transient effects in the wave signal from, e.g., wave-ramp-up, were assessed to be sufficiently low, see Figs. 14-17. Close-ups on the extracted waves with additional close-ups on the force extrema are given in Figs. 15 and 17. The surface elevation time series and wave excitation force time series of each setup are aligned from trigger signals.

The close-ups on the extracted waves show virtually overlapping F_x and F_z time series for all setups in both R01 and R12. It should be noted that F_z is only measured in Setups 1 and 3. The additional close-ups around force extrema show somewhat minor deviations between the force time series with the generally largest deviations between Setup 1 and 3. The relative deviations in force extrema and standard deviation (global value) of the extracted waves are denoted δ and are given in Table III with the minimum absolute value as reference and subscripts *min*, *max*, and *std* indicating minima, maxima, and standard deviation, respectively. The relative deviations are highest for R01 relative to R12 presumably due to the lower loads of R01 yielding relatively larger impacts from offset-type uncertainties in the force measurement process with the setups (rather than the force transducers themselves which calibration uncertainties are significantly smaller). This is supported by the nearly constant offsets between force time series around force extrema for R01 in Fig. 15 and is further indicated from the nearly constant deviations of F_z within each setup in wave condition R01, i.e., 1-2% for Setup 2a, 2-3% for Setup 2b, 6-8% for Setup 3 relative to Setup 1, see Table III. In wave condition R12, the force time series around force extrema and the relative deviations vary more as shown in Fig. 17 and Table III indicating not only

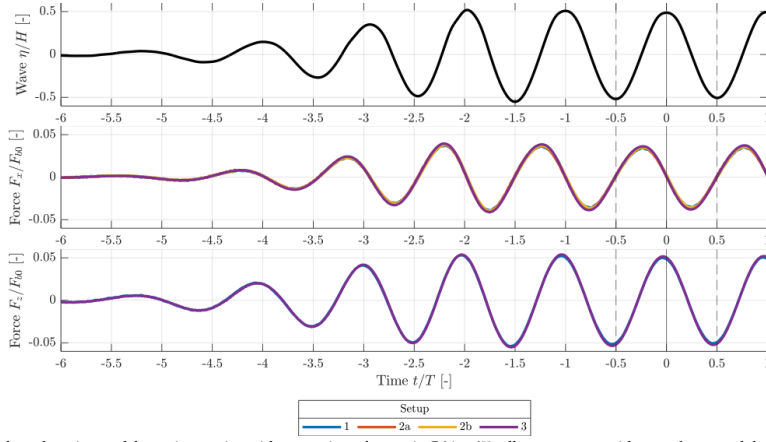


Fig. 14. Surface elevation and force time series with extraction of wave in R01. η/H adheres to tests without sphere model.

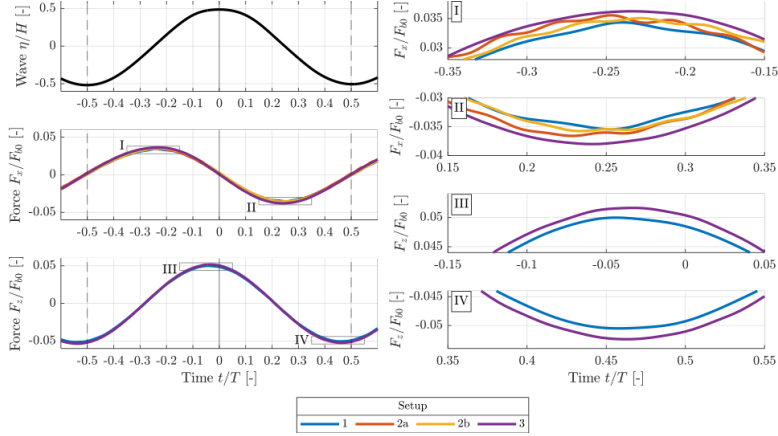


Fig. 15. Surface elevation and force time series of extracted wave with close-ups on force extrema in R01.

measurement uncertainties but differences in the experienced hydrodynamics between setups such as the detected different interactions between overtopping waves and measurement equipment. That being said, the relative deviations are in general low with deviations less than 8% in R01 and less than 5% for R12 for all setups. The high consistency of the measured force time series substantiates that all experimental setups are capable of accurately capturing the wave excitation forces on a fixed sphere as per the idealized testcase. Small oscillations in x were present in Setups 2a and 2b after dynamic amplification filtering as can be seen in Fig. 15. Furthermore, small oscillations are present in z for Setup 1 in R12, see Fig. 17, which gives a slight edge to Setup 3 – the only other setup measuring both F_x and F_z . The large deviation of Setup 3 relative to Setup 1 at about $t/T = -1$ in the F_z time series of wave condition R12 occurs at the impact of the high, leading wave after ramp-up to the load cell, see Fig. 16.

TABLE III
RELATIVE DEVIATIONS OF FORCE EXTREMA AND STANDARD DEVIATIONS
BETWEEN SETUPS (REFERENCE TO THE MINIMUM ABSOLUTE VALUE).

| R01 | | | | | | |
|-------|-------------------------|-------------------------|-------------------------|-------------------------|-------------------------|-------------------------|
| Setup | $\delta_{min,x}$ (%) | $\delta_{max,x}$ (%) | $\delta_{std,x}$ (%) | $\delta_{min,z}$ (%) | $\delta_{max,z}$ (%) | $\delta_{std,z}$ (%) |
| 1 | 0.0 | 0.0 | 0.0 | 0.0 | 0.0 | 0.0 |
| 2a | 3.3 | 3.5 | 3.7 | - | - | - |
| 2b | 0.9 | 2.1 | 2.3 | - | - | - |
| 3 | 7.3 | 5.5 | 8.0 | 3.7 | 3.3 | 3.7 |
| R12 | | | | | | |
| Setup | $\delta_{min,x}$ (%) | $\delta_{max,x}$ (%) | $\delta_{std,x}$ (%) | $\delta_{min,z}$ (%) | $\delta_{max,z}$ (%) | $\delta_{std,z}$ (%) |
| 1 | 0.0 | 0.0 | 0.0 | 0.0 | 2.4 | 0.0 |
| 2a | 0.5 | 1.3 | 1.2 | - | - | - |
| 2b | 1.7 | 2.5 | 1.4 | - | - | - |
| 3 | 4.7 | 2.9 | 2.4 | 1.0 | 0.0 | 0.9 |

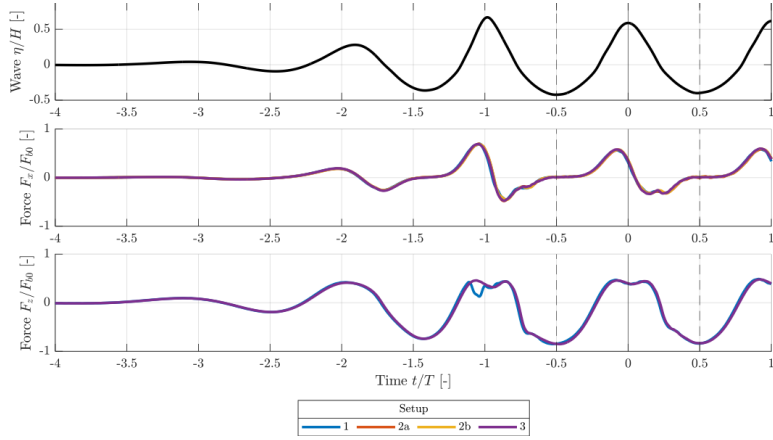


Fig. 16. Surface elevation and force time series with extraction of wave in R12. η/H adheres to tests without sphere model.

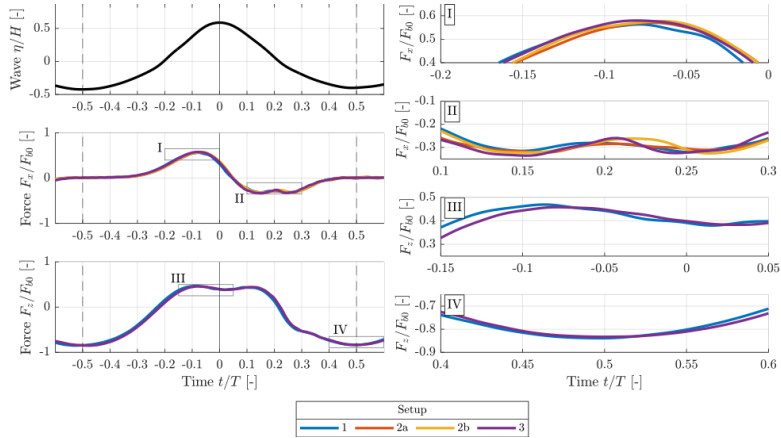


Fig. 17. Surface elevation and force time series of extracted wave with close-ups on force extrema in R12.

VI. CONCLUSIONS AND FURTHER WORK

The accuracy of three physical wave basin setups to represent an idealized testcase on wave excitation of a fixed sphere with the center at the SWL was investigated. Setup 3 (system of pretensioned wires) was the most rigid setup with the least corrections due to dynamic amplification for the investigated wave conditions, i.e., R01 and R12 (extrema of wave heights and steepness included in the testcase). Setup 3 further had the least interference with overtopping waves (estimated from video recordings) and the least projected area normal to the wave propagation direction – especially if weighting with the intermediate- to deep-water velocity profiles of the incident waves. Wave excitation force time series were extracted for F_x for all setups whereas F_z was only measured in Setups 1 and 3. Low inter-experiment variability on wave excitation force time series were found across all setups, i.e., maximally 8% and 5% deviation on force extrema and standard deviation for R01 and R12,

respectively. The deviations of the wave excitation force between setups in the close to linear wave condition R01 were ascribed to measurement uncertainties while in the higher, nonlinear wave condition R12 the deviations were ascribed to both measurement uncertainties and differences in the disturbances from measurement equipment to the wave field due to wave-overtopping. Accordingly, Setup 3 is assessed to be the more accurate representation of the idealized testcase from the investigated range of setups. However, the low inter-experiment variability on the measured wave excitation force time series (after dynamic amplification filtering) indicates how all the experimental setups accurately represent the idealized testcase with relatively small implications from the detected differences in dynamic properties and disturbances from measurement equipment on the wave excitation forces.

Further work with Setup 3 is currently undertaken including quantification of uncertainty of the force measurement process. Two testcases with, respectively, an

idealized [8] and a physical/detailed [9] representation of the physical tests were made public to encourage numerical modelling of the testcase. Results based on Setup 3 are planned to be released as a public benchmark dataset with confidence bounds and comparison to numerical models of various fidelity.

REFERENCES

- [1] M. B. Kramer *et al.*, “Highly accurate experimental heave decay tests with a floating sphere: A public benchmark dataset for model validation of fluid–structure interaction,” *Energies (Basel)*, vol. 14, no. 2, Jan. 2021, doi: 10.3390/en14020269.
- [2] J. D. Fenton, “The Numerical Solution of Steady Water Wave Problems,” *Comput Geosci*, vol. 14, no. 3, pp. 357–368, Jan. 1988, doi: 10.1016/0098-3004(88)90066-0.
- [3] B. Le Méhauté, “An Introduction to Water Waves,” in *An Introduction to Hydrodynamics and Water Waves*, Berlin, Heidelberg: Springer Berlin Heidelberg, 1976, pp. 197–211. doi: 10.1007/978-3-642-85567-2_15.
- [4] H. A. Schäffer, “Second-Order Wavemaker Theory for Irregular Waves,” *Ocean Engineering*, vol. 23, no. 1, pp. 47–88, 1996, doi: [https://doi.org/10.1016/0029-8018\(95\)00013-B](https://doi.org/10.1016/0029-8018(95)00013-B).
- [5] H. Zhang and H. A. Schäffer, “Approximate Stream Function Wavemaker Theory for Highly Non-Linear Waves in Wave Flumes,” *Ocean Engineering*, vol. 34, no. 8, pp. 1290–1302, 2007, doi: <https://doi.org/10.1016/j.oceaneng.2006.04.010>.
- [6] P. Frigaard and T. L. Andersen, *Analysis of Waves: Technical Documentation for WaveLab 3*, no. 33. in DCE Lecture notes. Denmark: Department of Civil Engineering, Aalborg University, 2014.
- [7] S. R. K. Nielsen, *Vibration Theory, Vol. 1: Linear Vibration Theory*, 3rd edition. in U/. Denmark: Department of Civil Engineering, Aalborg University, 2004.
- [8] M. B. Kramer, J. Andersen, and K. Nielsen, *Wave Excitation Forces on a Sphere: Description of an Idealized Testcase*, 1st ed., no. 307. in DCE Technical Reports. Department of the Built Environment, Aalborg University, 2023.
- [9] M. B. Kramer and J. Andersen, *Wave Excitation Forces on a Sphere: Description of a Physical Testcase*, 1st ed., no. 307X. in DCE Technical Reports. Department of the Built Environment, Aalborg University, 2023.

Paper F

Development of the Exowave Oscillating Wave Surge Converter

Sarah Krogh Iversen
Jacob Andersen
Lars Wigant
Peter Frigaard

Accepted preprint submitted to the 15th European Wave and Tidal Energy Conference (EWTEC), 2023, appended.

The paper has been published in:
Proceedings of the 15th European Wave and Tidal Energy Conference,
EWTEC, DOI: 10.36688/ewtec-2023-368, 2023.

Development of the Exowave Oscillating Wave Surge Converter

Sarah K. Iversen, Jacob Andersen, Lars Wigant, and Peter Frigaard

Abstract—With increasing demand for renewable energy resources, the development of alternative concepts is still ongoing. The wave energy sector is still in vast development on the way to contribute to the energy production world wide. The present study presents the development of the Exowave wave energy converter made so far. A numerical model has been established supported by wave flume tests performed at Aalborg University during the first phase of the development. Furthermore, a successful open sea demonstration has been performed on 7 meters of water at Blue Accelerator, Belgium, from which the concept has been proven. As part of the ongoing research, validation of the numerical model will be made through experimental testing in the wave tank of Aalborg University, and an open sea demonstration at 14 meters of water depth will be executed off the coast of Hanstholm, Denmark.

Index Terms—Wave energy, WEC, Morison equation, numerical modelling, wave flume tests.

I. INTRODUCTION

THE political push towards renewable energy sources along with strategies to mitigate audible and visual pollution have encouraged offshore deployment of renewable energy devices such as wave energy converters (WECs) which if integrated with offshore windfarms can increase utilization of otherwise dedicated marine spaces and critical infrastructure, i.e., substations, transformers, grid, etc. Exowave is a wave energy converter of the oscillating wave surge type with a bottom-hinged wave-activated body that moves in pitch when excited by waves. Of other wave energy converters of the oscillating wave surge type, Oyster [1], or WaveRoller [2] can be mentioned. Common for these two devices is the flap-like shape of the wave-activated body. In both cases, the flap covers more or less the entire water column from seabed to water surface, and with a width/height ratio larger than 1. For the Exowave device, the original idea was to create a smaller device, with a flap arm connecting the flap in the upper part of the water column with the hinge at the foundation and place the devices in clusters. The Exowave WEC is a multifunctional device, that can produce fresh water or electricity as needed. As other WECs of this type, the concept is a

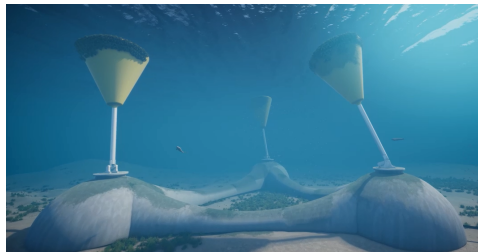


Fig. 1. Exowave Cluster.

fully submerged solution to secure survivability during extreme events, which is known to be a challenge for many other wave energy devices. Furthermore, audible and visual pollution is avoided, when the device is fully submerged. The aim for the implementation of Exowave is a better utilization of dedicated offshore wind energy areas, as it can be integrated in offshore wind farms and connected to critical infrastructure, i.e. substations, transformers, grid, etc. The WEC consists of a gravity-based foundation. Attached to the foundation is a bottom-hinged power-take-off (PTO), which is driven by a buoy-like wave-activated body, which is connected to the PTO. Through a flow line pipe system, the PTO is connected to a water turbine electrical generator.

For estimation of power production and structural design of wave energy converters, numerical modelling is key. The development of a numerical model is highly dependent on the design and size of the wave-activated body in proportion to the sea state at the target location of the device, as the model must be able to capture the relevant phenomena associated with the specific wave regime as given by [3]. This paper will therefore present the development of the Exowave wave energy converter as seen in Fig. 1, with focus on the design of the wave-activated body and numerical modelling of the movement hereof including power production. An overview of research performed so far will be given, which has lead to the current design of the device. Additionally, the plans for the ongoing and future development will be presented.

II. RESEARCH PERFORMED UNTIL NOW

The development of Exowave kickstarted with the project *Exowave, Water, Electricity and PtX* which was supported by The Danish Energy Agency under The Energy Technology Development and Demonstration

Accepted preprint submitted to the 15th European Wave and Tidal Energy Conference (EWTEC), 3-7 September 2023, Bilbao.

This work was supported by the Danish Energy Agency under the Energy Technology Development and Demonstration Program (EUDP) contract number 64022-1062, Niels Bohrs Vej 8D, 6700 Esbjerg, Denmark.

S. K. Iversen, J. Andersen, and P. Frigaard are with the Department of the Built Environment at Aalborg University, Thomas Manns Vej 23, 9220 Aalborg Ø, Denmark (e-mail: ski@build.aau.dk).

L. Wigant is with Exowave ApS, Kanalen 1, 6700 Esbjerg, Denmark (e-mail: law@exowave.com).

Program, wherefore it will in the following be referred to as EUDP1. The objective of EUDP1 was to develop a numerical model for estimation of power production and for use in structural design of the device, to investigate the feasibility and business case for a combined wave energy and offshore wind plant, to perform wave tank testing and CFD analysis, and lastly to demonstrate the device in open water for validation of the numerical model. The following sections will present the outcomes of EUDP1 performed by Aalborg University, which relates to the design of the wave-activated body and the numerical modelling and wave flume testing hereof.

III. NUMERICAL MODEL

For estimation of the power production and for use in the structural design of the device, a numerical model for the interaction between the wave loads and the wave-activated body has been developed by Aalborg University. The numerical model is described in the following. Based on the wave force regime by Chakrabarti [3], the numerical model is designed to include the inertia and drag effects. The numerical model for the Exowave converter is therefore based on the Morison equation [4], which is applicable in the inertia and drag dominated wave force regimes. It is therefore assumed that there are no diffraction effects. The wave kinematics used in the numerical model are evaluated using linear wave theory for regular or irregular waves.

For structural design of the device as well as estimation of the energy production, the loads involved in movement of the wave-activated body must first be defined. The wave forces are calculated from the Morison equation as given by [4], as it is assumed that the characteristic length of the WEC is small relative to the characteristic wavelengths of the target wave climates. For a moving body, the Morison force is calculated using (1) consisting of two inertia contributions, one from the Froude-Krylov force and one from added mass, and a contribution from drag. The resulting wave force and moment at the point of rotation are calculated using Simpson integration.

$$f_{\perp}(t) = \rho A \frac{du_{\perp}}{dt} + \rho C_A A \left(\frac{du_{\perp}}{dt} - \ddot{\theta} r \right) + \frac{1}{2} \rho C_D D \left(u_{\perp} - \dot{\theta} r \right)^2 \text{sgn}(u_{\perp} - \dot{\theta} r) \quad (1)$$

where

| | |
|-------------------------------|------------------------------------------------------------------------------------|
| ρ | Density of water, [kg/m ³] |
| A, D | Characteristic cross area and length normal to flow direction [m ² , m] |
| u | Horizontal wave particle velocity, [m/s] |
| u_{\perp} | Wave particle velocity orthogonal to body [m/s] |
| C_A, C_D | Added mass and drag coefficients, [-] |
| $\dot{\theta}, \ddot{\theta}$ | Angular velocity and acceleration of body [rad/s, rad/s ²] |
| r | Distance from hinge to point on body [m] |

The hydrostatic forces on the energy-collector are the buoyancy and the gravity, which work in opposite directions, wherefore the hydrostatic moment at the point of rotation is expressed from (2).

$$M_{hydro} = M_{buo} - M_{gravity} = \rho g V \sin(\theta) r_b - m g \sin(\theta) r_m \quad (2)$$

where

| | |
|-------|-------------------------------------------------|
| g | Gravitational acceleration, [m/s ²] |
| V | Volume of energy-collector, [m ³] |
| r_b | Distance from hinge to centre of buoyancy, [m] |
| m | Mass of energy-collector, [kg] |
| r_m | Distance from hinge to centre of gravity, [m] |

The power take-off (PTO) consists of a double acting hydraulic system with a pressure p_{hydr} . The PTO is activated when $\theta > 0 \wedge \dot{\theta} > 0$ or $\theta < 0 \wedge \dot{\theta} < 0$. The reacting force from the PTO piston is $F_{piston} = p_{hydr} A_{hydr}$, where A_{hydr} is the effective internal area of the hydraulic cylinder. The moment at the point of rotation due to the PTO is then calculated from (3) with respect to the arm, d , which is calculated from trigonometry as a function of θ .

$$M_{PTO} = F_{piston} d(\theta) \quad (3)$$

The WEC is modelled as a one degree-of-freedom (DoF) system, which is free to move in pitch, when it is excited by waves. The dynamic system is described from the equation of motion as stated in (4), where K is the rotational stiffness, C is the rotational damping coefficient, I is the moment of inertia and M_{res} is the resulting moment of the system as specified in (5).

$$K\theta(t) + C\dot{\theta}(t) + I\ddot{\theta}(t) = M_{res}(\theta, \dot{\theta}, \ddot{\theta}) \quad (4)$$

The resulting moment consists of the resulting Morison moment, M_{mor} , the hydrostatic moment, M_{hydro} , and the PTO moment, M_{PTO} :

$$M_{res}(\theta, \dot{\theta}, \ddot{\theta}) = M_{mor}(\theta, \dot{\theta}, \ddot{\theta}) + M_{hydro}(\theta) + M_{PTO}(\theta, \dot{\theta}) \quad (5)$$

The equation of motion is then represented in state space as two ordinary differential equations. When the PTO is active, the system is considered highly nonlinear, wherefore it is solved using a Runge-Kutta solver following the implementation by [5] and [6].

IV. DEVELOPMENT OF WEC DESIGN

During the numerical modelling with regard to the target wave climate at the future position of the WEC, simulations showed that the system was more inertia dominated than drag dominated, wherefore the design of the wave-activated body was lead to an idea of a more cylindrical shape. The shape was therefore changed from the initial idea of having a flat flap-like shape to being frustum of a cone to reduce the drag coefficient, as the drag will damp the movement of the system. Furthermore, the idea of the conical design was

to increase the width at the top of the body to match the velocity profile of the water particles.

A first estimate of the inertia, $C_M = C_A + 1$, and drag, C_D , coefficients was therefore based on literature review. The estimations are based on the recommendations from [7]. For two-dimensional bodies, the added mass coefficient of a cylinder in infinite fluid is $C_A = 1.0$. As a two-dimensional body, no effects from the free surface or other 3-dimensional effects are taken into account. Intuitively, this implies that the added mass coefficient of the system might be below 1.0, when the 3D effects are considered. For a fixed cylinder in a steady flow with Reynolds number of approximately 10^5 , the drag coefficient is in the range of $C_D = 0.5 - 1.0$ depending on the roughness of the surface. The determination of added mass and drag coefficients for a cone-like structure for a given wave climate is however associated with large uncertainties, wherefore experimental testing in the wave flume were performed to support the choice of coefficients in the numerical model.

V. WAVE FLUME TESTS

This section will describe the wave flume tests performed in the flume at the Ocean and Coastal Engineering Laboratory at Aalborg University as part of EUDP1. The test included different float model designs and the determination of Morison coefficients hereof. The outcome of the tests is given in the following.

A. Morison Coefficients

The test setup for the flume tests conducted at Aalborg University was based on a potential design for a 100 kW rated power WEC cell to be deployed at the site Thor off the coast of Hvide Sande, Denmark. The scope of the model tests were to calculate Morison coefficients for different shapes of the wave-activated body for various sea states defined based on the Keulegan-Carpenter (K_C) number, and secondly to assess the influence of the geometry of the body on the wave loading. Test specimens were delivered by Exowave Aps. The different designs tested are illustrated in Fig. 2. The tests were performed in the wave flume with a horizontal bed and water depth of 0.645m, corresponding to 25.8m in prototype scale. The test setup in the flume appears from Fig. 3 and 4. Force transducers to measure loads in the wave propagation

direction were installed at the top of the model as illustrated in Fig. 5. All tests were repeated with no model floats but instead a wave gauge installed at the model float location. Identical steering signals for wave generation were applied between repeated sea states. The force transducers and wave gauge signals were logged utilizing WaveLab 3.858 [8]. The different designs were all tested for target sea states of which the K_C -numbers were kept constant for all three designs. The K_C numbers were calculated from:

$$K_C = \frac{u_{max,0}T}{D_{av}} \quad (6)$$

where $u_{max,0}$ is the horizontal maximum particle velocity at SWL [m/s], T is the wave period [s], and D_{av} is the average of D_1 and the bottom diameter [m]. $u_{max,0}$ was calculated from stream function theory, i.e., specifically from the Fourier approximation method by [9]. Only regular sea states were investigated. The waves were generated from second order theory as per [10] with modifications by [11] for K_C of max. 3 or from approximate stream function theory as per [12] for larger K_C numbers.

For calculation of the wave loads, the Morison equation was applied, which models the wave force on a structure as a linear combination of inertia and drag loads. For the static float, the horizontal force per unit length, f [N], is expressed from the Morison equation in (1), here with the velocity of the body being equal to 0. With the velocity of the body being equal to 0, the first two terms of the Morison force in (4) can be combined in a total inertia term with the coefficient $C_M = 1 + C_A$. The first part of the term represented by the 1 corresponds to the Froude-Krylov force due to the pressure field generated by the undisturbed waves. The second part of the inertia force represented by C_A consists of the added mass due to the acceleration of the surrounding fluid.

The resulting force F_x was calculated by integrating f over the height of the float. The Morison coefficients, $C_M = C_A + 1$ and C_D , were calculated by a least squares approach adopted from [13]. For inertia dominated regimes, the experimental determination of the drag coefficient is associated with very high sensitivity, wherefore $C_D = 0.8$ was imposed as found from numerical tests with computational fluid dynamics (CFD), see Section V-B.

B. Calculation of Drag Coefficient from CFD

Numerical tests with CFD were carried out by Delft University and Aalborg University to calculate the drag coefficient for a fixed float model with the top point tangential to the still water level. The open-source, cell-centred finite volume CFD framework of OpenFOAM [14] was used to set up a three-dimensional, two-phase (water and air) model with uniform inflow velocity of 0.5 m/s ($Re \approx 1e5$). The grid was structured with predominantly hexahedrals and wall functions were employed at the no-slip boundaries of the float model. A domain size of 5 float diameters upstream of the model, 15 float diameters

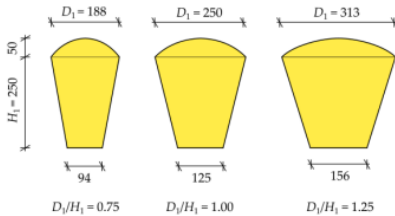


Fig. 2. Dimensions of investigated float model designs (axisymmetric) [mm].

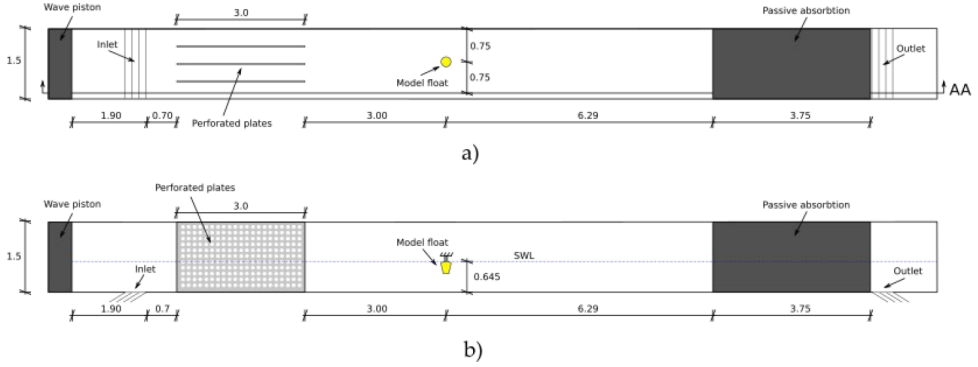


Fig. 3. Setup of the wave flume, a) top view, b) Section view A-A [m].

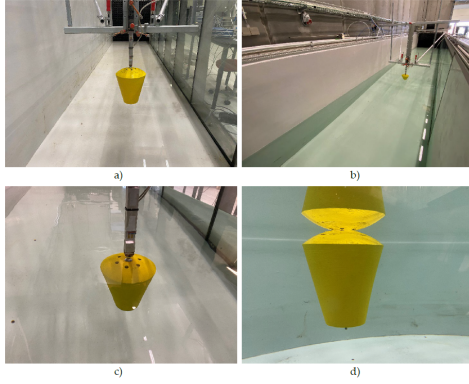


Fig. 4. Photos of the test setups: a) Installed model float with no water in flume, b) Installed float model with water, passive absorption in the background, c) Force transducer mounted on top of float model, d) SWL and top of float model coinciding.

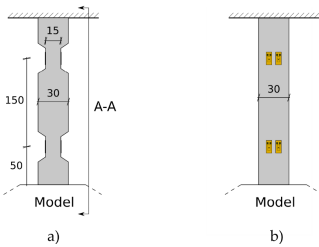


Fig. 5. Force transducer mounted on top of the float models [mm]. a) Transverse of the wave propagation direction view, b) Section A-A view.

downstream, and about 3 diameters to either side patch was used. The interFoam solver of OpenFOAM-v2012 (ESI) was employed to numerically solve the Reynolds-Averaged Navier-Stokes equations with turbulence closure from the k-omega-SST model as per [15]. Time

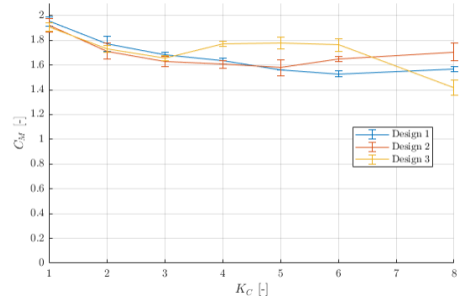


Fig. 6. Mean inertia coefficients, $C_M = 1 + C_A$, as function of investigated KC numbers. Error bars of plus/minus 2 standard deviations are included.

stepping was done by a maximum Courant criterion of 0.1. The fluid-structure interaction problem yielded $C_D = 0.8$ after development of a steady state.

C. Results

The measured wave height and wave periods are used to calculate five time series of the resultant F_x . The measured surface elevation time series and the measured force time series were aligned from adjacent zero-down-crossings from the surface elevation time series. The least squares error approach is utilized to estimate the Morison coefficients for each of the calculated resultant time series (5 repetitions) with each of the measured force time series (5 repetitions). Thus, a total of 25 sets of Morison coefficients is calculated for each sea state. Fig. 6 illustrates the average inertia coefficient, $C_M = 1 + C_A$, with plus/minus two standard deviations for each sea state (K_C) for all three designs. For all designs, the inertia coefficients are seen to depend significantly on the K_C number. E.g. a decrease from approximately $C_M = 1.9$ at $K_C = 1$ to approximately $C_M = 1.6$ at $K_C = 3$ is present for all designs. From [16], the inertia coefficient of a 2D-cylinder for $K_C < 4(Re \approx 2 \cdot 10^4)$ is 2.0 (from U-tube

experiments). Intuitively, 3D effects of flow under and over a cylindrical structure will mitigate wave loads relative to a 2D cylinder, in compliance with the C_M values in Fig. 6. An increase in C_M occurs for all three designs for K_C values corresponding to a wavelength of around 4.8m, i.e. $K_C = 8$ for Design 1, $K_C = 6$ for Design 2, and $K_C = 4$ for Design 3. Reflective wave loads will be more dominant for longer waves, as these waves will have ramped further up when re-impacting the float model than for shorter waves. The aforementioned increases of C_M are ascribed to reflective wave effects, and considering C_M of the shorter wavelengths in suggests that C_M will equal 1.5-1.6 for the highest investigated K_C numbers. No significant differences between inertia coefficients of the different designs are present for K_C corresponding to wavelengths less than 4.8m. Variations between trials were present for most tested sea states. These are ascribed to inaccuracies in the trigger signal system, and could in further analyses be mitigated from cross-correlation analysis of both surface elevation and force signals.

D. Conclusion on Wave Flume Tests

Inertia coefficients, C_M , are determined for seven different K_C numbers for three different designs. The inertia coefficients strongly depend on the K_C numbers, and ranges from approximately 1.9 for $K_C = 1$ to approximately 1.5-1.6 for $K_C = 6$. Calculated inertia coefficients for K_C numbers corresponding to longer wavelengths are more subjected to reflective wave loads in the wave flume. For wavelengths larger than 4.8m in the present tests, inertia coefficients are expected to be overestimated. No significant differences of the inertia coefficients are found between designs for wavelengths shorter than 4.8m. Thus, Design 3 will yield the largest amplitude of a wave load cycle, since the cross-sectional area of this design is larger than for Design 1 and 2.

VI. OPEN SEA DEMONSTRATION

The EUDP1 project terminated with an open sea demonstration of the WEC10 converter. The demonstration was performed at Blue Accelerator, Belgium. The location provided a water depth of 7 meters with 4-5m tidal deviations and a 1m/s tidal current, which is rather different from the future intended location of the Exowave converter. The demonstration provided a proof of the installation principles for future use. The foundation was assembled on land. The PTO was installed in the foundation, and the wave-activated body was installed on top. The WEC10 can be seen in Fig. 7 before launch. Furthermore, a ballast test was performed as seen in Fig. 8, before the WEC was successfully towed to the desired location at sea as shown in Fig. 9, where it was ballasted with seawater and placed on the sea bed. The WEC was calibrated to start production at 45 bar counter pressure, which should be possible at a sea state with a significant wave height of 1m. The production during the demonstration was measured as the flow produced by the hydraulic

piston. The data acquisition took place during September and October 2022. Due to a very mild climate during the data acquisition period, the recorded data was mainly useful for proof of the concept. More data will be necessary for further validation of the numerical model. After demonstration, the device was successfully uninstalled and transported back to the workshop, where it will be used for further analysis of the components.



Fig. 7. WEC10 prepared for launch at Blue Accelerator, Belgium.



Fig. 8. Ballast test, Blue Accelerator, Belgium.



Fig. 9. Towing of WEC to site, Blue Accelerator, Belgium.

VII. CONCLUSION

During the research performed so far at Aalborg University of the Exowave wave energy converter, a numerical model has been developed. The design of the wave-activated body has been concluded to be of a conical shape. The Morison coefficients used in the formulation of the numerical model have been derived from physical wave flume test performed in the wave flume at the Ocean and Coastal Engineering Laboratory at Aalborg University, and by numerical tests from two-phase CFD analyses, from which it is concluded that the drag coefficient used in the numerical model should be equal to $C_D = 0.8$ and the inertia coefficient should be $C_M = 1.7$, corresponding to an added mass coefficient of $C_A = 0.7$. Furthermore, the current design of the wave energy device has been demonstrated in open sea at Blue Accelerator, Belgium, from which the installation principles and conceptual design are found successful.

VIII. FUTURE DEVELOPMENT

The future development is already in process with a new project supported by The Danish Energy Agency under The Energy Technology Development and Demonstration Program as well, therefore referred to in the following as EUDP2. The objectives of the EUDP2 project is to validate the numerical model for demonstration at 14 m water depth in the North Sea for a cell power of 35 kW (WEC35), to implement yaw control of the device, to optimize the flap shape and to balance the system pressure to improve the capacity factor. Another degree of freedom is added to the WEC system to reduce the loads in the direction perpendicular to the mean direction of wave propagation, wherefore the system will be free to move in roll. The power production will still be for the movement in pitch. The numerical model and demonstration from the EUDP1 project did not cover this movement, wherefore additional wave tank tests will be performed at Aalborg University, before the demonstration at open sea will take place.

A. Wave tank tests

New wave tank tests performed at Aalborg University aims to test a moving system of the WEC35. An active PTO will be added to the small scale model to validate the power production estimated from the numerical model. Furthermore, the behavior of the system that is free to move in roll will be investigated for multidirectional waves. The study will furthermore investigate the loss of efficiency due to multidirectionality of the waves. Where the designs in the wave flume tests presented in this paper primarily focused on different sizes of the conical body, the coming tests will furthermore focus on the influence of different shapes, to see if any significant difference is experienced for the new system. The tests will consider the amplitude of the response as well and the band-width hereof.

B. Demonstration North Sea

For EUDP2 a open sea demonstration at 14 m water depth is planned. The demonstration will take place at the Danish Wave Energy Centre (DanWEC) off the coast of Hanstholm, Denmark, in the North Sea. The aim of the demonstration is to verify the energy production. The hydraulic system of the PTO will be connected to a water turbine electrical generator onshore. Performance wise, the demonstration aims to implement yaw control of the device in order to orientate the device according to the measured mean wave direction on the site. Furthermore an active control system of the hydraulic PTO system is expected to be implemented. For validation of the numerical model in relation to power production and structural design, the motion of the wave-activated body will be monitored as well as the loads, which will be monitored by strain gauges on the arm connecting the body to the PTO and foundation. The demonstration furthermore seeks to prove a new installation procedure for a concrete foundation in stead of the steel foundation used for the demonstration in EUDP1. Of other materials, it is considered using glass fibres from wind turbine blade waste material to produce the wave-activated body.

NOMENCLATURE

| | |
|-------------|---------------------------------------------------------------------|
| d | Moment arm for piston force, [m] |
| f_{\perp} | Morison force per unit height, [N/m] |
| g | Gravitational acceleration, [m/s ²] |
| m | Mass of wave-activated body, [kg] |
| p_{hydr} | Pressure in hydraulic piston, [Pa] |
| r | Distance from hinge to point on wave-activated body [m] |
| r_m | Distance from hinge to centre of gravity of wave-activated body [m] |
| t | Time, [s] |
| u | Horizontal wave particle velocity, [m/s] |
| u_{\perp} | Wave particle velocity orthogonal to wave-activated body [m/s] |
| $u_{max,0}$ | Horizontal maximum particle velocity at SWL, [m/s] |

| | |
|-----------------|----------------------------------------------------------------------------------------------|
| A | Characteristic cross area of wave-activated body normal to flow direction, [m ²] |
| A_{hydr} | Effective internal area of hydraulic cylinder, [m ²] |
| C | Rotational damping coefficient, [-] |
| C_A | Added mass coefficient, [-] |
| C_D | Drag coefficient, [-] |
| C_M | Inertia coefficient, $C_M = 1 + C_A$, [-] |
| D | Characteristic length of wave-activated body normal to flow direction, [m] |
| D_{av} | Average of maximum diameter and bottom diameter of test specimen, [m] |
| F_x | Resulting horizontal wave force on test specimen, [N] |
| F_{piston} | Reacting force from the PTO piston, [N] |
| I | Moment of inertia, [kg·m ²] |
| K | Rotational stiffness |
| K_C | Keulegan-Carpenter number, [-] |
| M_{buo} | Moment at point of rotation caused by buoyancy, [Nm] |
| $M_{gravity}$ | Moment at point of rotation caused by gravity, [Nm] |
| M_{hydro} | Hydrostatic moment at point of rotation, [Nm] |
| M_{PTO} | Moment at point of rotation caused by power take-off, [Nm] |
| M_{res} | Resulting moment in the equation of motions of the wave-activated body, [Nm] |
| Re | Reynolds number, [-] |
| T | Wave period, [s] |
| V | Volume of wave-activated body, [m ³] |
| ρ | Density of water, [kg/m ³] |
| θ | Angular position of wave-activated body, [rad] |
| $\dot{\theta}$ | Angular velocity of wave-activated body [rad/s] |
| $\ddot{\theta}$ | Angular acceleration of wave-activated body [rad/s ²] |

REFERENCES

- [1] T. Whittaker, D. Collier, M. Folley, M. Osterried, A. Henry, and M. Crowley, "The development of oyster — a shallow water surging wave energy converter." *Proceedings of the 7th European wave and tidal energy conference*, 2007.
- [2] AW Energy. (2022) Waveroller. Accessed: 2023-05-22. [Online]. Available: <http://https://aw-energy.com/>
- [3] S. K. Chakrabarti, *Hydrodynamics of Offshore Structures*. Springer Verlag, 1987.
- [4] J. R. Morison, M. P. O'Brien, J. W. Johnson, and S. A. Schaaf, "The forces exerted by surface waves on piles," *Petroleum Transactions*, vol. 189(5), pp. 149–154, 1950.
- [5] J. R. Cash and A. H. Karp, "A variable order runge-kutta method for initial-value problems with rapidly varying right-hand sides," *ACM Transactions on Mathematical Software*, vol. vol. 16, pp. 201–222, 1990.
- [6] H. P. Gavin, *Numerical Integration in Structural Dynamics*. Department of Civil & Environmental Engineering, Duke University, 2020.
- [7] Det Norske Veritas, "DNV-RP-C205: Environmental conditions and environmental loads," DNV A/S, Recommended Practice, Sep. 2019.
- [8] P. Frigaard and T. L. Andersen, *Analysis of Waves: Technical Documentation for WaveLab 3*. Department of Civil Engineering, Aalborg University; ISSN:1901-7286, 2014.
- [9] M. M. Rienecker and J. D. Fenton, "A Fourier approximation for steady water waves," *J. Fluid Mech.*, vol. 104, 1981.
- [10] H. A. Schäffer, "Second-order wavemaker theory for irregular waves," *Ocean Engineering*, vol. 23, pp. 47–88, 1996.
- [11] M. R. Eldrup and T. L. Andersen, "Applicability of nonlinear wavemaker theory," *J. Mar. Sci. Eng.*, vol. 7, 2019.
- [12] H. Zhang and H. A. Schäffer, "Approximate stream function wavemaker theory for highly nonlinear waves in wave flumes," *Ocean Engineering*, vol. 34, pp. 1290–1302, 2007.
- [13] H. F. Burcharth, *Strøm- og Bølgekræfter på Stive Legemer*. Aalborg University, 2002.
- [14] H. Weller, G. Tabor, H. Jasak, and C. Fureby, "A tensorial approach to cfd using object oriented techniques," *Comp in Phys.*, vol. 12, pp. 620–631, 1998.
- [15] F. R. Menter, M. Kuntz, and R. Langtry, "Ten years of industrial experience with the sst turbulence model," *Proc. Int. Symp. Turbul. Heat Mass Transf.*, vol. 4, pp. 625–633, 2003.
- [16] T. Sarpkaya, *Wave Forces on Offshore Structures*. Cambridge University Press: Cambridge, UK., 2014.

Paper G

Wave Propagation over a Submerged Bar:
Benchmarking of VoF, Sigma Transformation, and SPH
Numerical Models against Physical Wave Flume Tests

Jacob Andersen
Mads Røge Eldrup
Gael Verao Fernandez
Francesco Ferri

The paper has been submitted to:
Journal of Hydrodynamics, ISSN: 1878-0342.

Wave Propagation over a Submerged Bar: Benchmarking of VoF, Sigma Transformation, and SPH Numerical Models against Physical Wave Flume Tests

Jacob Andersen^{a,*}, Mads Røge Eldrup^a, Gael Veroa Fernandez^a, Francesco Ferri^a

^a Dept. of the Built Environment, Aalborg University, Thomas Manns Vej 23, 9220 Aalborg Ø, Denmark

* Corresponding author.

E-mail addresses: jacoba@build.aau.dk (J. Andersen), mrel@build.aau.dk (M. R. Eldrup), gvf@build.aau.dk (G. Veroa Fernandez), ff@build.aau.dk (F. Ferri).

ABSTRACT

Accurate prediction of wave transformation is key in the design of coastal and nearshore structures which typically depends on numerical models. Turbulent and rotational effects call for the use of Navier-Stokes solvers (CFD), of which a large range of formulations including free surface treatments exists. Physical wave flume tests of wave propagation over a submerged bar with various levels of nonlinearity, regularity, and wave-breaking, dedicated to numerical model benchmarking or validation, were carried out in the Ocean and Coastal Engineering Laboratory of Aalborg University. Three fundamentally different CFD models each widespread within their category are benchmarked against the experimental data. The CFD models are based on i) the VoF-based interFoam solver of OpenFOAM, ii) the sigma-transformation solver of MIKE 3 Waves Model FM, and iii) the weakly compressible delta-SPH solver of DualSPHysics. Accuracy of the numerical models is assessed from surface elevation time series, evaluation metrics (averaged errors on surface elevations, amplitudes, phases, and wave set-up), and spectral analyses to calculate the amplitude and phase contents of primary and higher-order components along the wave flume. Applicability is assessed from computational costs and ease-of-use factors such as the effort to configure the numerical models and achieve convergence. In general, the numerical models have high correlation to the physical tests and are as such suitable to model complex wave transformation with an accuracy sufficient for most coastal engineering applications. The VoF model performs more accurately under the turbulent conditions of breaking waves, increasing its relative accuracy in the prediction of downwave surface elevation. The sigma transformation model has simulation times one to two orders of magnitude lower than those of the VoF and SPH models.

Keywords: Wave transformation, Submerged bar, Shoaling, Breaking, Regular waves, Bichromatic waves, Wave flume, CFD, VoF, OpenFOAM, sigma transformation, MIKE 3 Wave Model FM, SPH, DualSPHysics

1. Introduction

Accurate prediction of wave transformation is fundamental in the design of coastal infrastructure, including sea dikes, sea walls, breakwaters, and substructures for nearshore wind turbines. The demand for such infrastructure is expected to increase in the coming years owing to climate change and the global energy (H. K. Jacobsen et al., 2019; Kantamaneni et al., 2022). Wave transformations encompass shoaling, refraction, diffraction, and breaking, and govern design parameters such as wave loads, wave run-up, and sediment transport which are critical for the design of coastal infrastructure. Wave transformations can be highly nonlinear and complex, e.g., from inherently

random, turbulent wave-breaking, nonlinear wave-wave interactions, and wave-decomposition (e.g., under deshoaling). Such complex wave transformations cannot be accurately predicted by the otherwise widely used Boussinesq-type equations (Beji & Battjes, 1994; Brocchini et al., 1992; Dingemans, 1994) or the shallow water equations (Kobayashi et al., 1987) forming the basis of many coastal engineering tools for modelling of wave transformation. Multiple correction modules to these models have been developed to account for physical processes not captured with the governing equations – however, with limited accuracy or application range. To reduce the influence from simplifying assumptions in the investigation of complex wave transformation, physical tests or computational fluid dynamics (CFD) models numerically solving the

Navier-Stokes equations may be employed. Physical tests in laboratory facilities are expensive, and scale effects, size restrictions, construction accuracy as well as disturbances of the flow field from physical measurement equipment may reduce the accuracy of physical model tests. On the other hand, CFD models allow for a less expensive analysis (e.g., through use of open-source codes) with no inherent uncertainty from measurement equipment. Besides, CFD models have high agility in the test setups, meaning for example the inclusion of different coastal structures can be handled rather easily relative to physical tests. That being said, CFD models rely on accurate physical tests in the validation stages of V&V (validation and verification) procedures prior to any practical application (Roache, 1998). Verification refers to the assessment of numerical uncertainty from discretization, iterative, and round-off errors, whereas validation refers to the assessment of model errors by comparison to other work – most often physical tests capturing the governing physics of the problem at hand (ASME, 2006).

1.1 High Fidelity Numerical Modelling of Wave Transformation

Today, most of the two-phase CFD codes used for engineering purposes employ interface capturing methods with advection of a scalar field that represents the free surface such as the distance to the free surface in Level-Set methods or a volume fraction of water in Volume of Fluid (VoF) methods (Bhushan et al., 2021; Wroniszewski et al., 2014). Within the topic of complex wave transformation including wave-breaking, the VoF-based, incompressible interFoam solver under the open-source framework OpenFOAM (Weller et al., 1998) is a highly popular and commonly used to solve the Unsteady Reynolds-Averaged Navier-Stokes (URANS) equations with closure from a turbulence model as in, e.g., Fernandez-Mora et al. (2017), Higuera et al. (2013), Li et al. (2022), Stagonas et al. (2018), and Torres-Freyermuth et al. (2007). Brown et al. (2016) investigated the performance of interFoam with several popular turbulence models against physical tests with spilling and plunging breaking waves by Ting and Kirby (1994). They highlighted the importance of the choice of turbulence model and recommended the nonlinear $k-\varepsilon$ model by Shih et al. (1993). The interFoam solver has somewhat high requirements for spatial and temporal resolutions for accurate performance in wave propagation applications (Gruwez et al., 2020b; Schmitt et al., 2020). Erroneous behaviour of interface wiggles, overestimation of crest velocities, and spurious air velocities have been reported predominantly at moderate to low resolutions (Johan Roenby et al., 2017; Larsen et al., 2019; Wroniszewski et al., 2014). The VoF method assumes a smooth density variation at the interface. However, for air-water interfaces the density gradient is very large and consequently not resolved which has been shown to cause an imbalance of the

momentum equation at the air-water interface (Qvist & Christensen, 2023; Vukčević et al., 2017) presumably leading the high requirements to resolution. Due to the high density ratio between water and air, the solution of the air phase is insignificant in the simulation of wave propagation in most coastal applications, i.e., where air entrainment is unimportant (Larsen et al., 2019). Based on this, single-phase solvers pose a feasible alternative to two-phase solvers in simulation of wave propagation as air velocities is often limiting time steps using maximum Courant-Friedrichs-Lewy (C_{FL}) conditions and the number of grids is decreased. Besides, directly imposing boundary conditions at the free surface can increase accuracy and mitigate the requirements for high resolutions at the interface in VoF methods (Ma et al., 2012; Qvist & Christensen, 2023). A computationally efficient method to achieve this is to transform the vertical coordinate into a sigma coordinate which encompasses the free surface and bathymetry (Lin & Li, 2002). A single-phase URANS solver utilizing the sigma-transformation approach is the MIKE 3 Wave Model FM (DHI, 2023c) from Danish Hydraulic Institute. An important restriction on the sigma-transformation approach is the free surface must be a single-valued function of class C^2 , i.e., continuous and two-times differentiable (Hicks, 2020), limiting the approach to model energy dissipation without modelling the actual wave-overturning (Ma et al., 2012).

Up till now, only CFD methods of Eulerian nature have been introduced. However, the Lagrangian method of Smoothed Particle Hydrodynamics (SPH) has grown increasingly popular in the past decade for especially large surface deformation cases within coastal engineering (Bhushan et al., 2021). The SPH method discretises the fluid domain into a set of fully Lagrangian computational grids or so-called particles. Hence, the method is meshless with inherent tracking of the free surface avoiding the challenges of (re-)gridding and special treatment of the free surface typically encountered in Eulerian methods. Single-phase models by weakly compressible SPH of the open-source framework DualSPHysics (Domínguez et al., 2021) have been applied in several studies on complex wave transformation, e.g., Zhu et al. (2019), Lowe et al. (2019), and Zhang et al. (2018). Spurious oscillations in the pressure and density fields of weakly compressible SPH is commonly mitigated by the addition of diffusive terms in the continuity equation referred to as delta-SPH (Antuono et al., 2012). Given the immaturity of the SPH method, relative to the more conventional Eulerian methods, five grand challenges (Vacondio et al., 2021) have been formulated by the international organisation SPHERIC to increase the credibility of SPH regarding, among others, convergence, consistency, and stability. Moreover, the method remains computationally expensive wherefore graphics processing unit (GPU) acceleration is made available with DualSPHysics.

As communicated above, the variety of high-fidelity numerical methods to simulate complex wave transformation is vast. Nevertheless, the advantages regarding the accuracy and applicability of the various methods are only scarcely described and, in particular, quantified in literature. Gruwez et al. (2020a) compared the VoF-based solver *interFoam* (OpenFOAM), weakly compressible SPH (DualSPHysics), and a nonlinear shallow water equation solver (SWASH) for wave interactions with sea dikes on shallow foreshores. *interFoam* had the best overall performance but also the highest computational cost while the overall performance of the SPH model was assessed high as well. Wroniszewski et al. (2014) inter-compared four VoF-based Navier-Stokes solvers (including *interFoam*) for solitary wave propagation and run-up on a plane beach. The study found that issues associated with the smeared interface of the *interFoam* solver (e.g., erroneous crest velocities as previously described in the present section) were mitigated with increasing resolutions but lacked experimental data. González-Cao et al. (2019) investigated regular, breaking waves impacting with a vertical sea wall on a steep foreshore with *interFoam* and weakly compressible SPH from DualSPHysics. For high resolutions, the models were reported to perform similarly in terms of accuracy whereas at low to moderate resolutions *interFoam* was more accurate. Park et al. (2018) benchmarked two VoF-based Navier-Stokes solvers (*interFoam* and Ansys Fluent) in interactions of non-breaking and breaking waves with elevated coastal structures. The study stressed the importance of the prediction of wave-breaking to accurately capture forces and pressure distributions on coastal structures and found that the models had similar accuracy relative to the physical tests with the highest deviations under breaking wave conditions. The benchmarking was, however, mostly qualitative and focused on two rather similar CFD models.

A strenuous test case for complex wave transformation that to the best of the authors' knowledge has not been used in the benchmarking of multiple CFD models is that of wave propagation over a submerged bar encompassing the complex wave transformations of wave-shoaling, nonlinear wave-wave interaction, wave-breaking, and wave-decomposition. Such wave transformations were investigated in the seminal, experimental work of Beji and Battjes (1993) which was reproduced and upscaled in Dingemans (1994). These experiments have been used widely to benchmark lower-fidelity models than CFD as, for example, Boussinesq-like models in Dingemans (1994) or for validation purposes of CFD models in, e.g., Jorge Gadelho et al. (2014), Kamath et al. (2015), and Schmitt et al. (2020), with most studies focusing on qualitative comparisons and/or disregarding wave-breaking.

1.2 Aim and Structure of Paper

The aim of the present paper is to assess the accuracy and applicability of three fundamentally different CFD models each prevalent within its own category, i.e., the VoF-based *interFoam* solver of OpenFOAM, the sigma-transformation solver of MIKE 3 Waves Model FM, and the weakly compressible delta-SPH solver of DualSPHysics. The numerical models are benchmarked against physical tests of wave propagation over a submerged bar under wave conditions of various nonlinearity, regularity, and wave-breaking. To this end, physical wave flume tests inspired by the tests of Beji and Battjes (1993) were carried out to generate dedicated datasets for numerical model benchmarking, or validation, allowing for the quantification of all physical parameters and measurement uncertainty – information which is rarely given in experimental papers in the engineering literature, and, e.g., lacks in the works of Beji and Battjes (1993) and Dingemans (1994).

An idealized test case was formulated to represent the physical tests in an accurate and simple manner aiming to maintain only the aspects of the physical test setup that govern the evolution of the free surface. Numerical models were then set up based on the idealized test case. The reason behind this strategy rather than seeking to do a full 3-D replicate of a physical wave flume was to decrease complexity and, hence, increase practicability to motivate further numerical or even physical tests on the test case by others. Datasets with the results of the physical wave flume tests and all numerical simulations are publicly available from the Mendeley Data repository of Andersen et al. (2023). To enhance transparency and reproducibility of numerical simulations, the input files of the numerical models are available from this repository as well.

The remainder of the present paper is structured as i) presentation of the idealized test case, ii) physical test setup, iii) governing equations of the numerical models and test setups, iv) uncertainty analysis of physical tests, v) definition of evaluation metrics, vi) convergence analysis of numerical tests, vii) results with comparisons in both time and frequency domain, snapshots of numerical free surface representation of turbulent bore, and computational costs, viii) discussion and interpretation of results with regard to the physics of the wave transformations in the test case and benchmarking of the numerical models in terms of both accuracy and applicability, and ix) conclusions.

1.3 Idealized Test Case

Consider a fully submerged bar with a trapezoidal cross-section. In a two-dimensional Cartesian coordinate system, the bar cross section is uniquely defined from four coordinate sets, see Fig. 1, corresponding to a front

slope of 1:10 and a rear slope of 1:5. The bathymetry up- and downwave of the bar is horizontal, and the water depth from the still water level (SWL) to the horizontal bed is $|y_2|$. The water density is ρ and the local acceleration due to gravity is g .

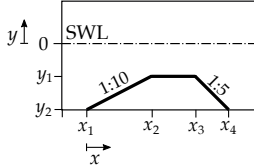


Fig. 1. Submerged bar with coordinates.

Table 1: Values of physical parameters of the idealized test case.

| Parameter | Unit | Value |
|-----------|-------------------|-------|
| x_1 | mm | 0 |
| x_2 | mm | 1510 |
| x_3 | mm | 2514 |
| x_4 | mm | 3261 |
| y_1 | mm | 147 |
| y_2 | mm | 300 |
| ρ | kg/m ³ | 998.2 |
| g | m/s ² | 9.82 |

Four wave conditions now describe incident, long-crested waves propagating in positive x , see Fig. 1 and Table 2. Wave conditions 1-3 are regular waves with increasing nonlinearity for increasing wave condition number and wave condition 4 is a bichromatic, nonlinear wave. Wave condition 1 can be considered a linear (Airy) wave prior to shoaling, whereas wave condition 2 has significant nonlinearity. Wave conditions 3 and 4 are nonlinear mono- and bichromatic waves, respectively, with plunging wave breaking at the horizontal crest of the bar. The four wave conditions are summarized in Table 2. Boundaries up- and downwave of the bar are assumed far away, therefore the only wave reflection occurring in the idealized test case is from the bar itself.

Table 2: Wave conditions in the idealized test case.

| Wave Condition | Note | H_1 [mm] | H_2 [mm] | T_1 [s] | T_2 [s] |
|----------------|-------------|---------------|---------------|--------------|--------------|
| 1 | Linear | 24 | - | 1.5 | - |
| 2 | Nonlinear | 56 | - | 1.5 | - |
| 3 | Breaking | 101 | - | 1.5 | - |
| 4 | Bichromatic | 47 | 52 | 1.5 | 1.0 |

2 Physical Test Setup

Physical tests with wave propagation over a submerged bar were carried out in the wave flume of the Ocean and

Coastal Engineering Laboratory of Aalborg University, Denmark. A conceptual layout of the physical tests is shown in Fig. 2. The overall dimensions of the wave flume are 22 m \times 1.5 m \times 1.5 m. The wave flume has a piston-type wavemaker (mean position at $x_0 = -2813$ mm) with active wave absorption capabilities and passive wave absorption from perforated panels at the end of the flume (starting at $x_5 = 12159$ mm and extending downwave). The coordinates of the bar profile are equal to those presented for the idealized test case in Table 1. Regular waves were generated with approximate stream function wavemaker theory as per Zhang and Schäffer (2007) whereas bichromatic waves were generated with second order wavemaker theory as per Schäffer (1996) with the adjustments of Eldrup and Lykke Andersen (2019).

The submerged bar was constructed out of marine plywood plates supported by three interior wooden rafters which were bolted to the flume floor. Thin metal sheets were installed at the front and rear toe of the bar to avoid flow underneath the bar. Gaps between the bar and flume side walls were sealed with silicone.

Resistance wave gauges were installed at 20 locations in the wave flume, see Fig. 2 and Table 3. Wave gauge numbers (WGnos.) 1-5 and 13-19 were set up in arrays with inter-distances appropriate for reflection analyses. A pressure transmitter (VEGAWELL 52, permanent installation) was used to measure the water depth in the flume. The wave gauges were calibrated with five points over the expected surface elevation measurement range.

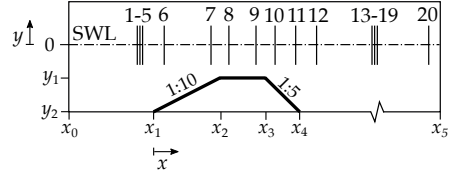


Fig. 2. Conceptual layout of the physical tests. Numbered vertical lines indicate wave gauge locations while bold lines indicate bar geometry. x is downscaled by 5 relative to y for better overview.

Table 3: Coordinates of wave gauges as illustrated in Fig. 2.

| WGno. | 1 | 2 | 3 | 4 | 5 |
|----------|-------|-------|------|------|-------|
| x [mm] | -1983 | -1311 | -760 | -453 | -205 |
| WGno. | 6 | 7 | 8 | 9 | 10 |
| x [mm] | 199 | 1300 | 1708 | 2305 | 2707 |
| WGno. | 11 | 12 | 13 | 14 | 15 |
| x [mm] | 3051 | 3460 | 6703 | 6775 | 6890 |
| WGno. | 16 | 17 | 18 | 19 | 20 |
| x [mm] | 7172 | 7461 | 8023 | 8690 | 11966 |

3 Numerical Model Fundamentals and Test Setups

The three investigated numerical models are denoted i-VoF, M-sigma, and D-SPH and are presented in Sections 3.1, 3.2, and 3.3, respectively. The numerical models are all based on the Navier-Stokes equations which express the conservation of mass and momentum of a Newtonian fluid. The general Navier-Stokes equations read

$$\frac{\partial \rho}{\partial t} + \nabla \cdot \rho \mathbf{U} = 0 \quad (3.1)$$

$$\frac{\partial}{\partial t} \rho \mathbf{U} + \nabla \cdot (\rho \mathbf{U} \mathbf{U}) = \nabla \cdot \boldsymbol{\tau} - \nabla p + \rho \mathbf{g},$$

where \mathbf{U} denotes the fluid velocity vector, t the time, ρ the fluid density, p the pressure, \mathbf{g} the acceleration due to gravity vector, and $\boldsymbol{\tau}$ the viscous stress tensor which under the Stokes hypothesis is given as

$$\boldsymbol{\tau} = \left(\mu (\nabla \mathbf{U} + (\nabla \mathbf{U})^T) - \frac{2}{3} \mu (\nabla \cdot \mathbf{U}) \mathbf{I} \right) \quad (3.2)$$

where μ is the dynamic viscosity. Imposing the constraint of incompressibility and constant viscosity, the equations take the form

$$\nabla \cdot \mathbf{U} = 0$$

$$\frac{\partial \mathbf{U}}{\partial t} + \nabla \cdot (\mathbf{U} \mathbf{U}) = \nu \nabla^2 \mathbf{U} - \frac{1}{\rho} \nabla p + \mathbf{g}, \quad (3.3)$$

where ν is the kinematic viscosity. The governing equations of the three numerical models are further presented in the following sections. All numerical models are set up as two-dimensional as the geometry is nominally two-dimensional and no scale-resolving methods are employed for turbulence treatment.

3.1 i-VoF (interFoam VoF model)

OpenFOAM (Weller et al., 1998) is an open-source CFD framework based on the finite volume method (FVM). The i-VoF model is based on the interFoam solver under OpenFOAM v2206 (Open CFD Ltd, 2023) using the incompressible URANS equations with turbulence closure from the nonlinear k - ε model (Shih et al., 1993). The incompressible URANS equations are derived from Reynolds-decomposition of Eq. (3.3) yielding

$$\nabla \cdot \bar{\mathbf{U}} = 0$$

$$\frac{\partial}{\partial t} \bar{\mathbf{U}} + \nabla \cdot (\bar{\mathbf{U}} \bar{\mathbf{U}}) = \nu \nabla^2 \bar{\mathbf{U}} - \frac{1}{\rho} \nabla \bar{p} + \mathbf{g} - \nabla \cdot (\overline{\mathbf{U}' \mathbf{U}'}), \quad (3.4)$$

where $\bar{\phi}$ indicates the mean (ensemble average) of the general flow field ϕ and ϕ' indicates fluctuations. The last term in Eq. (3.3) is the divergence of the Reynolds stress tensor which by the Boussinesq hypothesis can be accounted for by modelling of a turbulent (eddy) viscosity ν_t that relates the mean strain-rate tensor to the Reynolds stress tensor analogously to how the molecular viscosity relates the mean strain-rate tensor to the mean shear tensor. The nonlinear k - ε model by (Shih et al., 1993) utilizes the eddy viscosity assumption but includes a nonlinear stress term τ_{NL} in the Reynolds stress tensor and τ_{NL} goes into the production terms of

the transport equations of k and ε (Brown et al., 2014; Shih et al., 1993).

The interFoam solver captures the interface between phases by solving a transport equation for the phase fraction field α which can take on values between 0 and 1, see Eq. (3.5). Sharpness and boundedness of the interface is handled by a numerical interface compression method, introducing an artificial compression term to the α transport equation (last term in Eq. (3.5)), and the multi-dimensional limiter for explicit solution MULES (Larsen et al., 2019).

$$\frac{\partial \alpha}{\partial t} + \nabla \cdot \alpha \mathbf{U} + \nabla \cdot (\alpha (1 - \alpha) \mathbf{U}_r) = 0, \quad (3.5)$$

where \mathbf{U}_r is a modelled relative velocity vector. Refer to Deshpande et al. (2012) for further details on the numerical implementation. Inherent fluid properties are then calculated by the phase fraction as

$$\psi = \alpha \psi_1 + (1 - \alpha) \psi_2, \quad (3.6)$$

where ψ is any inherent fluid property and subscripts denote different phases.

Wave generation and absorption are handled by the relaxation zone method integrated in the waves2Foam toolbox by Jacobsen et al. (2012). The relaxation zone method weights analytical target solutions ϕ_{target} of the phase fraction and velocity fields with computed solutions ϕ_{comp} at defined zones at the inlet/outlet.

$$\phi = w_R \phi_{comp} + (1 - w_R) \phi_{target}, \quad (3.7)$$

where $w_R \in [0, 1]$ is a relaxation weight distribution taking on values of 0 and 1 at the domain boundary and relaxation zone interface, respectively, and applying the exponential weight distribution as per Fuhrman et al. (2006).

Stream function wave theory (Fenton, 1988) and second order bichromatic wave theory with wave-wave interaction (Madsen & Fuhrman, 2006) are employed as target solution in the inlet relaxation zone whereas zero velocity and surface elevation are employed as target solutions for the outlet relaxation zone. The inlet and outlet relaxation zones have lengths of one and two L_1 , respectively, see Fig. 3, where L_1 denotes the wavelength from T_1 following linear dispersion. The bar geometry and distances to relaxation zones follows that of the physical test, see Fig. 2 and Table 3, with x_0 and x_5 corresponding to $w_R = 1$ in the relaxation zones. A no-slip boundary condition (BC) is used for the bed while zero pressure and zero velocity gradient are employed as BCs at the top boundary. Initial conditions (ICs) for velocity, pressure, and phase fraction were chosen to represent stagnant water. The inlet BC and IC for the turbulence kinetic energy k and the turbulence dissipation rate ε were calculated based on Lin and Liu (1998) which simulated wave-breaking with the nonlinear k - ε model of Shih et al. (1993). To allow the production of k (in the k -transport equation) and avoid singularities in the ε -transport equation small values

were seeded at the inlet and initialization. k and ε at the inlet and initialization were calculated from

$$k = \frac{1}{2} (I_t L_1 / T_1)^2$$

$$\varepsilon = C_d \frac{k^2}{\chi v}, \quad (3.8)$$

where L_1/T_1 is the wave celerity and I_t and χ are constants set in accordance with Brown et al. (2016). Brown et al. (2016) based the constants on the original work of Lin and Liu (1998). However, at a late stage it was found that the k -equation given in Brown et al. (2016) was inconsistent with that of Lin and Liu (1998), presumably due to a typo; the equation of Brown et al. (2016) used I_t instead of I_t^2 . As Eq. (3.8) was primarily applied to seed non-zero values, a simple sensitivity analysis of the values following the equations given in Brown et al. (2016) and Lin and Liu (1998), respectively, were taken on. Only insignificant impacts on the surface elevation time series were detected. Wall functions were adapted for estimation of turbulence fields at the bed and $y^+ \in [30, 100]$ was sustained throughout all simulations.

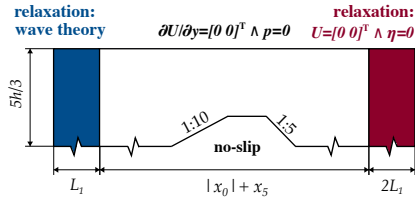


Fig. 3. Domain and BCs for the i-VoF model.

A structured mesh of predominantly hexahedral-type with two refinement zones around the SWL was used. Cells close to the free surface had aspect ratios of one which is encouraged for simulations of wave breaking with interFoam (Jacobsen et al., 2012). The vertical extent of the refinement zones were parameterized with the wave height such that first and second level refinement zones extended $\pm 2H$ and $\pm 1.5H$ relative to the SWL, respectively, where $H = H_1$ for wave conditions 1-3 and $H = H_1 + H_2$ for wave condition 4, see Fig. 4. Polyhedral cells were used at the refinement zone interfaces.

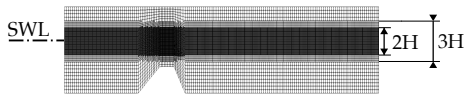


Fig. 4. Conceptual layout of mesh with refinement zones (distorted x/y).

Variable time stepping was computed from a maximum C_{FL} criterion and time marching of the solution was carried out with a first order accurate temporal discretization scheme (backward Euler) to retain stability. Second-order accurate spatial discretization schemes were employed for diffusion, gradient, and Laplacian terms (central-differencing) as well as

momentum convection (upwind central-differencing) and phase fraction convection (MUSCL). First-order upwind schemes were applied for the convection of k and ε .

3.2 MIKE 3 Waves FM sigma model (M-sigma)

The M-sigma model is based on the MIKE 3 Wave Model FM developed by DHI (DHI, 2023c) to solve the incompressible URANS equations, see Eq. (3.4), with a transformation of the vertical coordinate y into the sigma coordinate

$$\sigma = \frac{y + h}{\eta + h}, \quad (3.9)$$

where y has origin at SWL (Fig. 1) and h is the vertical distance from the SWL to the bed. It then follows $\sigma = 0$ at the bed and $\sigma = 1$ at the free surface, see Fig. 5.

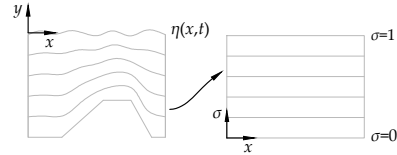


Fig. 5. Concept of the sigma transformation.

M-sigma is solved on a structured mesh with equidistantly spaced cells in σ (so-called sigma layers) and x , respectively. The convergence with the number of sigma-layers and horizontal faces on the wave transformation are considered in Section 6.2.

Wave generation and absorption in the M-sigma model were handled by a relaxation zone upwave of the bar while sponge layers were used for wave absorption downwave of the bar, see Fig. 6. Similarly to the i-VoF model, the domain geometry follows that of the physical test, see Fig. 2 and Table 3, with x_0 corresponding to the end of the relaxation zone and x_5 corresponding to the beginning of the sponge layers.

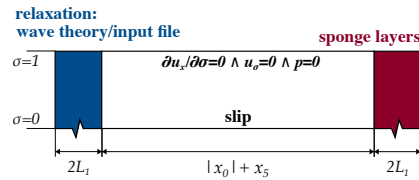


Fig. 6. Domain and BCs for the M-sigma model.

The implemented relaxation zone technique follows that of the i-VoF model, see Eq. (3.7), with the same exponential weight function as default. The analytical values were calculated with the built-in stream function wave method (Fenton, 1988) for the regular waves. For the bichromatic waves no built-in function exists but there is the possibility to provide an input file with amplitudes, frequencies, wavenumbers, phases, and

directions for any number of wave components from which surface elevations and kinematics are calculated and superimposed. Wave parameters were calculated by the method of Schäffer (1996) and applied as wave generation input for wave condition 4.

The sponge layer technique is based on the method by (Larsen & Dancy, 1983). In the sponge layer, the surface elevation and the velocities are multiplied with $1/c_s$ where c_s is the sponge coefficient. c_s is close to unity at the beginning of the sponge and increase towards the end following

$$c_s = \kappa e^i, \quad (3.10)$$

where κ and ϱ are constants that depend on the total number of horizontal cells in the sponge layers N_{sponge} , see Table 4, and i is the horizontal cell number with $i = N_{\text{sponge}}$ at the start and $i = 0$ at the end. DHI, (2023a) recommends a width of 1-2 wavelengths of the most energetic wave and thus a width of $2L_1$ is applied.

Table 4: Sponge layer coefficients.

| $N_{\text{sponge}} <$ | κ | ϱ |
|-----------------------|----------|-----------|
| 20 | 5 | 0.5 |
| 50 | 7 | 0.7 |
| 100 | 10 | 0.85 |
| 200 | 10 | 0.92 |
| ∞ | 10 | 0.98 |

The model uses a variable time step based on a maximum C_{FL} criteria. The temporal and spatial discretization schemes were chosen as first order accurate (backwards Euler and upwind, respectively). More details on the numerical solution procedures can be seen in (DHI, 2023b). The interface fluxes are calculated with an approximate Riemann solver. In the M-sigma model, the HLLC solver by Toro et al. (1994) is used. The HLLC works as a shock-capture to enhance the stability, which is especially important for simulations with breaking waves.

The k - ε turbulence model presented by Rodi (1980, 1984) is employed for closure of the sigma-transformed URANS equations (only k - ε or k - ω models are available in MIKE 3 Waves Model FM). The model is extended with bouncy terms and limiters to stabilize the eddy viscosity in regions where the flow is nearly potential, see Larsen and Fuhrman (2018). Default values are used for the initial conditions of k and ε (DHI, 2023a) Initial conditions of η , U , and p were chosen to represent stagnant water.

3.3 DualSPHysics SPH model (D-SPH)

In the SPH method, the fluid is discretized to a set of particles where the field ϕ_i (position, velocity, density, and pressure) of the particle i is calculated as an interpolation of the corresponding field of the neighboring particles j . The contribution of each neighboring particle is determined using a weighting

function W_{ij} , referred to as a kernel, with an area of influence depending on a characteristic smoothing length β_h within which fields are interpolated (or smoothed) based on their distance to particle i .

The D-SPH model is based on weakly compressible delta-SPH in the open-source CFD framework DualSPHysics (Domínguez et al., 2021). delta-SPH refers to the inclusion of a numerical density diffusion term (DDT) in the continuity equation to reduce spurious pressure and density fluctuations (Antuono et al., 2012). The weakly compressible delta-SPH formulation of the compressible Navier-Stokes equations (Eq. (3.1)) can be written in discrete form as

$$\begin{aligned} \frac{d\rho_i}{dt} &= \sum_j m_j (U_i - U_j) \cdot \nabla_i W_{ij} + D_i \\ \frac{dU_i}{dt} &= - \sum_j m_j \left(\frac{p_j + p_i}{\rho_j \rho_i} + \Pi_{ij} \right) \nabla_i W_{ij} + g, \end{aligned} \quad (3.11)$$

where t is time, U is the velocity, p is the pressure, ρ is the density, m is the mass, g is the acceleration due to gravity, D is the DDT, and Π_{ij} is an artificial viscosity term. In this study, the Quintic kernel (Wendland, 1995) was adopted as W_{ij} . This kernel interpolates fields from neighboring particles within a radius of $2\beta_h$. The DDT proposed by Fournakos et al. (2019) was employed as it has proven to increase the accuracy of the results for the pressure field near the boundaries without compromising the computational time. The artificial viscosity term Π_{ij} proposed by Monaghan (1992) was used as a viscous dissipation term depending on the artificial viscosity coefficient γ_v .

Due to the assumption of weak compressibility an equation of state is needed for closure. The Tait's equation with a high speed of sound couples the density and pressure as

$$p = \frac{C^2 \rho_0}{7} \left(\left(\frac{\rho}{\rho_0} \right)^7 - 1 \right), \quad (3.12)$$

where ρ_0 is the reference fluid density, 7 is the polytropic constant and C is the numerical speed of sound at the reference fluid density (Monaghan, 1994). This formulation adjusts the fluid compressibility by artificially lowering C resulting in reasonable time steps (Monaghan, 1994). Wave generation in D-SPH is generally handled in three different ways: i) moving boundary particles imitating a physical wavemaker, ii) relaxation zones, and iii) open boundaries. For the present study, wave generation method i) with 2nd order wavemaker theory (Hughes, 1993) was employed for all regular sea states as it is the standard wave generation method in DualSPHysics (higher order wavemaker theories have not been implemented in current releases). A detailed description of the implementation can be found in Altomare et al. (2017). Higher order irregular wavemaker theory is not included in current DualSPHysics releases, and the bichromatic wave of condition 4 was therefore generated from an input file

with prescribed motion of the piston-type wavemaker calculated from the irregular second order wave maker theory of (Schäffer, 1996). The physical wavemaker were adjusted to account for leakage wherefore the logged wavemaker signal were not used as direct input. The free surface is extracted from the D-SPH model where kernels are 40% water based on mass (recommended limit for two-dimensional simulations). In case of multi-valued free surface functions, as seen with plunging waves, the coordinate closest to the bed is extracted (discussed in Section 8.2). The two-dimensional domain of the D-SPH model can be seen in Fig. 7. Five layers of boundary particles was used to represent the piston-type wavemaker. The no-slip BC was imposed to the bed which was made up of minimally five layers of boundary particles to ensure proper interaction between the fluid particles and the boundary particles of the bed. At $x = x_5$ a dissipative beach with a slope of 1:16 and horizontal length of $7L_1/2$ was implemented as passive absorption. Additionally, a relaxation zone was defined with weighting towards stagnant water from a quadratic weighting function along the length of the dissipative beach. Modified Dynamic Boundary Conditions (mDBC) as per English et al. (2021) were employed at the wavemaker and bed to mitigate unphysical gaps between boundary and fluid particles otherwise known to occur with the conventional DBC.

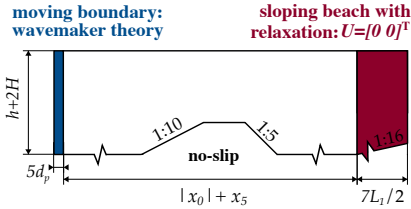


Fig. 7. Domain and BCs for the D-SPH model.

4 Uncertainty Analysis of Physical Tests

Measurement uncertainties of the physical tests are accounted for by the construction of uncertainty intervals (UIs) with a 95% level of confidence in Section 4.1. Uncertainties of the physical parameters of the idealized test case are given in Section 4.2.

4.1 Expanded Uncertainty on Surface Elevation Time Series

Five repetitions were used for all physical tests. Two-sided 95% UIs around the sample mean surface elevation time series $\bar{\eta}(t)$ were constructed as

$$\bar{\eta}(t) \pm t_{0.95,4} u_{\bar{\eta}}(t) = \bar{\eta}(t) \pm U_{\bar{\eta}}(t), \quad (4.1)$$

where $t_{0.95,4}$ is the Student's t-factor (95% confidence level, 4 degrees of freedom, two-sided), $u_{\bar{\eta}}$ is the combined standard uncertainty, and $U_{\bar{\eta}}$ is the expanded standard uncertainty. The surface elevation η was

measured by resistance wave gauges from the linear function

$$\eta = z_2(V - V_0), \quad (4.2)$$

where V is the voltage output during testing, V_0 is reference voltage output at SWL (prior to testing), and z_2 is a calibration constant. The uncertainties of the input quantities of Eq. (4.2) were propagated to η by the law of combination of uncertainty (first order Taylor series approximation) in accordance with BIMP et al. (2008), which takes the form

$$u_{\eta}^2 = (V - V_0)^2 u_{z_2}^2 + (z_2 - z_2 V_0)^2 u_V^2 + (z_2 V - z_2)^2 u_{V_0}^2. \quad (4.3)$$

The discretization uncertainty of the measured voltage is found as a Type B estimate based on the resolution of the signal (± 10 V, 16 bits) and assuming a rectangular distribution within the resolution limits (BIMP et al., 2008). As V and V_0 are estimated from the sample mean of $N = 5$ repetitions their uncertainties from repeatability were simply taken as the standard deviation of the estimates, i.e.,

$$s_{\bar{X}} = s_X / \sqrt{N}, \quad (4.4)$$

where $s_{X,N}$ is the sample standard deviation of X . The calibration parameter z_2 and associated uncertainty were estimated using a weighted total least squares (WTLS) approach (Krystek & Anton, 2007), accounting for uncertainties in the input data (errors-in-variables), on the linear calibration function

$$h^* = z_1 + z_2 V, \quad (4.5)$$

where h^* denote the water level from a given reference point, z_1 is the intercept, z_2 is the slope, and V is the voltage signal from the wave gauges. The standard uncertainty of the measured h^* was estimated as the maximum of the standard uncertainty of the pressure transmitter (technical datasheet, ISO Type A) and that of a vertically mounted laser distance measurer (declared accuracy of 2 mm, interpreted as the semi-interval, ISO Type B) which was used as a secondary measurement method. The two measurement methods had no detectable deviations in measured water level variations and the maximum standard uncertainty was thus conservatively applied for h^* . The uncertainty of V was taken as the discretization uncertainty. The standard uncertainties of each the input quantity X as given in Eq. (4.2) and propagated to u_{η} in Eq. (4.3) were calculated as the root-sum-square of the elemental uncertainties of X . These are summarized in Table 5.

Table 5: Uncertainty table.

| X | Note | u_{x_i} | ISO Types |
|-------|---------------|-----------|-----------|
| V | Resolution | 0.15 mV | B |
| | Repeatability | Eq. (4.4) | A |
| V_0 | Resolution | 0.15 mV | B |
| | Repeatability | Eq. (4.4) | B |
| z_2 | Bias | WTLS | A |

4.2 Uncertainty of Test Case Parameters

The uncertainty of the physical test parameters which are the basis of the idealized test case are presented in Table 6. These uncertainties have not been propagated into uncertainties on the surface elevation time series (which is non-trivial) and are therefore not included in the constructed 95% UI. Nevertheless, they are given to present the variability of the physical test parameters, i.e., the benchmark. The distances of wave gauges to the mean-position of the piston wavemaker were measured meticulously with a laser distance measurer (declared accuracy of 2 mm). Upper and lower bounds of the measurement process were estimated as ± 10 mm. A rectangular distribution with a semi-interval of 10 mm (ISO Type B) around the measured values was assumed to estimate the standard uncertainty of the wave gauge locations – denoted x_{WG} in Table 6. The standard uncertainty of ρ and g are adopted from (Kramer et al., 2021) in which the same laboratory under similar conditions (temperature) were used. y -coordinates were measured at 6 spanwise coordinates between the flume side walls at the toe and the back edge while 5×6 measurements were carried out at the bar crest. The standard uncertainties of the y -coordinates were estimated from combining, by root-mean-square, the uncertainty of a laser distance measurer (2 mm semi-interval), used for profiling of the bar, with the standard deviation of y -coordinates from the multiple measurements point at the bar toe and back edge and the horizontal bar crest. x -coordinate measurements were carried out at a single spanwise coordinate and the uncertainties are assumed equal to those of y_2 . The uncertainties of H were derived from those of the free surface elevation time series and are given in Table 6 where the first subscript denotes primary/secondary component, and second subscript denotes wave condition. The uncertainties of T are assumed negligible.

Table 6: Uncertainties of parameters from the physical tests

| Parameter | Unit | Value | Standard Uncertainty |
|-----------|-------------------|---------|----------------------|
| x_1 | mm | 0 | 2.3 |
| x_2 | mm | 1510 | 2.3 |
| x_3 | mm | 2514 | 2.3 |
| x_4 | mm | 3261 | 2.3 |
| x_{WG} | mm | Table 3 | 5.8 |
| y_1 | mm | 147 | 2.3 |
| y_2 | mm | 300 | 1.5 |
| ρ | kg/m ³ | 998.2 | 0.4 |
| g | m/s ² | 9.82 | 0.003 |
| $H_{1,1}$ | mm | 24 | 0.1 |
| $H_{1,2}$ | mm | 56 | 0.3 |
| $H_{1,3}$ | mm | 101 | 1.2 |
| $H_{1,4}$ | mm | 47 | 0.7 |
| $H_{2,4}$ | mm | 52 | 1.7 |

5 Evaluation Metrics

Surface elevation time series are compared to reference time series quantitatively by evaluation metrics. These metrics are utilized in both the convergence analyses of the individual models and in the physical- and inter-model comparison with the only difference being the reference. The evaluation metrics are statistical scalars extracted from a given surface elevation time series $\eta(t)$ and a reference surface elevation time series $\eta_{ref}(t)$. The evaluation metrics include the normalized mean absolute error δ_{direct} , the residual relative standard deviation δ_{std} , the residual correlation coefficient δ_{corr} , and the normalized error on means δ_{mean} . The evaluation metrics are thus selected to represent various error types between signals and are defined in Eqs. (5.1)-(5.4). All evaluation metrics tend to zero when $\eta(t)$ tends to $\eta_{ref}(t)$.

The normalized mean absolute error δ_{direct} reflects the direct absolute difference between two signals, and is given as

$$\delta_{direct} = \frac{\sum_{j=1}^N |\eta_j - \eta_{ref,j}|}{N(\max(\eta) - \min(\eta))}, \quad (5.1)$$

where N is the total number of data points contained within the analyzed time window. The residual relative standard deviation δ_{std} reflects differences in the amplitude/energy content between two signals with positive values indicating higher energy content in the considered time series than in the reference and vice versa.

$$\delta_{std} = 1 - \frac{\sqrt{\sum_{j=1}^N (\eta_{ref,j} - \bar{\eta}_{ref})^2}}{\sqrt{\sum_{j=1}^N (\eta_j - \bar{\eta})^2}}, \quad (5.2)$$

where the overbar indicates time averaging (rather than ensemble averaging as in Eq. (3.4)). The residual correlation coefficient δ_{corr} reflects phase differences between two signals with values of 1 and 2 signifying zero correlation and anticorrelation, respectively.

$$\delta_{corr} = 1 - \frac{\sum_{j=1}^N (\eta_j - \bar{\eta})(\eta_{ref,j} - \bar{\eta}_{ref})}{\sqrt{\sum_{j=1}^N (\eta_j - \bar{\eta})^2} \sqrt{\sum_{j=1}^N (\eta_{ref,j} - \bar{\eta}_{ref})^2}}. \quad (5.3)$$

The normalized error on means δ_{mean} reflects differences in mean water levels from, e.g., wave set-up with positive values indicating a higher mean water level in the considered surface elevation time series relative to the reference.

$$\delta_{mean} = \frac{\bar{\eta} - \bar{\eta}_{ref}}{\max(\eta) - \min(\eta)}. \quad (5.4)$$

6 Convergence of Numerical Models

The convergence of the three investigated numerical models is accounted for in the present section. The

convergence analyses are based on qualitative assessments from surface elevation time series and quantitative assessments from evaluation metrics, see Section 5. Surface elevation time series are extracted from wave gauges 5, 7, 10, and 12, representing wave gauge positions upwave of the bar (pre-shoaling), at the bar (shoaling and deshoaling), and downwave of the bar (re-adjustment to horizontal bed), see Fig. 2. Time windows of $2T_1$ are extracted from the second zero-up-crossing after propagation (linear celerity) to the wave gauge position and wave-ramp-up. Only the convergence analyses for wave condition 4 (bichromatic breaking waves) are included in the present section. The convergence analyses of wave conditions 1-3 are included in Appendix A.

6.1 Convergence of i-VoF

A typical normalized measure of the spatial resolution of cell-based numerical models with wave propagation is the number of cells per wave height N_{ch} (e.g., Roenby et al., 2017; Larsen et al., 2019), which in the present is adopted as

$$N_{ch} = H/r_c, \quad (6.1)$$

where r_c is the cell size in the finest refinement zone and $H = H_1$ for wave conditions 1-3 and $H = H_1 + H_2$ for wave condition 4. It should be noted that the cell aspect ratio is approximately one and that N_{ch} thus indicate both the horizontal and vertical resolutions. As mentioned in Section 3.1, maximum C_{FL} criteria were employed for time stepping, wherefore the maximum C_{FL} is used as a measure for the temporal resolution. The spatial resolution was varied with $N_{ch} \in \{10, 20, 30, 40, 50\}$ with a constant maximum $C_{FL} = 0.10$ found to be sufficiently small to not lead the discretization error at up to $N_{ch} = 40$. Likewise, the temporal resolution was varied (independently) with a maximum $C_{FL} \in \{0.30, 0.20, 0.15, 0.10, 0.05\}$ with a constant $N_{ch} = 40$. The finest resolutions were used as references in the calculation of evaluation metrics. The influence of N_{ch} and C_{FL} on the selected surface elevation time series and evaluation metrics are shown in Figs. 8-11.

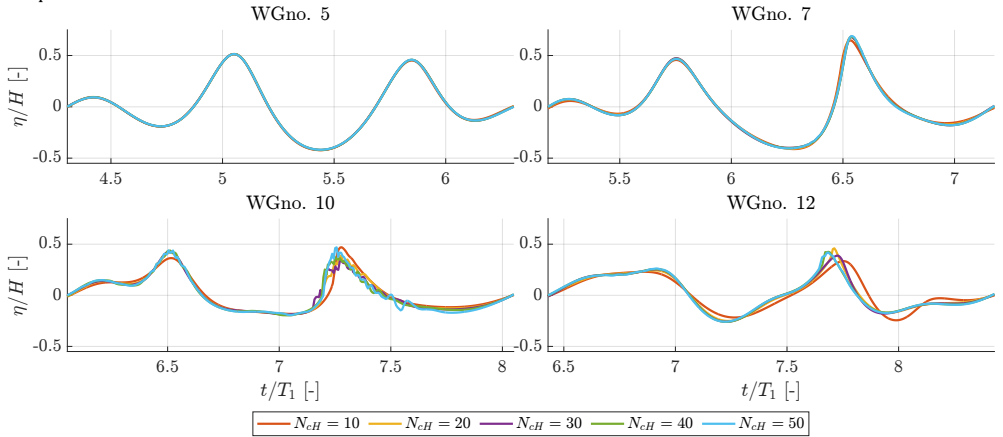


Fig. 8. Influence of N_{ch} on the surface elevation time series for selected WGnos.; wave condition 4 and maximum $C_{FL} = 0.10$.

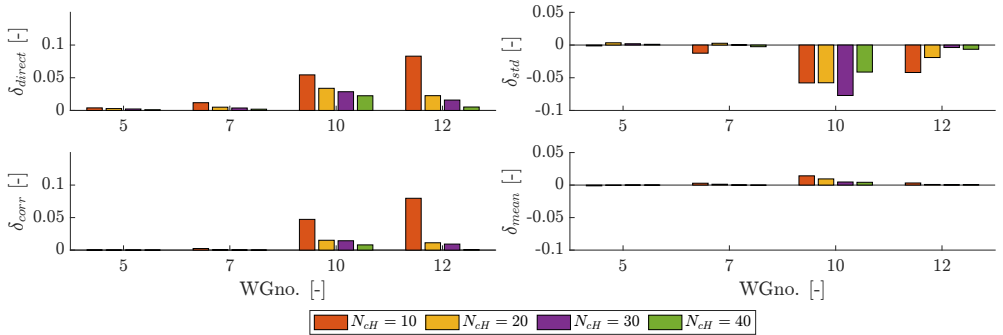


Fig. 9. Influence of N_{ch} on evaluation metrics for selected WGnos.; wave condition 4 and maximum $C_{FL} = 0.10$.

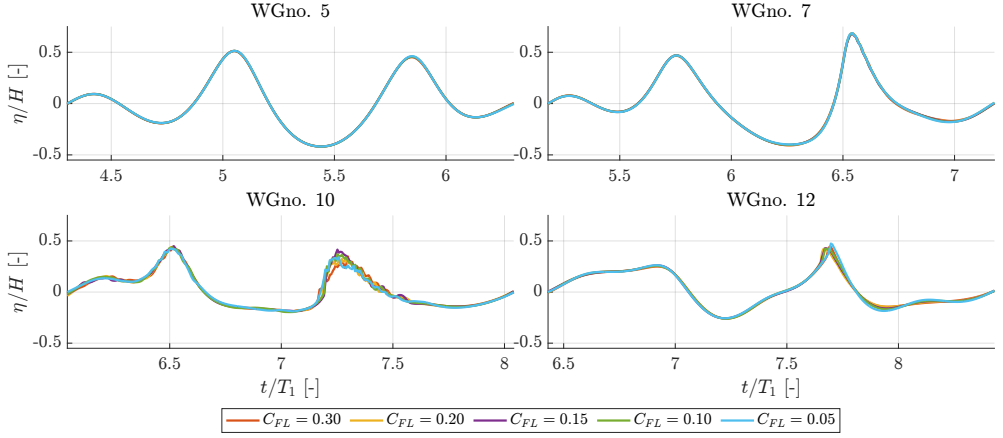


Fig. 10. Influence of maximum C_{FL} on surface elevation time series for selected WGnos.; wave condition 4 and $N_{CH} = 40$.

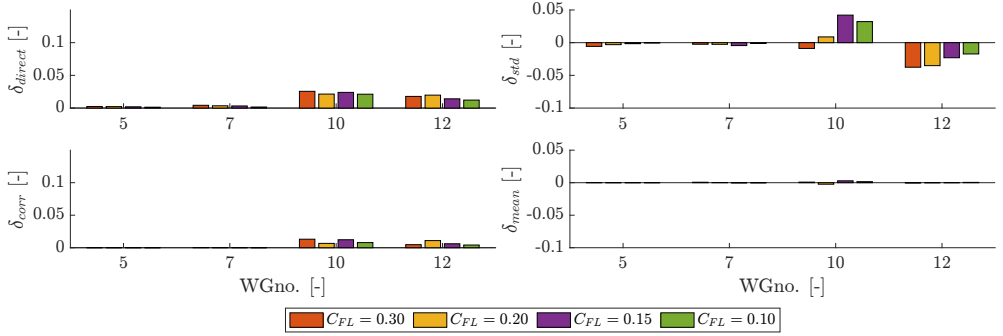


Fig. 11. Influence of maximum C_{FL} on evaluation metrics for selected WGnos.; wave condition 4 and $N_{CH} = 40$.

While wave propagation seems largely independent of N_{CH} in the tested range at WGnos. 5 and 7 (pre-shoaling and shoaling), the wave breaking is affected significantly by N_{CH} as can be seen from WGno. 10, at $t/T_1 \approx 7.2$. With evaluation metrics well below 5% and surface elevation time series basically indistinguishable, see Figs. 8 and 9, $N_{CH} \geq 40$ is assessed converged. The different numerical diffusive balances obtained with meshes of lower N_{CH} spur delayed breaking onsets and differences from the decomposed waves downwave of the bar at WGno. 12 can be detected, see WGnos. 10 and 12 in Fig. 8. The variation of maximum C_{FL} affects the surface elevation time series and evaluation metrics less than N_{CH} over the tested ranges. The breaking point in the WGno. 10 time series is not altered significantly from C_{FL} , but rather the level of interface wiggles and (partly as a consequence) the amplitude immediately prior to breaking vary with the maximum C_{FL} . These effects are presumably due to the light air phase dictating the time steps with the maximum C_{FL} criterion from which C_{FL} in

the water phase remains well below the maximum C_{FL} and the water phase thus remains largely unaltered from the variation hereof. Nonetheless, the erroneous formation of interface wiggles is mitigated by lowering the maximum C_{FL} . The crest height at $t/T_1 \approx 7.2$ at WGno. 10 is approximately 25% smaller with $C_{FL} = 0.30$ relative to $C_{FL} = 0.05$ though $\delta_{std} < 5\%$. Lowering C_{FL} to 0.20 and 0.15 gives a slightly oscillatory convergent behavior in predicting crests at WGnos. 10 and 12 and does not mitigate interface wiggles at the wave crest. $C_{FL} = 0.10$ is assessed sufficiently converged with all evaluation metrics well below 5% and only minor qualitative differences at WGnos. 10 and 12 in Fig. 10. $C_{FL} \geq 0.40$ was also tested and yielded unstable simulations.

Similar analyses were carried out for the i-VoF model with wave conditions 1-3, see Appendix A.1. Conclusions are summed up in Table 7.

Table 7: Selected N_{ch} and $\max(C_{FL})$ after convergence analysis of each wave condition.

| Wave condition | N_{ch} | $\max(C_{FL})$ |
|----------------|----------|----------------|
| 1 | 10 | 0.50 |
| 2 | 20 | 0.40 |
| 3 | 30 | 0.10 |
| 4 | 40 | 0.10 |

6.2 Convergence of M-sigma

The horizontal resolution of the M-sigma model is given from the number of cells per wavelength:

$$N_{cl} = L_m / r_{cl}, \quad (6.2)$$

where N_{cl} is the number of cells horizontally per wavelength, r_{cl} is the horizontal cell size, and L_m is the smallest wavelength in the domain estimated as the wavelength at the horizontal bar crest from T_1 by linear dispersion. The horizontal resolution was varied with $N_{cl} \in \{40, 60, 80, 100, 150, 200\}$. The vertical resolution is given from N_σ which denotes the number of sigma-layers. The recommended values given by DHI, 2023a are $N_\sigma = 4-7$ for non-breaking waves and $N_\sigma = 8-12$ for breaking waves. In the present work $N_\sigma \in \{5, 10, 15, 20\}$ which covers the recommended values. The maximum C_{FL} was varied with $C_{FL} \in \{0.8, 0.6, 0.4\}$ which yielded only negligible variations of surface elevations and associated evaluation metrics, <1%. A higher maximum C_{FL} criteria was not imposed due to stability reasons. DHI, 2023a recommends a default value of 0.8. Hence,

results with C_{FL} of 0.8 is only shown in the present paper.

The influence of N_{cl} and N_σ on the selected surface elevation time series and evaluation metrics are shown in Figs. 12-15. Figs. 12 and 13 show the sensitivity of N_{cl} with $N_\sigma = 15$. At WGno. 5, the wave profiles are very similar for all N_{cl} with minor deviations $\delta_{direct} \leq 3\%$. At WGno. 12, this error increases to >7% for $N_{cl} \leq 60$. The error is mainly governed by the phase error shown by δ_{corr} which is between 6-11%. Increasing the horizontal resolution to $N_{cl} = 100$ yields <5% for all evaluation metrics. However, from the qualitative assessment of the surface elevation time series in Fig. 12, the shape of the breaking wave at around $t/T_1 = 7.25$ at WGno. 10 differs notably between $N_{cl} = 100$ and $N_{cl} \geq 150$ with an overestimation of the crest elevation of about 20%. Consequently, $N_{cl} = 150$ is assessed converged. Figs. 14 and 15 show the sensitivity to N_σ using $N_{cl} = 150$. Again, evaluation metrics are largest at WGnos. 10 and 12, but with the variation of the vertical resolution rather than the horizontal, the leading error now shifts from δ_{corr} to δ_{std} . To obtain metrics well below 5%, $N_\sigma \geq 10$. However, similar to the variation of N_{cl} , the wave profile and crest elevation at around $t/T_1 = 7.25$ at WGno. 10 varies considerably when comparing $N_\sigma = 10$ and $N_\sigma \geq 15$ (wave elevation deviation of 13%). Ultimately, M-sigma is assessed converged in wave condition 4 with $N_{cl} = 150$, $N_\sigma = 15$, and $C_{FL} = 0.8$.

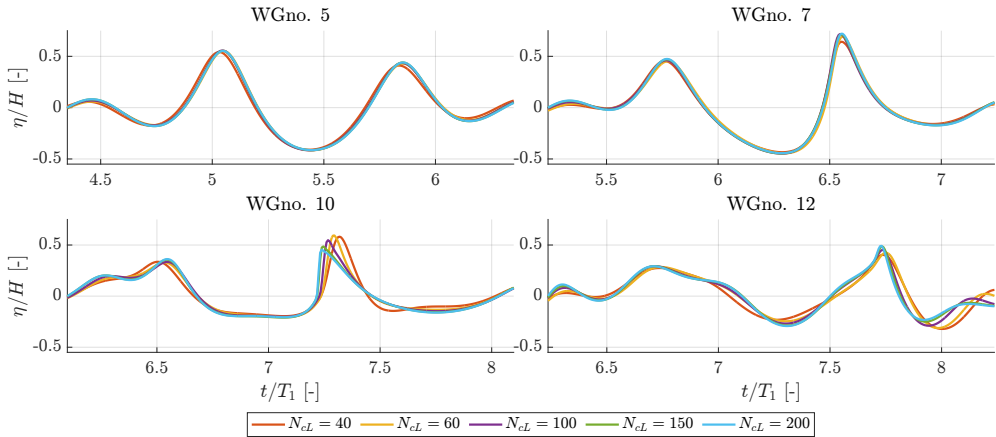


Fig. 12: Influence of N_{cl} on the surface elevation time series for selected WGnos.; wave condition 4 and $N_\sigma = 15$.

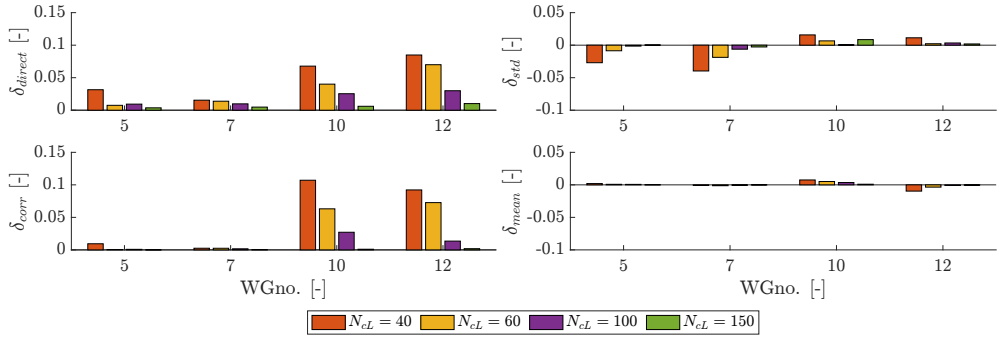


Fig. 13. Influence of N_{CL} on evaluation metrics for selected WGnos.; wave condition 4 and $N_\sigma = 15$.

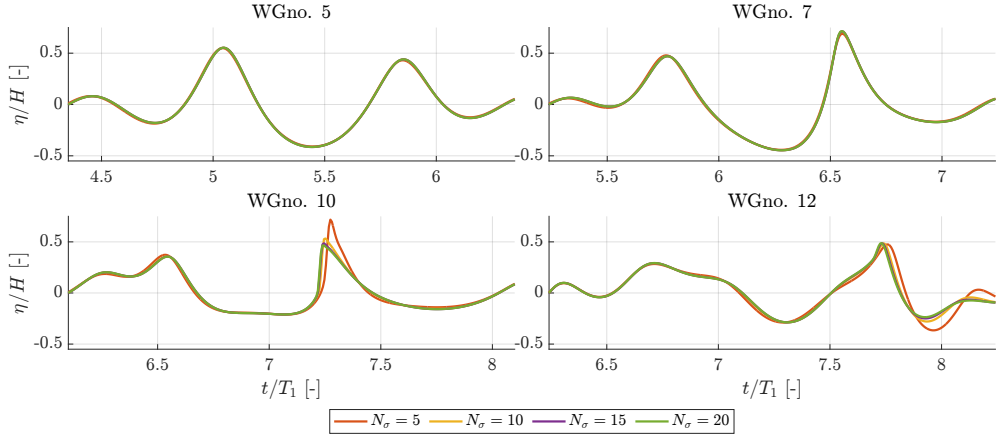


Fig. 14. Influence of N_σ on the surface elevation time series for selected WGnos.; wave condition 4 and $N_{CL} = 150$.

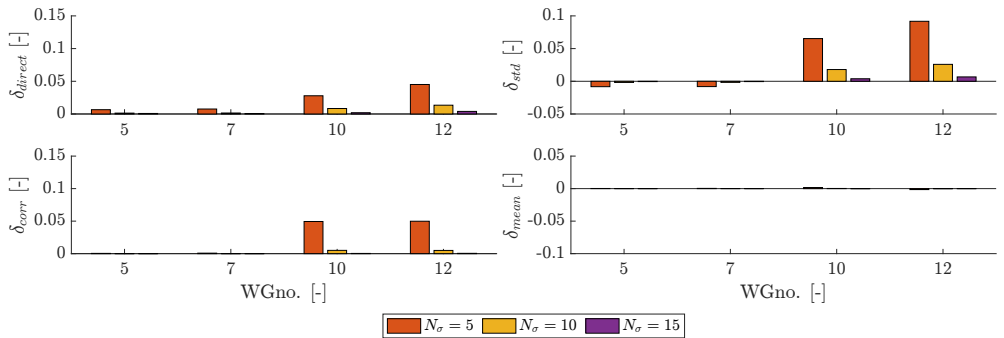


Fig. 15. Influence of N_σ on evaluation metrics for selected WGnos.; wave condition 4 and $N_{CL} = 150$.

Similar analyses were carried out for the M-sigma model with wave conditions 1-3, see Appendix A.2. Conclusions on the discretization used are summed up in Table 8.

Table 8: Selected N_{cL} , N_σ , and $\max(C_{FL})$ after convergence analysis of each wave condition.

| Wave condition | N_{cL} | N_σ | $\max(C_{FL})$ |
|----------------|----------|------------|----------------|
| 1 | 60 | 5 | 0.8 |
| 2 | 100 | 5 | 0.8 |
| 3 | 150 | 15 | 0.8 |
| 4 | 150 | 15 | 0.8 |

6.3 Convergence of D-SPH

In SPH models, the spatial resolution is given from the initial particle spacing d_p . A typical normalization of the spatial resolution of a meshless-based numerical model with wave propagation is the number of particles per wave height N_{pH} (e.g., Altomare et al., 2015; Gruwez et al., 2020a; Padova et al., 2014), which in the present is adopted as

$$N_{pH} = H/d_p. \quad (6.1)$$

Using weakly compressible SPH with DualSPHysics to simulate nonlinear wave propagation Rota Roselli et al. (2018) identified, in addition to N_{pH} , the smoothing length β_h and the artificial viscosity coefficient γ_v as important parameters for the accuracy of nonlinear wave propagation. β_h denotes the interaction range between particles during computation, and impacts the accuracy and computational efficiency of the model. In D-SPH, $\beta_h = c_h d_p \sqrt{2}$. As shown in Padova et al. (2014), high values of γ_v can lead to wave height underprediction, whereas very low values can lead to model instability. Preliminary sensitivity analyses of the smoothing length (by c_h) and artificial viscosity term were carried out with $c_h \in \{1.2, 1.5, 1.8\}$ and $\gamma_v \in \{0.01, 0.03, 0.05\}$. Qualitatively, the analyses showed only little influence on the surface elevation time series and to avoid tuning the D-SPH model, commonly used values for wave transformation cases with wave-breaking of $c_h = 1.8$ and $\gamma_v = 0.01$ were deployed for all simulations (Rota Roselli et al., 2019; Lowe et al., 2019). Resultantly, the convergence analysis of D-SPH focused on the variation of N_{pH} which was also identified as the most important SPH parameter for wave transformation over a shallow foreshore in Gruwez et al. (2020a). The convergence analysis of D-SPH was accordingly based

on $N_{pH} \in \{8, 10, 20, 40\}$. The influence of N_{pH} for the selected surface elevation time series and evaluation metrics are shown in Figs. 16-17. From the qualitative assessment of the surface elevation in the non-breaking region (WGnos. 5 and 7) wave profiles are rather similar for all N_{pH} except for a negative offset for $N_{pH} = 10$ yielding $\delta_{mean} < -5\%$ indicating a lower wave set-up for this spatial resolution. At WGnos. 10 and 12, where turbulent effects from wave-breaking are present, the influence on wave profiles from N_{pH} is significantly larger with large visible deviations at around $t/T_1 = 7.25$ and $\delta_{direct} > 10\%$ for $N_{pH} \leq 10$. Sufficient convergence is obtained with $N_{pH} \geq 20$ where all evaluation metrics are $< 5\%$ and only slight variations at the turbulent bore is visible from the surface elevation time series in Fig. 16.

Similar analyses were carried out for the D-SPH model with wave conditions 1-3, see Appendix A.3, with conclusions summed up in Table 9. It should be noted the convergence with N_{pH} was somewhat weak for namely the breaking wave condition 3, where small variations of d_p could lead to erratic changes of the surface elevations at the turbulent bore, as seen for WGnos. 10 and 12 in Figs. A 21 and A 22. Divergence was also identified when increasing the resolution further, i.e., to $N_{pH} \geq 40$, without varying multiple other parameters underlining the weak convergence of the D-SPH model with N_{pH} under the specified conditions. Despite the lack of formal convergence in wave condition 3, $N_{pH} = 40$ was used for further analysis and comparison as relatively good agreement were found between $N_{pH} = 20$ and $N_{pH} = 40$ and these posed less erratic and more physically plausible than $N_{pH} = 60$ as interpreted from Figs. A 21 and A 22. The observed case-specific convergence is further discussed in Section 8.3.

Table 9: Selected N_{pH} after convergence analysis of each wave condition.

| Wave condition | N_{pH} |
|----------------|----------|
| 1 | 20 |
| 2 | 20 |
| 3 | 40 |
| 4 | 20 |

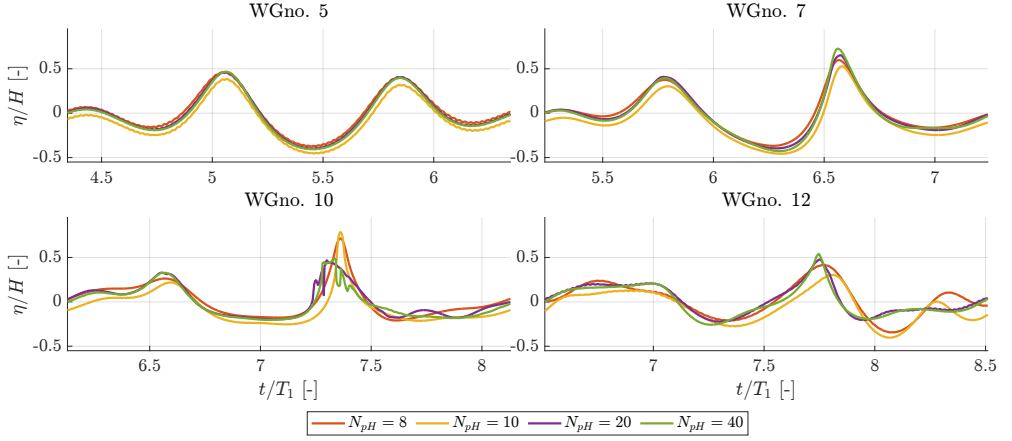


Fig. 16. Influence of N_{pH} on the surface elevation time series for selected WGnos.; wave condition 4.

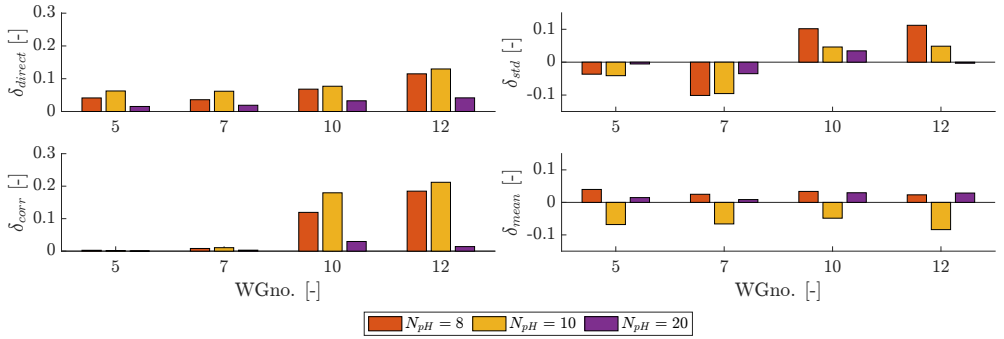


Fig. 17. Influence of N_{pH} on evaluation metrics for selected WGnos.; wave condition 4.

7 Results

The various numerical models and physical test results are compared in time domain qualitatively with surface elevation time series and quantitatively with evaluation metrics at four selected wave gauges in Section 7.1. In Section 7.2, results are analyzed in frequency domain with calculation of amplitudes and phases of primary and higher-order harmonics along the x -coordinate of the wave flume. An inter-model comparison of the free surface representation of the turbulent bore from wave-breaking is presented in Section 7.3. Ultimately, the computational costs of the numerical models are reported in Section 7.4. Results are interpreted and discussed in Section 8.

All numerical surface elevation time series are aligned to the physical tests at WGno. 1 by maximizing the cross-

correlation of the surface elevation time series over a time-window of $2T_1$ extracted from the second zero-up-crossing after wave propagation (estimated by L_1/T_1) to the position of WGno. 1. Prior to the alignment, signals were up-sampled to 1000 Hz by linear interpolation to obtain a higher precision in the alignment of the signals.

7.1 Time Domain Comparison

Surface elevation time series are extracted for the wave gauge positions also considered in the convergence analyses of Section 6, i.e., WGnos. 5, 7, 10, and 12. Time series are extracted based on the second zero-up-crossing after wave propagation (estimated by L_1/T_1) to the wave gauge positions and wave-ramp-up of $2T_1$ based on the physical test results – thus revealing possible phase-shifts from the numerical models.

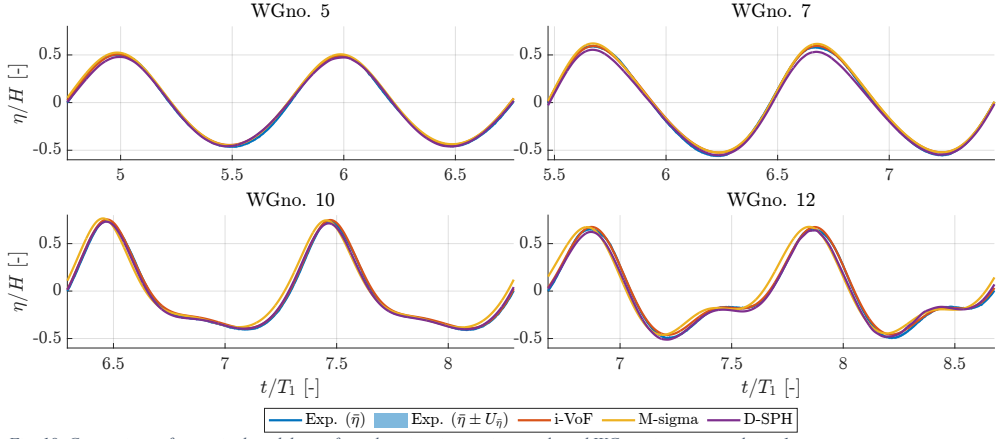


Fig. 18. Comparison of numerical models; surface elevation time series at selected WGnos. in wave condition 1.

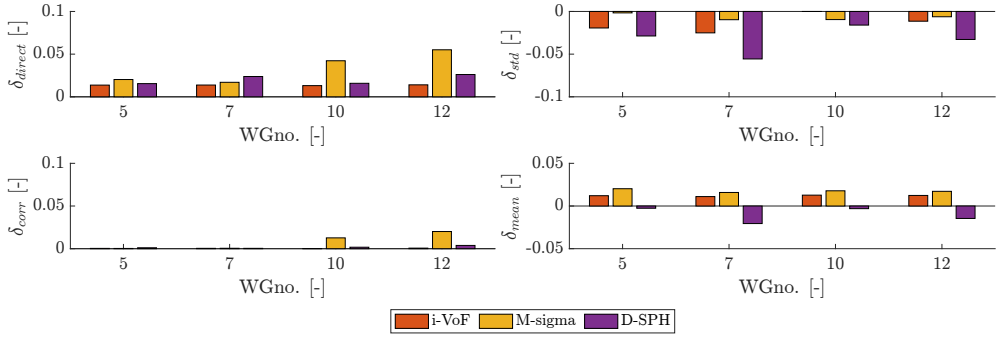


Fig. 19. Comparison of numerical models; evaluation metrics for selected WGnos. in wave condition 1.

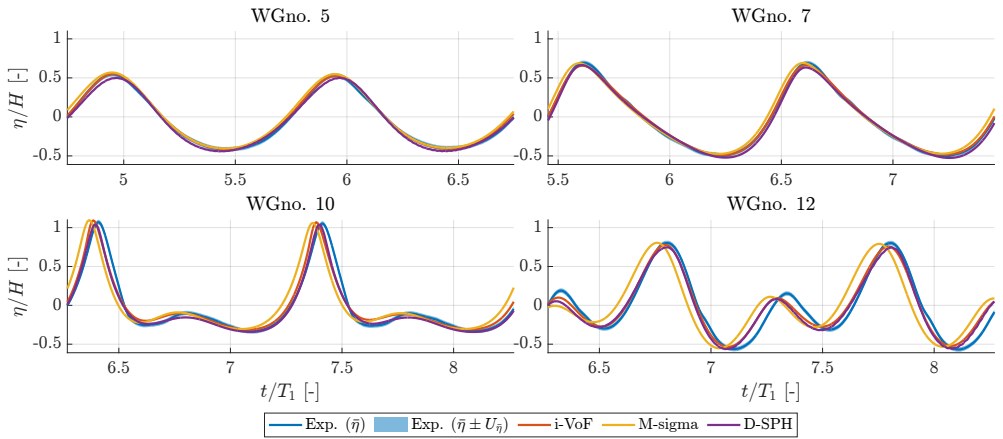


Fig. 20. Comparison of numerical models; surface elevation time series at selected WGnos. in wave condition 2.

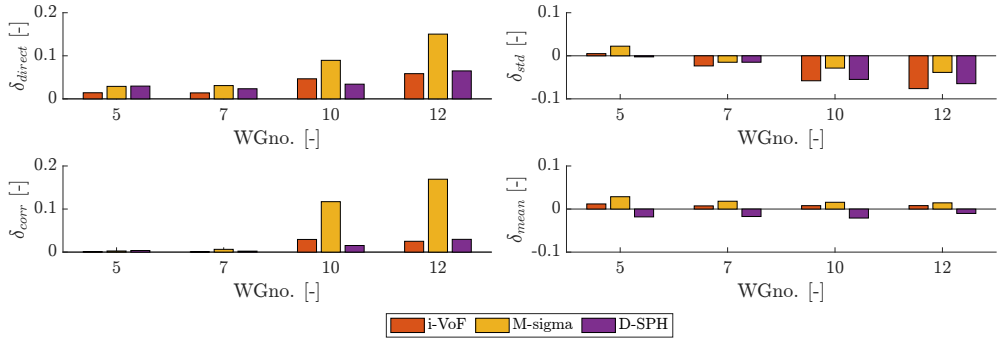


Fig. 21. Comparison of numerical models; evaluation metrics for selected WGnos. in wave condition 2.

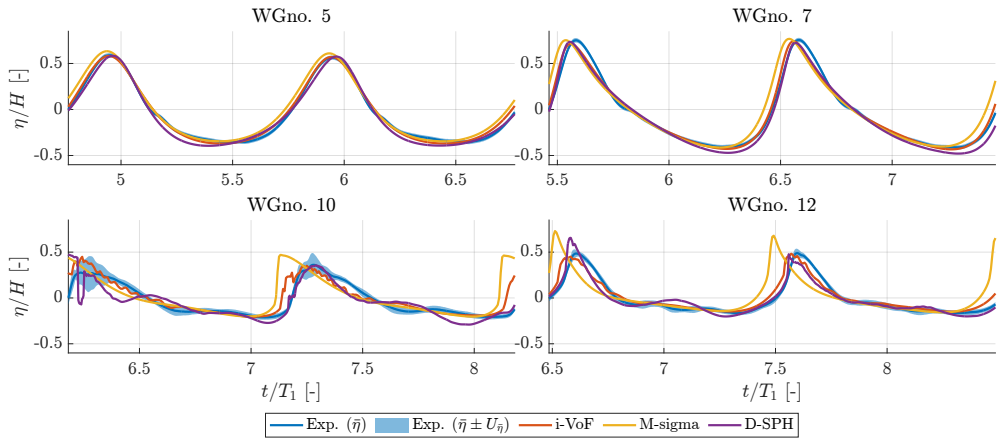


Fig. 22. Comparison of numerical models; surface elevation time series at selected WGnos. in wave condition 3.

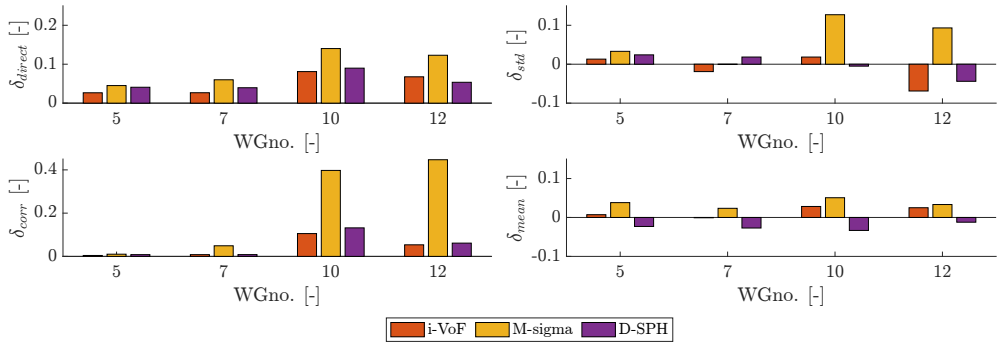


Fig. 23. Comparison of numerical models; evaluation metrics for selected WGnos. in wave condition 3.

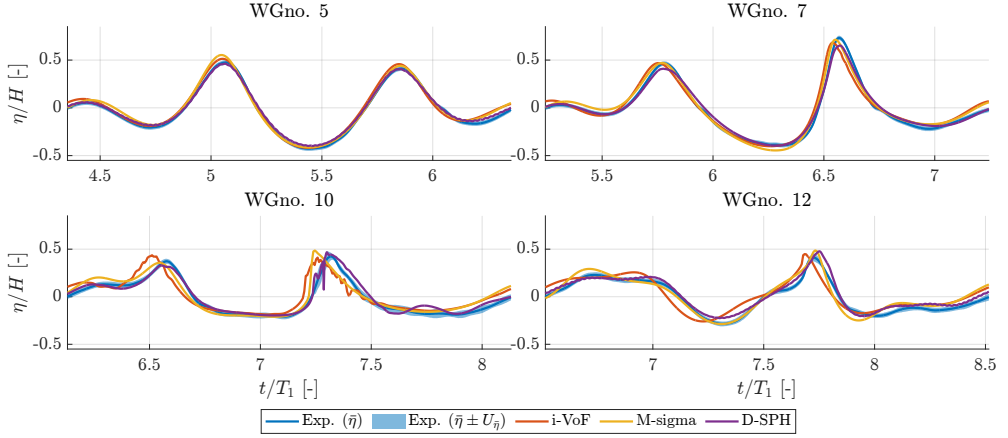


Fig. 24. Comparison of numerical models; surface elevation time series at selected WGnos. in wave condition 4.

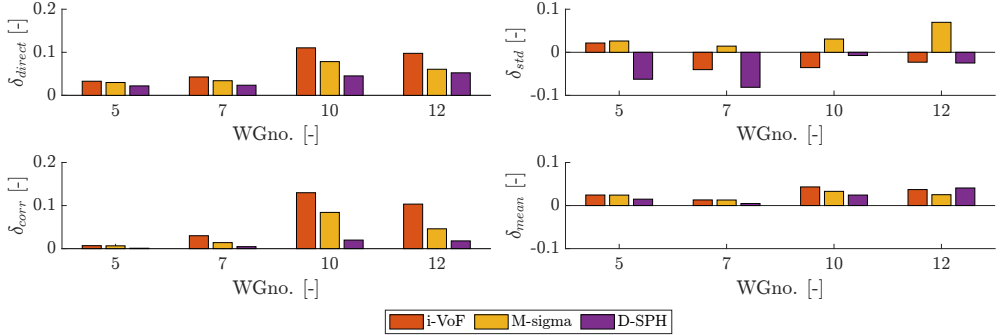


Fig. 25. Comparison of numerical models; evaluation metrics for selected WGnos. in wave condition 4.

7.2 Frequency Domain Comparison

The amplitude a and phase θ of primary and higher-order harmonics were calculated from FFT analyses as a function of x . To this end, numerical models were employed with a high number of numerical wave gauges (150 equidistantly spaced in x) to attain smooth amplitude and phase curves from numerical results with discrete comparisons to physical test results at physical wave gauge positions. Phases were unwrapped and linearly upsampled to 1500 points in x and rewrapped in $[0; 2\pi]$ radians to obtain proper sawtooth depictions of phase variation with x . The FFT analyses were carried out for time windows with lengths of $2T_1$. x_{refl} is the highest x -coordinate where the FFT analyses can be carried out from the physical test results without

reflections from the passive absorption entering the analyses and with waves assessed fully developed (ramp-up of $2T_1$ and an additional T_1 to disregard the leading wave after ramp-up). As the extracted time window for the FFT is $2T_1$, $x_{refl} = x_5 - 5L_1/2$. Consequently, the time window begins at $t_{refl} = x_{refl}/(L_1/T_1) + 3T_1$ and ends at $t_{refl} + 2T_1$ where t_{refl} denotes the time just before reflection from the end of the flume reaches x_{refl} . Amplitudes and phases at f_1 , $2f_1$, and $3f_1$ are calculated for the regular wave conditions 1-3, see Figs. 26-28 and 30-32, while the contents at f_1 , f_2 , and f_1+f_2 are calculated for wave condition 4, see Figs. 29 and 33. The contents on $2f_1$, $2f_2$, and f_2-f_1 in wave condition 4 are omitted due to brevity.

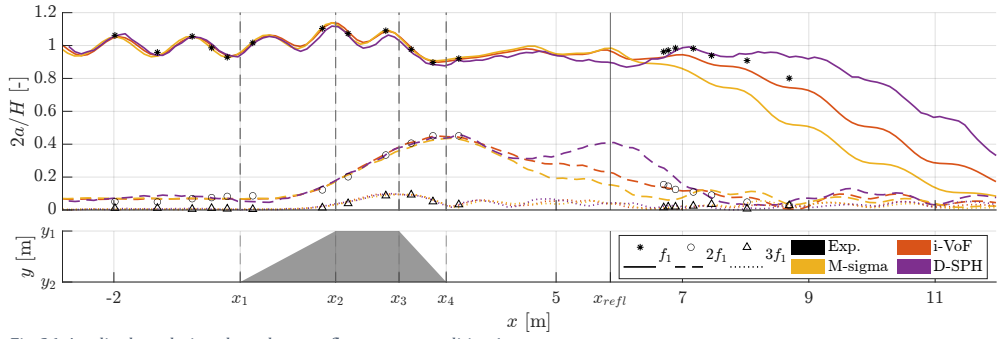


Fig. 26. Amplitude evolution along the wave flume; wave condition 1.

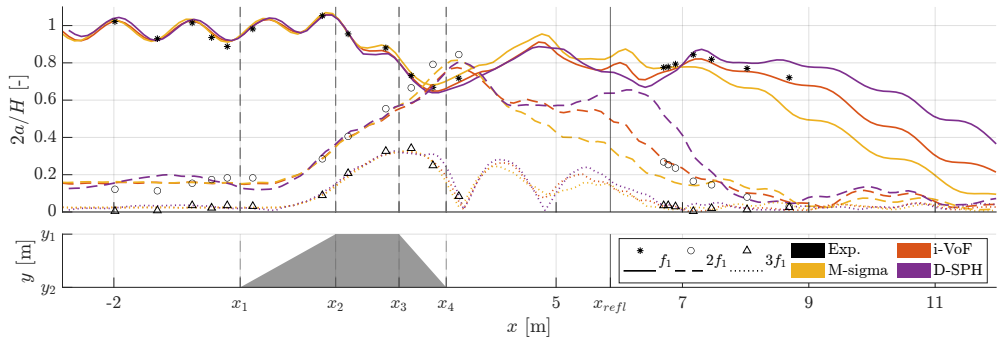


Fig. 27. Amplitude evolution along the wave flume; wave condition 2.

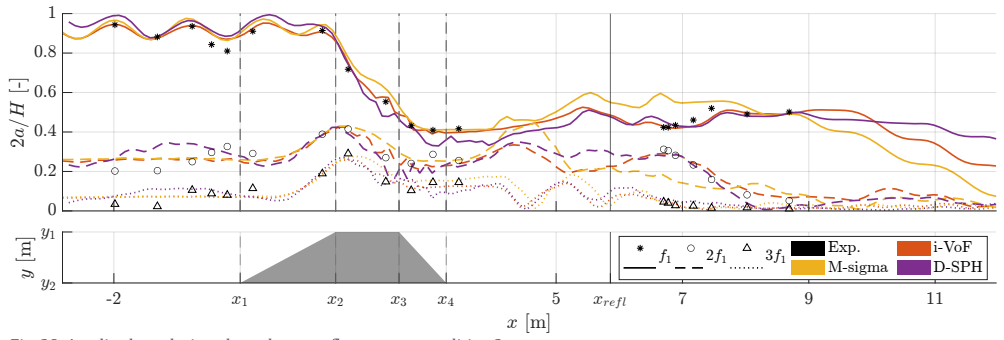


Fig. 28. Amplitude evolution along the wave flume; wave condition 3.

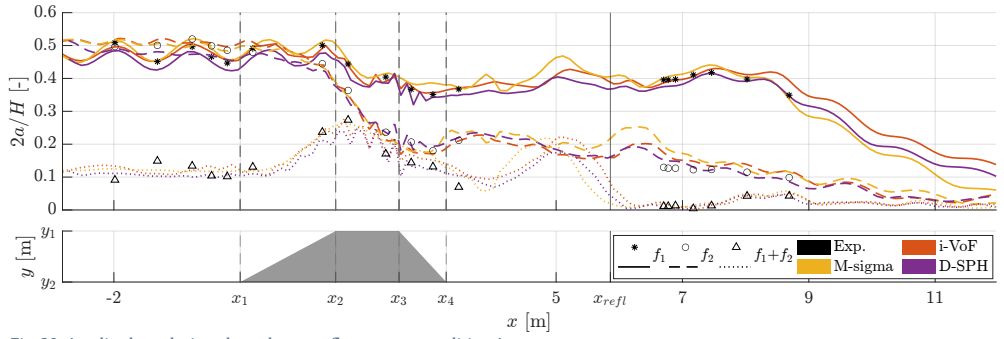


Fig. 29. Amplitude evolution along the wave flume; wave condition 4.

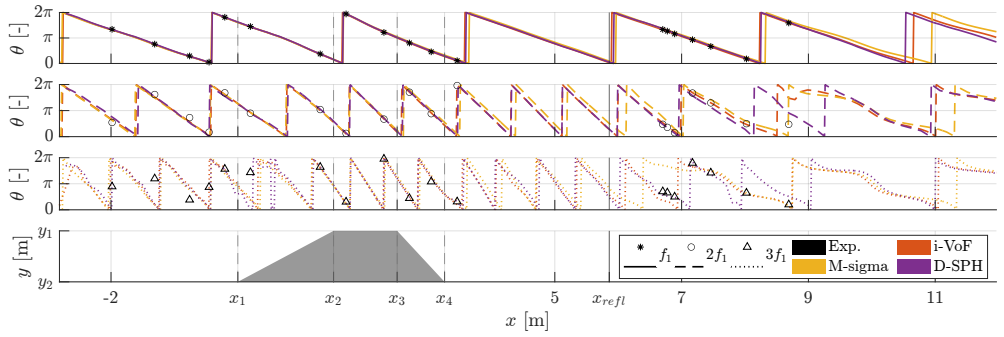


Fig. 30. Phase evolution along the wave flume; wave condition 1.

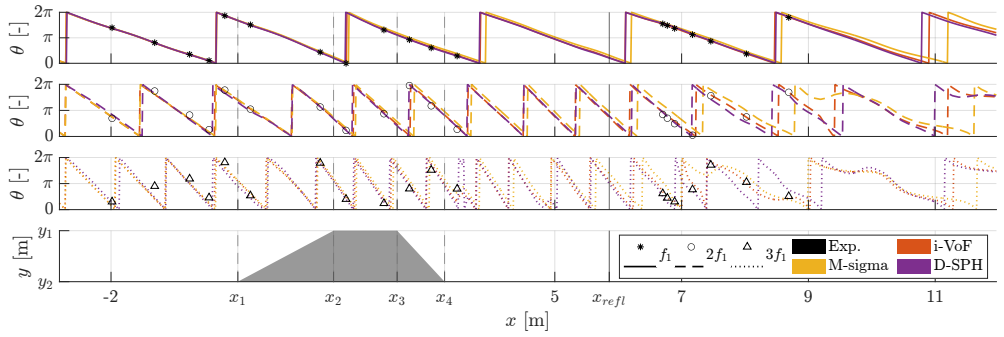


Fig. 31. Phase evolution along the wave flume; wave condition 2.

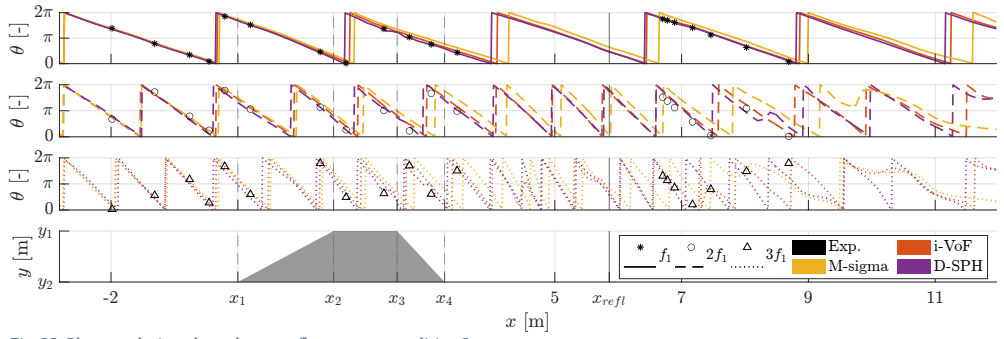


Fig. 32. Phase evolution along the wave flume; wave condition 3.

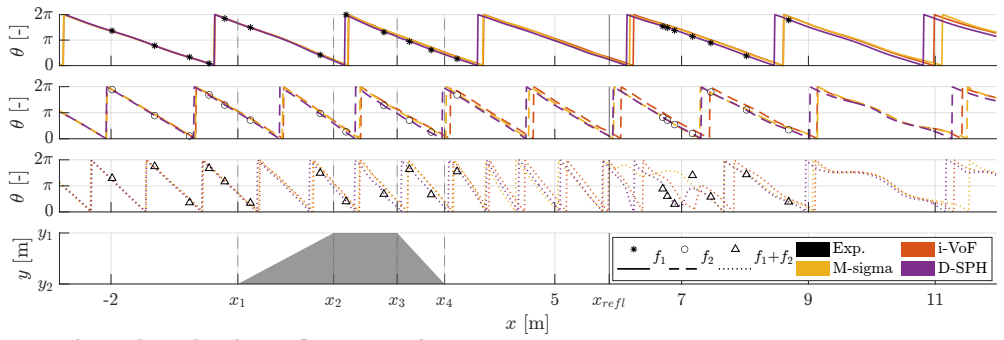


Fig. 33. Phase evolution along the wave flume; wave condition 4.

7.3 Inter-Model Comparison of Turbulent Bore

Free surface representations of the turbulent bore by the various numerical models are given in Figs. 34-35 for wave condition 4 at time coordinates corresponding to the second zero-up-crossing at WGno. 10 in Fig. 24, i.e., $t/T_1 \approx 7.25$. The free surfaces are represented by the phase fraction field $\alpha = 0.5$ in the i-VoF model, the sigma coordinate $\sigma = 1$ (re-transformed into y-coordinates in Fig. 35) with the M-sigma model, and the mass limit of 0.4 in the D-SPH model.

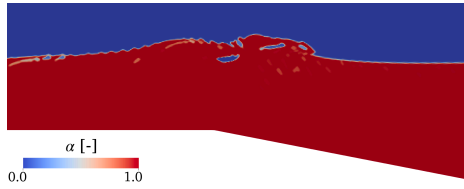


Fig. 34. Free surface of the i-VoF model at $t/T_1 = 7.20$



Fig. 35. Free surface of the M-sigma model at $t/T_1 = 7.22$ with the sigma domain (red) seen in Cartesian coordinates.

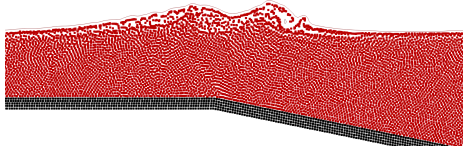


Fig. 36. Free surface of the D-SPH model at $t/T_1 = 7.24$ with fluid particles in red and boundary particles in black.

7.4 Computational Costs

Beside the accuracies of the considered numerical models against the physical test results, the benchmarking will be based on the computational costs, i.e., hardware and wall clock time.

All simulations with the i-VoF model were run in parallel on 30 cores on a single CPU (AMD EPYC 7702; base clock speed 2.0 GHz). The scotch decomposition method (Pellegrini & Roman, 1996) was employed to decompose the mesh into the 30 subdomains while minimizing connectivity. The number of computational grids (cells) and wall clock time of the converged i-VoF simulations of each wave condition are shown in Table 10. It should be noted the number of cells per core varies between 13e3 and 40e3 which typically is the

interval in which strong scaling speed-up performance degenerates somewhat rapidly, see, e.g., Axtmann and Rist (2016).

The M-sigma model ran on 16 cores on a single AMD Ryzen 9 3950X CPU (base clock speed 3.5 GHz). Domain decomposition was carried out with the METIS graph partitioning library minimizing connectivity between subdomains on the allocated cores (Karypis & Kumar, 1998).

The D-SPH models were executed with an AMD 7302 CPU accelerated with the Tesla A10 GPU having 9216 CUDA-cores and single precision processing power of 31240 GFLOPS. The computational costs are summed up in Table 10.

Table 10: Computational cost of the considered numerical models. 'c.' denotes cores.

| Wave condition | Comp. grids count [-] | Wall clock time [h] | Hardware |
|----------------|-----------------------|---------------------|-----------------|
| i-VoF | | | |
| 1 | 0.4e6 | 0.5 | 30 CPU-c. |
| 2 | 0.6e6 | 2.4 | |
| 3 | 0.7e6 | 17.2 | |
| 4 | 1.2e6 | 23.0 | |
| M-sigma | | | |
| 1 | 0.4e4 | 0.01 | 16 CPU-c. |
| 2 | 0.7e4 | 0.02 | |
| 3 | 3.1e4 | 0.16 | |
| 4 | 3.1e4 | 0.14 | |
| D-SPH | | | |
| 1 | 3.5e6 | 12.6 | 9216 CUDA-c. |
| 2 | 0.7e6 | 1.9 | |
| 3 | 0.8e6 | 3.6 | |
| 4 | 0.2e6 | 1.4 | |

8 Discussion

The wave transformation physics of the presented test case is discussed in Section 8.1 and will primarily be based on the physical test results but in the areas of the physical wave flume where wave gauges were not installed, conclusions are drawn from the numerical tests with dense numerical wave gauges. The numerical models are benchmarked against the physical tests in terms of accuracy in Section 8.2, while inter-model applicability is discussed in Section 8.3.

8.1 Wave Transformations

Upwave of the submerged bar, at $x < x_1$, symmetric wave profiles with increasing nonlinearity with wave condition number can be seen from the surface elevation time series in Figs. 18, 20, 22, and 24. The

relative distribution of energy on primary components and their respective superharmonics are shown in Figs. 26-29. From the numerical results on spatial evolution of phases in Figs. 30-32 the second and third order components from wave conditions 1-3 have wavelengths of half and one-third of that of the primary component, i.e., equal celerity, as expected for bound superharmonics. For wave condition 4, the primary components can be seen to have a wavelength ratio of about $L_1/L_2 = 1.7$ from Fig. 33 which approximately corresponds to the wavelength ratio as calculated from linear dispersion. The same holds for the superharmonic $f_1 + f_2$ which wavelength corresponds to $k_1 + k_2$ (additional super- and subharmonics are omitted due to brevity).

At the upslope of the submerged bar, at $x_1 < x < x_2$, the shoaling process initiates, and the wave nonlinearity increases which can be seen from the increasing amplitudes with x on higher-order components in Figs. 26-29. Consequently, skewness increases, and asymmetric wave profiles emerge, which is apparent from the surface elevation time series at WGno. 7 for all wave conditions (though only mildly for wave condition 1) as can be seen in Figs. 18, 20, 22, and 24.

At the horizontal crest of the submerged bar, at $x_2 < x < x_3$, the re-adjustment to a horizontal bathymetry releases higher-order bound energy to symmetrize the asymmetric incident wave profiles. This effect is significant for large changes in the bathymetry slopes, see Eldrup and Lykke Andersen (2020) The h/L_1 ratio is around the conventional shallow-water limit of 5% and waves in this region are accordingly rather non-dispersive. The near-resonant conditions of triad wave-wave interactions are met (Holthuijsen, 2007) which yields a rapid transfer of energy from primary to higher-order harmonics. For the non-breaking wave conditions 1 and 2 this exchange of energy is clearly seen from significant increases in second and third order energy (third order mainly in wave condition 2), see Figs. 26 and 27. Interestingly, for the breaking wave conditions 3 and 4, dissipation seems to be the dominant wave transformation rather than triad wave-wave interaction. Dissipation by the formation of turbulent eddies from the onset of wave-breaking and the development of a turbulent bore is apparent from the significant reduction of energy on virtually all harmonics with the dissipation of primary energy being larger on f_2 than f_1 in wave condition 4 as expected due to the higher wave-steepness of f_2 , see Figs. 28 and 29. From the variation of phases with x , the celerity at the horizontal bar crest decreases less for the relatively higher amplitude wave conditions indicating amplitude dispersion and thus the relatively higher nonlinearity in these wave conditions.

At the downslope and downwave of the submerged bar, at $x > x_4$, the finite amplitude waves from the horizontal bar crest propagate into deeper water and the wave nonlinearity decreases and energy is transferred between components. With sufficiently high

downslopes energy will not solely be transferred from higher-order bound components to primary components, i.e., deshoaling is not simply the inverse of shoaling, but a decomposition into free harmonics with smaller amplitudes occur as found in Beji and Battjes, 1994 and Eldrup and Andersen (2020) for downslopes of 1:10 and 1:30, respectively. The oscillating amplitudes in space as seen particularly for the second- and third-order harmonics of wave conditions 2 and 3 are characteristic of this exact phenomenon (Eldrup & Lykke Andersen, 2020) which comply with the steeper downslope of 1:5 in the presented tests, see Figs. 27 and 28. For multiple wavelengths, the exchange of energy transpires, and ultimately a steady state will develop, assuming a continued flat bathymetry (Beji & Battjes, 1993). Such a steady state is not reached in the analyzed domain of the presented tests.

8.2 Accuracy of the Numerical Models

Close agreement between the numerical models and the physical tests resides in the prediction of the spatial evolution of amplitude on both primary and higher order components (if present) with no numerical model clearly standing out from the rest, see Figs. 26-29. The overall transfer of energy between components as attained from the physical tests is very well captured by the numerical models along the domain with deviations increasing at about midway of x_3 and x_{refl} ($x \approx 4$ m, particularly clear from Figs. 26 and 27. At $x > x_{refl}$ reflections and transients due to ramp-up enter the FFT analyses. However, released higher order harmonics from transients due to ramp-up enter the FFT analyses upwave of this region due to their lower celerity, i.e., a released component on $2f_1$ from the first wave after ramp-up will enter analyses at about $x > 4$ m. Since various ramp-up formulations are used in the numerical models the largest inter-model deviations are present in this region wherefore $x > 4$ is not taking into account in the assessment of model accuracy but is sustained in the results for completeness. It should be noted that the physical tests now pose as the reference for evaluation metrics as introduced in Section 5.

The M-sigma model have the highest direct errors in wave conditions 1-3 which is driven by phase shifts increasing with nonlinearity, i.e., $\delta_{corr} = [2,12,40]\%$ at WGno. 10 for wave condition 1-3, respectively. The phase shifts primarily develop at the horizontal crest of the submerged bar as seen in Figs. 30-32, where the celerity of M-sigma can be seen to be overestimated in both primary and higher order harmonics for wave conditions 1-3. Interestingly, in wave condition 4, δ_{corr} for M-sigma is reduced to 9% where that of i-VoF is maximum with 13% resulting in the largest direct error in wave condition 4. This is the highest evaluation metric for i-VoF which remains consistently accurate in both the general shape of the surface elevation time series and crest and trough elevations throughout all

wave conditions. D-SPH and M-sigma have considerable overestimations on maximum crest elevations with deviations of 30% and 38%, respectively, relative to the upper bound of the 95% UI, whereas i-VoF lies within the UI.

Considering the spatial evolution of amplitudes in the nonbreaking wave conditions 1-2, see Figs. 26 and 27, the largest deviations are on the second order energy at deshoaling, $x_3 < x < x_4$. The amplitudes on f_1 are predicted with deviations of less than 5% for all numerical models in this region while the amplitude on $2f_1$, which has increased to be of equal magnitude to that of f_1 , is generally less accurately captured. Slightly higher accuracy is obtained with the M-sigma model having a maximum deviation of 10% where i-VoF and D-SPH have 15%. The amplitudes on $3f_3$ match the physical tests with maximum deviations of 5% with i-VoF and M-sigma while D-SPH has an overestimation at WGno. 11 seemingly due to a delay in the decomposition process, but otherwise correlates well with i-VoF and M-sigma.

The inter-model variability of the predicted amplitudes generally increases with increasing nonlinearity of the considered wave condition with additional variability introduced in the breaking wave conditions 3 and 4. The turbulent bore generated from wave breaking at the horizontal bar crest and measured from surface elevations at WGno. 10 (Figs. 22 and 24) is, not surprisingly, found to contain some of the most challenging physical processes from a modelling perspective, as also seen in the convergence analyses in Section 6. It is largely in this region of the domain the characteristics of the tested numerical models with their different free surface treatments manifest as underpinned from the free surface representations in Figs. 34-35: in the i-VoF model, the turbulent bore is simulated with a complex free surface with air entrainments from plunging, and oscillations are transpiring at the interface; the M-sigma model develops a steep, nearly vertical bore-front activating turbulent dissipation while maintaining a continuous, single-valued free surface as per the sigma transformation method; while the D-SPH model simulates a bore with complex free surface deformations with particle clustering and particle voids forming at the vicinity of the free surface which can result in sudden drops in the extracted surface elevation time series, as seen for $t/T_1 = 7.29$ at WGno. 10 in Fig. 24. In case of multi-valued free surfaces, the lowest value was extracted as surface elevation in D-SPH whereas in i-VoF the highest value was extracted (due to the inclusion of air entrainment). The definition of the surface elevation with resistance wave gauges is unclear at multi-valued free surfaces which is most pronounced in the present testcase with the plunging waves in wave conditions 3 and 4. However, the effect from different definitions of the surface elevation in numerical models

and physical tests is assessed to be small in the present benchmarking where the surface elevations of plunging waves are not included directly, i.e., wave gauges were not installed in the physical tests to measure the plunging waves but rather the evolution of the surface elevation including the turbulent bore downwave hereof.

The dissipation from wave-breaking in the M-sigma model does not fall short of the i-VoF and D-SPH models where full free surface deformations are possible, see Figs. 28 and 29. In the dissipative region of $x_2 < x < x_4$, the numerical models generally comply with the physical test data points relative to which the largest deviations are 10% for all numerical models on the primary components in wave condition 4 and 19%, 11%, and 5% for D-SPH, M-sigma, and i-VoF, respectively, in wave condition 3. The corresponding deviations with reference to $H/2$ rather than the individual amplitudes (which is somewhat small for higher order components) are 2-5% in wave condition 4 and 6%, 8%, and 3% in wave condition 3. i-VoF is thus the most accurate model with respect to turbulent dissipation while all the numerical models perform rather accurately with deviations of less than 10% of $H/2$ on the prediction of amplitudes during breaking on all components – abundant for most practical engineering.

For all wave conditions the generated waves correlate well between numerical models and physical tests as seen from the surface elevation time series at WGno. 5 with evaluation metrics generally low (most are below 5%), see Figs. 18-25. Most notably at $x < x_1$ is the underestimation of the energy content in wave condition 4 with the D-SPH model yielding $\delta_{std} = 6\%$ which also can be seen as the slight negative offset in the amplitude on f_1 in Fig. 29. The influence hereof is mitigated at wave-breaking whereafter D-SPH obtain the overall lowest evaluation metrics and has a profile very close to the those of the physical tests at the challenging WGnos. 10 and 12, see Figs. 24 and 25. In wave conditions 2 and 3 variations in the amplitudes upwave of the submerged bar, $x < x_1$, are present, see Figs. 27 and 28. The primary amplitudes from the physical test results differ locally in x (just upwave of $x = x_1$) with about 10% from all numerical models whose inter-model variability is very low. This could signify that the physical tests do not perfectly match the idealized test case, e.g., from geometrical imperfections or structural flexibility of the bar. Additionally, higher order components at $x < x_1$ obtained from D-SPH and the physical tests differ somewhat from one another and from i-VoF and M-sigma which are nearly equal and constant. Re-reflections are mitigated in the i-VoF and M-sigma models which utilize the relaxation zone technique at the inlet whereas D-SPH and the physical tests utilize piston motion with distinctive wavemaker theories. The effects hereof, besides general differences

in the model/physical test behavior, are expected to cause the deviations in second order energy upwave of the bar in wave conditions 2 and 3 which impact in the context of the dominating wave transformation of shoaling, breaking, and decomposition are assessed insignificant.

8.3 Applicability of the Numerical Models

Different hardware was used for the numerical models as presented in Section 7.4. The D-SPH model was accelerated with a GPU while M-sigma and i-VoF ran on CPU. The CPU for M-sigma had a significantly higher base clock speed relative to that used for i-VoF, 3.5 and 2.0 GHz, respectively, where the latter on the other hand was parallelized to about the double number of cores. The different hardware architectures are chosen to fit advantageously with the different numerical formulations with hardware solutions accessible in typical research laboratories or engineering companies. Consequently, the wall clock time is directly used as metric for the computational costs, which is sufficiently accurate for a gross inter-model comparison of computational costs. The wall clock time on the M-sigma model was one to two orders of magnitude smaller than those of i-VoF and D-SPH regardless of wave condition, see Table 10. This significant reduction in simulation time is led by the sigma transformation approach from which the free surface is not resolved in the vertical direction as in i-VoF and D-SPH yielding substantial reductions in the computational grid counts of the M-sigma model. The total grid counts of i-VoF is two orders of magnitudes higher than those of M-sigma for each wave condition which decreases the timestep due to the imposed maximum C_{FL} criterion where the C_{FL} bounds in themselves are also significantly lower in i-VoF, see Table 7. Similar to i-VoF, the D-SPH model varies with orders of magnitude in total grid count relative to M-sigma, but somewhat contra intuitive the total grid count in D-SPH decrease with increasing nonlinearity of the wave condition opposite of i-VoF and M-sigma. With constant normalized particle resolutions of $N_{pH} = 20$ for wave conditions 1, 2, and 4 and $N_{pH} = 40$ for wave condition 3, the simulation of small-amplitude waves requires higher absolute particle resolutions which upon initialization is uniformly scattered in the entire domain and not restricted to the vicinity of the free surface due to the lack of local grid refinement options in D-SPH. These are significantly more challenging to implement in Lagrangian frameworks than Eulerian and the i-VoF model use local grid refinement extensively and have parameterized grid refinement zones by H from which grid counts can be reduced significantly with decreasing nonlinearity. The i-VoF model is based on a structured mesh generated with OpenFOAM utilities which obviously introduces the inconvenience of the user having to design such – not required with the meshless D-SPH model or automatically generated with the M-sigma model (equidistant spacing in x and sigma

is simply selected). However, for the utilized meshes with the i-VoF model this task is simple and should not last more than a few hours even for users with limited experience with OpenFOAM.

The M-sigma and i-VoF models converged with increasing resolutions in time and space to evaluation metrics well below 5% consistently across all wave conditions whereas the D-SPH model showed divergence with increasing N_{pH} in wave condition 3 and somewhat erratic behavior with small variations of d_p in the breaking wave conditions, see Section 6.3 and Appendix A.3. Convergence has been identified as a grand challenge of the SPH method (Vacondio et al., 2021) since currently convergence is not guaranteed by reducing smoothing and discretization errors by variation of the smoothing length and initial particle spacing but can depend critically on the particle distributions and hence the flow field itself due to its Lagrangian formulation (Quinlan et al., 2006). As the particle distribution can play a pivotal role in the accuracy of SPH it is presumed that the chaotic nature of turbulence in the breaking wave conditions triggers particle disordering yielding the observed erratic behavior. Despite the lack of formal convergence, the SPH method has a wide range of successful coastal engineering applications and in the present test case the D-SPH model accurately simulates wave transformation across the investigated wave conditions. However, relative to M-sigma and i-VoF more caution should be exercised in the convergence analysis of D-SPH as particle disordering may govern the accuracy which poses as a drawback of the model. Further work may include the influence from particle redistribution methods such as particle shifting to increase convergence and consistency, see, e.g., Vacondio et al. (2013) and Khayyer et al. (2019).

The free surface descriptions of i-VoF and D-SPH allow for straightforward advancement of the numerical models to include wave-structure interactions from, e.g., installation of a vertical crown wall at the submerged bar crest, from which the free surface is made discontinuous, and the sigma transformation accordingly breaks down without implementation of special measures such as artificial interior free surfaces as in Hicks (2020). The M-sigma model further has the disadvantage of not being based on an open-source code, unlike DualSPHysics and OpenFOAM, therefore not allowing for users to implement any such measures.

Numerical wave generation was most easily handled in i-VoF where no inputs other than the parameters given in the idealized test case were required as inputs across all wave conditions. The i-VoF and M-sigma models both utilized relaxation zone techniques of weighting analytical stream function wave theory solutions to computational fields accommodating undemanding wave generation of regular waves without restrictions

on wave steepness. In D-SPH the standard wavemaker theory used with the piston wavemaker was second order (Hughes, 1993) introducing generation of spurious free waves at too high wave steepness or for intermediate- to shallow-water waves, which could introduce deviations for D-SPH in the presently investigated wave condition 3. However, the second order wavemaker theory was maintained for all regular wave cases as the use of standard options within the respective numerical frameworks were pursued. Second order bichromatic wave theory was used as target solution in the inlet relaxation zone in the i-VoF model and the user needs only input wave parameters for the two primary wave components to generate the full wave-wave interactions. More work (and experience) was required in the D-SPH and M-sigma to generate wave condition 4. Irregular wave generation from bichromatic or user-defined spectra is not supported in current releases of D-SPH (first order irregular wave generation from JONSWAP or Pierson-Moskowitz spectra is). Therefore, wave condition 4 was generated from an input file with prescribed motion of the piston-type wavemaker calculated from external software through irregular second order wave maker theory of Schäffer (1996). In MIKE 3 Waves FM, the user can specify an input file with wave parameters for any number of wave components. Wave generation in M-sigma was thus initiated from an input file with amplitudes, periods, wavenumbers, and phases for *all* wave components (including interactions) in wave condition 4. An additional calculation was thus required to obtain the amplitudes of all wave components based on the two wave heights provided in the idealized test case. For this purpose, second order wavemaker theory as per Schäffer (1996) was used.

9 Conclusions

The wave transformation over a submerged bar was investigated for four wave conditions with various levels of nonlinearity, regularity, and turbulence due to wave-breaking. Physical wave flume tests were carried out to generate a dataset dedicated to numerical model validation. Three fundamentally different CFD models highly popular within their respective category were benchmarked against the physical tests in terms of accuracy while inter-model applicability in terms of computational cost and ease-of-use was discussed.

In general, the numerical models had high correlation with the physical tests with the very low inter-model variability for especially the nonlinear, non-breaking wave transformations in wave conditions 1 and 2. Accuracy of the numerical models was assessed with reference to the physical tests from direct comparisons of surface elevation time series and derived evaluation metrics, indicating averaged errors on elevations, amplitudes, phases, and wave set-up, respectively, at multiple positions and the spatial evolution of

amplitudes and phases on primary and higher order components. Considering accuracy alone, the i-VoF model was found to have some advantages over D-SPH and M-sigma in primarily breaking wave conditions. Energy dissipation from turbulent bores formed from wave-breaking was captured with less than 5% deviation on primary amplitudes where those of M-sigma and D-SPH were 11% and 19%, respectively. As a possible effect from these deviations, D-SPH and M-sigma significantly overestimate maximum crest elevations downwave of the submerged bar where i-VoF lies within the 95% UI of the physical test results. Namely in wave condition 3, the wave celerity in the M-sigma model is overestimated at the horizontal crest of the bar resulting in rather large phase shifts of surface elevation time series and correlation errors downwave of the bar. D-SPH had the overall smallest phase shift errors. The highlighted deviations might seem somewhat minor in the context of the overall wave transformation from wave propagation over a submerged bar as seen from the spatial evolution of amplitudes along the wave flume (Figs. 26-29) but may turn critical in delicate design situations based on, e.g., maximum crest elevations at a given position.

In terms of the cost-accuracy trade-off of the numerical models, the M-sigma performed the best with computational costs between one and two orders of magnitude lower than D-SPH and i-VoF as measured from wall clock time (see Sections 7.4 and 8.3) with the nearly linear wave condition 1 being solved in close to real-time. The significant reduction in computational cost of the M-sigma model was led by the sigma transformation of the vertical coordinate reducing computational grid counts two orders of magnitude relative to D-SPH and i-VoF and the knock-on effect of larger time steps from maximum *CFL* criteria. The accuracy of M-sigma followed that of D-SPH and i-VoF for the non-breaking wave conditions whereas for the breaking wave conditions accuracy were lower than i-VoF but generally higher than D-SPH. In wave condition 3, wave celerity at the horizontal bar crest is overestimated and the maximum wave crest elevations were overestimated at a position downwave of the bar, however, the energy dissipation as reflected by evolution of amplitudes from spectral analysis were generally well captured with an accuracy adequate for most coastal engineering applications.

An important caveat of the D-SPH model is the significantly more challenging task of obtaining converged results for especially breaking wave conditions compared to i-VoF and M-sigma. Convergence of SPH methods is an ongoing research topic and may depend critically on particle disordering (Quinlan et al., 2006), which is particularly unfortunate in the simulation of turbulent regions with a Lagrangian framework. In the present work, similar convergence criteria were retained in D-SPH as with i-VoF and M-

sigma for all wave conditions except wave condition 3 which diverged with decreased initial particle spacing. The meshless nature of D-SPH and the automatically generated, simple meshes in sigma domain in M-sigma gives these models a slight edge over i-VoF in time spent on model setup. Advancement of the numerical models to handle more complex wave-structure interactions such as surface piercing structures like a crown wall may be more easily implemented in i-VoF and D-SPH than M-sigma due to their free surface descriptions and open-source accessibility of the OpenFOAM and DualSPHysics.

10 Research Artifacts

To encourage further numerical model benchmarking or validation against the experimental data of the present paper, datasets with results from the physical flume tests as well as numerical simulations are provided through Mendeley Data – refer to Andersen et al. (2023). This repository further contains the input files for all numerical models to increase transparency and reproducibility.

11 Conflicts of Interest

The authors declare that they have no conflict of interest.

12 Funding

The work was partially supported by EU Horizon through the MSCA-PF Grant No. 101068736.

13 Ethical Approval

This article does not contain any studies with human participants or animals performed by any of the authors.

14 References

- Altomare, C., Crespo, A. J. C., Domínguez, J. M., Gómez-Gesteira, M., Suzuki, T., & Verwaest, T. (2015). Applicability of Smoothed Particle Hydrodynamics for estimation of sea wave impact on coastal structures. *Coastal Engineering*, 96, 1–12. <https://doi.org/https://doi.org/10.1016/j.coastaleng.2014.11.001>
- Altomare, C., Domínguez, J. M., Crespo, A. J. C., González-Cao, J., Suzuki, T., Gómez-Gesteira, M., & Troch, P. (2017). Long-crested wave generation and absorption for SPH-based DualSPHysics model. *Coastal Engineering*, 127, 37–54. <https://doi.org/https://doi.org/10.1016/j.coastaleng.2017.06.004>
- Andersen, J., Eldrup, M. R., Vero Fernandez, G., & Ferri, F. (2023). *Wave Propagation over a Submerged Bar: Datasets from Physical and Numerical Tests*. Mendeley Data, V1. <https://doi.org/10.17632/k2z62dxj.1>
- Antuono, M., Colagrossi, A., & Marrone, S. (2012). Numerical diffusive terms in weakly-compressible SPH schemes. *Computer Physics Communications*, 183(12), 2570–2580. <https://doi.org/10.1016/j.cpc.2012.07.006>
- ASME (2006). ASME V&V 10-2006 : Guide for Verification and Validation in Computational Solid Mechanics. American Society of Mechanical Engineers. New York, NY.
- Axtmann, G., & Rist, U. (2016). Scalability of OpenFOAM with Large Eddy Simulations and DNS on High-Performance Systems. In D. H. and R. M. M. Nagel Wolfgang E. and Kröner (Ed.), *High Performance Computing in Science and Engineering 16* (pp. 413–424). Springer International Publishing.
- Beji, S., & Battjes, J. A. (1993). Experimental investigation of wave propagation over a bar. *Coastal Engineering*, 19(1), 151–162. [https://doi.org/https://doi.org/10.1016/0378-3839\(93\)90022-Z](https://doi.org/https://doi.org/10.1016/0378-3839(93)90022-Z)
- Beji, S., & Battjes, J. A. (1994). Numerical simulation of nonlinear wave propagation over a bar. *Coastal Engineering*, 23(1–2), 1–16. [https://doi.org/10.1016/0378-3839\(94\)90012-4](https://doi.org/10.1016/0378-3839(94)90012-4)
- Bhushan, S., El Fajri, O., Hubbard, G., Chambers, B., & Kees, C. (2021). Assessment of Numerical Methods for Plunging Breaking Wave Predictions. *Journal of Marine Science and Engineering*, 9(3). <https://doi.org/10.3390/jmse9030264>
- BIMP, IEC, IFCC, ILAC, ISO, IUPAC, IUPAP, & OIML. (2008). *100:2008 Evaluation of Measurement Data—Guide to the Expression of Uncertainty in Measurement*. https://www.bipm.org/documents/20126/2071204/JCGM_100_2008_E.pdf/cb0ef43f-baa5-11cf-3f85-4dcd86f77bd6
- Brocchini, M., Drago, M., & Iovenitti, L. (1992). The Modelling of Short Waves in Shallow Waters. Comparison of Numerical Models Based on Boussinesq and Serre Equations. In *Coastal Engineering* (pp. 76–88). <https://doi.org/10.1061/9780872629332.006>
- Brown, S. A., Greaves, D. M., Magar, V., & Conley, D. C. (2016). Evaluation of turbulence closure models under spilling and plunging breakers in the surf zone. *Coastal Engineering*, 114, 177–193. <https://doi.org/https://doi.org/10.1016/j.coastaleng.2016.04.002>
- Brown, S. A., Magar, V., Greaves, D. M., & Conley, D. C. (2014). An Evaluation of Rans Turbulence Closure Models For Spilling Breakers. *Coastal Engineering Proceedings*, 1(34), waves.5. <https://doi.org/10.9753/icce.v34.waves.5>
- Deshpande, S. S., Anumolu, L., & Trujillo, M. F. (2012). Evaluating the performance of the two-phase flow solver interFoam. *Computational Science & Discovery*, 5(1). <https://doi.org/10.1088/1749-4699/5/1/014016>
- DHI (2023a). *MIKE 3 Wave Model FM. Hydrodynamic Module and Sand Transport User Guide*.
- DHI (2023b). *MIKE 3 Wave Model FM. Hydrodynamic module. Scientific Documentation*.
- DHI (2023c, June 29). *MIKE 3 Wave Model FM*. <https://www.mikepoweredbydhi.com/products/mike-3-wave-fm>
- Dingemans, M. W. (1994). *Comparison of computations with Boussinesq-like models and laboratory measurements (Report No. H1684.12)*.
- Domínguez, J. M., Crespo, A. J. C., Hall, M., Altomare, C., Wu, M., Stratigaki, V., Troch, P., Cappiotti, L., & Gómez-Gesteira, M. (2019). SPH simulation of floating structures with moorings. *Coastal Engineering*, 153, 103560. <https://doi.org/https://doi.org/10.1016/j.coastaleng.2019.103560>
- Domínguez, J. M., Fourtakas, G., Altomare, C., Canelas, R. B., Tafuni, A., García-Feal, O., Martínez-Estévez, I., Mokos,

- A., Vacondio, R., Crespo, A. J. C., Rogers, B. D., Stansby, P. K., & Gómez-Gesteira, M. (2021). DualSPHysics: from fluid dynamics to multiphysics problems. *Computational Particle Mechanics*.
<https://doi.org/10.1007/s40571-021-00404-2>
- Eldrup, M. R., & Lykke Andersen, T. (2019). Applicability of Nonlinear Wavemaker Theory. *Journal of Marine Science and Engineering*, 7(1).
<https://doi.org/10.3390/jmse7010014>
- Eldrup, M. R., & Lykke Andersen, T. (2020). Numerical Study on Regular Wave Shoaling, De-Shoaling and Decomposition of Free/Bound Waves on Gentle and Steep Foreshores. *Journal of Marine Science and Engineering*, 8(5).
<https://doi.org/10.3390/jmse8050334>
- English, A., Domínguez, J. M., Vacondio, R., Crespo, A. J. C., Stansby, P. K., Lind, S. J., Chiapponi, L., & Gómez-Gesteira, M. (2021). Modified dynamic boundary conditions (mDBC) for general-purpose smoothed particle hydrodynamics (SPH): application to tank sloshing, dam break and fish pass problems. *Computational Particle Mechanics*.
<https://doi.org/10.1007/s40571-021-00403-3>
- Fenton, J. D. (1988). The numerical solution of steady water wave problems. *Computers & Geosciences*, 14(3), 357–368. [https://doi.org/10.1016/0098-3004\(88\)90066-0](https://doi.org/10.1016/0098-3004(88)90066-0)
- Fernandez-Mora, A., Ribberink, J. S., van der Zanden, J., van der Werf, J. J., & Jacobsen, N. G. (2017). RANS-VOF modeling of hydrodynamics and sand transport under full-scale non-breaking and breaking waves. *Coastal Engineering Proceedings*, 1(35), sediment.29.
<https://doi.org/10.9753/icce.v35.sediment.29>
- Fourtakas, G., Domínguez, J. M., Vacondio, R., & Rogers, B. D. (2019). Local uniform stencil (LUST) boundary condition for arbitrary 3-D boundaries in parallel smoothed particle hydrodynamics (SPH) models. *Computers & Fluids*, 190, 346–361.
<https://doi.org/https://doi.org/10.1016/j.compfluid.2019.06.009>
- Fuhrman, D., Madsen, P., & Bingham, H. B. (2006). Numerical simulation of lowest-order short-crested wave instabilities. *Journal of Fluid Mechanics*, 563, 415–441.
<https://doi.org/10.1017/S0022112006001236>
- Gadelho, J., Lavrov, A., & Soares, C. G. (2014). Modelling the effect of obstacles on the 2D wave propagation with OpenFOAM. In C. Guedes Soares & E. Lopez Peña (Eds.), *Developments in Maritime Transportation and Exploitation of Sea Resources*. Taylor & Francis Group.
- González-Cao, J., Altomare, C., Crespo, A. J. C., Domínguez, J. M., Gómez-Gesteira, M., & Kısacık, D. (2019). On the accuracy of DualSPHysics to assess violent collisions with coastal structures. *Computers & Fluids*, 179, 604–612.
<https://doi.org/https://doi.org/10.1016/j.compfluid.2018.11.021>
- Gruwez, V., Altomare, C., Suzuki, T., Streicher, M., Cappietti, L., Kortenhaus, A., & Troch, P. (2020a). An Inter-Model Comparison for Wave Interactions with Sea Dikes on Shallow Foreshores. *Journal of Marine Science and Engineering*, 8(12).
<https://doi.org/10.3390/jmse80120985>
- Gruwez, V., Altomare, C., Suzuki, T., Streicher, M., Cappietti, L., Kortenhaus, A., & Troch, P. (2020b). Validation of RANS Modelling for Wave Interactions with Sea Dikes on Shallow Foreshores Using a Large-Scale Experimental Dataset. *Journal of Marine Science and Engineering*, 8(9). <https://doi.org/10.3390/jmse8090650>
- Hicks, J. B. H. (2020). *Development of a high-order potential flow solver for nonlinear wave-structure interaction*. [PhD Thesis]. Technical University of Denmark (DTU).
- Higuera, P., Lara, J. L., & Losada, I. J. (2013). Simulating coastal engineering processes with OpenFOAM®. *Coastal Engineering*, 71, 119–134.
<https://doi.org/https://doi.org/10.1016/j.coastaleng.2012.06.002>
- Holthuijsen, L. H. (2007). *Waves in Oceanic and Coastal Waters*. Cambridge University Press.
<https://doi.org/10.1017/CBO9780511618536>
- Hughes, S. A. (1993). *Physical Models and Laboratory Techniques in Coastal Engineering*. WORLD SCIENTIFIC.
<https://doi.org/10.1142/2154>
- Jacobsen, H. K., Hevia-Koch, P., & Wolter, C. (2019). Nearshore and offshore wind development: Costs and competitive advantage exemplified by nearshore wind in Denmark. *Energy for Sustainable Development*, 50, 91–100.
<https://doi.org/10.1016/j.esd.2019.03.006>
- Jacobsen, N. G., Fuhrman, D. R., & Fredsøe, J. (2012). A wave generation toolbox for the open-source CFD library: OpenFoam®. *International Journal for Numerical Methods in Fluids*, 70(9), 1073–1088.
<https://doi.org/https://doi.org/10.1002/fld.2726>
- Kamath, A., Bihs, H., Chella, M. A., & Arntsen, Ø. A. (2015). CFD Simulations of Wave Propagation and Shoaling over a Submerged Bar. *Aquatic Procedia*, 4, 308–316.
<https://doi.org/https://doi.org/10.1016/j.aqpro.2015.02.042>
- Kantamaneni, K., Rice, L., Du, X., Allali, B., & Yenneti, K. (2022). Are Current UK Coastal Defences Good Enough for Tomorrow? An Assessment of Vulnerability to Coastal Erosion. *Coastal Management*, 50(2), 142–159.
<https://doi.org/10.1080/08920753.2022.2022971>
- Karypis, G., & Kumar, V. (1998). A Fast and High Quality Multilevel Scheme for Partitioning Irregular Graphs. *SIAM Journal on Scientific Computing*, 20(1), 359–392.
<https://doi.org/10.1137/S1064827595287997>
- Khayyer, A., Gotoh, H., & Shimizu, Y. (2019). A projection-based particle method with optimized particle shifting for multiphase flows with large density ratios and discontinuous density fields. *Computers & Fluids*, 179, 356–371.
<https://doi.org/https://doi.org/10.1016/j.compfluid.2018.10.018>
- Kobayashi, N., Otta, A. K., & Roy, I. (1987). Wave Reflection and Run Up on Rough Slopes. *Journal of Waterway, Port, Coastal, and Ocean Engineering*, 113(3), 282–298.
[https://doi.org/10.1061/\(ASCE\)0733-950X\(1987\)113:3\(282\)](https://doi.org/10.1061/(ASCE)0733-950X(1987)113:3(282))
- Kramer, M. B., Andersen, J., Thomas, S., Bendixen, F. B., Bingham, H., Read, R., Holk, N., Ransley, E., Brown, S., Yu, Y.-H., Tran, T. T., Davidson, J., Horvath, C., Janson, C.-E., Nielsen, K., & Eskilsson, C. (2021). Highly Accurate Experimental Heave Decay Tests with a Floating Sphere: A Public Benchmark Dataset for Model Validation of Fluid–Structure Interaction. *Energies*, 14(2). <https://doi.org/10.3390/en14020269>
- Krystek, M., & Anton, M. (2007). A weighted total least-squares algorithm for fitting a straight line. *Measurement Science and Technology*, 18(11), 3438.
<https://doi.org/10.1088/0957-0233/18/11/025>
- Larsen, B. E., & Fuhrman, D. R. (2018). On the over-production of turbulence beneath surface waves in Reynolds-averaged Navier-Stokes models. *Journal of Fluid Mechanics*, 853, 419–460.
<https://doi.org/10.1017/jfm.2018.577>
- Larsen, B. E., Fuhrman, D. R., & Roenby, J. (2019). Performance of interFoam on the simulation of progressive waves. *Coastal Engineering Journal*, 61(3), 380–400.
<https://doi.org/10.1080/21664250.2019.1609713>
- Larsen, J., & Dancy, H. (1983). Open boundaries in short wave simulations—A new approach. *Coastal Engineering*, 7, 285–297. [https://doi.org/10.1016/0378-3839\(83\)90022-4](https://doi.org/10.1016/0378-3839(83)90022-4)
- Li, Y., Larsen, B. E., & Fuhrman, D. R. (2022). Reynolds stress turbulence modelling of surf zone breaking waves. *Journal of Fluid Mechanics*, 937, A7.
<https://doi.org/10.1017/jfm.2022.92>

- Lin, P., & Li, C. W. (2002). A σ -coordinate three-dimensional numerical model for surface wave propagation. *International Journal for Numerical Methods in Fluids*, 38(11), 1045–1068.
<https://doi.org/https://doi.org/10.1002/fld.258>
- Lin, P., & Liu, P. L.-F. (1998). A numerical study of breaking waves in the surf zone. *Journal of Fluid Mechanics*, 359, 239–264.
<https://doi.org/10.1017/S002211209700846X>
- Lowe, R. J., Buckley, M. L., Altomare, C., Rijnsdorp, D. P., Yao, Y., Suzuki, T., & Bricker, J. D. (2019). Numerical simulations of surf zone wave dynamics using Smoothed Particle Hydrodynamics. *Ocean Modelling*, 144, 101481.
<https://doi.org/https://doi.org/10.1016/j.ocemod.2019.101481>
- Ma, G., Shi, F., & Kirby, J. T. (2012). Shock-capturing non-hydrostatic model for fully dispersive surface wave processes. *Ocean Modelling*, 43–44, 22–35.
<https://doi.org/https://doi.org/10.1016/j.ocemod.2011.12.002>
- Madsen, P., & Fuhrman, D. (2006). Third-order theory for bichromatic bi-directional water waves. *Journal of Fluid Mechanics*, 557, 369–397.
<https://doi.org/10.1017/S0022112006009815>
- Monaghan, J. J. (1992). Smoothed Particle Hydrodynamics. *Annual Review of Astronomy and Astrophysics*, 30(1), 543–574.
<https://doi.org/10.1146/annurev.aa.30.090192.002551>
- Monaghan, J. J. (1994). Simulating Free Surface Flows with SPH. *Journal of Computational Physics*, 110, 399–406.
<https://doi.org/http://dx.doi.org/10.1006/jcph.1994.1034>
- OpenCFD Ltd (2023). *OpenCFD*. <https://www.openfoam.com>
- Padova, D. De, Dalrymple, R. A., & Mossa, M. (2014). Analysis of the artificial viscosity in the smoothed particle hydrodynamics modelling of regular waves. *Journal of Hydraulic Research*, 52(6), 836–848.
<https://doi.org/10.1080/00221686.2014.932853>
- Park, H., Do, T., Tomiczek, T., Cox, D. T., & van de Lindt, J. W. (2018). Numerical modeling of non-breaking, impulsive breaking, and broken wave interaction with elevated coastal structures: Laboratory validation and inter-model comparisons. *Ocean Engineering*, 158, 78–98.
<https://doi.org/https://doi.org/10.1016/j.oceaneng.2018.03.088>
- Pellegrini, F., & Roman, J. (1996). Scotch: A software package for static mapping by dual recursive bipartitioning of process and architecture graphs. *High-Performance Computing and Networking*, 493–498.
- Quinlan, N. J., Basa, M., & Lastiwka, M. (2006). Truncation error in mesh-free particle methods. *International Journal for Numerical Methods in Engineering*, 66(13), 2064–2085.
<https://doi.org/https://doi.org/10.1002/nme.1617>
- Qwist, J. R. K., & Christensen, E. D. (2023). Development and implementation of a Direct Surface Description method for free surface flows in OpenFOAM. *Coastal Engineering*, 179, 104227.
<https://doi.org/https://doi.org/10.1016/j.coastaleng.2022.104227>
- Roache, P. J. (1998). *Verification and validation in computational science and engineering*. Albuquerque, N.M.: Hermosa Publishers.
- Rodi, W. (1980). *Turbulence Models and Their Application in Hydraulics - A State of The Art Review*. IAHR.
- Rodi, W. (1984). *Turbulence Models and Their Application in Hydraulics*. IAHR.
- Roenby, J., Larsen, B. E., Bredmose, H., & Jasak, H. (2017, June 15). A new volume-of-fluid method in OpenFOAM. *7th International Conference on Computational Methods in Marine Engineering*.
- Rota Roselli, R. A., Vernengo, G., Altomare, C., Brizzolara, S., Bonfiglio, L., & Guercio, R. (2018). Ensuring numerical stability of wave propagation by tuning model parameters using genetic algorithms and response surface methods. *Environmental Modelling & Software*, 103, 62–73.
<https://doi.org/https://doi.org/10.1016/j.envsoft.2018.02.003>
- Rota Roselli, R. A., Vernengo, G., Brizzolara, S., Brizzolara, S., & Guercio, R. (2019). SPH Simulation of Periodic Wave Breaking in the Surf Zone – A Detailed Fluid Dynamic Validation. *Journal of Ocean Engineering*, 176, 20–30.
<https://doi.org/10.1016/j.oceaneng.2019.02.013>
- Schäffer, H. A. (1996). Second-order wavemaker theory for irregular waves. *Ocean Engineering*, 23(1), 47–88.
[https://doi.org/10.1016/0029-8018\(95\)00013-B](https://doi.org/10.1016/0029-8018(95)00013-B)
- Schmitt, P., Windt, C., Davidson, J., Ringwood, J. V., & Whittaker, T. (2020). Beyond VoF: alternative OpenFOAM solvers for numerical wave tanks. *Journal of Ocean Engineering and Marine Energy*, 6(3), 277–292.
<https://doi.org/10.1007/s40722-020-00173-9>
- Shih, T.-S., Zhu, J., & Lumley, J. (1993). A Realizable Reynolds Stress Algebraic Equation Model. *Symposium on Turbulence Shear Flows*.
- Stagonas, D., Higuera, P., & Buldakov, E. (2018). Simulating Breaking Focused Waves in CFD: Methodology for Controlled Generation of First and Second Order. *Journal of Waterway, Port, Coastal, and Ocean Engineering*, 144(2), 6017005.
[https://doi.org/10.1061/\(ASCE\)WW.1943-5460.0000420](https://doi.org/10.1061/(ASCE)WW.1943-5460.0000420)
- Ting, F. C. K., & Kirby, J. T. (1994). Observation of undertow and turbulence in a laboratory surf zone. *Coastal Engineering*, 24(1), 51–80.
[https://doi.org/https://doi.org/10.1016/0378-3839\(94\)90026-4](https://doi.org/https://doi.org/10.1016/0378-3839(94)90026-4)
- Toro, E. F., Spruce, M., & Speares, W. (1994). Restoration of the contact surface in the HLL-Riemann solver. *Shock Waves*, 4(1), 25–34.
<https://doi.org/10.1007/BF01414629>
- Torres-Freyermuth, A., Losada, I. J., & Lara, J. L. (2007). Modeling of surf zone processes on a natural beach using Reynolds-Averaged Navier-Stokes equations. *Journal of Geophysical Research: Oceans*, 112(C9).
<https://doi.org/https://doi.org/10.1029/2006JC004050>
- Vacondio, R., Altomare, C., De Leffe, M., Hu, X., Le Touzé, D., Lind, S., Marongiu, J.-C., Marrone, S., Rogers, B. D., & Souto-Iglesias, A. (2021). Grand challenges for Smoothed Particle Hydrodynamics numerical schemes. *Computational Particle Mechanics*, 8(3), 575–588.
<https://doi.org/10.1007/s40571-020-00354-1>
- Vacondio, R., Rogers, B. D., Stansby, P. K., Mignosa, P., & Feldman, J. (2013). Variable resolution for SPH: A dynamic particle coalescing and splitting scheme. *Computer Methods in Applied Mechanics and Engineering*, 256, 132–148.
<https://doi.org/https://doi.org/10.1016/j.cma.2012.12.014>
- Vukčević, V., Jasak, H., & Gatin, I. (2017). Implementation of the Ghost Fluid Method for free surface flows in polyhedral Finite Volume framework. *Computers & Fluids*, 153, 1–19.
<https://doi.org/https://doi.org/10.1016/j.compfluid.2017.05.003>
- Weller, H. G., Tabor, G., Jasak, H., & Fureby, C. (1998). A tensorial approach to computational continuum mechanics using object-oriented techniques. *Computer in Physics*, 12(6), 620–631.
<https://doi.org/10.1063/1.168744>
- Wendland, H. (1995). Piecewise polynomial, positive definite and compactly supported radial functions of minimal degree. *Advances in Computational Mathematics*, 4(1), 389–396.
<https://doi.org/10.1007/BF02123482>

Wroniszewski, P. A., Verschaeve, J. C. G., & Pedersen, G. K. (2014). Benchmarking of Navier–Stokes codes for free surface simulations by means of a solitary wave. *Coastal Engineering*, 91, 1–17. <https://doi.org/https://doi.org/10.1016/j.coastaleng.2014.04.012>

Zhang, F., Crespo, A., Altomare, C., Domínguez, J., Marzeddu, A., Shang, S., & Gómez-Gesteira, M. (2018). DualSPHysics: A numerical tool to simulate real breakwaters. *Journal*

of Hydrodynamics, 30(1), 95–105. <https://doi.org/10.1007/s42241-018-0010-0>

Zhang, H., & Schäffer, H. A. (2007). Approximate Stream Function wavemaker theory for highly non-linear waves in wave flumes. *Ocean Engineering*, 34(8–9), 1290–1302. <https://doi.org/10.1016/J.OCEANENG.2006.04.010>

Appendix A. Convergence Analyses

The convergence analyses of wave conditions 1-3 are provided in the present appendix. Refer to Section 6 for the description of the convergence criteria and the convergence analyses of wave condition 4.

Appendix A.1 Convergence of i-VoF (wave conditions 1-3)

The convergence of wave condition 1 with N_{CH} can be seen in Figs. A1 and A2, and the convergence of wave condition 2 with N_{CH} can be seen in Figs. 3 and 4. With wave conditions 1 and 2, for maximum C_{FL} above 0.5 and 0.4, respectively, instabilities in the simulations arose. Variation of the maximum C_{FL} below these values yielded only very small differences in the surface elevation time series with evaluation metrics smaller than 1% (the nature of which is discussed in Section 6); these figures have therefore been omitted. The convergence of wave condition 3 with N_{CH} can be seen in Figs. 5 and 6 while the convergence with the maximum C_{FL} can be seen in Figs. 7 and 8.

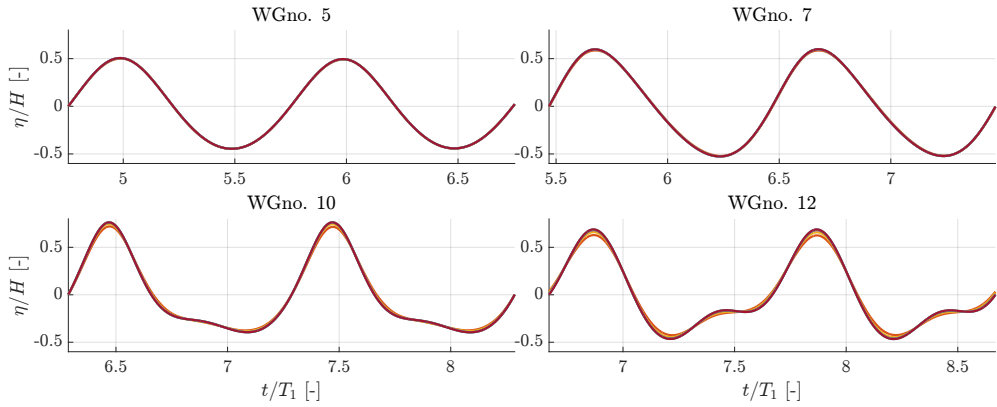


Fig. A1. Influence of N_{CH} on the surface elevation time series for selected WGnos.; wave condition 1 and maximum $C_{FL} = 0.10$.

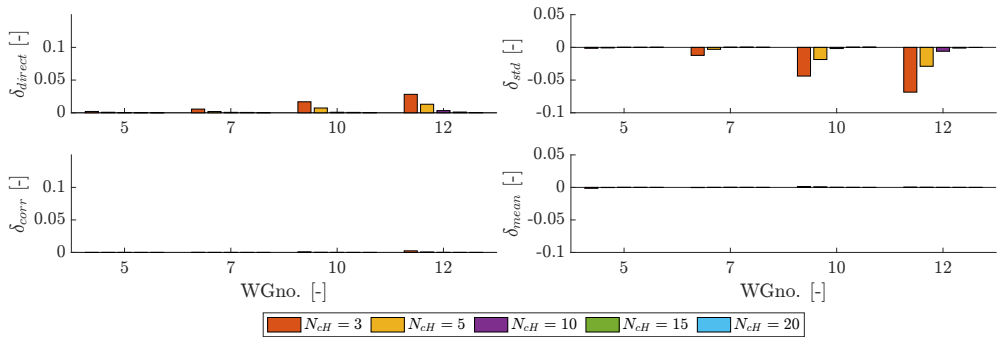


Fig. A2. Influence of N_{CH} on evaluation metrics for selected WGnos.; wave condition 1 and maximum $C_{FL} = 0.10$.

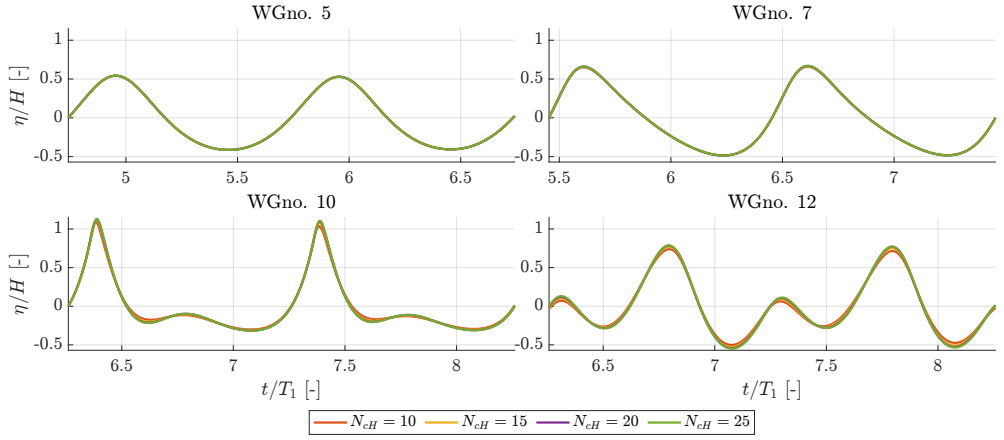


Fig. A 3. Influence of N_{CH} on the surface elevation time series for selected WGnos.; wave condition 2 and maximum $C_{FL} = 0.10$.

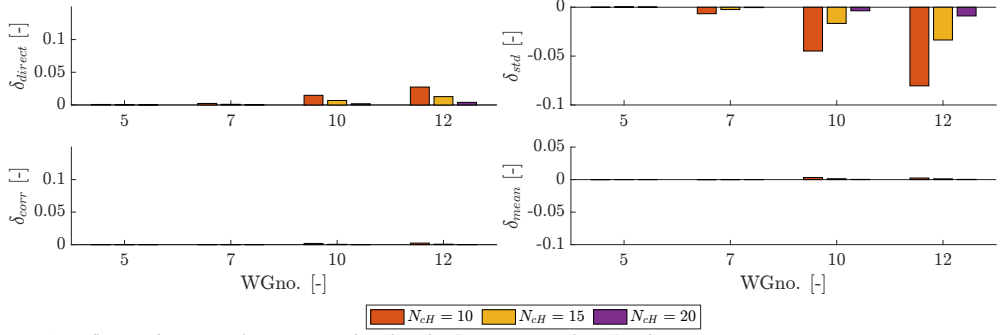


Fig. A 4. Influence of N_{CH} on evaluation metrics for selected WGnos.; wave condition 2 and maximum $C_{FL} = 0.10$.

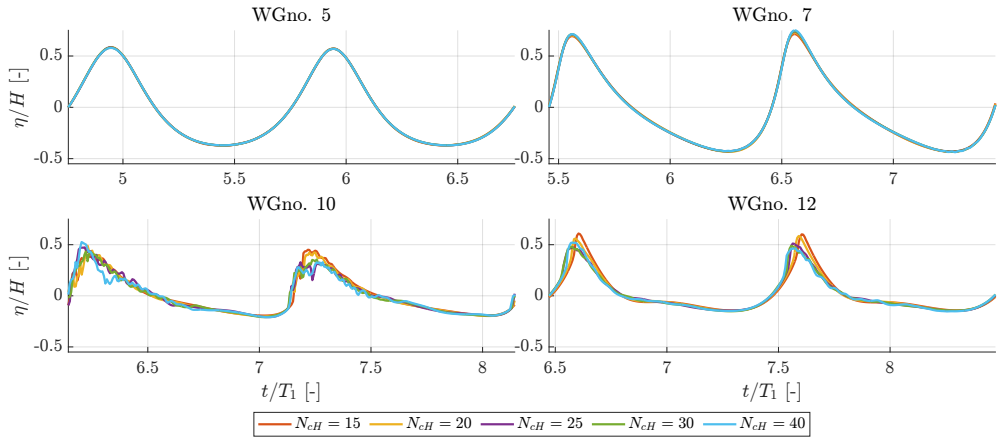


Fig. A 5. Influence of N_{CH} on the surface elevation time series for selected WGnos.; wave condition 3 and maximum $C_{FL} = 0.10$.

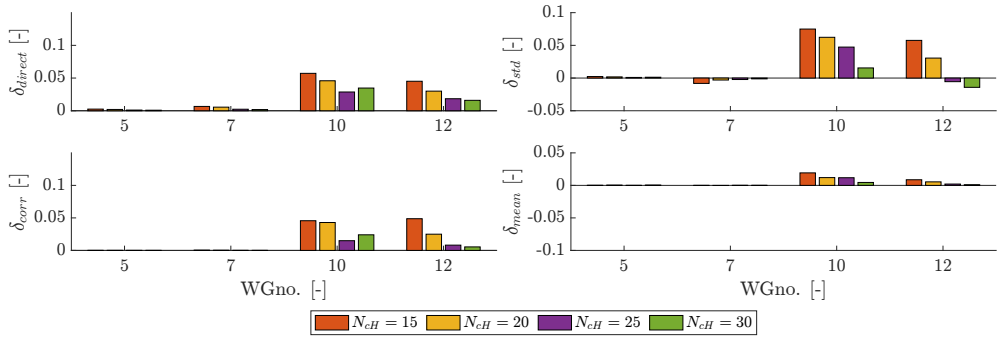


Fig. A 6. Influence of N_{CH} on evaluation metrics for selected WGnos.; wave condition 3 and maximum $C_{FL} = 0.10$.

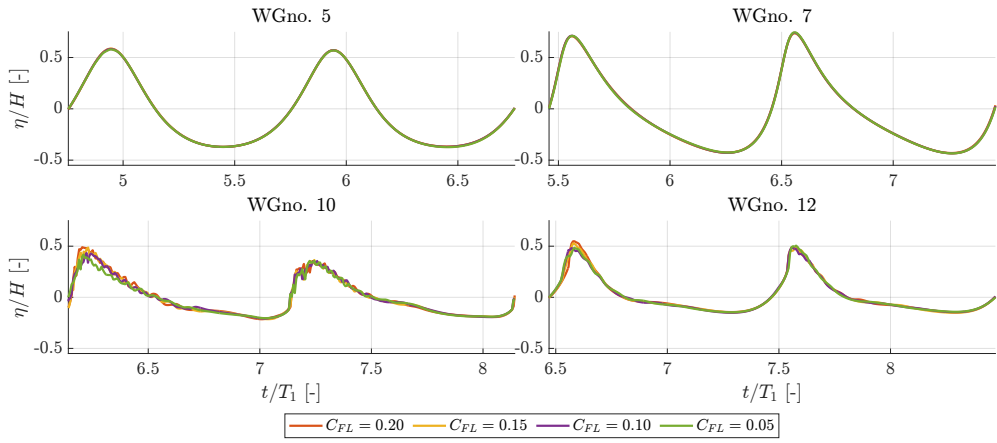


Fig. A 7. Influence of the maximum C_{FL} on the surface elevation time series for selected WGnos.; wave condition 3 and $N_{CH} = 30$.

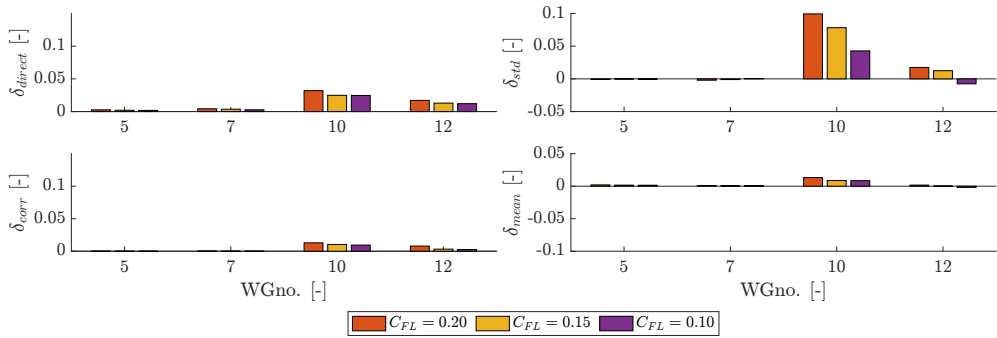


Fig. A 8. Influence of the maximum C_{FL} on the evaluation metrics for selected WGnos.; wave condition 3 and $N_{CH} = 30$.

Appendix A.2 Convergence of M -sigma (wave conditions 1-3)

The convergence with N_{cL} in wave conditions 1 and 2 can be seen in Figs. 9-10 and Figs. 11-12, respectively. With $N_{cL} = 60$, $N_{\sigma} \geq 5$ yielded negligible differences in both surface elevation time series and associated evaluation metrics ($<1\%$) for wave conditions 1 and 2, and the variation herewith are therefore not included as figures. The convergence with N_{cL} and N_{σ} in wave condition 3 can be seen in Figs. 13-16. For wave condition 3, the crest height at $t/T_1 \approx 7.2$ recorded with WGno. 10 deviates with about 10% for $N_{cL} = 100$ relative to $N_{cL} = 200$, whereas for $N_{cL} = 150$ the deviation is about 1%, see Fig. A 13. Based on this $N_{cL} = 150$ is assessed sufficiently converged rather than $N_{cL} = 100$ despite of both having all evaluation metrics less than 5%.

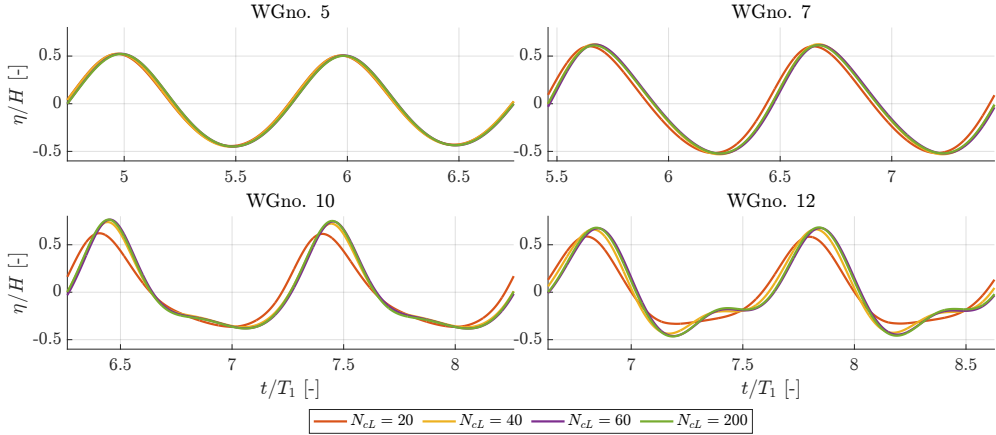


Fig. A 9. Influence of N_{cL} on the surface elevation time series for selected WGnos.; wave condition 1 and $N_{\sigma}=5$.

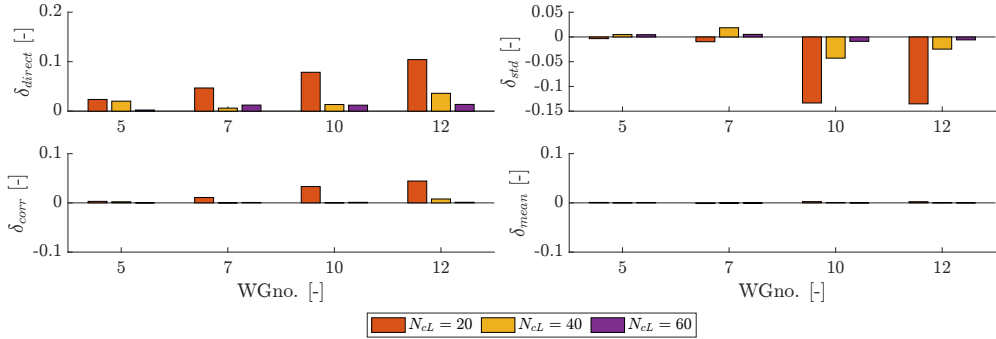


Fig. A 10. Influence of N_{cL} on evaluation metrics for selected WGnos.; wave condition 1 and $N_{\sigma}=5$.

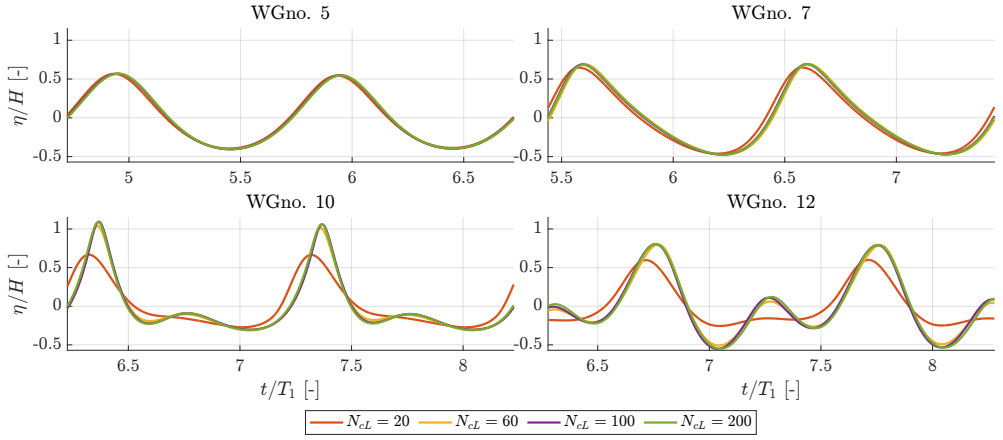


Fig. A 11. Influence of N_{cL} on the surface elevation time series for selected WGnos.; wave condition 2 and $N_\sigma=5$.

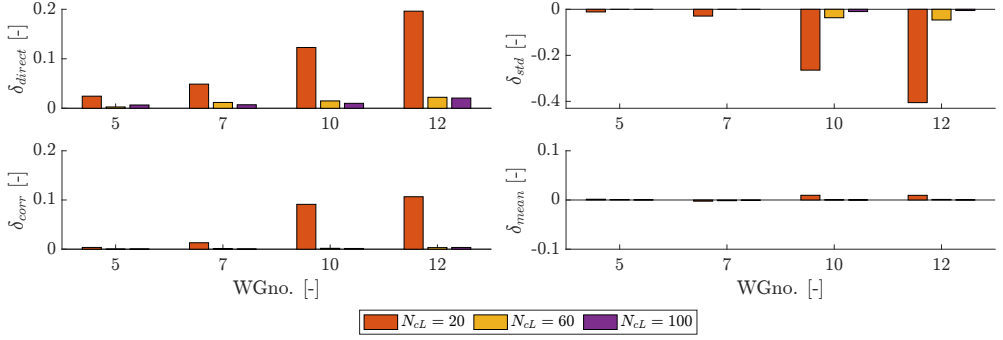


Fig. A 12. Influence of N_{cL} on evaluation metrics for selected WGnos.; wave condition 2 and $N_\sigma=5$.

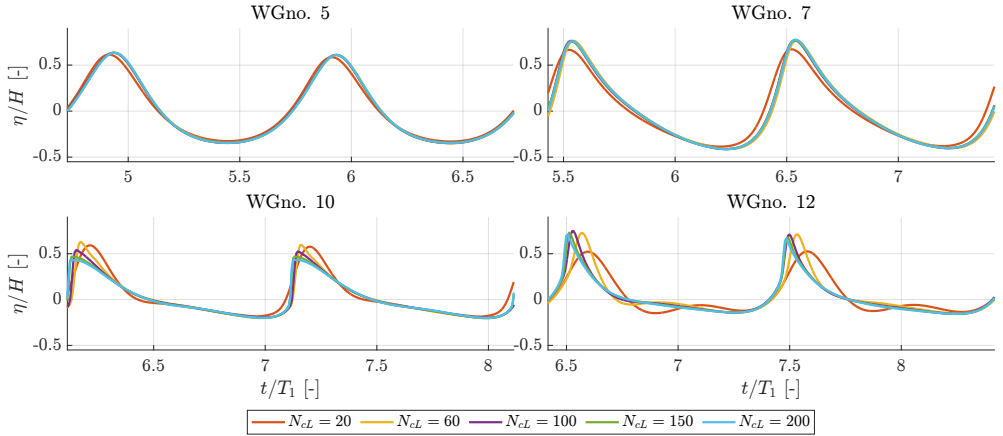


Fig. A 13. Influence of N_{cL} on the surface elevation time series for selected WGnos.; wave condition 3 and $N_\sigma=15$.

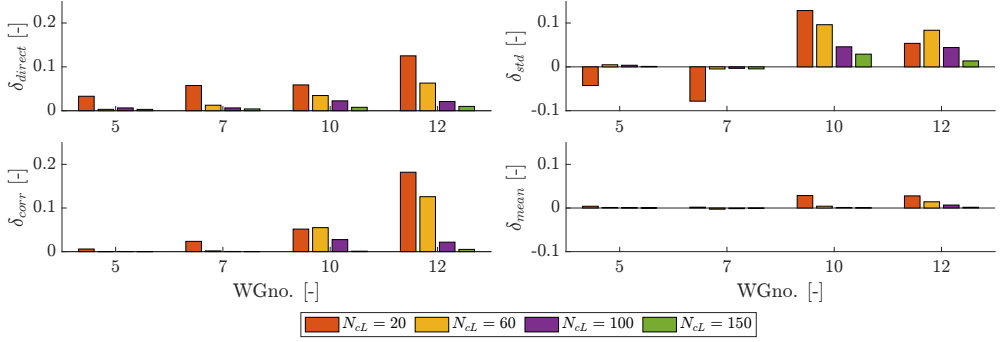


Fig. A 14. Influence of N_{cL} on evaluation metrics for selected WGnos.; wave condition 3 and $N_g=15$.

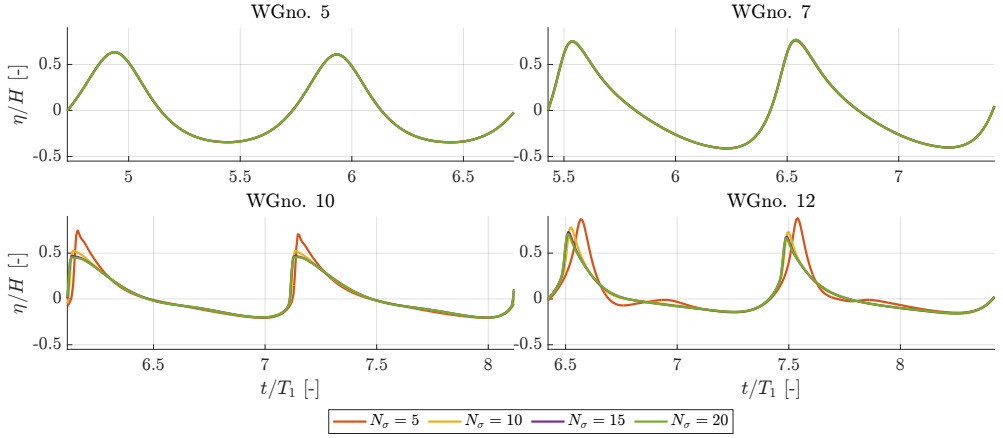


Fig. A 15. Influence of N_σ on the surface elevation time series for selected WGnos.; wave condition 3 and $N_{cL} = 150$.

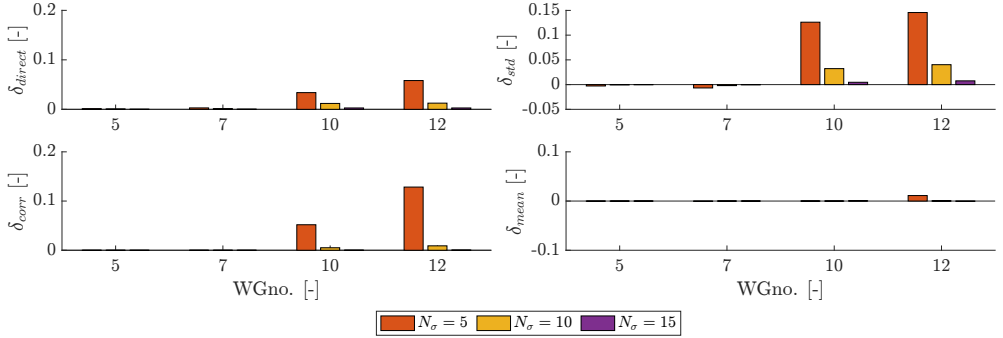


Fig. A 16. Influence of N_σ on evaluation metrics for selected WGnos.; wave condition 3 and $N_{cL} = 150$.

Appendix A.3 Convergence of D-SPH (wave conditions 1-3)

The convergence of the D-SPH model with N_{cH} in wave conditions 1-3 can be seen in Figs. 17-22. In wave conditions 1 and 2, $N_{pH} \geq 20$ yields only small differences in the surface elevation time series and all evaluation metrics are below 5%. Based on this D-SPH is assessed converged for $N_{pH} = 20$. Notable deviations and evaluations metrics above 5% were

present between $N_{pH} = 20$ and $N_{pH} = 40$ at WGnos. 10 and 12 in wave condition 3 from which an additional simulation with $N_{pH} = 60$ was completed. The surface elevation time series with $N_{pH} = 60$ was significantly more erratic at WGno. 10 than the simulations with $N_{pH} \in \{20,40\}$. The convergence criteria imposed in the other convergence analyses (across numerical models) was thus not met for wave condition 3 as discussed in Sections 6.3 and 8.3. Small variations in N_{pH} was found to have the potential to change results significantly in the breaking wave conditions which could have altered the conclusion of the convergence analysis of wave condition 3 but not removed the issue of inconsistency hereof.

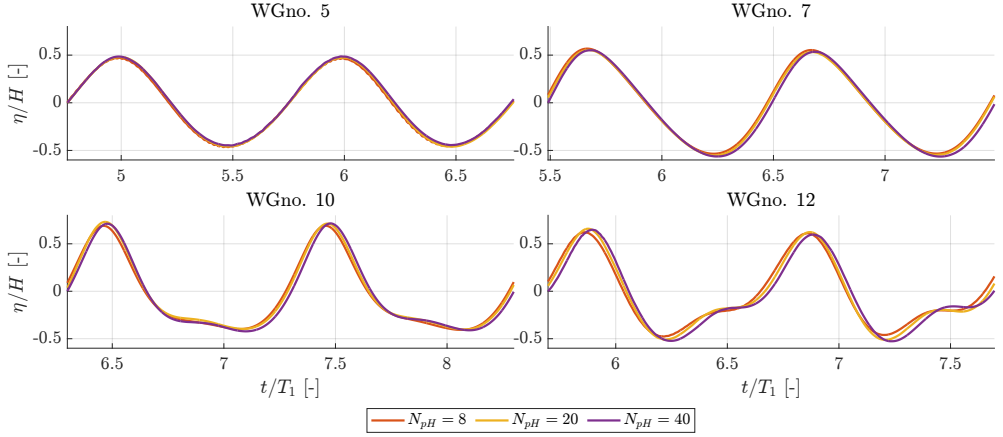


Fig. A 17. Influence of N_{pH} on the surface elevation time series for selected WGnos.; wave condition 1.

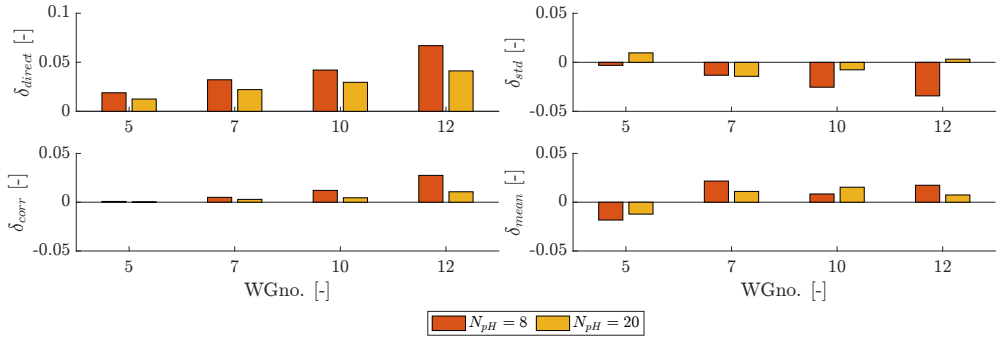


Fig. A 18. Influence of N_{pH} on evaluation metrics for selected WGnos.; wave condition 1.

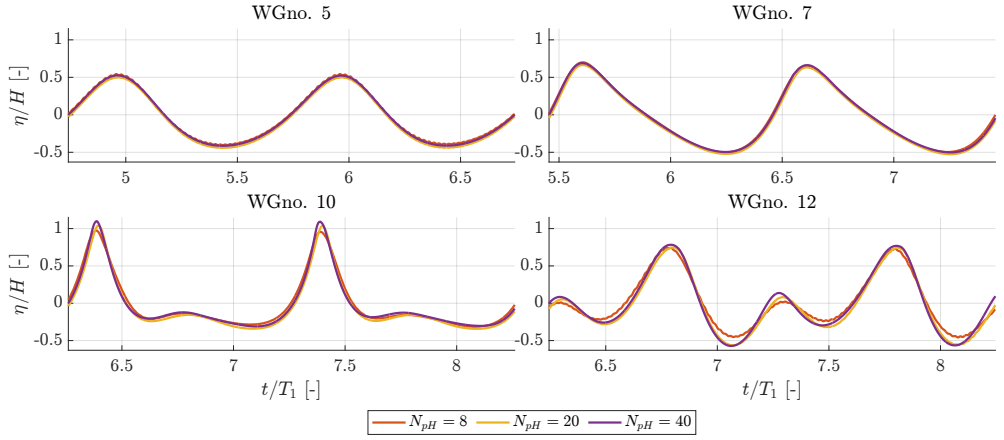


Fig. A 19. Influence of N_{pH} on the surface elevation time series for selected WGnos.; wave condition 2.

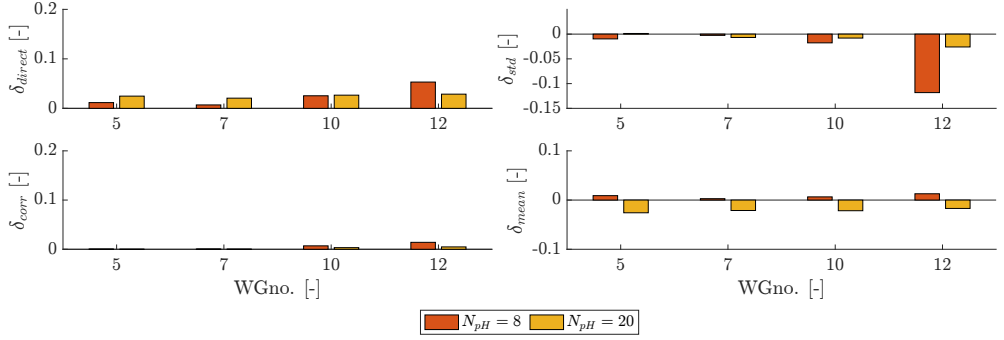


Fig. A 20. Influence of N_{pH} on evaluation metrics for selected WGnos.; wave condition 2.

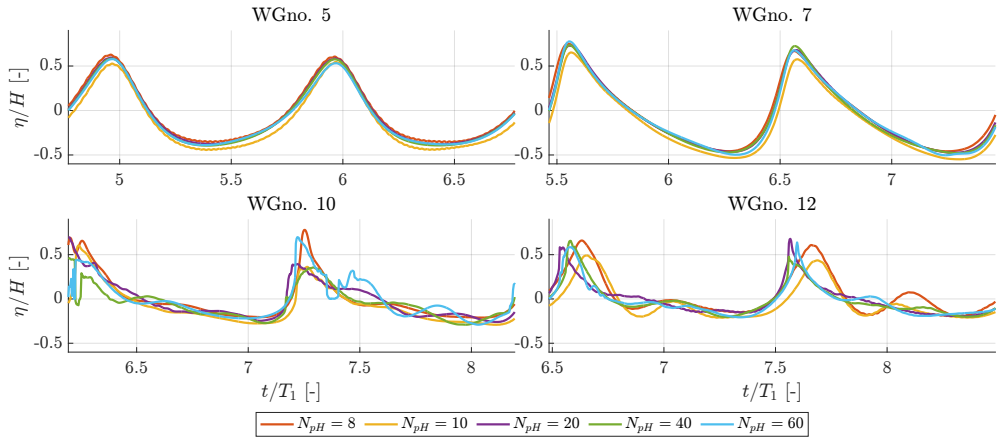


Fig. A 21: Influence of N_{pH} on the surface elevation time series for selected WGnos.; wave condition 3.

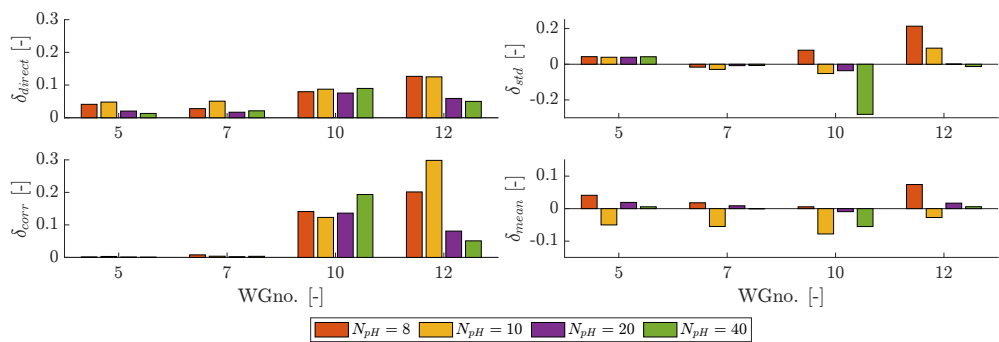


Fig. A 22: Influence of N_{pH} on evaluation metrics for selected WGnos.; wave condition 3.

Hydrodynamic Modelling of Offshore Renewables
Experimental Benchmark Datasets and Numerical Simulation

by Jacob Andersen

SUMMARY

The transition from fossil fuels to renewable energy sources is critical to reduce greenhouse gas emissions and increase global energy access and security. To harness the abundant renewable energy resources from and at the ocean, the European Union has set ambitious targets to increase its installed capacity of offshore renewable energy technologies by 2050. To reach these targets, the levelized cost of energy of emerging offshore renewables must be reduced in which accurate and efficient hydrodynamic models are paramount to maintain low expenditures and agility throughout the design process.

The present dissertation revolves around the hydrodynamic modelling of offshore renewables with emphasis on offshore wind turbines (bottom-fixed and floating) and wave energy converters. To establish credibility of hydrodynamic models, verification and validation are vital. The dissertation presents validation experiments dedicated to the construction of public experimental benchmark datasets as well as numerical studies aimed at improving the understanding of the governing hydrodynamics and the suitability of different hydrodynamic models for selected flow problems. Furthermore, the dissertation accounts for hydrodynamic investigations of the early designs of a large monopile with perforations, to reduce fatigue wave loads, and the wave-activated body of a wave energy converter.